Hydrodynamic and Magnetohydrodynamic Flows Around a 180-Degree Sharp Bend

by

Mohd Azan Mohammed Sapardi

A Thesis submitted to Monash University

for the degree of

Doctor of Philosophy

March 2018

Department of Mechanical and Aerospace Engineering

Monash University

To my beautiful family.

Statement of Originality

This thesis contains no material that has been accepted for the award of a degree or diploma in this or any other university. To the best of the candidate's knowledge and belief, this thesis contains no material previously published or written by another person except where due reference is made in the text of this thesis.

Candidate: Mohd Azan Mohammed Sapardi

December 2017

The knowledge of anything,
since all things have causes,
is not acquired or complete
unless it is known by its causes.

Avicenna.

Abstract

The increasing demand for energy around the world, especially those that require the depleting fossil resources, has encouraged the invention of renewable energy technology. Nuclear fusion is theoretically known to be very promising as an alternative energy source. It is promised to be clean, cheap, self-sustained and renewable. One experimental technology for harnessing nuclear fusion is magnetic fusion. However, a significant problem in energy conversion from nuclear energy to electric energy is the efficiency of heat transfer due to magnetohydrodynamic effects caused by the magnetic field used to confine the plasma. This indirectly reduces the thermal-hydraulic performance of the liquid metal coolant in the cooling blankets. There have been numerous efforts to improve the heat transfer efficiency; especially by introducing a solid bluff body as a vortex promoter. In this thesis, the main focus is on a key element of heat exchangers, namely the 180-degree sharp bend, where the liquid metal coolant is brought to the vicinity of the plasma-facing wall and turned away with extra heat accumulated in the turning part. A numerical investigation of an electrically conducting liquid metal moving in a 180-degree sharp bend is presented. The primary motivation of this study is to understand the characteristics of the flow around a 180-degree sharp bend in detail and to exploit its nature to improve the heat transfer from a heated wall in a duct under a strong uniform magnetic field.

For a steady hydrodynamic flow around a 180-degree sharp bend, at all bend opening ratios (ratio between the bend opening width and the inlet height), β, the flow is found to be unstable beyond a critical Reynolds number to three-dimensional. By using a linear stability analysis, it is predicted that the three-dimensional transition is via a synchronous instability of the steady flows. An accurate global linear stability analysis was conducted within a range of Re and β where the flow is steady-state and two-dimensional. For $0.2 \leq \beta \leq 1$, the two-dimensional base flow changed from steady to unsteady at higher Reynolds number as bend opening ratio increases. The analysis shows that at the onset of instability, the base flow becomes three-dimensionally unstable via two different modes; a spanwise oscillating mode for $\beta = 0.2$ and a spanwise synchronous mode for $\beta \geq 0.3$. The critical Reynolds number and the spanwise wavelength of perturbations increase as β increases. For $1 < \beta \leq 2$, the critical Reynolds number for the onset of unsteadiness and the spanwise wavelength decrease as β increases. Finally, for $2 < \beta \leq 5$, the critical Reynolds number and spanwise instability wavelength remain

almost constant.

The stability analysis is complemented by the study of the transient energy growth of two-dimensional optimal linear perturbations to two-dimensional flow. This study only focused on the evolution of infinitesimal two-dimensional perturbations as these are the most relevant to the quasi-two-dimensional magnetohydrodynamic flows considered later in this thesis. It is found that the two-dimensional steady state flow is convectively unstable at Reynolds numbers much lower than the onset of three-dimensional global instability. The critical Reynolds number increases as the bend opening ratio increases from $\beta = 0.2$ to 0.8, but decreases when $\beta \geq 0.8$. The location of the centroid of the energy distribution for maximum transient growth is downstream of the reattachment point of the primary recirculation bubble behind the bend. Direct numerical simulations with perturbed inflow are found to agree with the prediction from the transient growth analysis.

The critical Reynolds number for the transition from steady to unsteady magnetohydrodynamic flow is determined as a function of Hartmann friction parameter H and bend opening ratio. The variation of the primary recirculation bubble length in the steady flow regime is determined as a function of Reynolds number, Hartmann friction parameter and bend opening ratio, and a general correlation is introduced. The characteristic of heat transfer on the heated side wall is weakly dependant on the Hartmann number but is strongly dependant on the bend opening ratio. Finally, the overall pressure drop for $0.2 \leq \beta \leq 2$, $100 \leq H \leq 500$ and $1 \leq Re \leq 2000$ is found to be almost linear with the ratio of H/Re.

Acknowledgments

For the unrelenting support and guidance throughout my candidature, I would like to thank my supervisor Associate Professor Gregory J. Sheard. This thesis would not be advanced to the present state without his continuous encouragement and positivity. Hence, I really appreciate his enthusiasm and persistence.

I would also like to thank to my co-supervisor, Dr. Wisam, who has guided me from the beginning until now. He generously shared his ideas on my research everyday made this work more manageable. My special thanks also extend to my another co-supervisor, Professor Alban Pothèrat for providing fresh ideas and advices. His willingness to share his knowledge has significantly improved my understanding on my work.

I am grateful to the Department of Mechanical Engineering, Monash University, for providing the resources necessary for the completion of this study. This research would not have been possible without the financial support provided by the Ministry of Education Malaysia (MOE) and International Islamic University Malaysia. I would also like to acknowledge the Monash e-Research Centre and the National Computational Infrastructure (NCI) for granting access to their high performance computing facilities, which were crucial to this research. Thank you also to Lilian Khaw and Jane Moodie for guiding me with my papers and thesis writing.

Special thanks also given to my colleagues, Ahmad, Tony, Tze Kih, Zhi, Oliver, Mehdi and Sajjad for the good company at the lunch times that provided some relief and encouragement to keep working hard and strive for success. I wish you all the very best in your future endeavours.

To my parents, Sapardi and Mislijah, my parents in-law, Zainan and Sharifah, thank you for continuously praying for my success. For my children, Luqman and Izzah, thanks for being a part of my life, their cuteness and laughter are my best medicine. Finally, my warmest appreciation to my wife and best friend, Nur Hidayah, for giving me love, encouragement and support more than I ever deserved.

Publications arising from thesis

Sapardi, Azan M., Hussam, Wisam K., Pothérat, Alban and Sheard, Gregory J. 2017 Linear stability of confined flow around a 180-degree sharp bend. *J. Fluid Mech.* **822**, 813–847.

Sapardi, Azan M.,d Hussam, Wisam K.,d Pothérat, Alban and Sheard, Gregory J. 2014 Three-dimensional linear stability analysis of the flow around a sharp 180-degree bend. *In Proceedings of the 19th Australasian Fluid Mechanics Conference (19th AFMC)*, (Eds: H. Chowdhury & F. Alam, Pub: Australasian Fluid Mechanics Society, ISBN: 978-0-646-59695-2, Paper 222), RMIT University, Melbourne, Australia, 8-11 December 2014.

Sapardi, Azan M., Hussam, Wisam K., Pothérat, Alban and Sheard, Gregory J. 2014 Quasi-two-dimensional MHD duct flow around a 180-Degree sharp bend in a strong magnetic field. *In Proceedings of the 19th Australasian Fluid Mechanics Conference (19th AFMC)*, (Eds: H. Chowdhury & F. Alam, Pub: Australasian Fluid Mechanics Society, ISBN: 978-0-646-59695-2, Paper 223), RMIT University, Melbourne, Australia, 8-11 December 2014.

Sapardi, Azan M., Hussam, Wisam K., Pothérat, Alban and Sheard, Gregory J. 2014 Influence of strong spanwise magnetic field on the quasi-two-dimensional MHD flow in a 180-degree sharp bend. *In Proceedings of the Eleventh International Conference on CFD in the Minerals and Process Industries*, (Eds: C. B. Solnordal, P. Liovic, G. W. Delaney, S. J. Cummins, M. P. Schwarz and P. J. Witt, Pub: CSIRO, Australia, 163HAM), Melbourne Convention and Exhibition Centre, Melbourne, Australia, 7-9 December, 2015.

Nomenclature

List nomenclature here.

Symbol	Description
$\S$	Thesis section
$\int$	Integration
∇	Vector gradient operator (grad)
∇^2	Del squared (or div grad) operator
$\sum_{i=a}^{b}$	Sum of arguments with j incrementing from a
$\log$	Logarithm to the base-10
$\log_{\mathrm{e}}$	Natural logarithm
β	Bend opening ratio
β_{eff}	Effective opening ratio
$\triangle t$	Time step
δ_H	Hartmann boundary layer thickness
δ_S	Shercliff boundary layer thickness
μ	Complex eigenvalue
μ_m	Magnetic permeability
ν	Kinematic viscosity
ρ	Mass density
θ	Temperature field
σ	Growth rate of linear instability mode over n^{th} period in linear stability analysis
σ_e	Electrical conductivity
σ_n	Linear growth rate in the Landau equation
σ_w	Electrical conductivity of the channel walls perpendicular to the magnetic field

Continued on the next page.

Continued from previous page.

Symbol	Description
Ω	Computational domain
ω	Angular velocity
A	Non-dimensional angular velocity amplitude
A_n	Complex amplitude in Landau equation
a	Characteristic length scale, duct height
α	Aspect ratio of rectangular cross-section
$\mathscr{A}(\tau)$	Linear evolution operator over a time τ
$\mathscr{A}^*(\tau)$	Adjoint of linear evolution operator over a time τ
B	Magnetic field strength
β	Bend opening ratio
β_{eff}	Effective bend opening ratio
$\mathbf{B}$	Magnetic field vector
B_i	Induced magnetic field
C	Constant
c_n	Landau constant
C_{p}	Constant pressure specific heat of the liquid metal
C_{Re}	Critical parameter ratio
DN**u'**	Linearized advection term of perturbation field
$\text{DN}^*\mathbf{u}*$	Adjoint advection operator
E	Kinetic energy per unit mass of the perturbation
$\mathbf{E}$	Electrical field vector
erf	Gauss error function
ϵ	Electric permittivity
ε	Vorticity profile
G	Energy growth
$G_{\max}$	Global maximum of energy growth
i	Imaginary number ($i = \sqrt{-1}$)
Ha	Hartmann number
H	Hartmann friction parameter

Continued on the next page.

Continued from previous page.

Symbol	Description
$\mathbf{J}$	Current density vector
K_p	Non-dimensional pressure gradient
k	Spanwise wavenumber of the infinitesimal perturbations
k_c	Critical spanwise wavenumber
k_p	Thermal conductivity
L_z	Length of the duct in the spanwise direction
L_R1	Length of the primary recirculation bubble
L_R2	Length of the secondary recirculation bubble
Ma	Mach number
N	Stuart number (Interaction parameter)
Nu	Nusselt number
N_{el}	Number of elements employed in computations
N_p	Element polynomial degree employed in computations
n_H	Number of Hartmann walls
P	Pressure
p	Kinematic pressure field
p'	Infinitesimal fluctuating disturbance pressure
ϕ	Electrical potential
Pr	Prandtl number
Q_v	Non-dimensional flow rate
R^2	The coefficient of determination
Re	Reynolds number
Re_c	Critical Reynolds number for the onset of two-dimensional unsteadiness
Re_3D	Critical Reynolds number for the onset of three-dimensional linear global instability
Re_TG	Critical Reynolds number for the onset of transient energy growth
Re_m	Magnetic Reynolds number
q	Volume charge density
t	Time

Continued on the next page.

Continued from previous page.

Symbol	Description
t_w	Thickness of the walls perpendicular to the field
t_H	Hartmann braking time
τ	Time interval
$\tau_{\max}$	Maximum time interval for the maximum energy growth
$\mathbf{U}$	Steady two-dimensional base flow velocity
$\mathbf{u}$	Velocity vector
u	x-direction velocity component
$\mathbf{u}'$	Infinitesimal fluctuating disturbance velocity
St	Strouhal number

Contents

Chapter 1

Introduction

A numerical study of the flow around a 180-degree sharp bend has been studied. This thesis covers the stability of the hydrodynamic flow and also the effect of a strong spanwise magnetic field on an electrically conducting fluid (e.g. liquid metal). In this chapter, a brief overview of the fundamental concepts relating to hydrodynamics and magnetohydrodynamics is presented. A description of the problem is discussed later in this chapter. The aims of this study are stated, and finally, the structure of the thesis is outlined.

1.1 Magnetohydrodynamics

The first recorded use of the word magnetohydrodynamics was initiated by Alfvén (1942) who was awarded a Nobel Prize in Physics for his contribution in that field. Magnetohydrodynamics (MHD), also known as hydromagnetics, is the branch of continuum fluid mechanics which involves the motion of electrically conducting fluids such as liquid metals, electrolytes, and plasma in the presence of a magnetic field.

However, the first study on magnetohydrodynamics was conduced earlier than that by Michael Faraday in 1832. He studied the generation of electricity from the interaction of salty water in the River Thames in London with the Earth's magnetic field. The experiment was not successful; however, his study did provide evidence that the interaction between the motion of salty water which is electrically conducting and the Earth's magnetic field induces electric current (Malghan 1996).

Later, Hartmann & Lazarus (1937) investigated more thoroughly on the laminar flow of mercury liquid in a magnetic field theoretically and experimentally. Their studies showed evidence that the current induced in the flow interacts with the magnetic field, producing a Lorentz force which opposes the direction of the fluid motion.

1.2 MHD flow in ducts

The study of the flow of electrically conducting fluid (either gas or liquid) in the presence of a spanwise magnetic field is important because of its applications in magnetohydrodynamic generators (Slavin *et al.* 2001; Kerrebrock 1965), pump (Hughes *et al.* 1995; Park & Seo 2003) and metallurgical processing (Branover *et al.* 1985; Kharicha *et al.* 2016). The present study focus on the application of MHD in fusion reactor that is a promising technology to produce a massive amount of energy while causing minimal pollution to the environment.

In a very energy demanding era, it is important to find a way to generate renewable energy rather than mainly depend on fossil fuels (i.e. coal, oil, and gas). Theorised in the 1950's, an energy generator has been introduced, and a prototype reactor is expected to be built in the 2030s. The project is known as ITER (International Thermonuclear Experimental Reactor)[1] which applies fusion nuclear physics to generate energy. Conceptually, as happens in stars in practice, energy can be created by forming iron which is the most stable nucleus located in the middle of the periodic table. This may be achieved either by fission of heavier elements or fusion of lighter elements. The most popular method used currently is by fission reaction of uranium that splits to form iron. This is readily achieved but produces an abundance of radioactive waste. Meanwhile, the proposed fusion technology combines two isotopes of hydrogen: deuterium, which is heavy hydrogen that can be obtained from seawater, and tritium, which is super-heavy hydrogen. These fuse to form inert Helium, neutrons, and a substantial amount of energy with no radioactive waste.

The fusion reaction occurs when the deuterium and tritium nuclei collide in the correct manner, forming Helium 5 and energy. Helium 5 then splits out to form Helium 4 and a free neutron which also releases further energy (figure 1.1).

The fusion reaction is confined within a plasma within the torus by the toroidal, poloidal and vertical magnetic fields supplied by superconducting coils located at the exterior of a vacuum vessel as shown in figure 1.2(a) (Dobran 2012). The fusion blanket surrounding the plasma is used to absorb the heat to cool the wall facing the plasma and to transfer the heat energy to the steam generator to produce electricity. The fusion blanket also can act as a tritium breeder from lithium lead ($PbLi$) liquid metal to be fed to the reactor. To optimize the heat transfer, the flow needs to be at least

[1] https://www.iter.org/

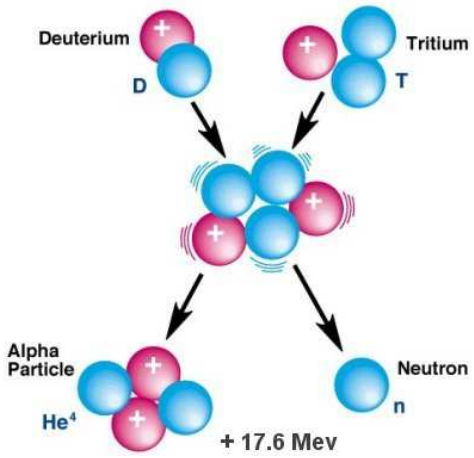

FIGURE 1.1: Fusion reaction between two hydrogen isotopes: deuterium and tritium.

unsteady. However, head losses decreased by the Lorentz force due to the confinement field tends to damp the flow of metal in the blanket into a laminar state. Hence, vortex promoters such as bluff body obstacles or sharp bends may be introduced in the ducts (figure 1.3). It is also of interest to optimise the geometries to cary as much heat and mass as possible in the flow. This thesis focuses on one of the constituent geometries within this ductwork: the 180-degree sharp bend.

The flow of an electrically conducting fluid in a rectangular duct with a 180-degree sharp bend under the effect of an externally applied magnetic field is studied. In this thesis, there are two main objectives. Firstly, to investigate the mechanism that causes the flow around a 180-degree sharp bend to be unstable. This study will provide a good understanding of the characteristics of the flow with and without the effect of the magnetic field. The study will cover a range of ratios of the bend opening width and the channel inlet height. Secondly, to demonstrate the effect of magnetic field on the characteristics of the quasi-two-dimensional flow. From these two main aspects, this thesis systemically investigates the related flow patterns and dynamics between the MHD and non-MHD flows.

1.3 Governing parameters in MHD

There are four non-dimensional parameters used to characterize MHD flows. The first is the Reynolds number,

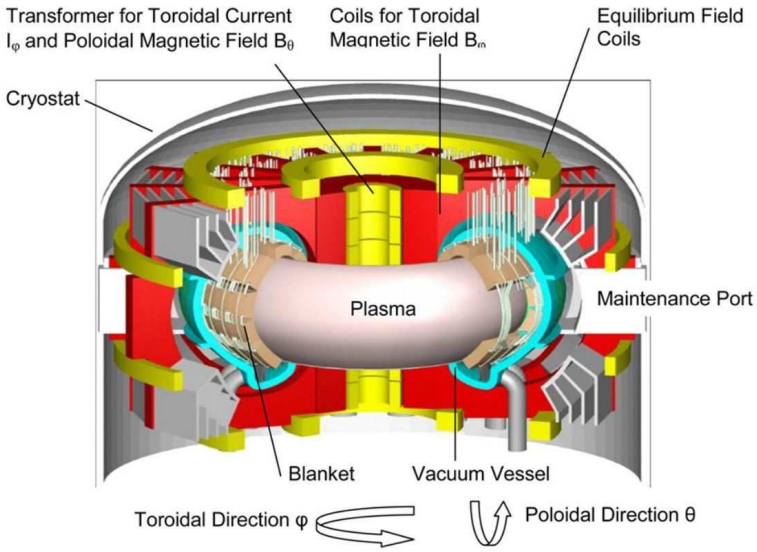

FIGURE 1.2: The concept of tokamak fusion reactor design is shown in (a), where the plasma is in a torus shape surrounded by a self-cooled liquid metal blanket. This figure is reproduced from Dobran (2012), with the permission from Elsevier.

$$Re = ua/\nu, \tag{1.1}$$

where a is a characteristic length scale, u is a typical flow velocity, and ν is the kinematic viscosity of the fluid. As in conventional fluid mechanics, the Reynolds number represents the ratio of inertia to viscous forces. The next two non-dimensional parameters are the Hartmann number and the interaction parameter. The Hartmann number characterizes the square root of the ratio of electromagnetic to viscous forces, while the interaction parameter characterizes the ratio of electromagnetic to inertia forces. They are defined as

$$Ha = aB\sqrt{\frac{\sigma_e}{\rho\nu}}, \tag{1.2}$$

and

$$N = \frac{\sigma_e B^2 a}{\rho u} \tag{1.3}$$

where B, ρ and σ_e are the magnetic field strength, mass density, and the electrical conductivity, respectively. The interaction parameter can also be expressed in terms of Ha and Re as $N = Ha^2/Re$; hence, only any two of Re, Ha and N are required to

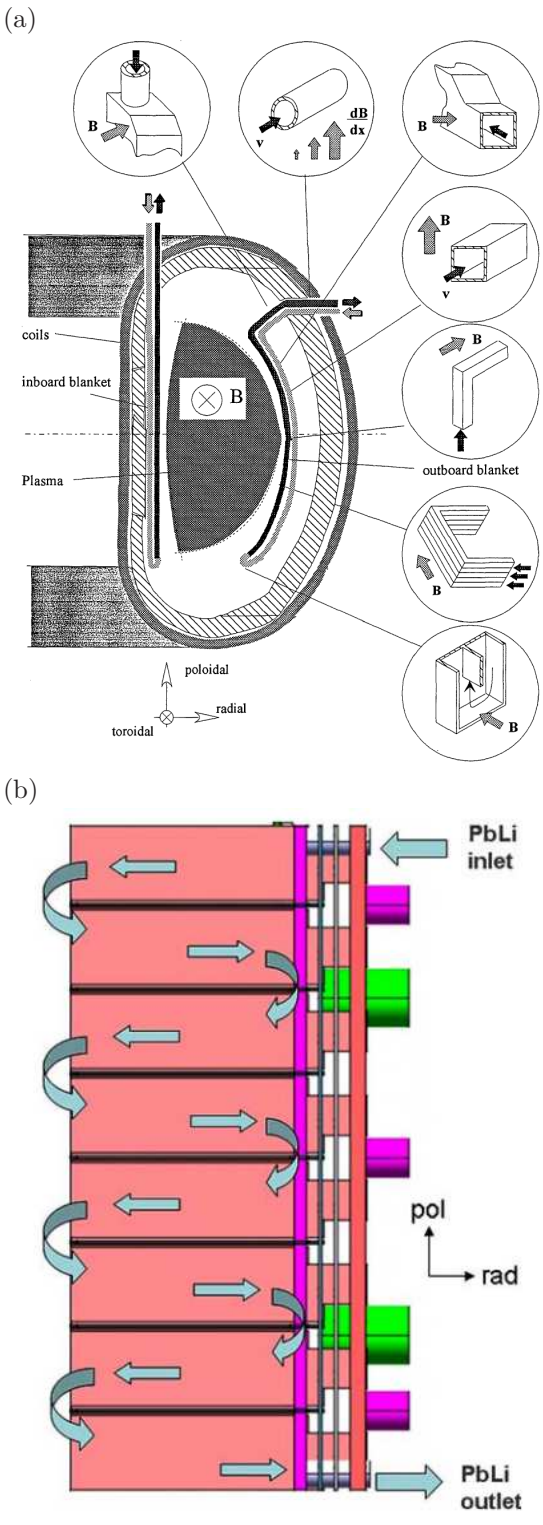

FIGURE 1.3: Combination of geometries in the blanket concepts and their location is shown in (a) which is adopted from Barleon *et al.* (1996). The use of repetitive 180-degree sharp bend in a blanket is shown in (b) which is adopted from Boccaccini *et al.* (2004), with the permission from Elsevier.

characterise the MHD flow.

Pothérat (2007) introduced a more relevant parameter than the Hartmann number for quasi-two-dimensional MHD duct flow, which is known as the friction parameter,

$$H = n\left(\frac{\alpha}{2}\right)^2 Ha, \tag{1.4}$$

where n represents the number of Hartmann walls (e.g. $n = 1$ for a free-surface channel flow and $n = 2$ for a closed duct flow) and α represents the aspect ratio of rectangular duct cross-section.

The heat transfer at the from the surface to the fluid is determined by the Nusselt number, which represents the ratio of convective to conductive heat transfer across the boundary (Bergman & Incropera 2011)

$$Nu = \frac{ha}{k}, \tag{1.5}$$

where h is the convective heat transfer coefficient and k is the thermal conductivity. When a Nusselt number is unity, the convection and conduction are comparable, which is a characteristic of laminar flow. Large Nusselt numbers represents convection dominated heat transfer, whereas small Nusselt numbers represents conduction dominating heat transfer.

The final non-dimensional parameter is the magnetic Reynolds number, which represents the ratio of the induced and applied magnetic fields. It is defined as

$$Rm = \mu_m \sigma_e u a, \tag{1.6}$$

where μ_m is the magnetic permeability. When the value of this parameter is very small, u does not have a strong influence on B; hence, the induced magnetic field is negligible when compared to the imposed magnetic field.

1.4 Overview of the study

This study considers the fluid flow and heat transfer of an electrically conducting, incompressible and viscous fluid (e.g. the eutectic alloy $Ga^{67}In^{20.5}Sn^{12.5}$) around a 180-degree sharp bend in a duct. The physical properties of a typical alloy $Ga^{67}In^{20.5}Sn^{12.5}$ are shown in table 1.1 (Karcher *et al.* 2003; Morley *et al.* 2008). The general configuration of the system investigated in this thesis is shown schematically in figure 1.4.

Density ρ	6360 kg m^{-3}
Kinematic viscosity ν	$3.4 \times 10^{-}7\mathrm{m}^2\mathrm{s}^{-1}$
Electrical conductivity σ_e	$3.46 \times 10^6 \Omega^{-1}\mathrm{m}^{-1}$
Thermal conductivity k	$39\mathrm{Wm}^{-1}\mathrm{K}^{-1}$
Specific heat C_p	$320\mathrm{Jkg}^{-1}\mathrm{K}^{-1}$

TABLE 1.1: Physical properties of $Ga^{67}In^{20.5}Sn^{12.5}$ (Yang *et al.* 2016).

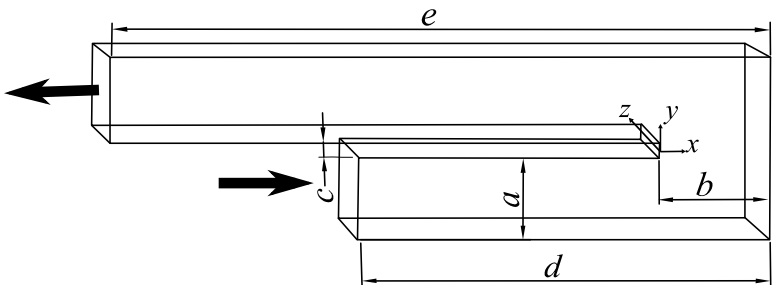

FIGURE 1.4: Schematic diagram and coordinates for the system investigated in this study. The big arrows indicate the direction of the flow.

It consists of a rectangular duct with a sharp bend U-turn. The duct walls are assumed to be electrically insulated. The homogeneous external magnetic field is in the spanwise direction (z-direction). Flow enters the lower duct moving to the right, turns counter-clockwise around the bend, and exits leftward out of the upper duct.

The control parameters in this study are Hartmann number Ha, Reynolds number (Re) and the opening ratio (β). The opening ratio is defined as the ratio between the bend opening width and the inlet height,

$$\beta = b/a. \tag{1.7}$$

The effect of varying these parameters on the flow characteristics and heat transfer enhancement has been discussed in numerous studies for different cases previously. More relevant details on the effect of the parameters can be found in Chapter 2.

1.5 Problem statement

Many studies focus on the effect of strong magnetic field on an electrically conducting fluid in duct flow motivated by the magnetic confinement fusion problem. In some existing applications such as metallurgical processing, the effect of MHD is very desirable; however, the effect of MHD in fusion blanket is often undesirable. The application

of the steady strong magnetic fields provides a convenient means for the contactless damping of turbulent fluctuations and for the laminarization of flows (Branover 1978; Moffatt 1967; Mutschke *et al.* 1997) which may worsen the effectiveness of heat transfer in the fusion blanket.

To overcome the downside of the presence of the strong magnetic field on an electrically conducting liquid flow, vortex promoters have been introduced into the fusion blanket cooling system (Kolesnikov & Tsinober 1974; Sukoriansky *et al.* 1989; Branover *et al.* 1995; Huang & Li 2010; Hamid *et al.* 2015; Cassells *et al.* 2016). Other than using static geometrical vortex promoters, some other mechanisms have been suggested to improve the heat mixing in the fluid, such as torsional oscillating cylindrical bluff body (Hussam *et al.* 2012a) and vortex generation via modulating current injection (Hamid *et al.* 2015, 2016). However, the introduction of a solid bluff body into the flow causes significant pressure loss although it has potential to enhance the heat transfer efficiency (Malang *et al.* 1995).

Although a 180-degree sharp bend has been considered a few times (Barleon *et al.* 1996; Boccaccini *et al.* 2004), there remains no detailed study on this effect of the geometry on the heat transfer in a fusion reactor application. The fundamental understanding of the effect of the geometry in non-MHD flow is also very limited. Zhang & Pothérat (2013) studied the two-dimensional behavior of non-MHD flow around the geometry. According to the results of their study, it can be concluded that the kinematics and dynamics of the two-dimensional flow have very strong resemblance with those of backward facing step flow. However, the three-dimensional characteristics of the flow have not yet been verified to further elucidate similarities with the backward facing step problem. Although the MHD flow is quasi-two-dimensional due to the strong Hartmann damping effect caused by the strong magnetic field acting in the spanwise direction of the flow, for completeness it is nevertheless desirable to gain an insight into the three-dimensional characteristics of a non-MHD flow around a 180-degree sharp bend. This study will provide some fundamental understanding on the types of three-dimensional instability mechanisms next manifest in 180-degree sharp bend non-MHD flow. The most widely used method to identify the three-dimensional modes that may cause a flow to become three-dimensionally unstable is global linear stability analysis (Barkley & Henderson 1996; Barkley 1992; Sheard 2009; Lanzerstorfer & Kuhlmann 2012).

Global linear instability is self-sustainable but can be challenging to observe in con-

fined flows due to convective instability effects. Blackburn *et al.* (2008a) and Griffith *et al.* (2008) have demonstrated that confined flows tend to become convectively unstable before becoming globally unstable. Convective instability is not self-sustainable, but if the location of the instability origin is known, it may be possible to sustain it by supplying small perturbation to the location to make the flow unstable for an extended period. Hussam *et al.* (2012b) numerically studied the optimal transient disturbance in a quasi-two-dimensional MHD duct flow with a circular cylinder and found that the optimal perturbations amplified near the shear layer downstream of the wake recirculation behind the cylinder for a finite period. Hamid *et al.* (2016) then imposed a small perturbation using an induced force using current injection near the location discovered by Hussam *et al.* (2012b) and found that the flow sheds vigorously; hence, having scope to significantly improve duct heat transfer.

The results of previous studies on MHD flow with various vortex promoters, such as circular cylinder (Hussam *et al.* 2012b, 2011a, 2012a; Hamid *et al.* 2016) and rectangular cylinder (Chatterjee *et al.* 2014; Chatterjee & Gupta 2015; Cassells *et al.* 2016) show significant enhancement in heat transport from a heated wall. However, there is still no study on the effect of the 180-degree sharp bend geometry on the heat transport despite that the geometry has been proposed a few times (Boccaccini *et al.* 2004; Barleon *et al.* 1996). It is, therefore, important to conduct a study to understand the fundamental structure of the flow with this geometry so that it can be fully utilized to enhance the transfer of heat.

This thesis focuses on the geometry that is already in the system, which is 180-degree sharp bend. Until now, there is still a lack of insights on the effect of the dimension of the opening bend ratio on the stability of the flow. As a prelude to the heat transfer analysis, it is of interest to learn the fundamental dynamics and kinematics of the flow through a linear stability analysis and transient growth analysis to investigate the globally linear stability and convective linear stability of the flow.

1.6 Aims of the study

This study aims primarily to understand the fundamental dynamics and kinematics of the flow around a 180-degree sharp bend in both hydrodynamic and magnetohydrodynamic problems. It is of interest to investigate the problems over a wide range of bend opening ratio to understand the different flow structures as this single geometric

parameter is changed.

There are three secondary aims underpinning the main aim. This study aims to investigate the global linear stability of the hydrodynamic flow around the sharp bend. A linear stability analysis is to be applied to gain predictions of the instabilities in the flow. The predicted global linear stability behaviour is to be assessed using Stuart–Landau model on full three-dimensional direct numerical simulation of the flow.

This study also aims to investigate the transient local convective instability that may emerge at much lower Reynolds number than global instability. The investigation is conducted using transient growth analysis.

This study also aims to understand the dynamic of the flow of an electrically conducting fluid in a rectangular duct with a 180-degree sharp bend with and without the influence of a strong uniform magnetic field when the opening ratio is changed. This study also aims to give insights on the effect of the alteration of the bend opening ratio and the strength of the magnetic field towards the heat transfer efficiency on the heated side wall.

1.7 Research delimitations

In this thesis, the parameters are delimited by using the objectives as delimiting factors. The bend opening ratio, β is in the range of $[0.1, 10]$, Hartmann parameter, $H = [0, 500]$ and $Re = [1, 3000]$ depending on the aims of the studies. The magnetic Reynolds number Re_m is assumed very small ($Re_m \ll 1$); hence, the induced magnetic field from the MHD flow is infinitesimal compared to the externally applied magnetic field (Branover 1978; Moreau 1990; Hunt & Stewartson 1965; Davidson 2001). The MHD flow in this study is assumed to be quasi-two-dimensional because it satisfies the quasi-two-dimensional condition which was established by Sommeria & Moreau (1982) and Pothérat *et al.* (2002).

For the heat transfer study, a Prandtl number $Pr = 0.022$ is used which is representative of Galinstan (GaInSn) liquid metal (ref. table 1.1) in preparation of possible future experiments. The low number of Pr indicates that heat diffuses significantly faster than momentum (Walter 2012).

1.8 Structure of the thesis

The thesis is divided into seven chapters. Following the present introduction, chapter 2 provides a review of previous works from the relevant literature. Chapter 3 describes the numerical methodologies and their validation. Results are then presented in chapters 4 to 6. Chapter 4 describes a linear stability analysis of the flow. Chapter 5 investigates the transient growth of infinitesimal perturbations in the non-MHD flow. Chapter 6 discusses the effect of the strong magnetic field onto the dynamics and heat transfer efficiency of the flow. Conclusions are presented in chapter 7, together with some suggested areas for future research relating to this thesis.

Chapter 2

A review of the literature

A review of the relevant literature related to flow past bends, linear instability, transient growth analysis and quasi-two-dimensional magnetohydrodynamic flow is presented in this chapter.

2.1 Flow past bends and backward facing step problems

The question raised by Thomson (1876) on why not the inner bank of a river bend wears away more than the outer one has opened a new chapter in fluid mechanics on how the bend geometry influences the flow regimes. Thomson proved that the bend geometry affects the balance between the centrifugal force and the friction in the flow that goes around the bend. Other than in a river (Fig. 2.1), this configuration also can be found elsewhere in nature, including the circulatory systems of humans that consist of curved arteries, veins, and capillaries. In the engineering systems, the use of bend geometry can be found particularly in heat exchangers such as radiators and the ITER fusion reactor.

This section will review and discuss the previous works on the incompressible Newtonian flow past the bends and backward facing step since both exhibit similar flow dynamics.

2.1.1 Flow separation

Separating and reattaching flows play a major role in numerous engineering applications, especially in heat transportation (Larson 1959; Krall & Sparrow 1966; Abu-Nada 2008). All moving fluid traveling through stationary solid objects or walls will create a boundary layer around the solid where viscous forces are present in the layer of fluid near the solid surface. Flow separation appears when the boundary layer travels far

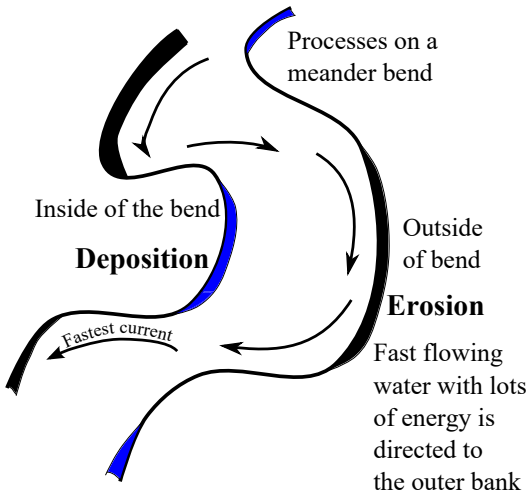

FIGURE 2.1: Effect of bend on river bank as questioned by Thomson (1876).

enough against an adverse pressure gradient where the speed of the boundary layer about the solid reduces almost to zero (Anderson 2010).

Considering a flow past a curved plate in figure 2.2, along the streamwise direction, an adverse pressure gradient appears in between S_2 and S_3 where p_2 is lower than p_3. The fluids near high pressure at point S_3 are driven to the low-pressure gradient creating a reversed flow and resulting in the formation of recirculation, as sketched in figure 2.3.

The fluid at point S_2 in figure 2.2 is moving very slowly and the shear stress at that point is cancelled: $\partial u/\partial y = 0$ (normal to the solid surface). The pressure near the vicinity is very low and remains constant. The length of the recirculation bubble decreases as the adverse pressure gradient increases (Pauley *et al.* 1990).

2.1.2 Flow past bends

There have been some studies on two-dimensional flow past a sharp bend (90- and 180-degree) (Yamashita *et al.* 1986, 1987; Chung *et al.* 2003; Astarita & Cardone 2000). Two-dimensional flow has only two independent spatial variables: e.g. cartesian x- and y-directions. Practically, in real life, it is hard to achieve a perfect two-dimensional flow. Nonetheless, it is still important to have a good understanding of the two-dimensional flow because many three-dimensional flows display similarities in flow dynamics with two-dimensional flows. The similarities between both flows are more significant in electrically conducting liquid flows under the effect of a strong magnetic field where

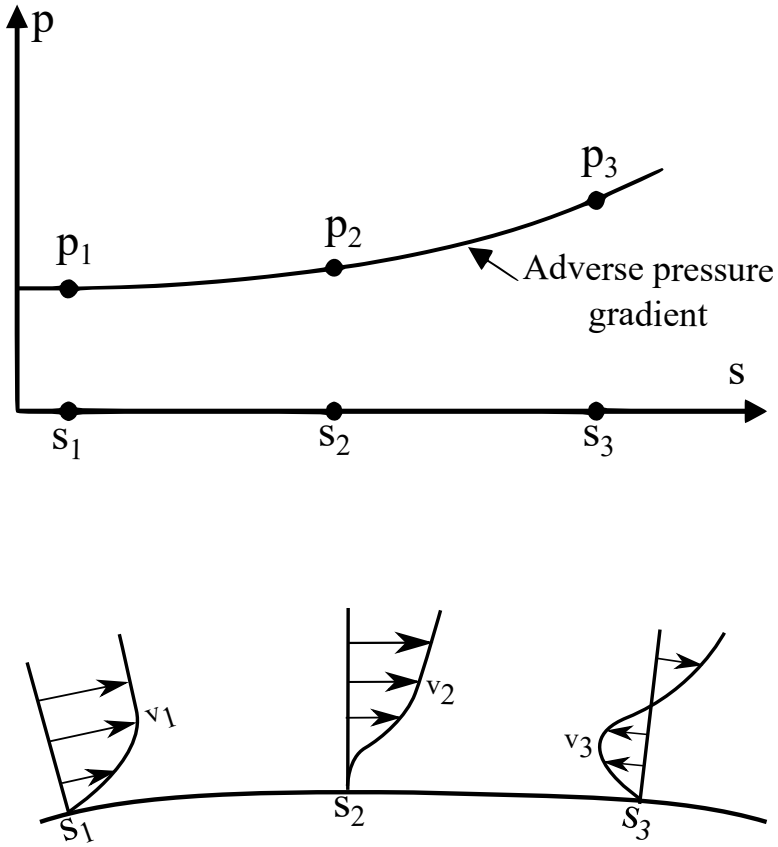

FIGURE 2.2: Reversed flow in presence of adverse pressure gradient.

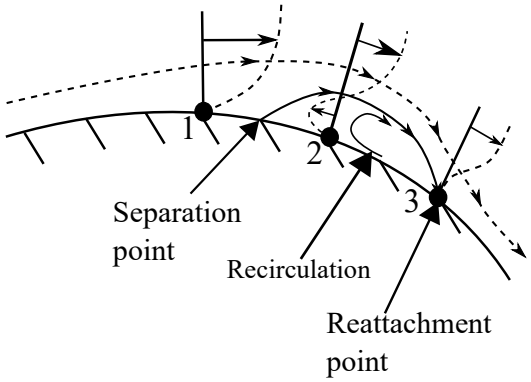

FIGURE 2.3: Sketch of separation flow.

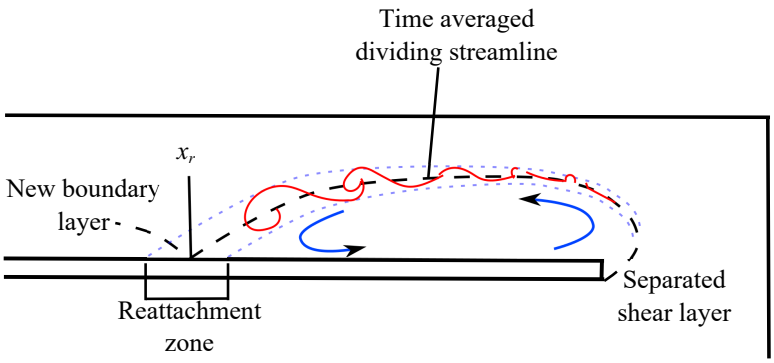

FIGURE 2.4: Principal flow features of the 180-degree sharp bend flow.

actual quasi-two-dimensionality can be physically achienved (Sommeria & Moreau 1982; Bühler 1996; Mück *et al.* 2000; Pothérat *et al.* 2000a; Dousset & Pothérat 2008).

When a flow passes a bend or any angle, a flow separation which in the transverse direction of primary flow appears when Reynolds number reaches a certain value. The separation plays an important role in the redistribution of streamwise momentum and also affects the shear stress. If a fluid is moving through a straight channel that suddenly becomes curved, the dynamics and kinematics of the fluid particles will be changed because of the existence of the bend. The bend generates an adverse pressure gradient with an increase in pressure, resulting in a decrease in velocity of the flow near to the inner wall of the bend, while acceleration will occur towards the outside of the channel. The illustration of the features of the flow is presented in figure 2.4.

In Yamashita *et al.* (1986, 1987), flow around a 90-degree bend was studied. The authors found that the flow became unsteady at $Re > 460$, (Re was based on the bulk mean inlet velocity). Vortices were formed due to the Kelvin–Helmholtz instability in the shear layer. They also found that the Strouhal number St, which measures the shedding frequency increased as Reynolds number increased. Maximum local Nu was reached at the region near the bend because of the very thin thermal boundary layer and the considerable turbulent energy in that vicinity. They concluded that the bend enhanced the heat transfer process in the flow.

Wang & Chyu (1994) studied the effects of a duct with a 180-degree bend with three different turning configurations: sharp corner, rounded corner, and circular turn. In their study, all walls were heated, and cold fluid was supplied from the inlet. Their results showed that the sharp bend had the strongest turn-induced heat transfer en-

hancement by approximately 30% as compared to the circular turn which had the weakest among the three configurations. In experimental studies by Metzger & Sahm (1986) and Astarita & Cardone (2000), heat transfer was found to be optimum downstream of the sharp bend turn. Hirota *et al.* (1999) studied experimentally the effect of the size of bend openings in ducts with sharp bends. With a channel cross-section of 50×25 mm, bend openings of 70 mm and 50 mm were found to have almost the same value of Sherwood number Sh (the ratio of convective to diffusive mass transport), whereas a smaller bend opening (30 mm) led to larger values of Sh, with Sh 1.3 times greater than that for 50 mm. Only a few studies focused on the effect of varying control parameters on the structure of the flow. Liou *et al.* (1999, 2000) experimentally showed that the divider thickness mainly influenced the intensity and uniformity of turbulence.

In a two-dimensional 180-degree sharp bend flow, flow separation causes a recirculation bubble to appear immediately after the sharp corner. In a numerical study performed by Chung *et al.* (2003), for a 180-degree sharp bend with an opening ratio $\beta = 1$, it was reported that the length of the bubble increased until the flow became unsteady around $500 < Re < 600$. Their findings were based on the analysis of the time history of instantaneous velocity at a specified location in the two-dimensional flow. Figure 2.5(a) shows the v-velocity time history for a steady flow reproduced from that study, where it fluctuates at the beginning due to the initial setup of the simulation, then decays and become steady. Meanwhile, figure 2.5(b) shows the time history for an unsteady flow in their study, where the fluctuation behind the sharp bend is sustained indefinitely. For the same geometry parameter, Zhang & Pothérat (2013) reported a more precise range of the onset of unsteadiness, which was around $560 < Re < 570$. Both Re mentioned here were based on the mean velocity of the bulk flow.

The only reported parametric study on the effect of the bend opening ratio on hydrodynamic flow around a 180-degree sharp bend was carried out numerically by Zhang & Pothérat (2013). They categorised the two-dimensional flow into five regimes (see figure 4 in Zhang & Pothérat 2013). Regime I was at very low Reynolds number, where the flow was laminar and remained attached to the walls throughout. Regime II emerged at higher Reynolds number, where flow separation appeared at the bend, leading to the creation of the primary recirculation bubble. Regime III occurred at a yet higher Reynolds number when the adverse pressure gradient at the top wall was strong enough to create a secondary recirculation bubble. Regime IV occurred when a small-

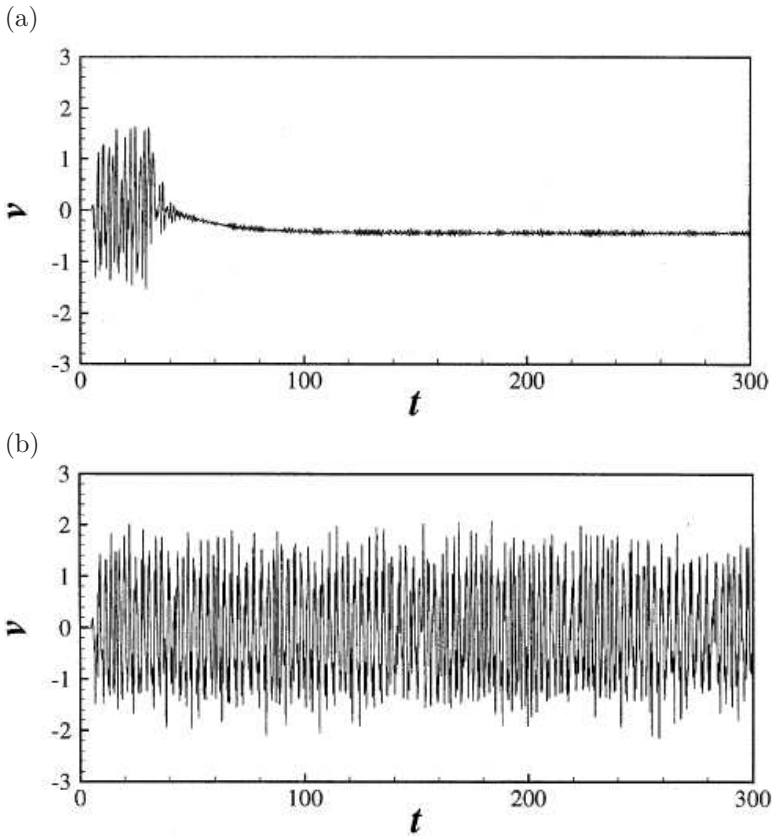

FIGURE 2.5: Instantaneous v-velocity at (a)$Re = 500$ and (b) $Re = 700$ reproduced from Chung *et al.* (2003), with the permission from Elsevier.

scale vortex structure was detected far downstream at high Reynolds number before the flow entered regime V, which featured vortex shedding originating from the sharp bend at higher Reynolds number. They also reported the results of some three-dimensional simulations. According to their results, at $Re = 2000$, two types of shedding structures were found in the spanwise direction reminiscent of A- and B-modes in the flow past a circular cylinder (Williamson 1988; Thompson *et al.* 1996; Brede *et al.* 1996; Henderson 1997). These shedding structures disrupted the two-dimensional vortex in the flow and tended to slow down the shedding mechanism. Although a very detailed study of the two-dimensional 180-degree bend flow has been provided by Zhang & Pothérat (2013), the three-dimensional stability of these flows is yet to be determined.

2.1.3 Flow past a backward facing step

At high Reynolds number, typically the flow patterns in the vicinity of a backward facing step show the formation of separation at the edge of the step and the emergence

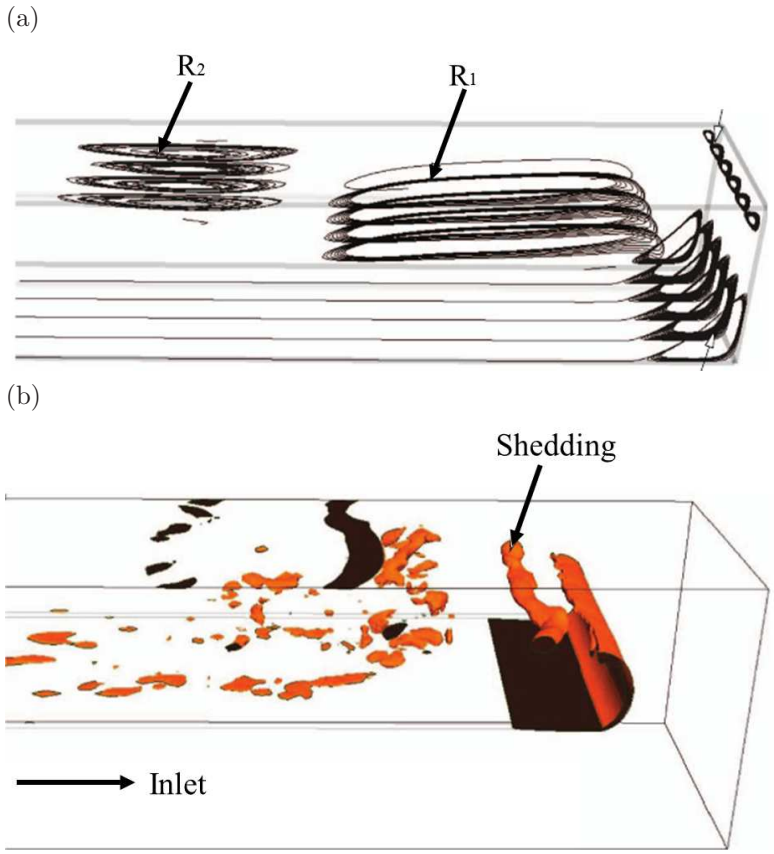

FIGURE 2.6: (a) Velocity streamlines for $Re = 400$ (steady) and (b) isosurface of streamwise vorticity for $Re = 2000$ (unsteady), reproduced from Zhang & Pothérat (2013), with the permission of AIP Publishing.

of reattached flow downstream of the step. The presence of the separation and reattachment affects the flow unsteadiness, pressure fluctuations, noise and vibrations of structure (Chun & Sung 1996). Study of the flow past backward facing step has been motivated by the important need to understand the impact of the separation due to the abrupt change in geometry, especially on flow stability.

The behavior of flow past a backward facing step is reminiscent of the recirculating flow behind a sharp bend. Hence, it is useful to gain further insight on this classical configuration problem to have a better understanding of the flow past a 180-degree sharp bend.

There are many studies which have covered a wide range of topics on backward facing step (Barkley *et al.* 2002; Chun & Sung 1996; Kaiktsis *et al.* 1996; Le *et al.* 1997; Terzi & Alexander 2004; Armaly *et al.* 1983; Blackburn *et al.* 2008a). This makes the studies on the backward facing step flow as the most useful and relevant reference for

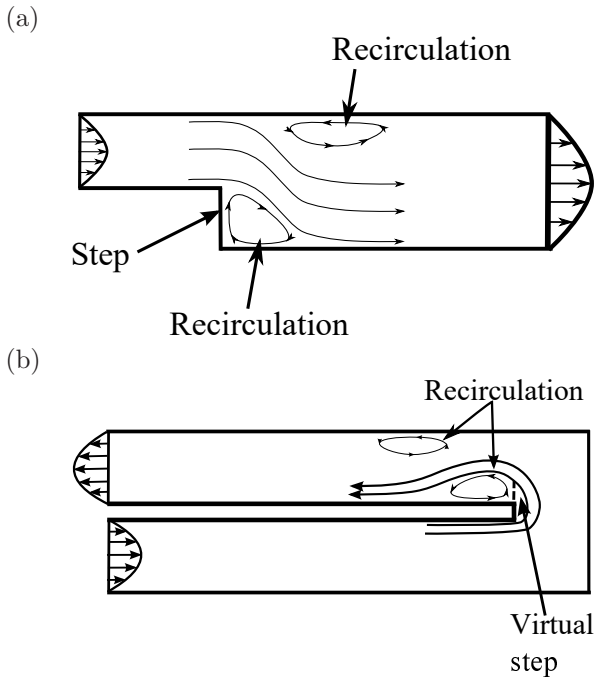

FIGURE 2.7: Sketch of flow past: (a) backward facing step, and (b) 180-degree sharp bend.

the current study on the flow past a 180-degree sharp bend.

Figure 2.7 shows the similarities between the backward facing step and the 180-degree sharp bend problems. When the flow passes over the sharp step of the backward facing step geometry and the sharp turning part of the 180-degree bend, a sudden change in pressure occurs. Hence behind both features, the flow separates, and under some conditions, this can be complemented by a recirculation bubble attached to the opposite duct wall.

Armaly *et al.* (1983) performed an in-depth experimental and theoretical investigation of backward facing step flow. Their study covered a large range of Reynolds number from 70 to 8000 and examined the correlation between Reynolds number and the length of recirculation bubbles. Figure 2.8 reproduces a regime map from that study. The recirculation length strongly depends on Reynolds number when the flow is steady. At $Re > 1200$, the flow becomes unsteady, hence making the recirculation bubble collapse and causing the recirculation length to reduce significantly. Furthermore, there is an additional recirculation that appears at the top of the channel as Reynolds number increases. The separation and reattachment points of the extra recirculation strongly depend on Reynolds number, with the separation point being mainly affected

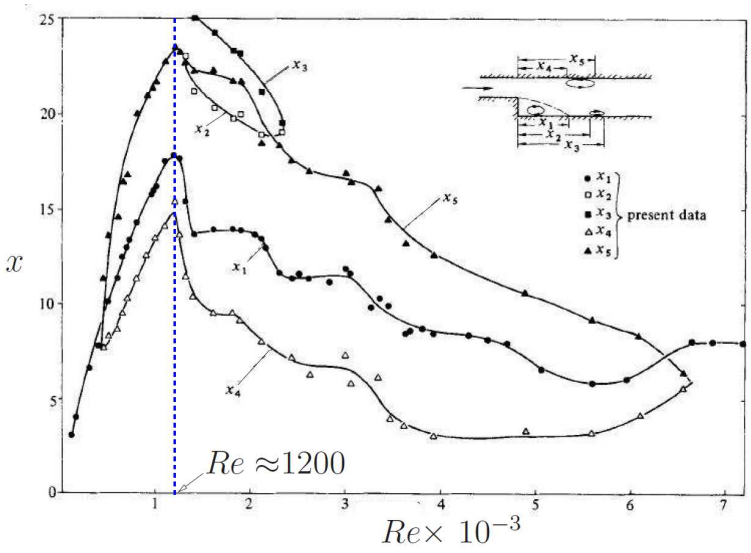

FIGURE 2.8: Location of separation and reattachment positions of backward facing step flow reproduced from Armaly *et al.* (1983), with the permission of Cambridge University Press.

by the reattachment position of the first recirculation (Schäfer *et al.* 2009; Barton 1997b; Nait Bouda *et al.* 2008). The ratio of step height to outlet height (expansion ratio) in backward facing step problem plays a significant role in determining the global stability of the two-dimensional flow (Lanzerstorfer & Kuhlmann 2012) which is also expected from the bend opening ratio in 180-degree sharp bend.

2.2 MHD flow

Advanced engineering applications such as in metallurgical processing (Davidson 1999) and the cooling system of fusion blankets (Smolentsev *et al.* 2010) attracts a lot of attention on the study of magnetohydrodynamic flows. Tokamak is an example of a magnetic confinement system used for fusion reactors which were first introduced in the 1960s in the Soviet Union that later attracted the attention of researchers from all around the world (Thomson 1958). The tokamak components are consist of vacuum vessel which contains the plasma. The plasma is held by a strong magnetic field to keep the hot plasma away from the walls. The magnetic field is produced by the combination of two sets of magnetic coils: toroidal and poloidal coils. The electrically conducting liquid metal fluid in the fusion blanket tends to be laminar because of the interaction with the strong uniform magnetic field. The interaction between the liquid metal in motion with the magnetic field induces currents. The induced currents in the fluid then

interact with the magnetic field and produce Lorentz forces which significantly change the pattern of the flow (Mück *et al.* 2000).

The viscous effects in the flow are confined to thin boundary layers at the walls. Krasnov *et al.* (2012) have proven this numerically in their study on the flow structure at different magnetic field strengths in a duct flow. Figure 2.9 presents their finding on the effect of the strength of the magnetic field on the instantaneous distributions of streamwise velocity at mid-plane cross-section for very high Reynolds number. Without the presence of the magnetic field, the flow is very unsteady and highly turbulent throughout the duct (figure 2.9(a)). As Hartmann number is increased to $Ha = 100$, the flow develops a laminar core, but the Shercliff and Hartmann layers remain turbulent. At $Ha = 200$, the Hartmann layers transition to a laminar state; only the Shercliff layers remain turbulent. As Hartmann number is increased to $Ha = 300$, the turbulence continues in the Shercliff layers, but the layers become thinner. It is also can be seen that as the Hartmann number increases, the red contour in the core region becomes lighter. This demonstrates that the strength of the magnetic field significantly suppresses the Hartmann layer, and weakly suppresses the Shercliff layer and the streamwise velocity in the core region.

2.2.1 Computation of the magnetohydrodynamic (MHD) flow

Magnetohydrodynamic flows can be described from the coupling of the fluid dynamic equations and the electromagnetic equations. Moreau (1990) and Davidson (2001) described that, according to Faraday's law of induction, the interaction between the motion of a conducting fluid $\hat{\mathbf{u}}$ and the imposed magnetic field $\hat{\mathbf{B}}_\mathbf{0}$ induces an electromotive force (EMF), which is represented as $\hat{\mathbf{u}} \times \hat{\mathbf{B}}_\mathbf{0}$. The EMF then interacts with the magnetic field to induce an electrical current of order $\sigma_e(\hat{\mathbf{u}} \times \hat{\mathbf{B}}_\mathbf{0})$, where σ_e is the electrical conductivity of the fluid. Ampere's law says that an electric current produces magnetic field $\hat{\mathbf{B}}_\mathbf{i}$ that is proportional to the size of the electric current. However, in the fusion blanket application, the induced magnetic field is negligible because of the low-velocity liquid metal and small length scale (Davidson 2001) which will be discussed further in § 2.2.1.3. The total magnetic field (i.e. $\hat{\mathbf{B}} = \hat{\mathbf{B}}_\mathbf{0} + \hat{\mathbf{B}}_\mathbf{i}$) interacts with the induced current to create a Lorentz force of order $\hat{\mathbf{J}} \times \hat{\mathbf{B}}$, where $\hat{\mathbf{J}}$ is the current density vector.

This thesis considers the fluids to be incompressible with density ρ and kinematic

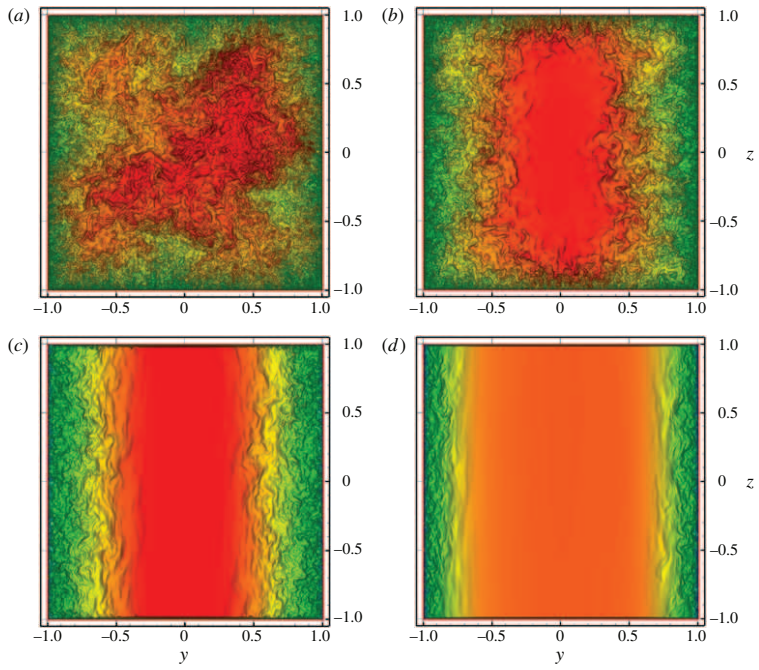

FIGURE 2.9: Instantenous streamwise velocity of the mid-plane cross-section for Reynolds nymber $Re = 1 \times 10^5$ and (a) $Ha = 0$ (hydrodynamic flow), (b) $Ha = 100$, (c) $Ha = 200$ and (d) $Ha = 300$. The contour levels ranging from 0 (blue) to 1.25 (red). Magnetic fields moves across the z-direction. In (a), the flow is turbulent everywhere. In (b), both Hartmann and Shercliff layers are turbulent. In (c) and (d), only Sherclift layers are turbulent. Figure was reproduced from (Krasnov *et al.* 2012), with the permission of Cambridge University Press.

viscosity ν. The flow is governed by the incompresible Navier–Stokes equations with an additional term representing the effect of the electromotive force:

$$\frac{\partial \hat{\mathbf{u}}}{\partial \hat{t}} + (\hat{\mathbf{u}} \cdot \hat{\nabla})\hat{\mathbf{u}} + \frac{\nabla \hat{p}}{\rho} = \nu \hat{\nabla}^2 \hat{\mathbf{u}} + \frac{1}{\rho}\hat{\mathbf{J}} \times \hat{\mathbf{B}}, \tag{2.1}$$

$$\hat{\nabla} \cdot \hat{\mathbf{u}} = 0, \tag{2.2}$$

where $\hat{t}$ is time, $\hat{\nabla}$ is the gradient operator, $\hat{\mathbf{u}}$ is the velocity field and p is the dynamic pressure. Meanwhile, the energy equation is written as

$$\rho C_{\hat{\mathrm{p}}} \frac{\partial \hat{\theta}}{\partial \hat{t}} + \rho C_{\mathrm{p}} (\hat{\mathbf{u}} \cdot \nabla)\hat{\theta} = k_{\mathrm{p}} \hat{\nabla}^2 \hat{\theta}, \tag{2.3}$$

where k_{p} is the thermal conductivity, C_{p} is the constant pressure specific heat of the liquid metal and $\hat{\theta}$ is the temperature field.

According to Burr *et al.* (2000) and Pothérat *et al.* (2000b), when the interaction parameter is large and the flow reaches a quasi-two-dimensional state, it is possible to assume the heat due to the viscous and Joule dissipation to be negligible in equation (2.3). Hussam *et al.* (2011b) reported that in the fusion blanket application, the heat contributed by the viscous and Joule dissipation were up to seven orders of magnitude smaller compared to the other terms in equation (2.3). Moreover, the influence of natural convection on heat transfer is not considered in this thesis; it has been reported that the effect of the natural convection tends to be inhibited by the strong external magnetic field imposed on the liquid metal (Gardner & Lykoudis 1971; Morley *et al.* 2000).

2.2.1.1 Electromagnetic equations

As mentioned earlier, MHD equations are derived from the coupling of the fluid dynamic equations, which are Galilean invariant, and electromagnetic equations, which are Lorentz invariant. To couple both equations together as Galilean invariant, it is necessary to apply the so-called *quasi-static approximation* (Shercliff 1965; Roberts 1967). It relies on 4 conditions (Müller & Bühler 2001):

1. typical fluid velocities are much smaller than the speed of light (i.e. non-relativistic approximation $u/c' \ll 1$, where c' is the velocity of light),

2. velocity of the charge carriers remains small with respect to the velocity of the fluid,

3. the charge carriers move within the fluid without inertia, and

4. no thermo-electric voltage sources are present.

The implications of the quasi-static approximations are:

1. the imposed magnetic field remains relatively unperturbed, hence the convection current can be neglected,

2. the displacement current is negligible (Moreau 1990),

3. the rate of change of the electric charge density is negligible.

Due to the implication of the approximations, the charge relaxation time $\tau_r = \epsilon/\sigma_e$ is extremely short (i.e. for liquid metals and eutectic alloys, τ_r is 10^{-18} s) (Davidson 2001).

The electromagnetic equations can be summarised into a set of four equations known as *Maxwell's equations* which read:

$$\hat{\nabla} \cdot \hat{\mathbf{E}} = \frac{q}{\epsilon}, \tag{2.4}$$

$$\nabla \cdot \hat{\mathbf{B}} = 0, \tag{2.5}$$

$$\nabla \times \hat{\mathbf{E}} = -\frac{\partial \mathbf{B}}{\partial t}, \tag{2.6}$$

$$\nabla \times \hat{\mathbf{B}} = \mu_m \hat{\mathbf{J}} + \mu_m \epsilon \frac{\partial \hat{\mathbf{E}}}{\partial t}, \tag{2.7}$$

$$\hat{\mathbf{J}} = q\hat{\mathbf{u}} + \sigma_e(\hat{\mathbf{E}} + \hat{\mathbf{u}} \times \hat{\mathbf{B}}), \tag{2.8}$$

where $\hat{\mathbf{J}}$, $\hat{\mathbf{E}}$ and $\hat{\mathbf{B}}$ are the current density, electrical field, and magnetic field, respectively. The equations are characterised by a volume charge density q, an electric permittivity ϵ, an electrical conductivity σ_e and a magnetic permeability of the liquid metal μ_m. Equation (2.4) describes how electric field is generated by the electric charges in the medium. Equation (2.5) is the Gauss' Law for Magnetism explaining that the divergence of $\hat{\mathbf{B}}$ is always zero through any volume and the magnetic fields always flow in a closed loop. Equation (2.6) is Faraday's Law, denoting that how a changing magnetic field induces an electric field. Equation (2.7) is Ampere's Law, showing how a magnetic field can be generated by a current density. Equation (2.8) furthermore expresses Ohm's Law where the current density as the sum of the convection current ($q\hat{\mathbf{u}}$) and the conduction current ($\sigma_e(\hat{\mathbf{E}} + \hat{\mathbf{u}} \times \hat{\mathbf{B}})$).

An analysis of the orders of magnitude of the convection current ($q\hat{\mathbf{u}}$) and ($\sigma_e(\hat{\mathbf{E}})$ in equation (2.8) can be expressed as $(q\hat{\mathbf{u}})/(\sigma_e(\hat{\mathbf{E}}) \sim \tau_r U_0/L$, where U_o and L is the fluid velocity and characteristic length, respectively. Due to the implication of the quasi-static approximations, the convection current ($q\hat{\mathbf{u}}$) can be neglected because of the extremely small value of charge relaxation time for liquid metals; hence, Ohm's Law can be rewritten as

$$\hat{\mathbf{J}} = \sigma_e(\hat{\mathbf{E}} + \hat{\mathbf{u}} \times \hat{\mathbf{B}}). \tag{2.9}$$

The conservation of electric charge is the principle that it can neither be created or destroyed; thus, the derivative of the total charge must be zero (Heilbron 1979; Purrington 1997)

$$\hat{\nabla} \cdot \hat{\mathbf{J}} = 0 \tag{2.10}$$

According to Moreau (1990), in a conducting media such as liquid metal, the displacement current ($\epsilon\mu\partial_t\hat{\mathbf{E}}$) can be neglected; hence, equation (2.7) can be rewritten as

$$\hat{\nabla} \times \hat{\mathbf{B}} = \mu_m \hat{\mathbf{J}}. \tag{2.11}$$

Using non-dimensional variables which are derived from dimensional variables,

$$\left.\begin{array}{lll} \hat{\mathbf{x}} = L\mathbf{x}, & \hat{\mathbf{u}} = U_0\mathbf{u}, & \hat{p} = \rho {U_0}^2 p, \\ \hat{t} = \dfrac{L}{U_0}t, & \hat{\nabla} = \dfrac{1}{L}\nabla, & \hat{\theta} = \theta(\hat{\theta_w} - \hat{\theta_0}) + \hat{\theta_0}, \\ \hat{\mathbf{B}} = B\mathbf{B}, & \hat{\mathbf{E}} = U_0 B\mathbf{E}, & \hat{\mathbf{J}} = \sigma U_0 B\mathbf{J}, \\ Re = \dfrac{U_0 L}{\nu}, & Ha = aB\sqrt{\dfrac{\sigma}{\rho\nu}}, & N = \sigma B^2 a/\rho U_0 = \dfrac{Ha^2}{Re}, \end{array}\right\} \tag{2.12}$$

the dimensionless form of equations (2.4)–(2.8) are respectively reduced to

$$\mathbf{E} = -\nabla\phi, \tag{2.13}$$

$$\mathbf{J} = -\nabla\phi + \mathbf{u} \times \mathbf{B}, \tag{2.14}$$

where ϕ is the electrical potential, $Ha = aB\sqrt{\sigma/(\rho\nu)}$ is the Hartmann number, which will be described shortly, and $Re = U_0 a/\nu$ is the Reynolds number. a represents the length of the duct in the direction parallel to the magnetic field, and a represents the height of the duct.

2.2.1.2 Induction equation

The magnetic field in MHD flows varies with time through diffusion and advection, which can be described by the induction equation. The equation is derived by taking the curl of equation (2.9)

$$\frac{\hat{\nabla} \times \hat{\mathbf{J}}}{\sigma} = \hat{\nabla} \times \hat{\mathbf{E}} + \hat{\nabla} + \times(\hat{\mathbf{u}} \times \hat{\mathbf{B}}), \tag{2.15}$$

and equation (2.6) and (2.7) then substituted into equation (2.15) for the expressions of $\hat{\mathbf{J}}$ and $\hat{\mathbf{E}}$ as a function of $\hat{\mathbf{B}}$ to get

$$\frac{\hat{\nabla} \times (\hat{\nabla} \times \hat{\mathbf{B}})}{\sigma\mu_m} = -\frac{\partial\hat{\mathbf{B}}}{\partial\hat{t}} + \hat{\nabla} \times (\hat{\mathbf{u}} \times \hat{\mathbf{B}}). \tag{2.16}$$

Taking the vecor identity $\hat{\nabla} \times (\hat{\nabla} \times \hat{\mathbf{B}}) = \hat{\nabla}(\hat{\nabla} \cdot \hat{\mathbf{B}}) - \hat{\nabla}^2 \hat{\mathbf{B}}$ and due to equation (2.5),

$$\hat{\nabla} \times (\hat{\nabla} \cdot \hat{\mathbf{B}}) = -\hat{\nabla}^2 \hat{\mathbf{B}}. \tag{2.17}$$

Thus, the induction equation may be expressed as

$$\frac{\partial \hat{\mathbf{B}}}{\partial \hat{t}} = \hat{\nabla} \times (\hat{\mathbf{u}} \times \hat{\mathbf{B}}) + \frac{1}{\sigma \mu_m} \hat{\nabla}^2 \hat{\mathbf{B}}. \tag{2.18}$$

The equation is rewritten in non-dimensional form using the scalings shown in equation (2.12) and $Rm = \sigma_e \mu_m U_0 L$ as

$$\frac{\partial \mathbf{B}}{\partial \hat{t}} = \nabla \times (\mathbf{u} \times \mathbf{B}) + \frac{1}{Rm} \nabla^2 \mathbf{B}. \tag{2.19}$$

The induction equation (Equation (2.19)) expresses the motion of a conducting fluid in an applied magnetic field in the domain induces a magnetic field in the fluid. The total magnetic field is the sum of the applied and the subsequently induced magnetic fields. The strength of the induced magnetic field is characterised by the magnetic Reynolds number Rm which denotes the ratio between the induced and the applied magnetic fields.

2.2.1.3 The low Rm quasi-static MHD equations

When the magnetic Reynolds number is very low $Rm \ll 1$, the magnetic field induced by the flow is relatively negligible compared to the external magnetic field applied onto the fluid (Branover 1978; Moreau 1990). Due to this, the total effective magnetic field is equivalent only to the applied magnetic field. Using the scalings in equation (2.12), the non-dimensional inductionless magnetohydrodynamic equations can be written as

$$\frac{\partial \mathbf{u}}{\partial t} + (\mathbf{u} \cdot \nabla \mathbf{u} = -\nabla p + \frac{1}{Re} \nabla^2 \mathbf{u} + \frac{Ha^2}{Re} (\mathbf{J} \times \mathbf{B}), \tag{2.20}$$

$$\nabla \cdot \mathbf{u} = 0, \tag{2.21}$$

$$\frac{\partial \theta}{\partial t} + (\mathbf{u} \cdot \nabla)\theta = \frac{1}{RePr} \nabla^2 \theta = \frac{1}{Pe} \nabla^2 \theta, \tag{2.22}$$

$$\nabla \cdot \mathbf{J} = 0, \tag{2.23}$$

$$\mathbf{J} = -\nabla \phi + \mathbf{u} \times \mathbf{B}, \tag{2.24}$$

$$\mathbf{E} = -\nabla \phi, \tag{2.25}$$

where the quadratic norm of $\mathbf{B_0}$ is used in $\mathbf{B} = \mathbf{B_0} / \|\mathbf{B_0}\|$.

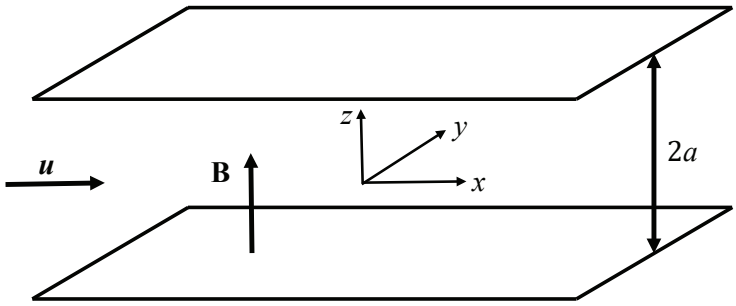

FIGURE 2.10: Schematic diagram of Hartmann flow between two parallel infinite walls with a transverse magnetic field.

2.2.1.4 Hartmann flow

Hartmann flow is a flow of an electrically conducting fluid between two insulated plates in parallel as shown in figure 2.10. This problem was first solved by Hartmann & Lazarus (1937). When there is no magnetic field presented ($\mathbf{B} = 0$), it becomes purely hydromagnetic of Poiseuille flow. Figure 2.10 considers the flow of an electrically conducting fluid in a rectangular channel exposed to a constant external magnetic field in the transverse direction (i.e. $\mathbf{B} = B\hat{\mathbf{z}}$). The flow is pressure driven.

In figure 2.10, the transverse direction is paralleled to the direction of the channel flow (in the streamwise direction), while the wall is located at $z = \pm a$.The channel is assumed to be infinite in $y-$direction. Thus, the flow variables solely depend on $z-$coordinate. From equation (2.18), since the flow is unidirectional and perpendicular to the applied magnetic field $\mathbf{B_0}$, it follows that the induced magnetic field is of the form $\mathbf{B_i} = B_i(z)\hat{\mathbf{z}}$. The pressure gradient in this configuration is also unidirectional, parallel to the streamwise direction and constant.

Following to Ampere's law in equation (2.7) that expresses the relationship between the induced field and the current density, the Lorentz force $\mathbf{J} \times \mathbf{B}$ in equation (2.20) can be expressed in terms of B_i. For fully developed flows, the left-hand side of both equations (2.7) and (2.20) can be neglected. The magnitude of the pressure gradient can be valued as unity by introducing a and $\frac{a^2(-\partial P/\partial x)}{\rho\nu}$ as characteristic length and velocity scales, respectively. The Hartmann flow is represented by the non-dimensional equations: the $x-$momentum equation (2.26), the $x-$induction equation (2.27) along with the boundary conditions (2.28) (Müller & Bühler 2001), i.e.

$$Ha\frac{\partial B_i}{\partial z} + \frac{\partial^2 u}{\partial z^2} = -1, \tag{2.26}$$

$$Ha\frac{\partial B_i}{\partial z} + \frac{\partial^2 B}{\partial z^2} = 0 \text{ for } -1 < z < 1, \tag{2.27}$$

$$u = 0, \pm\frac{\partial B_i}{\partial z} + \frac{1}{c}B_i = 0 \text{ at } z = \pm 1, \tag{2.28}$$

where c and Ha are the wall conductance and Hartmann number, respectively. The Hartmann number and wall conductance ratio are defined respectively as

$$Ha = aB\sqrt{\frac{\sigma_e}{\rho\nu}}, \tag{2.29}$$

$$c = \frac{t_w\sigma_w}{a\sigma_e}, \tag{2.30}$$

where B_i is the induced magnetic field, t_w is the thickness of the walls perpendicular to the field. For electrically insulating walls $c \to 0$, while perfectly conducting walls $c \to \infty$.

The detailed solution of the above equations was discussed by Moreau (1990) and Müller & Bühler (2001), with the final solutions are

$$u = u_c\left[1 - \frac{\cosh(Ha\ z)}{\cosh(Ha)}\right], \tag{2.31}$$

$$B_i = -\frac{z}{Ha} + u_c\frac{\sinh(Ha\ z)}{\cosh(Ha)}, \tag{2.32}$$

$$u_c = \frac{c+1}{Ha(cHa + \tanh(Ha))}. \tag{2.33}$$

Figure (2.11) shows the streamwise velocity profile obtained analytically from equation (2.31) as a function of Hartmann number. The hydrodynamic Poiseuille velocity profile is obtained when $Ha = 0$. As Hartmann number is increased, the Hartmann layers become thinner, and the core region dominates over the entire channel section.

For large Hartmann number (i.e. $Ha \gg 1$), the hyperbolic functions asymptotically approach

$$\sinh(Ha) \to \frac{1}{2}\mathrm{e}^{Ha}, \cosh(Ha) \to \frac{1}{2}\mathrm{e}^{Ha}, \tanh(Ha) \to 1.$$

Substituting those into equations (2.31)–(2.32), shows that at large Hartmann number, the equations can be simplified to

$$u = u_c\left[1 - \mathrm{e}^{Ha_{(|z|-1)}}\right], \tag{2.34}$$

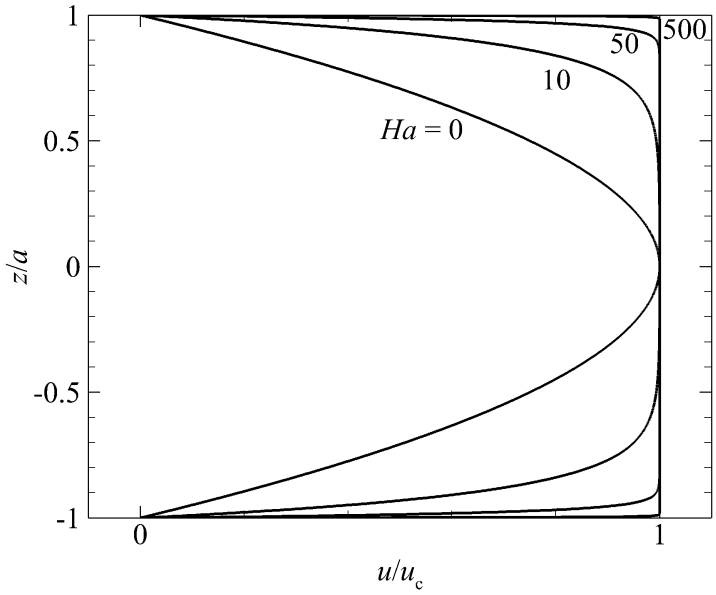

FIGURE 2.11: Hartmann velocity profile for different Hartmann numbers.

$$B_i = -\frac{z}{Ha} \pm u_c \mathrm{e}^{Ha_{(|z|-1)}}, \tag{2.35}$$

$$u_c \to \frac{1+c}{Ha(cHa+1)}. \tag{2.36}$$

Equations (2.34)–(2.35) show that for $Ha \gg 1$, the velocity field and the induced magnetic field decrease exponentially in the Hartmann layer that has thickness scale of Ha^{-1}. The Hartmann flow velocity profile is dependent on Ha, but is not dependent on the conductivity of the wall. For perfectly conducting and insulating walls, the core velocity at large Hartmann number can be respectively simplified to

$$u_c = Ha^{-2} \text{ for } c \to \infty, \tag{2.37}$$

$$u_c = Ha^{-1} \text{ for } c \to 0. \tag{2.38}$$

The integration of the velocity distribution across the cross-section of the channel yield the non-dimensional flow rate

$$Q_v = \int_{-1}^{1} u \, \mathrm{d}z = 2u_c \left[1 - \frac{1}{Ha} \tanh(Ha)\right]. \tag{2.39}$$

This equation can be used to predict the non-dimensional pressure gradient (K_p) as a function of the flow rate (Müller & Bühler 2001)

$$K_p = \frac{2}{Q_v} = \frac{1}{uc\left[1 - \frac{1}{Ha}\tanh(Ha)\right]}. \tag{2.40}$$

2.2.1.5 Duct flow

Shercliff (1953) introduced *Shercliff flow* representing a solution of a fully developed liquid metal flow surrounded by electrically insulated walls under a strong uniform spanwise magnetic field. Shercliff flow is driven by a constant pressure gradient, $\partial p/\partial x = -\rho P_x$. The walls perpendicular and parallel to the direction of the magnetic field are separated by $2a$ and $2b$, respectively. The walls that are normal to the magnetic field are called *Hartmann walls*; meanwhile, the walls that are tangential to the field are called *Shercliff walls*. The Lorentz force acts to retard the core region of the flow as it exerts in the opposite direction of the flow. In the region, the Lorentz force balances the driving pressure gradient. In the Hartmann layers (near the Hartmann walls), the velocity drops significantly and the direction of the induced current in this layer is opposite to those in the core region. For an electrically insulated duct (i.e. $\sigma_w = 0$), the induced currents in the core flow are closed in the Hartmann and Shercliff layers, where the current magnitude is small and the electric resistance is high. The thickness of the Hartmann layers ($\delta_H \sim Ha^{-1}$) is smaller than that of the Shercliff layers ($\delta_S \sim Ha^{-1/2}$).

For a fully developed flow, both velocity and induced magnetic fields are independent on the direction of the flow and have only one component, $\mathbf{u} = u(y,z)\hat{\mathbf{x}}$ and $\mathbf{B_i} = B_i(y,z,)\hat{\mathbf{x}}$.

From the low-Rm approximation, the non-dimensional velocity and the induced magnetic fields in the flow for $-\eta \leq y \leq \eta$ and $-1 \leq z \leq 1$ can be calculated using (Moreau 1990)

$$\Delta u_p + Ha\frac{\partial b_i}{\partial z} = -1,, \tag{2.41}$$

and

$$\Delta b_i + Ha\frac{\partial u_p}{\partial z} = 0,, \tag{2.42}$$

where Ha is the Hartmann number scaled with half duct height, $u_p = U\nu/((a/2)^2 P_x) = 4\hat{u}\nu/(a^2 P_x)$ is the non-dimensional velocity, $\hat{u}$ a dimensional velocity, $P_x = -(1/\rho)\partial p/\partial x$ the driving pressure gradient, ν the kinematic viscosity of the liquid metal, and a is the

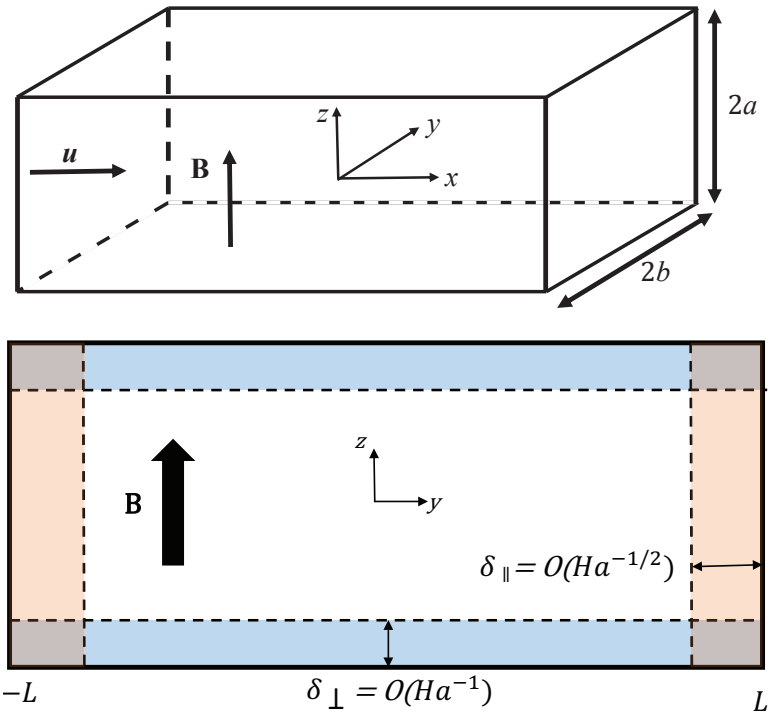

FIGURE 2.12: The configuration of the MHD flow in a rectangular duct under the effect of a uniform external magnetic field. $\delta_{\perp}$ and $\delta_{\parallel}$ represents the thickness of Hartmann layers (blue shaded) and Shercliff layers (orange shaded), respectively.

duct height. The non-dimensional induced magnetic field $b_i = 4B_i\sqrt{\nu/(\sigma\rho)}/(\mu_m a^2 P_x)$, where B_i is the dimensional induced magnetic field strength, while σ, ρ and μ_m are electrical conductivity, density and magnetic permeability of the liquid metal, respectively.

A no-slip boundary condition is imposed at $z = \pm 1$ and $y = \pm\alpha$ for u_p, where $\alpha = 2L/a$ is the aspect ratio of the duct. The induced magnetic field is set to an arbitrary value of zero at $z = \pm 1$ and $y = \pm\alpha$ because the duct walls are assumed to be electrically insulated (Dousset 2009). The governing equations (equations (2.41) and (2.42)) are decoupled with Elsasser variables, written as $A_1 = u_p + b_i$ and $A_2 = u_p - b_i$. Since the condition is symmetrical about the z-axis, only solution A_1 is needed to deduce A_2, u_p and b_i. The solution can be obtained by expanding the unknown A_1 into a Fourier series. Alternatively, the velocity and the induced magnetic field in the governing equations can be expanded directly, which yields

$$u_p(y,z) = \sum_{n=1,3,5,\ldots}^{\infty} u_n(z)\cos(\lambda_n y),, \tag{2.43}$$

and

$$b_i(y,z) = \sum_{n=1,3,5,\ldots}^{\infty} b_n(z)\cos(\lambda_n y), \tag{2.44}$$

with

$$\begin{aligned}
u_n(z) &= \frac{k_n}{\lambda_n^2}\left[1 - \frac{f_n(y)}{f_n(1)}\right], \\
b_n(z) &= \frac{k_n}{\lambda_n^2}\left[1 - \frac{g_n(y)}{f_n(1)}\right], \\
f_n(y) &= \sinh(p_{n2})\cosh(p_{n1}z) - \sinh(p_{n1})\cosh(p_{n2}z), \\
g_n(y) &= \sinh(p_{n2})\sinh(p_{n1}z) - \sinh(p_{n1})\sinh(p_{n2}z), \\
p_{n1,2} &= \frac{1}{2}\left(Ha \mp \sqrt{Ha^2 + 4\lambda_n^2}\right), \\
k_n &= 2\frac{\sin(\lambda_n\alpha)}{\lambda_n\alpha}, \\
\lambda_n &= \frac{n\pi}{2\alpha}.
\end{aligned}$$

Evaluating equation (2.43) for zero Hartmann number ($Ha = 0$) produces the fully developed hydrodynamic Poiseulle velocity profile. On the other hand, the fully developed hydrodynamic velocity profile can be obtained using the exact solution for hydrodynamic duct flow (White 1991; Shah 1972), i.e.

$$u_p(y,z) = \frac{16}{\pi^3}\sum_{n=1,3,5,\ldots}^{\infty}(-1)^{\frac{n-1}{2}}\left[1 - \frac{\cosh(m\pi y/2)}{\cosh(m\pi\alpha/2)}\right]\frac{\cos(m\pi z/2)}{n^3}. \tag{2.45}$$

At large Hartmann number $Ha \gg 1$, the computation of equations (2.41) and (2.42) may lead to a numerical problem (Drake & Abu-Sitta 1966; Müller & Bühler 2001) known as Gibbs phenomenon where trigonometric series exhibit poor convergence and wiggle artefacts near sharp changes in a profile, such as what occurs at the interface between the flat profile through the interior of the duct and the high gradients in the increasingly thin boundary layers towards higher Hartmann numbers. For such cases, both expressions for $u_p(y,z)$ and $b_i(y,z)$ can be computed using an asymptotic solution which is valid for large Ha (Moreau 1990),

$$u_p(y',z) = \frac{1-z}{Ha}[1 - F(\alpha)], \tag{2.46}$$

where

$$F(\alpha) = (1+\alpha^2)\left(1 - \mathrm{erf}\left(\frac{\alpha}{\sqrt{2}}\right)\right) - \alpha\sqrt{\frac{2}{\pi}}\exp\left(-\frac{\alpha^2}{2}\right),, \tag{2.47}$$

and

$$\alpha(y', z) = \frac{y'}{\sqrt{\frac{2}{M}(1-z)}}. \tag{2.48}$$

In equation 2.47 "erf(...)" is the Gauss error function and y' is the y-axis translated to one of the Hartmann walls (refer Figure 2.12).

$$\begin{aligned} y' &= \alpha + y \quad \text{if} \quad y \leq 0, \\ y' &= \alpha - y \quad \text{if} \quad y > 0. \end{aligned} \tag{2.49}$$

The vorticity profile in an x-y plane is then given by

$$\begin{aligned} \xi_z(y') &= \frac{\partial v(x)}{\partial x} - \frac{\partial u(y')}{\partial y'}, \\ &= -\frac{\partial u(y')}{\partial y'}, \\ &= -\frac{1}{u_{p,0}}\frac{\partial u_p(y')}{\partial y'}, \\ &= \frac{1}{u_{p,0}}\left[y'\mathrm{erf}\left(\frac{y'}{2\sqrt{(1-z)/Ha}}\right) + 2\sqrt{\frac{1-z}{\pi Ha}}\exp\left(-\frac{Hay'^2}{4(1-z)}\right) - y'\right]. \end{aligned} \tag{2.50}$$

2.2.1.6 Tendency to two-dimensional

In numerical studies by Schumann (1976) and Zikanov & Thess (1998), they proven that MHD turbulence becomes strictly two-dimensional in a three-dimensional domain with periodic boundaries in low-Rm at $N \gg 1$. Later, Boeck *et al.* (2008) found in their numerical study that the MHD flow could intermittently change between two- and three-dimensional, at moderate N. Quasi-two-dimensional cannot be achieved in the presence of the physical wall, as in experiments (Pothérat & Klein 2014).

When the value of Hartmann number and interaction parameter in an MHD flow are much larger than 1, the flow tends to be similar to two-dimensional flow because fluctuations parallel to the magnetic field are damped. Figure 2.13(a) shows the hydrodynamic case where a Kármán vortex street evolves with secondary instabilities forming

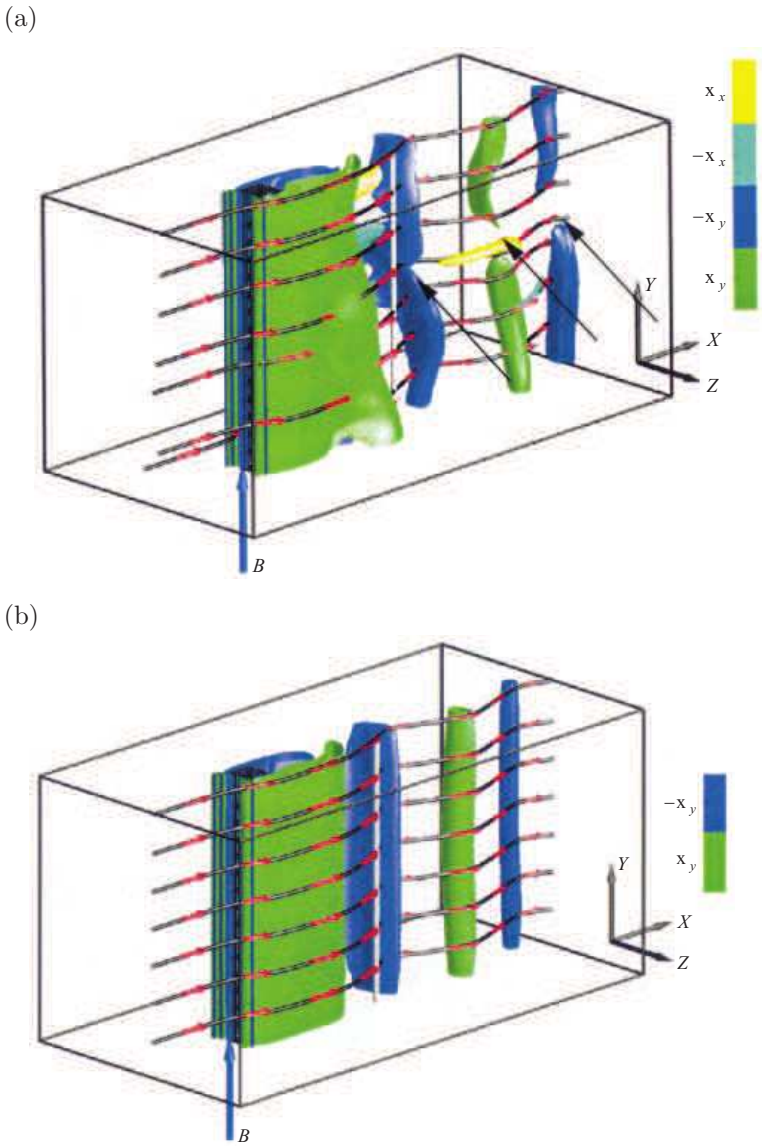

FIGURE 2.13: The isosurface of 3D DNS simulation reproduced from Mück *et al.* (2000), with the permission of Cambridge University Press, on a (a) non-MHD flow past a cylinder and an (b) MHD flow past a cylinder.

three-dimensional streamwise vortex structures. Under the effect of a magnetic field aligned with the cylinder span, the electrodynamic forces become dominant, and the flow becomes two-dimensional (figure 2.13(b)).

In MHD, the orientation of the magnetic field can be in any direction. The magnetic field makes the flow very stable, regardless it is imposed in which direction. The velocity of the flow is almost uniform at the core of the channel due to the induced Lorentz force and only varies near the wall, where Hartmann and Shercliff layers are located due to

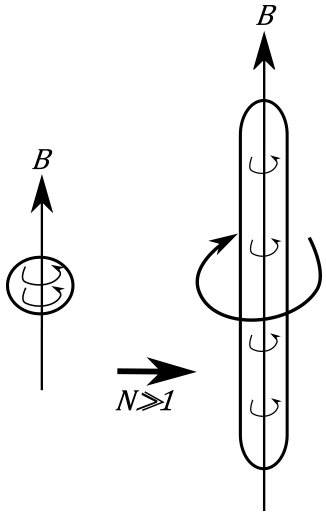

FIGURE 2.14: A sketch of the transition of a flow structure from three-dimensional to a quasi-two-dimensional state when $N \gg 1$ reproduced from Davidson (2001).

the viscous friction with the wall.

For a high Hartmann number, $Ha \gg 1$, and interaction parameter $N \gg 1$, the velocity gradient parallel to the direction of the magnetic field is very small due to the dissipation of velocity components, and vortical structures which are elongated in this direction. As a result of the dissipation of velocity parallel to the magnetic field, the vortical structures perpendicular to the magnetic field are significantly damped, whereas the vortices parallel to the magnetic field are weakly damped as illustrated in figure 2.14. According to Sommeria & Moreau (1982), the vortices parallel to the magnetic field may intensify under the effect of MHD. Due to the three-dimensional effects and the Ohmic and viscous effect in the thin boundary layers along the wall perpendicular to the magnetic field (the Hartmann layers), the MHD flow cannot be treated as a truly two-dimensional flow. In fact, it must be treated as a quasi-two-dimensional flow (Sommeria & Moreau 1982).

The quasi-two-dimensionalisation of MHD flows under a strong transverse magnetic field allows the equation of motion to be simplified from three-dimensional to a two-dimensional equation. This can be achieved by averaging the full Navier–Stokes equations along the direction of the magnetic field yielding a quasi-two-dimensional model, in which three-dimensional effects are confined to the Hartmann layers (Davidson 1995; Pothérat *et al.* 2000b, 2005). More details on SM82 model will be discussed in § 2.2.1.7.

2.2.1.7 Duct flow in the SM82 equations

A quasi-two-dimensional model named as SM82 proposed by Sommeria & Moreau (1982) has been used in the present work. This model approximates the MHD flow in two-dimensional perspective by averaging the flow quantities in the core flow and the Hartmann layers. The model modifies the two-dimensional Navier–Stokes by augmenting a linear braking term which represents the friction in the Hartmann layers. The quasi-two-dimensional model is accurate to order $\mathcal{O}(Ha^{-1}, N^{-1})$. Under this quasi-two-dimensional model, equation (2.1) can be reduced to

$$\frac{\partial \hat{\mathbf{u}}_\perp}{\partial \hat{t}} = -(\hat{\mathbf{u}}_\perp \cdot \hat{\nabla})\hat{\mathbf{u}}_\perp - \frac{1}{\rho}\hat{\nabla}\hat{p} + \nu\hat{\nabla}^2\hat{\mathbf{u}}_\perp - \frac{n}{\tau_H}\hat{\mathbf{u}}_\perp, \tag{2.51}$$

where $\hat{\mathbf{u}}_\perp$ and $\hat{p}_\perp$ are the velocity and pressure fields, projected onto a plane orthogonal to the magnetic field, respectively, $\tau_H = (a/B)\sqrt{\rho/\sigma\nu}$ is the Hartmann damping time (Pothérat 2007) and n is the number of Hartmann walls (i.e. $n = 2$ for a flow between two Hartmann walls).

Pothérat (2007) explained that the quasi-two-dimensionality happened when the time scale for the Lorentz force to diffuse the momentum of structure size of $l_\perp$ along the magnetic field lines over the length of $l_\parallel$, $\tau_{2D} = (\rho/\sigma B^2) l_\parallel^2/l_\perp^2$, is significantly small. The relevant time scales include the time scales for viscous diffusion in the perpendicular planes ($\tau_\nu^\perp = l_\perp^2/\nu$) and the parallel planes ($\tau_\nu^\parallel = l_\parallel^2/\nu$), and the time scale for inertia $\tau_U = l_\perp/U$. Those conditions are achieved when both Hartmann number and interaction parameter are much larger than unity meaning that the flow in the Hartmann layer is laminar (Pothérat & Schweitzer 2011) and variations in velocities in the same direction with the external magnetic field are instantaneously suppressed (Pothérat *et al.* 2000b). By substituting $l_\parallel = a$, the limiting length scales for those three conditions can be found as $l_\perp/a > Ha^{-1/2}$, $l_\perp/a > Ha^{-1}$ and $l_\perp/a > N^{-1/3}$, respectively. The second condition is always achieved if the first condition is achieved. Ekman recirculating flows are present in the Hartmann layer at a moderate value of the interaction parameter. (Pothérat *et al.* 2000b) introduced a more detailed model that takes into account the effect of the moderate inertia. A quasi-two-dimensional model with the presence of turbulent Hartmann layers in the flow was then introduced in the study by Pothérat & Schweitzer (2011).

SM82 model is practical for MHD duct flows under the influence of a strong spanwise magnetic field. However, some discrepancies in the quasi-two-dimensional behavior can

be seen in different situations (e.g. geometry duct). For rectangular duct flows, SM82 model has been verified by Pothérat *et al.* (2000b) against three-dimensional analytical solutions. The error in the velocity profile in the sidewall boundary layer is found to be less than 10%. In the same year, Mück *et al.* (2000) verified the accuracy of the model at high Hartmann number and interaction parameter against three-dimensional simulations of the MHD wake behind a circular cylinder. The same verification against three-dimensional simulation was also done by Kanaris *et al.* (2013), where they found maximum errors of 6% and 8% for the steady and time-dependent flows, respectively, for the averaged parameters at their highest Hartmann number studied. SM82 was also used by Smolentsev & Moreau (2007) to propose an MHD turbulence model.

2.3 Linear stability analysis

In some engineering applications, it is preferred to have steady flows instead of unsteady flows as these are associated with lower noise, less fatigue, lower skin friction drag, and more economical performance regarding fuel consumption. On the other hand, in some applications, fluid flows are preferred to be unsteady, or even turbulent, due to the enhanced mixing and cross stream transport in these flows, resistance to flow separation and stall, for instance. Hence understanding the stability of fluid flows is of critical importance.

One approach towards understanding the three-dimensional stability relies on a linear stability analysis, where the stability of infinitesimal three-dimensional perturbations to a two-dimensional flow is determined by obtaining the leading eigenmode(s) of the evolution operator of the linearised perturbation field. Combined with accurate numerical methods, this technique has been significantly contributing to a better understanding of separated flows in complex geometries over the past few decades. Relevant examples include the flow behind a backward facing step (Barkley *et al.* 2002; Blackburn *et al.* 2008a) and partially blocked channel flows (Griffith *et al.* 2008).

Studies elucidating the stability and the three-dimensionality of the flow past a backward facing step include Armaly *et al.* (1983); Ghia *et al.* (1989); Barkley *et al.* (2002); Wee *et al.* (2004); Griffith *et al.* (2007) and Lanzerstorfer & Kuhlmann (2012). Based on detailed experiments, Ghia *et al.* (1989) and Armaly *et al.* (1983) initially proposed that the curvature in the main flow caused by the second recirculation bubble led to a Taylor–Görtler instability (this type of instability occurs in flows with

curved streamlines when the fluid velocity decreases radially, and the centrifugal force drives pairs of counter-rotating streamwise vortices ((see e.g. Drazin & Reid 2004))). However, the linear stability analysis of Barkley *et al.* (2002) ruled out the effect of a Taylor–Görtler-type of instability because they found that the two-dimensional flow remained linearly stable long after the secondary recirculation bubble appeared. Instead, they found the critical eigenmode to consist of a flat roll localized in the primary recirculation region at the step edge at critical Reynolds number $Re_{3D} = 748$ with spanwise wavenumber $k = 6.9$ for expansion ratio (step to outlet height) of 0.5. Lanzerstorfer & Kuhlmann (2012) extended the study by examining at a various expansion ratio between 0.25 and 0.975. They found that the onset of instability Re_{3D} decreased as the expansion ratio increased from 0.25 to 0.7. The critical mode for these ratios was found to be stationary. As the expansion ratio increased further, the critical mode was changed to oscillatory and Re_{3D} keep decreasing before increased significantly as the expansion ratio goes beyond approximately 0.8.

Hammond & Redekopp (1998) studied the instability properties of separation bubbles. They found that the instability mode associated to the inflection point of the dividing streamline became globally unstable as the peak backflow velocity approached about 30% of the free stream value. As the size of the bubble grew, the peak velocity of the backflow increased correspondingly, and the conditions for local absolute instability could be predicted.

Sherwin & Blackburn (2005) and Blackburn *et al.* (2008a) have identified the modes of instability on a straight tube with a smooth axisymmetric constriction flow using linear Floquet stability and non-modal amplification analysis, and recognize the significant influence of shear layer convective instabilities in the transition of such flows, presented at lower Reynolds number than predicted by a global linear stability analysis.

The theory of flow stability usually deals with the mathematical analysis of the disturbances evolution superposed on a laminar base flow. In most cases, only infinitesimal perturbations are considered so that further simplifications can be justified. In particular, a linear equation governing the evolution of the perturbation is desirable. When the velocities of the disturbance grow above a few percent of the base flow, nonlinear effects become important and the linear equations no longer accurately predict the disturbance evolution. Even though the linear equations have a limited region of validity, they are important in detecting physical growth mechanisms and identifying dominant

disturbance types.

However, no such scenario has been established for the onset of unsteadiness of flows in 180-degree sharp bends. This thesis will discuss such a scenario using methods in the spirit of Barkley *et al.* (2002). The specific aim is to thoroughly characterize the three-dimensional stability of flow around a 180-degree sharp bend as a function of Reynolds number, bend opening ratio, and spanwise wavenumber of the three-dimensional disturbances. It is expected that this thesis will provide insights into more general separated confined flows, and this understanding may enhance the efficiency of heat transport in such systems.

2.4 Non-modal stability analysis

Although the critical Reynolds number and three-dimensional mode structure for primary global instability was determined in a study conducted by Barkley *et al.* (2002) on the backward facing step problem, Blackburn *et al.* (2008a) claimed that it was difficult to observe the predicted modes experimentally. Evidence of the inherently unstable three-dimensional mode can only be seen under thorough perusal. This is because the computations of numerical stability determined an asymptotic, global instability, meanwhile, the flow is unstable to a different type of instability at a much lower Reynolds number. This instability is known as transient local convective instability.

Similar to global linear stability, the analysis starts with the base flow, and considers infinitesimal perturbations to the base flow. The evolution of the perturbation is governed by linearized Navier–Stokes equations. Principally, if infinitesimal perturbations grow in time, the base flow is linearly unstable.

The competition between local instability and basic advection determines the global behavior of the flow (Sturrock 1958; Briggs 1964; Bers 1975). A globally linearly stable flow is possible to be locally convectively unstable because perturbations are constantly advected away from its unstable region. If perturbations are imposed externally, the perturbations will be amplified, specifically in the unstable region. On the contrary, if the flow is globally unstable in a finite region, self-sustained resonance will occur because of the linear global instability (Pierrehumbert 1984; Huerre & Monkewitz 1985; Chomaz *et al.* 1988; Monkewitz *et al.* 1993; Koch 2002).

The global and convective instability can be distinguished by understanding figure 2.15. The flow is globally unstable if an infinitesimal perturbation to parallel shear

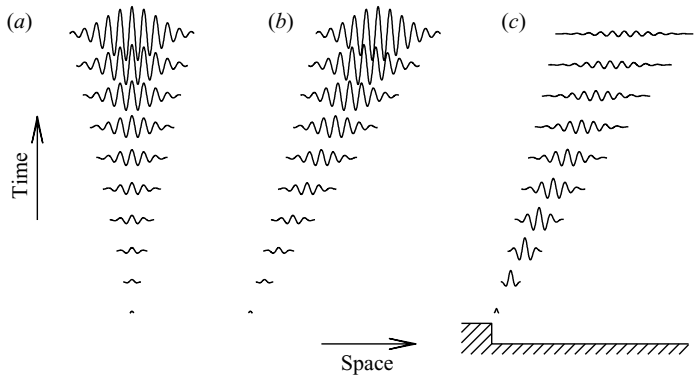

FIGURE 2.15: An infinitesimal perturbation which is localized in space (a) can grow at a fixed location (absolute instability), (b) decay at a fixed points (convective instability). (c) Convective instability surrounded by stable flow regions. Figure reproduced from Blackburn *et al.* (2008a), with the permission of Cambridge University Press.

flow, which initially localized in space, suddenly grows at that fixed spatial location (figure 2.15(a)). Meanwhile, the flow is considered convectively unstable if the initial infinitesimal perturbation propagates as it grows and decays at any fixed point in space (figure 2.15(b)). Practically, most researchers are interested studying inhomogeneous flow geometries where there is a convectively unstable region surrounded by stable region upstream and downstream (figure 2.15(c)).

Linearly global stable flows may experience significant transient growth of disturbances for a period of time before they decay to zero (Schmid & Henningson 2001). The mechanism producing this transient amplification of disturbance energy is the non-modal interaction of leading eigenmodes of the linearised evolution operator, which can produce transient growth even if the eigenmodes are asymptotically stable. Transient growth properties can be recovered from a singular value decomposition of the evolution operator. A substantial transient growth has been demonstrated in parallel shear flows for a plane channel (Reddy *et al.* 1998), pipe (Zikanov 1996), rectangular duct (Biau *et al.* 2008), and abrupt geometrical expansion flows (Blackburn *et al.* 2008a; Blackburn & Sherwin 2007). This instability is dominated by linear transient growth that arises owing to the non-normality of the eigenmodes associated to the linearised equations (Schmid & Henningson 2001; Chomaz 2005).

Kendall (1985) performed flow visualizations of a boundary layer subjected to free stream turbulence and observed the occurrence of elongated streamwise structures with

narrow spanwise scales. The boundary layer disturbances manifest themselves as a periodic spanwise modulation of the streamwise velocity, and it is believed that they give rise to bypass transition. Bypass transition describes the transition emanating from disturbance growth not associated with exponential instabilities (Morkovin 1985).

In a study on inviscid flow, Ellingsen & Palm (1975) introduced an infinitesimal disturbance without variation in the streamwise direction in a shear layer and showed that the velocity component in streamwise direction could increase linearly in time, producing low and high-velocity streaks in the streamwise velocity component. Landahl (1977, 1980) described that a fluid element in a shear layer initially retained its horizontal momentum when it was displaced a distance in the wall-normal direction, hence producing a perturbation in streamwise velocity component which is called as the lift-up effect. The constitution between this effect and the viscous damping is known as transient growth (Henningson *et al.* 1993; Andersson *et al.* 1999). In this application of transient growth analysis, parallel flow is assumed to allow a computation of the maximum transient growth and to correspond with disturbances by optimising the Orr–Sommerfeld operator. In the transient phase, the behavior of the growth function does not depend on the stability or instability of the flow because the stability of the flow is only revealed as $\tau \to \infty$ (Schmid & Henningson 2001).

The flow in an abrupt geometrical expansion, especially backward facing step, has the most resemblance with the flow around a 180-degree sharp bend. For backward-facing step flow (Blackburn *et al.* 2008a), the location of optimal energy distribution was found to be downstream of all the stagnation points of the steady base flow. The transient growth has been compared with full nonlinear system perturbed with white noise. The results seemed to agree very well; narrowband random velocity perturbations was observed at locations corresponding to maximum linear transient growth and the center frequency of the response matches with the streamwise wavelength and mean advection speed of the predicted optimal disturbance. Although three-dimensional perturbations are energetically favored over two-dimensional perturbations, little qualitative difference was observed.

According to Chomaz (2005), for flows which are stable or convectively unstable everywhere, a perturbation introduced in the flow grow while it is traveling the convectively unstable region, decays when enters the stable region. Hence, globally stable flows exhibit large transient growth associated with wave propagation downstream.

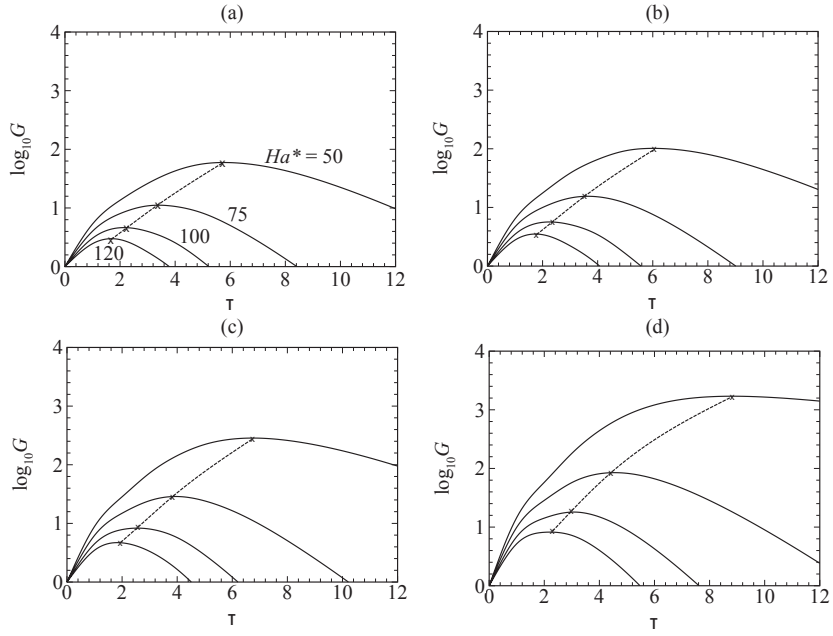

FIGURE 2.16: Plots of $\log_{10} G$ against τ , at blockage ratio and Hartmann numbers as shown for $Re = 400$. The dashed-line curve shows the locus of maximum growth as a function of τ. (a) $\beta = 0.1$; (b) $\beta = 0.2$; (c) $\beta = 0.3$; and (d) $\beta = 0.4$ reproduced from Hussam *et al.* (2012b), with the permission of AIP Publishing.

However, after a sufficiently long time, in the absence of external forcing or feedback, the flows return to their basic state. Knowing the location of the stable and unstable regions could help to sustain the perturbations by fitting additional localised vortex promoters downstream of the weak unstable region.

Hussam *et al.* (2012b) in his study on optimal transient disturbance behind a circular cylinder with the presence of magnetic field have discussed the dependence of energy amplification of the disturbances to Hartmann number and blockage ratio. Figure 2.16 and figure 2.17 explain the effect of Hartmann number and blockage ratio on transient energy growth and vorticity of the optimal initial perturbation, respectively. The damping effect of Hartmann number becomes more significant when increased, hence reducing the maximum energy growth of optimal disturbances (figure 2.16). However, for a fixed Hartmann number, the global maximum energy growth becomes larger at bigger blockage ratio.

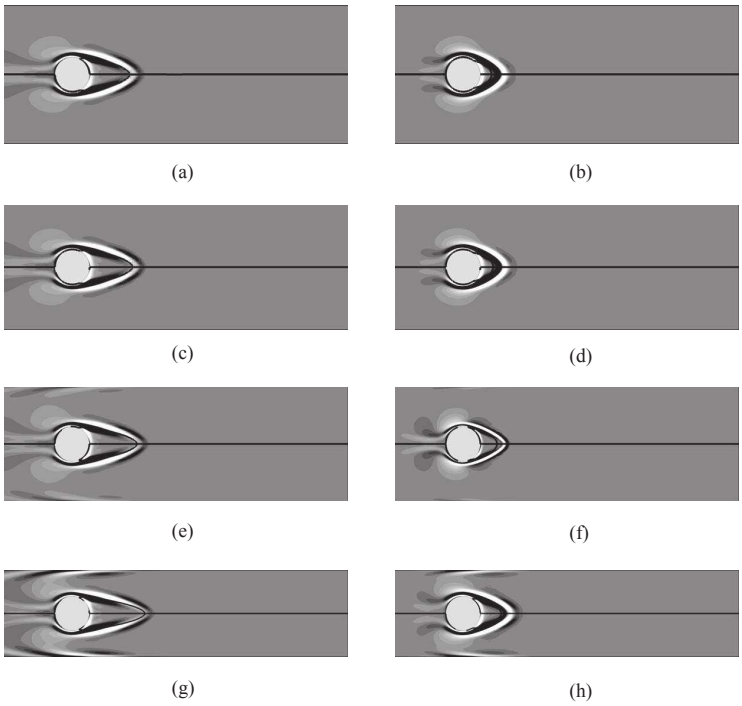

FIGURE 2.17: Plots of vorticity of the optimal initial perturbation for $Re = 400$. $Ha = 50$ (left) and 120 (right) are shown. (a) and (b) $\beta = 0.1$; (c) and (d) $\beta = 0.2$; (e) and (f) $\beta = 0.3$; and (g) and (h) $\beta = 0.4$ reproduced from Hussam *et al.* (2012b), with the permission of AIP Publishing.

2.4.1 Optimal growth in non-MHD flow

A flow that is globally stable may be sensitive to non-modal perturbation for some time before decaying to zero (Schmid & Henningson 2001). There were several studies which discussed this transient growth phenomenon in purely hydrodynamic parallel shear flows, such as a pipe (Zikanov 1996), plane channel (Reddy *et al.* 1998) and rectangular duct flows (Biau *et al.* 2008). The transient growth can be caused by the non-normality of the eigenmodes associated with many shear flows (Schmid & Henningson 2001; Chomaz 2005).

Blackburn *et al.* (2008b,a); Griffith *et al.* (2008) and Cantwell *et al.* (2010) investigated numerically the adjoint and direct eigenmodes in the region of primary instability for abrupt expansion flow that has similarities in the base flow. They discovered that the transient growth in the flows involved instability mechanisms initiated by a combination of shear layer instability and concentrated perturbations near the abrupt geometry change. Blackburn *et al.* (2008a) found that the nature of the two- and three-

dimensional disturbances in the backward facing step flow was similar, although the three-dimensional disturbances of large spanwise wavelength are moderately favoured compared to two-dimensional disturbances.

2.4.2 Optimal growth in MHD flow

Gerard-Varet (2002); Airiau & Castets (2004) and Krasnov *et al.* (2004) have investigated the effect of an applied magnetic field on the transient growth for the flow of an electrically conducting liquid in a channel under the presence of a uniform magnetic field (steady Hartmann flow). The optimal modes were found to have the form of streamwise rolls confined to the Hartmann layers. From the studies mentioned earlier, the energy gain of the optimal perturbations was proportional to $(Re/Ha)^2$, and the critical Reynolds number was much higher than pure hydrodynamic flow.

The optimal linear growth of perturbations in a rectangular duct with different aspect ratio subjected to a uniform transverse magnetic field was studied by Boeck *et al.* (2009) and Krasnov *et al.* (2010). The results showed Shercliff layers located on the wall parallel to the magnetic field confined the disturbances of optimal growth. The optimal perturbations were significantly damped by the magnetic field. Both authors conclude that the Hartmann boundary layers perpendicular to the magnetic field do not contribute to the transient growth.

2.5 Review summary

In conclusion, there has been considerable interest in the case where the magnetic field is parallel to the streamwise direction. However, very few works have been conducted for the case where the magnetic field is imposed transverse to the duct with 180-degree sharp bend. It has been shown by Yamashita *et al.* (1986, 1987); Chung *et al.* (2003) and Zhang & Pothérat (2013) that the sharp bend configuration could enhance turbulence and the heat transfer process. Hence, it is of interest to investigate the potential of the sharp corner configuration in 180-degree bend duct flow in improving the heat transfer process under the effect of a very strong transverse magnetic field.

For linear stability analysis, to the author's knowledge, no study on 180-degree sharp bend geometry has been reported. The closest configuration that has been studied for linear stability analysis is the backward facing step (Barkley *et al.* 2002; Lanzerstorfer & Kuhlmann 2012). Therefore, the objective of the present work is to investigate

numerically and to provide a detailed understanding of the system 1) of the quasi-two-dimensional flows at different Hartmann friction parameter (H) and opening ratio (β), 2) of the full three-dimensional problem in the case without magnetic field. This study could then open the way for a full three-dimensional analysis of the MHD problem, which is outside of the scope of the present work.

In the next chapter, numerical methodology used for this study is discussed, and the validation test of the numerical method is performed.

Chapter 3

Numerical methodology and validations

In this chapter, a brief explanation on the governing equations and the numerical methods used to solve the research problems are presented. The equations that govern the hydrodynamic flow problem are presented in §3.1. In §3.1.2, the computational analysis used to investigate the absolute instability in the hydrodynamic flow is explained. This is followed by the brief discussion on the technique used to study the convective instability in the flow in §3.1.4 and the model used to study the nonlinear behavior near the transition Reynolds number in §3.1.5. In §3.2, the governing equations for magnetohydrodynamic flow is discussed in detail. The problem setup and the boundary conditions for the current study are presented in §3.4.

3.1 Computation of the hydrodynamic (non-MHD) flow

3.1.1 The governing equations

By approximation the governing equations of motion for a fluid, subject to the various initial and boundary conditions and the system geometry, solutions can be obtained using computational methods. The governing equations are known as the Navier–Stokes equations which are named after the nineteenth-century scientists, Claude-Louis Navier and George Gabriel Stokes, as a credit to their derivation. The Navier–Stokes equations are typically written to apply to Newtonian fluids (i.e. fluids which exhibit a linear relationship between shear stress and rate of shear strain). Only Newtonian fluids are considered in this study, and the flow is assumed to be incompressible, which implies that a constant initial density will be preserved for all future instants. Flows at Mach numbers (ratio of the speed of flow to the speed of sound) $Ma \lesssim 0.3$ can

be considered incompressible (Anderson 2010). These assumptions are valid for flow systems discussed in the present work.

In vector form, the incompressible Navier–Stokes equations consist of the momentum equation (Equation (3.1)) and the mass conservation equation (Equation (3.2)), written as

$$\frac{\partial \hat{\mathbf{u}}}{\partial \hat{t}} = -(\hat{\mathbf{u}} \cdot \hat{\nabla})\hat{\mathbf{u}} - \frac{1}{\rho}\hat{\nabla}\hat{p} + \nu\hat{\nabla}^2\hat{\mathbf{u}}, \tag{3.1}$$

$$\hat{\nabla} \cdot \hat{\mathbf{u}} = 0, \tag{3.2}$$

where equation (3.1) describes the momentum relationship, and contains from left to right a non-linear advection term, a pressure term, and a diffusion term. If lengths are normalised by some characteristic length l_o, velocities by characteristic velocity u_o, time by l_o/u_o and pressure by $\rho_o u_o^2$ the equations may be written in non-dimensional form

$$\frac{\partial \mathbf{u}}{\partial t} = -(\mathbf{u} \cdot \nabla)\mathbf{u} - \nabla p + \frac{1}{Re}\nabla^2\mathbf{u}, \tag{3.3}$$

$$\nabla \cdot \mathbf{u} = 0, \tag{3.4}$$

where Re represents the ratio between inertial and viscous forces at scale l_o and is the sole governing parameter of the problems, leaving aside parameters arising from geometry and boundary conditions.

3.1.2 Linear stability analysis

The growth or decay of three-dimensional perturbations introduced into a steady-state solution of the base flow can be obtained by linear stability analysis. The method used to analyze the linear stability of perturbations is based on time integration of the linearized Navier–Stokes equations following Barkley & Henderson (1996) and references therein. The technique is, in fact, a Floquet problem for time-periodic base flows, but is applied to the steady-state base flows using an arbitrary time interval in the present problem for convenience. A brief description of the method will be described in this subsection.

Velocity and pressure fields are decomposed into a two-dimensional base flow and

infinitesimal fluctuating disturbance components as

$$\mathbf{u} = \mathbf{u}_{2\mathrm{D}} + \mathbf{u}', \tag{3.5}$$

$$p = p_{2\mathrm{D}} + p'. \tag{3.6}$$

Substituting equations (3.5) and (3.6) into (3.3) and (3.4), and retaining terms at the first order of the perturbation field yields the linearised Navier–Stokes equations describing the evolution of infinitesimal three-dimensional disturbances,

$$\frac{\partial \mathbf{u}'}{\partial t} = -\mathbf{DN}(\mathbf{u}') - \nabla p' + \frac{1}{Re}\nabla^2 \mathbf{u}', \tag{3.7}$$

$$\nabla \cdot \mathbf{u}' = 0, \tag{3.8}$$

where the linearised advection term is in convective form $\mathbf{DN}(\mathbf{u}') = (\mathbf{u}_{2\mathrm{D}} \cdot \nabla)\mathbf{u}' + (\mathbf{u}' \cdot \nabla)\mathbf{u}_{2\mathrm{D}}$.

Since the base flow is invariant in the spanwise direction, general perturbations may be decomposed into Fourier modes with spanwise wavenumber

$$k = \frac{2\pi}{\lambda}, \tag{3.9}$$

where λ is the wavelength in the spanwise direction. As per equation (3.7) and (3.8), the equations are linear in $\mathbf{u}'$ and therefore Fourier modes are linearly independent and coupled only with the two-dimensional base flow. The absence of any spanwise component to the base flow further permits a single phase of the complex Fourier mode to be considered, i.e.

$$\left.\begin{array}{rcl} u'(x,y,z,t) & = & \hat{u}(x,y,t)\cos(kz) \\ v'(x,y,z,t) & = & \hat{v}(x,y,t)\cos(kz) \\ w'(x,y,z,t) & = & \hat{w}(x,y,t)\sin(kz) \\ p'(x,y,z,t) & = & \hat{p}(x,y,t)\cos(kz) \end{array}\right\}. \tag{3.10}$$

The flow stability therefore reduces to a three-parameter problem in Re, β and k. Following Barkley & Henderson (1996) and others, spanwise phase locked perturbations of the form in equation (3.10) remain in this form under the linearised evolution equations (3.7)–(3.8): for a Re, β and spanwise wavenumber k, the three-dimensional/three-component perturbation field $\mathbf{u}'(x,y,z,t)$ then reduces to a two-dimensional/three-component field

$$\hat{\mathbf{u}}(x,y,t) = \langle \hat{u}(x,y,t), \hat{v}(x,y,t), \hat{w}(x,y,t) \rangle, \tag{3.11}$$

which is conveniently computed on the same two-dimensional domain as the base flow. The perturbation z-velocity features a sine function rather than a cosine as only z-derivatives of this term (yielding a cosine) interact with other terms under equations (3.7)–(3.8).

3.1.3 Mode stability

The evolution of a single Fourier mode can be determined by time integrating the Fourier transform of equation (3.3) and (3.4). By defining $\mathscr{A}(\tau)$ representing the linear evolution operator for time integration (via equations (3.8)–(3.7) of a perturbation field over time interval τ. Integration in time yields

$$\mathbf{u}'(t+\tau) = \mathscr{A}(\tau)\mathbf{u}'(t), \tag{3.12}$$

and, after application of the Fourier transform, an eigenvalue problem may then be constructed as

$$\mathscr{A}(\tau)\hat{\mathbf{u}} = \mu\hat{\mathbf{u}}. \tag{3.13}$$

The complex eigenvalue μ is a Floquet multiplier that relates to the exponential growth rate σ and angular frequency ω of the eigenmode through

$$\mu \equiv e^{(\sigma+\mathrm{i}\omega)\tau}, \tag{3.14}$$

and the eigenvector field is denoted by $\hat{\mathbf{u}}$. As the base flows are time-invariant in this study, the usual time period is replaced by an arbitrary time interval for τ. An appealing feature of this technique is that solutions to the eigenvalue problem (3.13) may be obtained using iterative methods involving time-integration of the linearised perturbation field via (3.7)-(3.8), which avoids the substantial cost of explicitly constructing the very large operator $\mathscr{A}(\tau)$.

Stability is dictated by the leading eigenmode (i.e. $\mu = \mu_k$ having largest $|\mu_k|$ as from equation (3.14)). Neutral stability corresponds to $|\mu| = 1$, while $|\mu| > 1$ and $|\mu| < 1$ describe unstable and stable flows, respectively. The bifurcation may be either synchronous ($\omega = 0$) or oscillatory ($\omega \neq 0$). The smallest Reynolds number for which any spanwise wavenumber k yields $|\mu| = 1$ is the critical Reynolds number for the onset of instability.

The following steps are taken to solve this problem numerically. The time-invariant base flow at a given Re and β is obtained by solving the two-dimensional Navier–Stokes equations (3.5)–(3.6). Subsequently, random initial perturbation fields are constructed for one or more spanwise wavenumbers k, and an implicitly restarted Arnoldi method in conjunction with time integration of the linearised Navier–Stokes equations (3.7) and (3.8) is used to determine the leading eigenmodes governing stability. The ARPACK (Lehoucq *et al.* 1998) implementation of the implicitly restarted Arnoldi method is used, and the present formulation has been validated and employed across Sheard *et al.* (2009); Sheard (2011); Vo *et al.* (2014, 2015).

3.1.4 Non-modal amplification analysis

Transient growth analysis is concerned with identifying the optimal disturbances that achieve maximum energy growth when evolved over a specified time interval. In the present work, the focus is on linearised transient growth, where energy growth is analysed on a linearised disturbance field. Transient growth is generated by the non-modal interaction between eigenmodes of the linearised evolution operator of the disturbance field.

Schmid & Henningson (2001) and Blackburn *et al.* (2008a) describe a method for determining the optimal energy growths and initial disturbance fields. For a given time interval τ, the linear perturbation velocity field $\mathbf{u}'(x, y, z)$ of the spanwise (z-direction) wavenumber k produces the optimal growth G in the L_2 energy norm at $t = \tau$ on the steady base flow $\mathbf{u}(x, y)$. The main aim of this analysis is to find the shape of the perturbation that leads to a maximal energy amplification, G, over some specified time, τ. The global maximum of G for a given wavenumber is denoted by G_{max} with its corresponding τ represented by τ_{max}. Asymptotically, the modes are stable. However, the transient disturbance the modes cause in the flow can be of sufficient magnitude to cause the flow to become nonlinear. This can lead to the transition at lower Reynolds number compared to the predicted onset of globally instability predicted by the linear absolute stability analysis. This is particularly the case for flows of long, thin shear layers where the convective instabilities can grow for a long time as they advect along separating shear layers.

A description of transient growth analysis begins with the linear evolution operator described in equation (3.12) The transient growth is defined about the energy norm of

the perturbation field derived from the L_2 inner product

$$2E(\mathbf{u}') = (\mathbf{u}', \mathbf{u}') \equiv \int \mathbf{u}' \cdot \mathbf{u}' \mathrm{d}v, \tag{3.15}$$

where E is the kinetic energy per unit mass of the perturbation, integrated over the spatial domain (v). The linear governing equations make it sufficient to consider the initial perturbation field $\mathbf{u}'(0)$ to have a unit norm. The transient energy growth over interval τ is (Blackburn *et al.* 2008a)

$$\frac{E(\tau)}{E(0)} = (\mathbf{u}'(\tau), \mathbf{u}'(\tau)). \tag{3.16}$$

In terms of the operator $\mathscr{A}(\tau)$ and its adjoint $\mathscr{A}^*(\tau)$ in the L_2 inner product,

$$\frac{E(\tau)}{E(0)} = (\mathscr{A}(\tau)\mathbf{u}'(0), \mathscr{A}(\tau)\mathbf{u}'(0)) \tag{3.17}$$

$$= (\mathbf{u}'(0), \mathscr{A}^*(\tau)\mathscr{A}(\tau)\mathbf{u}'(0)), \tag{3.18}$$

where $\mathscr{A}(\tau)$ is obtained by integrating the adjoint linearized Navier–Stokes equations over interval τ. The adjoint equations of the linearised equations are

$$\frac{\partial \mathbf{u}^*}{\partial t} = -\mathbf{DN}^*\mathbf{u}^* - \nabla p^* + \frac{1}{Re}\nabla^2\mathbf{u}^* \tag{3.19}$$

$$\nabla \cdot \mathbf{u}^* = 0. \tag{3.20}$$

where the adjoint advection operator is defined as $\mathbf{DN}^*(\mathbf{u}^*) = (\mathbf{u}\cdot\nabla)\mathbf{u}^* + (\mathbf{u}^*\cdot\nabla)\mathbf{u}$. Let λ_j and $\mathbf{v}_j$ denote eigenvalues and normalized eigenfunctions of the operator $\mathscr{A}^*(\tau)\mathscr{A}(\tau)$, then

$$\mathscr{A}^*(\tau)\mathscr{A}(\tau)\mathbf{v}_j = \lambda_j \mathbf{v}_j. \tag{3.21}$$

The maximum possible energy growth, denoted by $G(\tau)$, over a specified time τ, is given by the dominant eigenvalue of $\mathscr{A}^*(\tau)\mathscr{A}(\tau)$,

$$G(\tau) = \max(\lambda_j). \tag{3.22}$$

The global maximum for any time interval is denoted by

$$G_{\max} = \max(G(\tau)). \tag{3.23}$$

3.1.5 Stuart–Landau model analysis

The nonlinear mode evolution theory about the Stuart–Landau model provides a way to study the nonlinear behavior near the transition Reynolds number. The Stuart–Landau model is valid in the vicinity of the transition Reynolds number and has found wide application for classification of the non-linear characteristics of bifurcations in fluid flows. Examples include analysis of the Hopf bifurcation from steady-state flow past a circular cylinder producing the classical Kármán vortex street (Provansal *et al.* 1987; Dušek *et al.* 1994; Schumm *et al.* 1994; Albarède & Provansal 1995; Thompson & Le Gal 2004), the regular (steady-to-steady) bifurcation breaking axisymmetry in the flow behind a sphere (Thompson *et al.* 2001). and three-dimensional transition behind a cylinder (Henderson & Barkley 1996; Sheard *et al.* 2003a), staggered cylinders (Carmo *et al.* 2008), and rings (Sheard *et al.* 2004, 2003b). The model describes the growth and saturation of perturbation as (Landau & Lifshitz 1976)

$$\frac{\mathrm{d}A}{\mathrm{d}t} = (\sigma + i\omega)A - l(1 + ic_n)|A^2|A + ..., \tag{3.24}$$

where A is the amplitude of the evolving instability as a function of time, and the right side of the equation represents the first two terms of a series expansion. The growth rate and angular frequency of the mode in the linear regime ($|A| \to 0$) are respectively denoted by σ and ω, while weakly non-linear properties are determined by the second term on the right-hand side. The sign of l dictates whether the mode evolution is via a supercritical ($l > 0$) or subcritical ($l < 0$) bifurcation, and any frequency shift is described by Landau constant c (Dušek *et al.* 1994; Le Gal *et al.* 2001; Thompson *et al.* 2001). By taking $A(t)$ as the envelope of an oscillatory amplitude measure of the growing mode, phase information may be disregarded and only the real part of equation (3.24) need to be considered. It is convenient to then take

$$\frac{\mathrm{d}\log|A|}{\mathrm{d}t} = \frac{1}{A}\frac{\mathrm{d}A}{\mathrm{d}t} = \sigma - l|A|^2. \tag{3.25}$$

Hence a positive slope (l) in a plot of $\mathrm{d}(\log|A|)/\mathrm{d}t$ against $|A|^2$ will indicate a subcritical bifurcation, while a negative slope corresponds to a supercritical bifurcation. Whether a supercritical bifurcation is of a pitchfork or Hopf type is dependent on whether the growing mode is synchronous or oscillatory.

Other than sub- and supercritical bifurcation, there is another possible bifurcation

scenario called transcritical bifurcation. A dynamical system producing transcritical behavior takes the form

$$\frac{\mathrm{d}\rho}{\mathrm{d}t} = \sigma\rho - l\rho^2, \tag{3.26}$$

which differs from the amplitude part of the Stuart–Landau model equation (3.24) by the replacement of ρ^3 with ρ^2 in the non-linear term on the right hand side. Under an analogous manipulation,

$$\frac{\mathrm{d}\log\rho}{\mathrm{d}t} = \sigma - l\rho = \sigma - l\sqrt{\rho^2}. \tag{3.27}$$

The $\sqrt{\rho^2}$ term indicates that an infinite gradient would present at $|A|^2 = 0$ in a plot of $\mathrm{d}(\log|A|)/dt$ against $|A|^2$. Similarly, a transcritical dynamical system expressed in terms of the complex amplitude A,

$$\frac{\mathrm{d}A}{\mathrm{d}t} = (\sigma + i\omega)A - l(1 + ic)A^2, \tag{3.28}$$

features a real component that simplifies to

$$\frac{\mathrm{d}(\log\rho)}{\mathrm{d}t} = \sigma - l\sqrt{\rho^2}[\cos\phi - c\sin\phi]. \tag{3.29}$$

In the limit $|A| = \rho \to 0$, the oscillation described by the trigonometric term produces gradients in $\mathrm{d}(\log|A|)/\mathrm{d}t$ as a function of $|A|^2$ that approach infinity.

3.2 Computation of the magnetohydrodynamic (MHD) flow

3.2.1 The governing equations

The numerical scheme used in this research solves the viscous, incompressible Navier–Stokes and energy equations for both two-dimensional hydrodynamic and quasi-two-dimensional magnetohydrodynamic problems. By adopting the SM82 model derived by (Sommeria & Moreau 1982), both problems can be solved using the same equation. Using the non-dimensional scaling from equation (2.12), the non-dimensional magnetohydrodynamic equations of continuity, momentum and energy can be reduced to

$$\nabla \cdot \mathbf{u} = 0, \tag{3.30}$$

$$\frac{\partial \mathbf{u}}{\partial t} = (\mathbf{u} \cdot \nabla)\mathbf{u} + \nabla p = \frac{1}{Re}\nabla^2 \mathbf{u} - \frac{H}{Re}\mathbf{u}, \tag{3.31}$$

$$\frac{\partial \theta}{\partial t} + ((u) \cdot \nabla)\theta = \frac{1}{Pe}\nabla^2 \theta \tag{3.32}$$

where the parameter $H = n(a^2/L_z^2\sqrt{\sigma/(\rho\nu)}$ is a measure of the friction term with characteristic dimensional Hartmann friction time $t_H = nL_z/B\sqrt{\rho/(\sigma\nu)}$ (Pothérat 2007). The Hartmann parameter denotes the effect of the Lorentz force on the flow. n represents the number of Hartmann layers in the problem: for 180-degree sharp bend problem, $n = 4$, 2 at the inflow duct before the bend, and another 2 at the outflow duct after the bend. As for a rigid free surface problem, it could be defined that $n = 1$. As for L_z, instead of representing channel half-height like in Frank *et al.* (2001), this thesis uses L_z to represent the distance between the Hartmann walls as implemented by Sommeria & Moreau (1982). For the hydrodynamic problem, the absence of the spanwise magnetic field results in $H = 0$, which will revert equation (3.31) into hydrodynamic Navier–Stokes equation (Equation (3.3)).

Using the no-slip boundary conditions at the side walls on the exact solution of equation (3.31) results in fully developed quasi-two-dimensional flow, known as Hartmann profile which can be written as (Pothérat 2007)

$$u_\perp(y) = \frac{\cosh\sqrt{H}}{\cosh\sqrt{H} - 1}\left(1 - \frac{\cosh(\sqrt{H}y)}{\cosh\sqrt{H}}\right). \tag{3.33}$$

.

In the limit $H \to 0$, equation (3.33) recovers the two-dimensional Poiseuille profile, whereas, at non-zero Hartmann, it tends to give almost flat profile especially at higher Hartmann, except near the side wall as can be seen in figure 3.1. This behavior is caused by the Lorentz force which opposes the direction of the main bulk flow that is linearly dependent upon the strength of the spanwise magnetic field, or H (Barleon *et al.* 1996) and the component of velocity that perpendicular to the direction of the magnetic field (Müller & Bühler 2001). Due to the no-slip condition on the wall, the fluid at the core region has higher velocity, which interacts with the magnetic field to induce more electric current compared to the area near the wall. The higher the electric current density, the greater the Lorentz force induced from the interaction between the current and the magnetic field. This causes the Lorentz force in the core is stronger that attributes to the near-flat profile in that region.

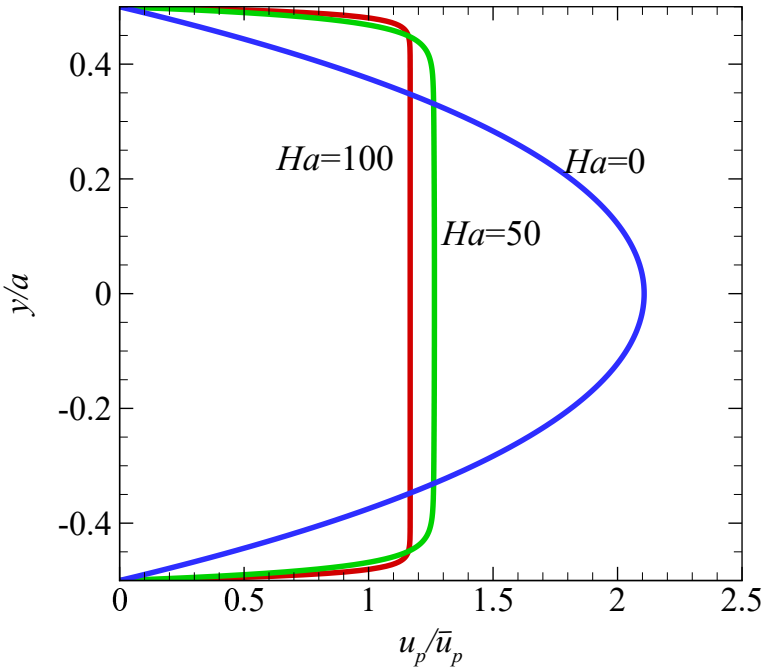

FIGURE 3.1: Streamwise velocity profiles of MHD rectangular duct flow with electrically insulating walls.

3.3 The spectral-element method

The spectral-element method is used to discretise the governing flow and energy equations in space (Karniadakis *et al.* 1991; Karniadakis & Sherwin 2013). Similarly to finite-element methods, the domain space is discretised into macro elements which are then further discretised into $N_p \times N_p$ interpolation points employing a high-order polynomial basis. The spectral element technique uses the tensor product of higher-order Lagrangian polynomials to interpolate the solution variables within each element.

3.3.1 Spatial discretisation

The two-dimensional computational domain is discretised into quadrilateral elements. Gauss–Lobatto–Legendre quadrature is employed for integration within each element. The Gauss–Lobatto–Legendre quadrature points include points fixed at the element edges to facilitate a continuous solution between adjoining elements. Hence, the quadrature points tend to be concentrated near the edges of the elements. Q nodes of ξ_i and weights (w_i) define the quadrature rule. The domain of integration for P-nodes quadrature rule is taking the following form (Karniadakis & Sherwin 2013)

$$\int_{-1}^{1} p(\xi)\mathrm{d}\xi = \sum_{i=0}^{Q-1} w_i p(\xi_i) + \varepsilon(p), \tag{3.34}$$

for all polynomials p, where ξ is the real variable in the equation solved to find Gauss-Legendre-Lobatto quadrature point, w_i and ξ_i correspond to the i^{th} Gauss–Legendre–Lobatto weighting coefficient and quadrature points, respectively, and $\varepsilon(p)$ is the approximation error. If $p(\xi)$ is a polynomial of degree $2Q-3$ or less, the approximation error will be $\varepsilon(p)=0$. In the Gauss–Legendre–Lobatto quadrature rule, the end points of the integration interval are forced to be among the quadrature nodes, which reduces the accuracy from the optimal exactness for polynomial of degree $2Q-1$ exhibited by Gaussian quadrature. The Q quadrature nodes are determined from the roots of the equation

$$(1-\xi^2)P_{Q-1}(\xi) = 0 \qquad \text{with} \qquad -1 \leq \xi \leq 1, \tag{3.35}$$

and the weighting coefficients are described by

$$w_i = \frac{2}{Q(Q-1)[P_{Q-1}(\xi_i)]^2} \qquad \text{with} \qquad i = 0, 1, ..., Q-1, \tag{3.36}$$

where P_{Q-1} is the Legendre polynomial of order $Q-1$. By using Rodriguez's formula, the Legendre polynomial can be defined as

$$P_{Q-1} = \frac{1}{2^{Q-1}(Q-1)!}\frac{\mathrm{d}^{Q-1}}{\mathrm{d}\xi^{Q-1}}(\xi^2-1)^{Q-1} \qquad \text{where} \qquad Q = 1, 2, ... \tag{3.37}$$

The quadrature points and the weighting coefficients allow integrals to be approximated using Gauss–Legendre–Lobatto quadrature.

3.3.2 Temporal discretisation

The solver used in the current study employs a high-order three-step splitting scheme for temporal discretisation following Karniadakis *et al.* (1991). In this scheme, an operator splitting treatment of the Navier–Stokes equations is applied, separating the advection, pressure and diffusion terms, and integrating these in three separate substeps. Taking the order of integration for the advection, pressure and diffusion terms to be J_e, J_p and J_i, respectively, the semi-discrete system is written as follows (Karniadakis & Sherwin 2013)

$$\frac{\mathbf{u}^* - \sum_{q=0}^{J_i-1} \alpha_q \mathbf{u}^{n-q}}{\Delta t} = -\sum_{q=0}^{J_e-1} \beta_q \left\{ [(\mathbf{u}\cdot\nabla)\mathbf{u}]^{n-q} \right\}, \tag{3.38}$$

$$\frac{\mathbf{u}^{**} - \mathbf{u}^*}{\Delta t} = -\nabla p^{n+1}, \tag{3.39}$$

$$\frac{\gamma_0 \mathbf{u}^{n+1} - \mathbf{u}^{**}}{\Delta t} = \frac{1}{Re}\nabla^2 \mathbf{u}^{n+1}. \tag{3.40}$$

The first substep involves an evaluation of an intermediate velocity field $\mathbf{u}^*$ from equation (3.38) using an explicit projection of the velocity field to the future time $(n+1)$ for evaluation of the right-hand side of equation (3.38).

In the second substep, equation (3.39) is solved by first taking the divergence of this equation to obtain a Poisson equation for pressure. Applying the divergence-free condition to the second intermediate velocity field (i.e. $\nabla \cdot \mathbf{u}^{**} = 0$), this Poisson equation is written as

$$\nabla^2 p^{n+1} = \nabla \cdot \left(\frac{\mathbf{u}^*}{\Delta t} \right). \tag{3.41}$$

This is solved with the appropriate high-order Neumann boundary conditions for pressure (Karniadakis *et al.* 1991).

In the third substep, implicit Helmholtz equations (equation (3.40)) is solved to evaluate the components of the velocity field $\mathbf{u}^{n+1}$. Overall, the splitting scheme achieves a second-order time-accuracy when the first-order pressure boundary conditions are imposed (Karniadakis *et al.* 1991).

The energy equation is solved using the same third-order backwards differentiation scheme, as used for the velocity field, and expressed as

$$\frac{\theta^* - \sum_{q=0}^{J_i-1} \alpha_q \theta^{n-q}}{\Delta t} = -\sum_{q=0}^{J_e-1} \beta_q \{ [(\mathbf{u}\cdot\nabla)\theta]^{n-q} \}, \tag{3.42}$$

and

$$\frac{\gamma_0 \theta^{n+1} - \theta^*}{\Delta t} = \frac{1}{Pe}\nabla^2 \theta^{n+1}. \tag{3.43}$$

The Hartmann friction term in the momentum equation of the SM82 model is evaluated using the extrapolated velocity field and is appended to equation (3.38) and written as

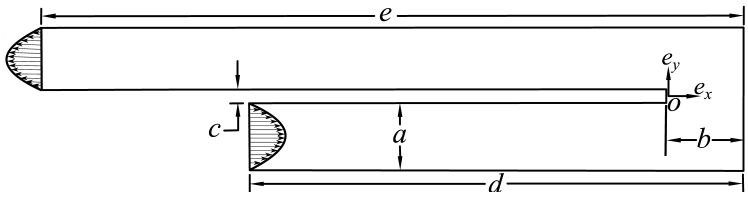

FIGURE 3.2: Flow geometry for the 180-degree sharp bend system. The fluid enters the bottom channel flowing to the right, and exits the top channel flowing leftwards.

$$\frac{\mathbf{u}^* - \sum_{q=0}^{J_i-1} \alpha_q \mathbf{u}^{n-q}}{\Delta t} = -\sum_{q=0}^{J_e-1} \beta_q \left\{ [(\mathbf{u}\cdot\nabla)\mathbf{u}]^{n-q} + \frac{H}{Re}\mathbf{u}^{n-q} \right\}. \tag{3.44}$$

3.4 Problem geometry and boundary conditions

Figure 3.2 shows the computational domain under consideration, including the geometric parameters for the problem. The channel widths in the inlet and at the bend are a and b, respectively. The heights of the inlet and outlet channels are identical. The divider thickness is c, with d and e, respectively, denoting the lengths from the far wall of the bend to the inlet and outlet. The ratio of the gap c to the channel height a is held fixed at 4% following Zhang & Pothérat (2013), while the lengths of the upstream and downstream channels are $(d-b) = 15a$ and $(e-b) = 30a$. Recall that the opening ratio of the bend is defined in equation (1.7).

Initial conditions need to be defined reasonably to confirm that physical solutions can be obtained from the governing equations. The conditions need to identify all the flow variables at this initial instant over the whole domain and the boundary conditions required at all boundaries of the flow domain. In most engineering applications, the fluid is confined to a finite domain bound by an interface, Γ, representing rigid walls. In the current study, the initial condition used for the flow is zero-velocity $\mathbf{u}$ everywhere in the domain.

Kinematic constraints must be applied at the interface between the fluid and rigid walls, free surface or in-out flow conditions typically. Due to viscosity, for the case of a rigid non-moving boundary, the velocity is zero at the interface, Γ, between the fluid and the boundary. The boundary condition is expressed as a no-slip boundary e.g. Batchelor (1967); Müller & Bühler (2001)

$$\mathbf{u} = 0 \text{ at } \Gamma. \tag{3.45}$$

Some modification is needed on the kinematic boundary condition if the walls are moving or if there is no wall (free surface).

The electromagnetic boundary conditions are controlled by the electrical conductivity (σ_w) of the channel wall. For insulating walls ($\sigma_w = 0$), the current from the fluid cannot enter the wall causing the component of current density normal to the interface is zero to be at the wall

$$\mathbf{J} \cdot \mathbf{n_n} = 0 \text{ at } \Gamma. \tag{3.46}$$

For conducting walls ($\sigma_w \to \infty$), the current density tangential to the interface is zero at the wall

$$\mathbf{J} \cdot \mathbf{n_t} = 0 \text{ at } \Gamma, \tag{3.47}$$

where $\mathbf{n_n}$ and $\mathbf{n_t}$ dictate a vector normal and tangential to the interface Γ, respectively.

In industrial and engineering applications, channel walls are usually made of metallic material with finite electrical conductivity. The boundary condition for the current density can be derived using equations (2.8) and (2.6)

$$\mathbf{J} \cdot \mathbf{n_n} = \frac{\sigma}{\sigma_w} \mathbf{J_w} \cdot \mathbf{n_n} \text{ at } \Gamma, \tag{3.48}$$

In this thesis, the duct walls are assumed to be electrically insulated, and under the SM82 model where the current and electric potential fields are not explicitly solved. Hence, electrical conditions will not be discussed further in this thesis.

Kinematic constraints must be applied at the interface between the rigid walls and fluid. Due to viscosity, the velocity is zero at the interface between the boundary and the fluid, and the hydrodynamic boundary condition reads (e.g. Müller & Bühler 2001)

$$\mathbf{u} = 0. \tag{3.49}$$

By assuming the flow in the inlet is steady and laminar between two infinite plates, the velocity profile only varies in the y-direction, i.e. $\mathbf{u}_x = \mathbf{u}_x(y)$. Therefore, a Poiseuille velocity profile is imposed at the inlet ($x = -15$)

$$\mathbf{u}_x(y) = \left[1 - \left(\frac{2y + 0.52}{L}\right)^2\right]. \tag{3.50}$$

However, for MHD case, as described in §3.2, under the condition of MHD, the flow is quasi-two-dimensional and consists of a core region, where the velocity is invariant along the direction parallel to the magnetic field, and a thin Hartmann layer at the wall perpendicular to the magnetic field. The inlet boundary for MHD case given by

$$\mathbf{u}_x(y) = \frac{\cosh\sqrt{Ha}}{\cosh\sqrt{Ha} - 1}\left[1 - \frac{2\cosh\sqrt{Ha}(y + 0.52)}{\cosh\sqrt{Ha}}\right]. \tag{3.51}$$

As Ha approaching 0, the inlet velocity profile will be recovered as Poiseuille profile whereas for high values of Ha, the profile is almost flat, except in the near the wall where it exhibits Shercliff boundary layers having a thickness that scales with $Ha^{-1/2}$.

3.5 Validation and grid resolution studies

3.5.1 Solver validation

Finally, the present model is validated against published results for the position and length of the recirculation bubble. In a viscous flow (featuring boundary-layers adjacent to no-slip surfaces), the point of reattachment can be precisely measured by finding the location where the wall shear stress is zero

$$\tau_{\text{wall}} = \mu\partial u/\partial y = 0. \tag{3.52}$$

Figure 3.3 shows a comparison between the recirculation length of the first bubble (L_{R_1}/a) in a flow with $\beta = 1$ as a function of Reynolds number between the present and previously reported results digitised from figures in Zhang & Pothérat (2013) and Chung *et al.* (2003). The coefficient of determination, R^2, between the present data and those of these previous studies differ by just 2.2% and 0.2%, respectively. The comparison displays a strong agreement between the studies, with each curve increasing rapidly and linearly at Reynolds numbers $Re \lesssim 200$, before transitioning to a more gradual linear regime of further bubble elongation beyond $Re \approx 300$. This regime terminates with the onset of unsteady flow. The sudden drop in the data from Zhang & Pothérat (2013) at $Re \approx 600$ coincides with the onset of unsteady flow in that study. The present computations return a steady-state (in agreement with Chung *et al.* 2003) up to $Re \approx 700$.

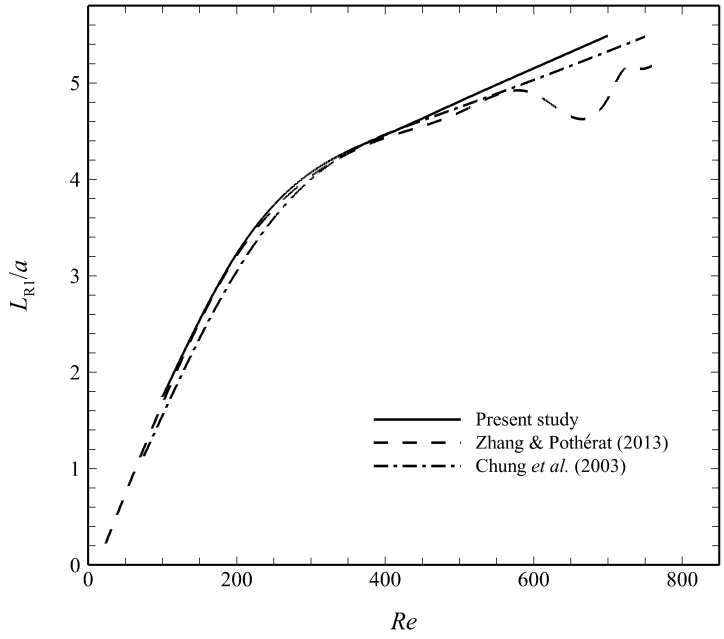

FIGURE 3.3: Length of the first recirculation bubble (L_{R_1}) against Reynolds number (Re), comparing the present results to those of Zhang & Pothérat (2013) and Chung *et al.* (2003).

The flow past a 180-degree sharp bend is a deceptively difficult problem to fully resolve, especially at large Reynolds number due to the sensitivity of the solution to the mesh structure mainly near the sharp bend. This section describes the tests used to validate the numerical algorithm, and to select appropriate meshes and element order. For the spatial resolution study, we varied element polynomial degree from $N = 4$ to $N = 8$ of a mesh based on domain length parameters from the mesh domain. For consistency with the domain size study, the mesh employed in this study models a 180-degree sharp bend with opening ratio $\beta = 1$ and $Re = 500$. In this regime, the flow is steady, with two recirculation bubbles. Figure 3.4 shows the detail of the mesh with $N = 3$. The mesh is structured and refined in the vicinity of the sharp bend as well as in the downstream channel to capture the detailed structure of the flow that passes around the bend.

3.5.2 Grid resolution study

To demonstrate the accuracy of computing recirculation length in the base flow, table 3.1 shows the relative error of several measured quantities as a function of polynomial order. From computation of error on the recirculation length (Table 3.1), it was

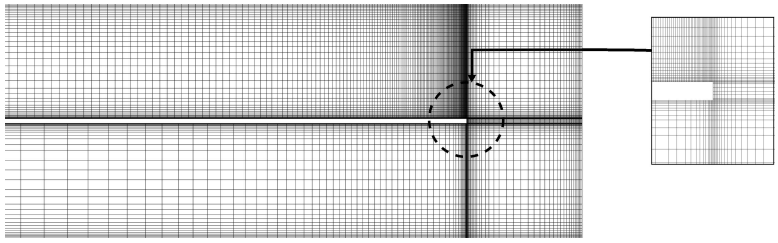

FIGURE 3.4: Details of the mesh around turning part area with polynomial order $N = 3$.

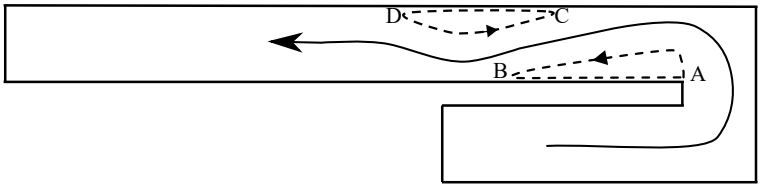

FIGURE 3.5: Sketch of separation and re-attachment points defining the locations of all recirculations. The unbroken arrow represents the direction of the main bulk flow as it navigates the bend.

found that the polynomial order $N = 5$ provides a good accuracy to run the base flow computations. To examine the effect of downstream channel length on the solutions, a convergence study was conducted on the lengths of the first recirculation bubble on the bottom wall of the downstream channel and the secondary recirculation bubble on the top wall. The results shown in Table 3.2 demonstrate that an outlet length of 10 results in an error in the determination of the primary recirculation bubble length of approximately 0.007%, and approximately 4.5% for the secondary bubble. The rel-

N	A	B	C	D	L_{R_1}	L_{R_2}	$\%L_{R_1}$	$\%L_{R_2}$
4	0	-4.8057	-3.7077	-9.7726	4.80573	6.06489	0.0307	0.0797
5	0	-4.8072	-3.7069	-9.7765	4.80716	6.06955	0.0009	0.0029
6	0	-4.8073	-3.7071	-9.7766	4.80730	6.06962	0.0019	0.0018
7	0	-4.8073	-3.7070	-9.7766	4.80725	6.06966	0.0009	0.0010
8	0	-4.8072	-3.7069	-9.7767	4.80720	6.06972	—	—

TABLE 3.1: Dependence of recirculation length on polynomial order. Parameter N indicates the independent polynomial order of the base flow. Two separation points (A and C) and two reattachment points (B and D) as indicated in figure 3.5 computed on the mesh at $Re = 500$ and $\beta = 1$ are given. L_{R_1} and L_{R_2} represent the recirculation length of the first and the second bubble, respectively. Errors on bubble lengths at each N relative to the highest N are also provided.

Outlet length $(e-b)$	L_{R_1}	L_{R_2}	$\%L_{R_1}$	$\%L_{R_2}$
10	4.80485494	5.79491686	0.00723577	4.482661
20	4.80452028	6.06684499	0.00027037	0.000483
30	4.80452020	6.06685749	0.00026858	0.000277
40	4.80452009	6.06685810	0.00026644	0.000267
50	4.80451921	6.06685923	0.00024807	0.000248
60	4.80451788	6.06686092	0.00022029	0.000220
70	4.80451875	6.06685982	0.00023848	0.000239
80	4.80451505	6.06686448	0.00016141	0.000161
90	4.80450991	6.06687100	0.00005442	0.000054
100	4.80450729	6.06687431	—	—

TABLE 3.2: Dependence of the length of the primary and secondary recirculation bubbles (L_{R_1} and L_{R_2}, respectively) on outlet channel length $(e-b)$. Percent differences between bubble lengths at each $e-b$ relative to the longest-outlet case $e-b=100$ are also provided. Outlet lengths of $e-b=20$ and higher capture the bubble lengths to a precision of at least 5 significant figures.

atively large error in the size of the secondary bubble is caused by its proximity to the outlet. Outlet lengths of 20 to 100 are required to achieve at least 5 significant figures of accuracy. Hence, an outlet length of 30 is considered adequately long to be used throughout this study. Barton (1997a) and Cruchaga (1998) studied the entrance effect for backward-facing step flow with expansion ratio of 2 and found that the inlet length of $10h$ and $2h$ (where h is the step height), respectively, return slightly different numerical solutions compared to that with zero inlet length. In this study, the inlet length is 15 which is adequately long for the velocity flow to be fully developed before reaching the bend.

3.6 Chapter summary

The governing equations for the hydrodynamic flow problems have been presented at the beginning of the chapter. This was followed by the explanation of the methods used to analyse the absolute and convective instability in the flow. In a separate section, the governing equations for the magnetohydrodynamic flow have been discussed. The computation scheme used to solve the problems and analysis were also briefly explained. Finally, the problem setup is discussed, followed by the solver validation and the grid-resolution dependence studies.

The next chapter reports on two-dimensional hydrodynamic flows in this geometry, their stability, and three-dimensional flow states.

Chapter 4

Three-dimensional instability in a two-dimensional flow around a 180-degree sharp bend

4.1 Introduction

This chapter seeks to characterise the linear stability of a two-dimensional channel flow involving a 180-degree sharp bend to infinitesimal three-dimensional disturbances using a linear stability analysis.

This chapter discusses the regimes that exist in the two-dimensional flow, including the onset of unsteadiness. Then, the role of linear infinitesimal perturbations in creating an absolute unsteady flow state is discussed. The linear stability analysis can contribute to an understanding of the physical processes which are associated with the instability of the flow.

Firstly, a brief description of the geometry and boundary conditions together with details of the grid-resolution study is given in § 4.2.1. The classification of two-dimensional base flow regimes is presented in § 4.3. The next sections discuss the growth rate and marginal stability curves (§ 4.4.1), structure of the complex eigenvalue spectra (§ 4.4.2) and the dependence of β and analogy with backward facing step and partially blocked channel (§ 4.4.3). And finally, the mechanism of the instability is discussed in § 4.4.4.

Some of the results in this chapter have been published in the Journal of Fluid Mechanics Sapardi *et al.* (2017).

N	$\lvert\mu_{max}\rvert$	Relative error
4	0.9941048	0.0143794%
5	0.9942509	0.0003180%
6	0.9942458	0.0001927%
7	0.9942469	0.0000837%
8	0.9942477	-

TABLE 4.1: Dependence of leading eigenvalues on polynomial order. Parameter N indicates the independent polynomial order of the base flow. Leading eigenvalues computed on the mesh at $Re = 500$, $\beta = 1$ and spanwise wavenumber $k = 6.4$ are provided. The relative error is to the highest polynomial order case ($N = 8$). Given eigenvalues are real.

4.2 Problem formulation

4.2.1 Test of eigenvalue computations

The precision of eigenvalue μ and eigenmode $\hat{\mathbf{u}}$ produced by subspace iteration are quantified by the residual

$$r = \| \mathscr{A}\hat{\mathbf{u}} - \mu\hat{\mathbf{u}} \| , \tag{4.1}$$

where $\| \cdot \|$ is the standard vector norm and where eigenmodes were normalised ($\| \hat{\mathbf{u}} \| = 1$). The linear stability analysis technique relied on an iterative process to obtain the leading eigenvalues and eigenmodes of the system. The process ceased when error threshold $r < 10^{-7}$ was achieved. Nevertheless, the eigenmodes will also be resolution-dependent.

Table 4.1 reports the accuracy of the eigenvalue computations as a function of element polynomial degree N. The leading eigenvalue for $Re = 500$, $\beta = 1$ and $k = 6.4$ is real and linearly stable. It is found that the eigenvalue converged to an error of merely 0.0003180% at $N = 5$, which is employed hereafter.

4.3 Two-dimensional base flows

In this subsection, the focus is on the behaviour of the two-dimensional base flow, especially around the sharp bend and along the downstream channel.

To analyse the two-dimensional base flow, a large number of simulation of combinations of Reynolds number and bend opening ratio was conducted. Simulations were conducted in a range of $1 \leq Re \leq 1000$ and $0.0125 \leq \beta \leq 5$ which in total is around 400 simulations all together to complete the regime map (figure 4.1). It took about

48-96 CPU hours for each simulation to achieve saturation depending on the Reynolds number.

Flow regimes observed from the simulations were mapped into figure 4.1. The thresholds of the emergence of the primary and secondary recirculation bubbles were determined from the zero wall shear stress (Equation (3.52)) at the bottom and upper wall of the outlet channel, respectively. Meanwhile, the threshold of transition from steady to unsteady flow was determined from the variation of L_2 norm in a function of time. In this study, the L_2 norm is adopted such that the amplitude is computed from

$$|A| = \left[\int_v \mathbf{u}^2 \, \mathrm{d}V\right]^{1/2}, \tag{4.2}$$

where V is the volume of the computational domain. The L_2 norm is an integral of the velocity magnitude throughout the entire computational domain. It captures the global velocity field, therefore, it is a useful parameter for monitoring solution convergence.

For the range of opening ratios β studied, four regimes are identified (figure 4.2). The first regime exhibits only a single recirculation bubble immediately behind the sharp bend. The second regime sees the emergence of a bubble at the opposite wall slightly downstream of the first bubble. The third regime reveals the appearance of a small counter-rotating recirculation bubble between the primary recirculation bubble and the bottom wall. Finally, the fourth regime marks the development of an unsteady two-dimensional flow. The Reynolds numbers at the onset of each regime are denoted by Re_{R_1}, Re_{R_2}, Re_{in} and Re_{c}, respectively as shown in Figure 4.1. The results of the current study agree with those of Zhang & Pothérat (2013) but small discrepancies are found for Re_{in} at $\beta \geq 1$, which are attributed to the different mesh densities at high Reynolds numbers and different numerical methods (Zhang & Pothérat (2013) used second order finite volumes which are less accurate). The present study also extends the lower end of the range of β from $\beta = 0.1$ (Zhang & Pothérat 2013) to $\beta = 0.0125$. The constriction at the bend at smaller β leads to high velocities and shear in that region.

For clarity, the main features of these regimes are highlighted here, but a more detailed description can be found in Zhang & Pothérat (2013). The onset of all regimes is delayed consistently to larger Reynolds numbers at larger β over $\beta \lesssim 1$, and remain almost constant when $\beta \gtrsim 1$. It is worth noting that the behaviour of the flow is different between $\beta < 0.2$, $0.2 < \beta < 1$ and $\beta \gtrsim 1$. For $\beta \lesssim 0.2$; a flow resembling

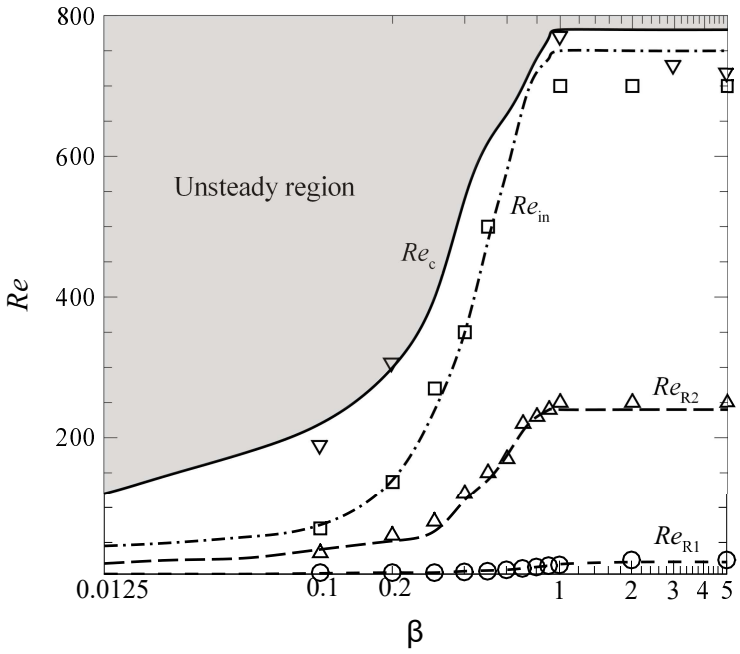

FIGURE 4.1: Reynolds number where primary recirculation bubble Re_{R_1}, secondary recirculation bubble Re_{R_2} and inside recirculation bubble Re_{in} regimes appear in the two-dimensional flow. Re_{c} is the transition from steady to unsteady. The lines are from current study and the symbols are results from Zhang & Pothérat (2013). ◯, △, □ and ▽ represent Re_{R_1}, Re_{R_2}, Re_{in} and Re_{c}, respectively.

a jet flow is created through the narrow bend orifice, causing the flow to accelerate transversely and hit the top wall before deflecting towards the streamwise direction. This causes the onset of each regime to occur at low Reynolds number with modest dependence on β. By contrast, at $0.2 \lesssim \beta \lesssim 1$, the width of the opening of the bend is sufficient for the flow to turn smoothly to the streamwise direction around the bend; hence, β influences the onset of each regime. However, at $\beta \gtrsim 1$, the onsets do not vary significantly because a recirculation bubble develops at the outer wall of the bend, which confines the turning flow, such that the true breadth of the bend opening is no longer apparent. Thus the flow behaves similarly to that of $\beta = 1$. This explains why the onset Reynolds number for the flow regimes remain almost constant for $\beta \gtrsim 1$.

Figure 4.2 shows the streamlines of steady two-dimensional base flow at $Re = 10, 200$ and 600, and contour of vorticity magnitude of an unsteady flow at $Re = 800$ for $\beta = 0.5$. At very low Re, the flow in the downstream and upstream channel is almost symmetrical with respect to $y = 0$. However, as Re increases, the flow streamlines at

the bottom wall move upward until an inflexion point becomes visible behind the edge of the sharp bend. Consequently, the flow separation occurs and a recirculation bubble is formed. In the range of β studied, the primary recirculation bubble appears at very small Reynolds number because of a strong adverse pressure gradient behind the bend, as can be seen in figure 4.2(a). Theoretically a sharp edge always causes separation to a flow, even at very low $Re \to 0$ (Taneda 1979). The finite Re_{R_1} captured in this study is a numerical artefact of finite spatial resolution at the sharp bend corner, as the finite discretisation obscures the bubble at very low Reynolds number.

As Reynolds number increases, the secondary recirculation bubble appears when the flow streamlines in the bulk flow above the primary recirculation bubble move away from the top wall. This coincides with the occurrence of high adverse pressure gradient at the wall, which causes another separation to occur at that location at Re_{R_2} (Figure 4.2(b)). Under the same circumstances, an inner counter-rotating recirculation bubble, as shown in figure 4.2(c), is formed between the primary recirculation bubble and the bottom wall when the backflow in the primary recirculation bubble moves away from the wall.

Figure 4.3 shows the streamlines of steady two-dimensional base flow at a fixed Reynolds number $Re = 150$ with various bend opening ratio. At $Re = 150$, $\beta = 0.2$ and 0.4 are in the region above Re_{R_2}; hence, the both primary and secondary recirculation bubbles appear in the outlet channel. At $\beta \geq 0.6$ the secondary recirculation bubble is not seen. The length of the primary recirculation bubble decreases as β increases, but it remains almost constant as $\beta \geq 1$. There is a recirculation bubble at the end wall of the bend at $\beta = 2$, and two bubbles at $\beta = 5$; due to the appearance of the bubble, an effective bend opening ratio which will be discussed later in § 4.3.1 plays more important role in determining the structure of the two-dimensional flow rather than the actual bend opening ratio. This phenomenon causes the onsets at $\beta \geq 1$ to be slightly vary in the function of actual bend opening ratio β.

Zhang & Pothérat (2013) found an additional regime between Re_{in} and Re_{c}, where they reported vortices of smaller scale were produced by the instability of the shear layer that carries the main stream between the primary and secondary recirculation bubbles. However, this state is not observed in the current study. Re_{c} in figure 4.1 indicates an unsteady flow where large eddies or vortices are shed downstream from the sharp corner of the bend as depicted in figure 4.2(d). Re_{c} is found to be in agreement

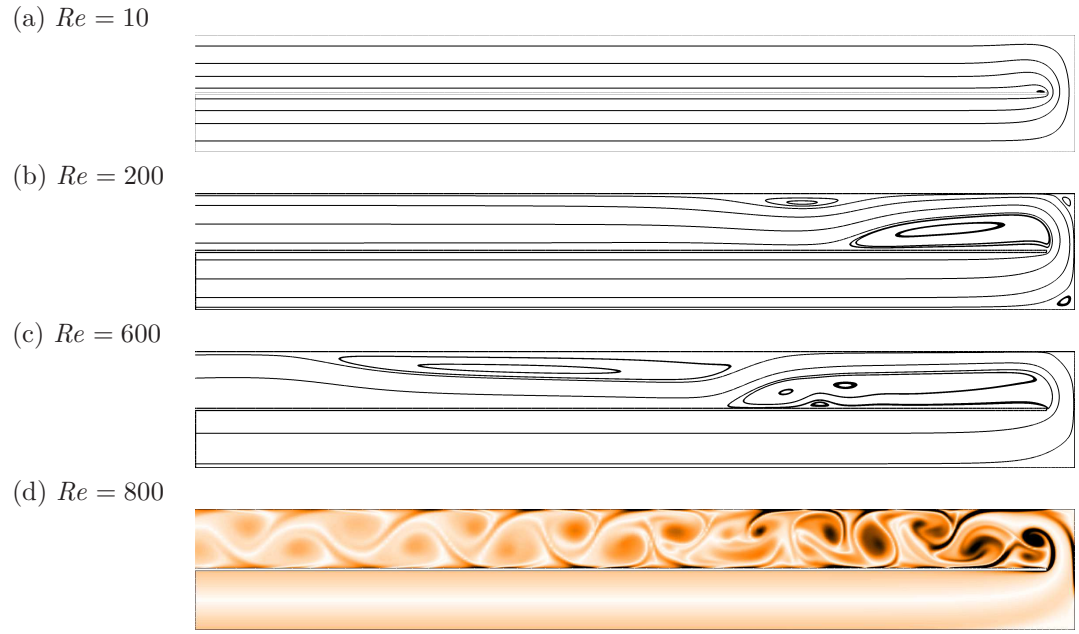

FIGURE 4.2: Streamlines of steady two-dimensional base flow at (a) $Re = 10$, (b) $Re = 200$,(c) $Re = 600$ and (d) contour of vorticity magnitude at $Re = 800$ for $\beta = 0.5$. In (d), white represents zero vorticity (no rotation), and darker shading denotes arbitrarily higher vorticity magnitude levels.

with those of the Zhang & Pothérat (2013) study, and it is important to note that both studies started simulations from a zero-velocity initial state to obtain this Re_c. Further analysis in the present study reveals hysteretic behaviour when some cases are started from different initial conditions. Figure 4.4 reveals hysteresis associated with this behavior in the vicinity of transition to unsteady flow.

Unsteady flow presents as a fluctuation in global measures of the flow. Taking the amplitude of this fluctuation in an L_2 norm measure of the flow time history, $|A|$, Figure 4.4 shows the variations of $|A|$ (and therefore regimes of unsteady flow where $|A| > 0$ when Reynolds number is incrementally varied in the flow. Two distinct onsets of two-dimensional unsteadiness are found by initiating the simulation from three different initial conditions which are from (i) scratch, or previously computed (ii) unsteady or (iii) steady flows at nearby Reynolds numbers. It is evident from the figure that the simulations starting from scratch and from an unsteady flow yield the same value of $Re_c = 742$, whereas the simulations starting from a steady flow become unsteady at a higher Reynolds number, $Re_c \gtrsim 1200$.

The location where the flow starts to shed at the onset of both conditions is different.

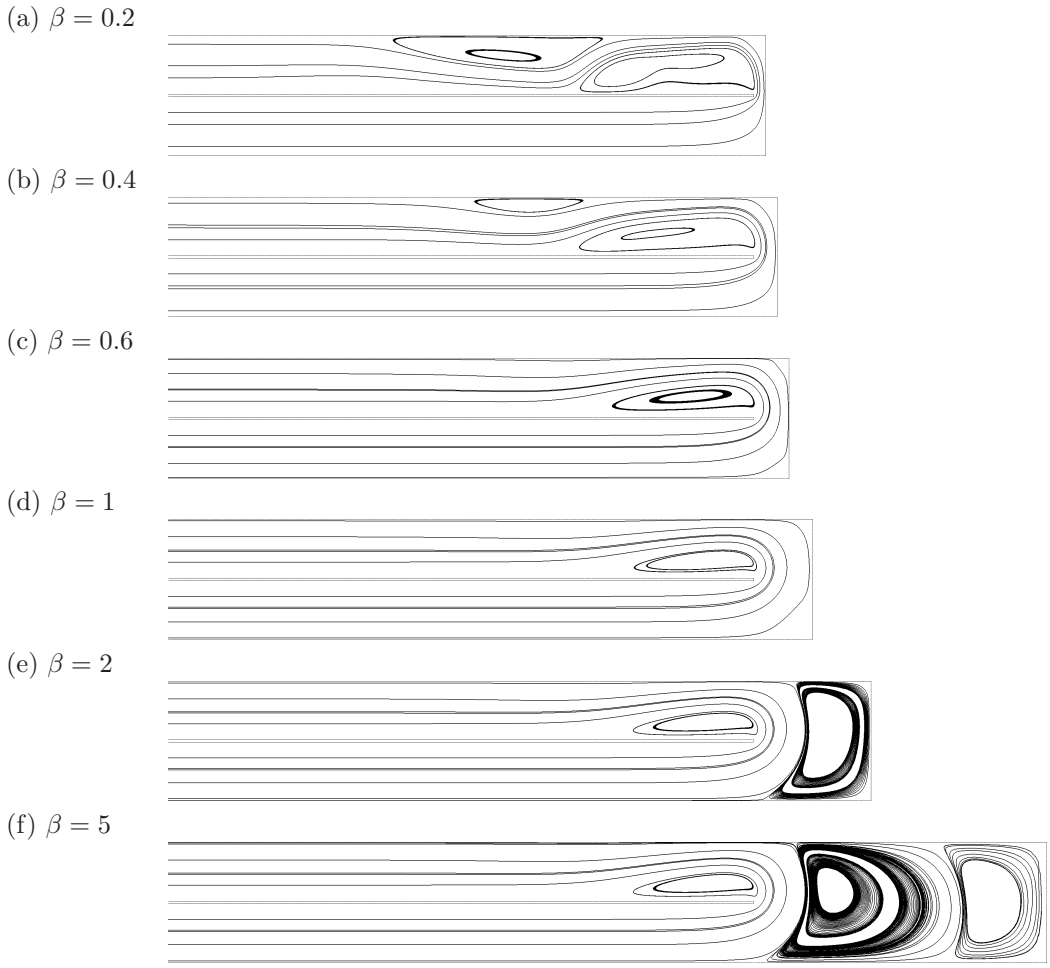

FIGURE 4.3: Streamlines of steady two-dimensional base flow $Re = 150$ for (a) $\beta = 0.2$, (b) $\beta = 0.4$, (c) $\beta = 0.6$, (d) $\beta = 1$, (e) $\beta = 2$ and (f) $\beta = 5$.

When Reynolds number is increased gradually along the steady-flow branch, the flow can maintain its steady state until the shear layers behind the secondary recirculation bubble become unstable and develop small vortices as shown in figure 4.5(b). This has some resemblance to the regime described by Zhang & Pothérat (2013) before the flow becomes unsteady in their study. It is likely that they found this regime at lower Reynolds number due to the high-resolution sensitivity of this feature. Since the flow is already unstable at that location, noise tended to be amplified and created small vortical structures. In testing, it is found that by increasing resolution of the mesh in this study, the onset of unsteadiness could be delayed significantly.

The location where shedding initiates at the onset depends on initial conditions too. When a simulation is initiated from scratch, the vortex shedding can be seen emerging

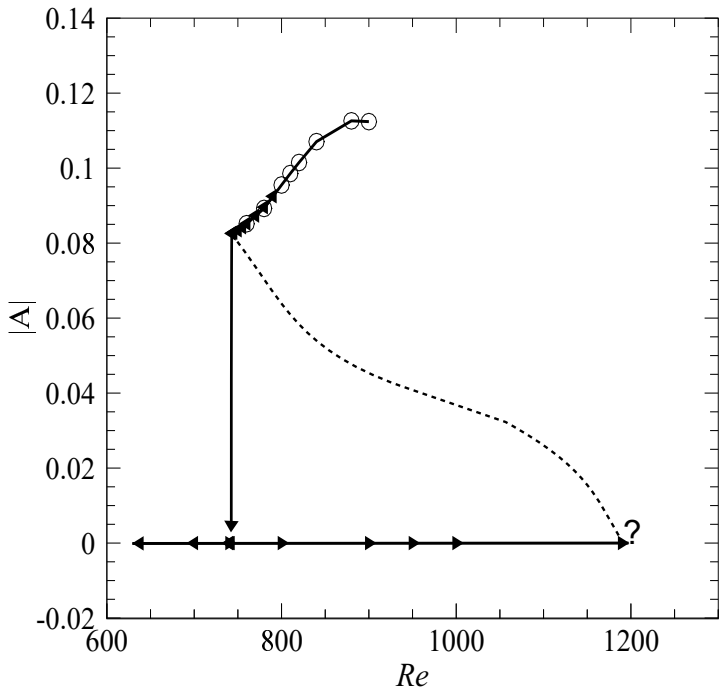

FIGURE 4.4: Hysteretic behavior described by the fluctuation of the integral of velocity magnitude throughout the domain as a function of Re at $\beta = 1$: reducing Re from an unsteady flow (◀), starting the simulations from scratch (◯) and increasing Re from a steady flow (▶) give different Re_c; $|A| = 0$ indicates steady flow solution.

from the sharp corner of the bend as illustrated in figure 4.5(a). It is likely that a large-amplitude perturbation caused by the impulsive initiation of flow is sufficient to provoke a shedding from the bend that bypasses the orderly downstream destabilisation, and beyond $Re_c = 742$ (at least in these simulations) is self-sustaining. A similar observation was seen when reducing Reynolds number from an unsteady flow: a large sudden decrease could revert the unsteady flow to steady state at a Reynolds number of which the unstable state could be preserved via a gradual decrement in Reynolds number.

When Reynolds number is increased gradually along the steady-flow branch, the flow remains steady up to $Re \simeq 1150$. Figure 4.5(b)-(d) depicts the equilibrium flow at $Re = 1152$. This final state exhibits a wavy disturbance extending 25 inlet channel height downstream of the bend. In this case, unsteadiness first manifested in the shear layers behind the secondary recirculation bubble in the form of small eddies, but over time the flow in this region close to the turning point re-stabilised and the

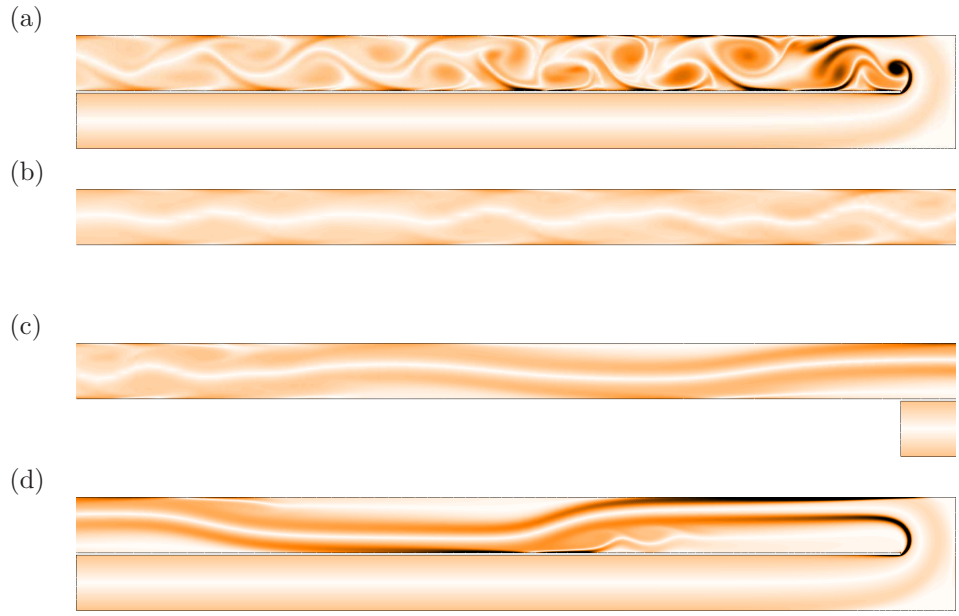

FIGURE 4.5: Flooded contours of vorticity magnitude demonstrating unsteady saturated flows for (a) $Re = 800$ at $\beta = 1$ (which was initiated from rest), and (b)-(d) $Re = 1152$ at $\beta = 1$ (which was initiated from a saturated steady-state flow solution at a lower Reynolds number). Contour levels are as per figure 4.2. (b), (c) and (d) show domain segments $-45 \leq x \leq -29$, $-30 \leq x \leq -14$ and $-15 \leq x \leq 1$, respectively.

unsteady region retreated to its ultimate position further downstream. This bears some resemblance with the regime described by Zhang & Pothérat (2013) before the flow becomes unsteady in their study. It is likely that they found this regime at lower Reynolds number due to the high sensitivity to mesh resolution of this feature. Since the flow is already unstable far downstream of the bend, noise tended to be amplified and created small vortical structures. In testing this hypothesis, it is found that by increasing resolution of the mesh in this study, the onset of unsteadiness could be delayed significantly when increasing Reynolds number gradually along the steady state-solution branch.

4.3.1 Bubble separation points (steady flows)

Figure 4.6 shows the Reynolds number dependence of the separation and reattachment points (expressed by their distance downstream of the bend, x_s) on both the bottom and top walls of the channel for $\beta = 1$. The empty circle symbol indicates the limit of the primary recirculation bubble behind the sharp corner. At $Re = 240$, a secondary recirculation bubble appears on the top wall at $x = 3.77$. At $Re \approx 700$, two additional

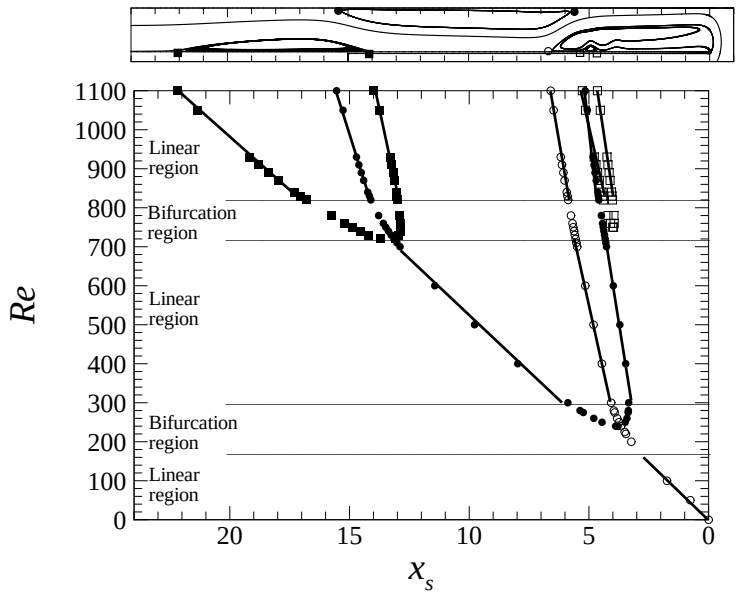

FIGURE 4.6: A plot showing the Reynolds-number-dependence of the locations of separation points (measured by their distances from the leading edge of the bottom outlet wall - left of the origin), x_s, for the base flows as functions of Reynolds number. Open circles represent the stagnation points for the primary recirculation bubbles. Solid circles denote the stagnation points for the secondary recirculation bubble which forms at $Re \approx 240$ at $x \approx 3.77$. Solid and open squares represent the stagnation points for third bubble and inner recirculation bubble, respectively, which are formed at higher Re. The top frame shows the streamlines of the base flow and the separation points of primary, secondary, inner and third recirculation bubbles at $Re = 1100$. The dashed line and the linear equation represent the envelope of the primary recirculation bubble before the secondary recirculation bubble appears.

recirculation bubbles appear at the bottom wall; one is a small bubble nested under the primary recirculation bubble, and the other is positioned near the reattachment point of the secondary recirculation bubble.

From figure 4.6, it may be observed that there are regions where the location of the separation and reattachment points vary almost linearly with respect to the Reynolds number. It can clearly be seen in figure 4.6 that when the bifurcation region around $Re = 300$ and 750 is being excluded, the locations of both points for all bubbles behave almost linearly with Reynolds number. When a new recirculation bubble appears, it affects the growth of the recirculation bubble upstream of it. Consequently, this changes the slopes of the stagnation points especially the reattachment points with respect to

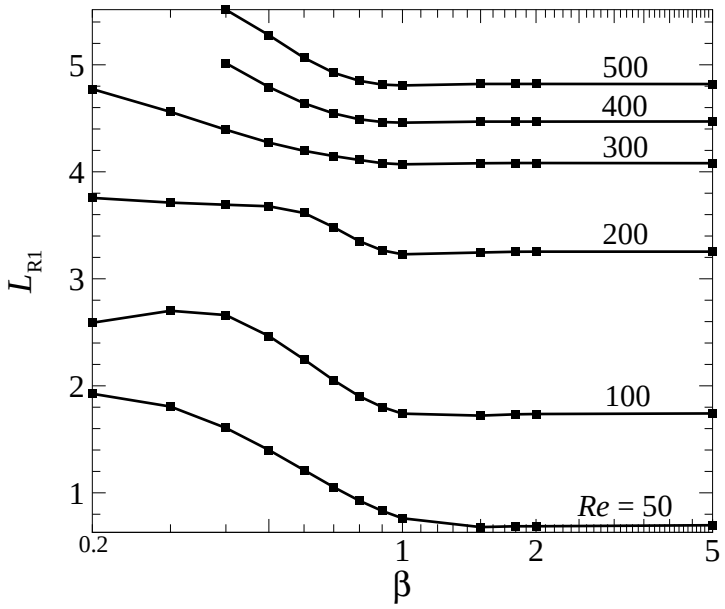

FIGURE 4.7: Length of primary recirculation bubble as a function of β.

Reynolds number. The same behaviour was also found in the backward facing step flow by Erturk (2008).

The effect of β to the size of the primary recirculation bubble is illustrated in figure 4.7. At small values of β, the main bulk flow is accelerated by the small jet opening. This makes the primary recirculation bubble elongated in the streamwise direction which causes the bubble to be bigger than that at larger β. At a given Reynolds number, L_{R1} decreases as β increases, but as $\beta > 1$ and $Re \gtrsim 200$, the size of the bubble increases due to the effect of the recirculation bubble at the far end of the bend wall.

Since for $\beta > 1$, part of the flow in the bend is trapped in a closed eddy outside of the through-flow taking the bend, Zhang & Pothérat (2013) defined an effective opening ratio β_{eff} as the horizontal thickness of the flow effectively turning from inlet to outlet at $y = 0$. For $\beta \lesssim 1$, $\beta_{\mathrm{eff}} = \beta$ (figure 4.8(a)), but for $\beta > 1$, starting from $Re \approx 30$, β_{eff} was smaller than β. At $Re > 200$, β_{eff} saturated close to 0.7. This degradation of β_{eff} to values below β, and its saturation behaviour at large Reynolds number, can be observed in figure 4.8(c). In this study, the distance of the opening for main bulk flow was measured from the inner vertical bend to the nearest closed streamlines of the big

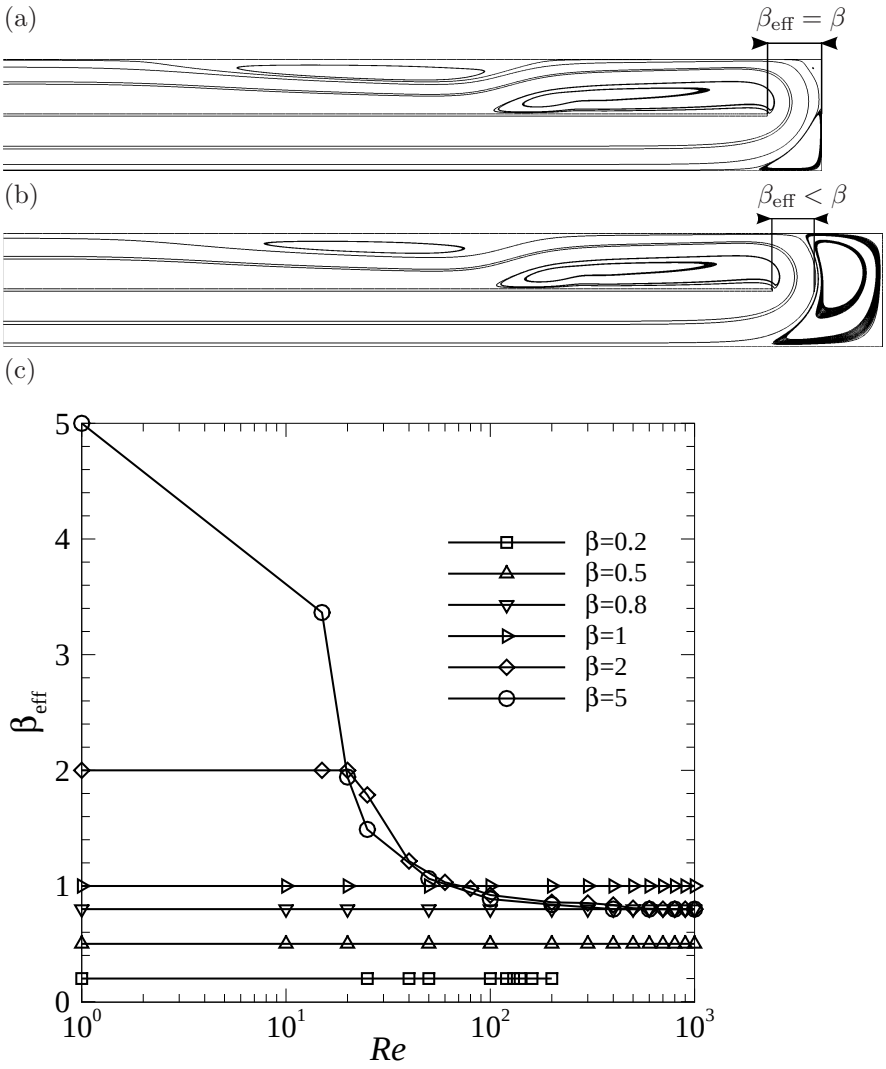

FIGURE 4.8: Streamlines of steady two-dimensional flow for $Re = 600$, (a) $\beta = 1$ and (b) $\beta = 2$. A big recirculation bubble appears at the far end of the wall when $\beta > 1$ causing the effective bend opening ratio to be lesser than the actual opening. $\beta_{\text{eff}}(Re)$ is plotted in (c) for several value of β.

recirculation at the far end of the bend wall. For $\beta = 2$ in figure 4.8(b), the effective β is found to be $\beta_{\text{eff}} \approx 0.8$ which is slightly higher than what was found by Zhang & Pothérat (2013).

4.4 Linear stability

4.4.1 Growth rates and marginal stability

This subsection analyses the dependence of the perturbation growth on Reynolds number Re, spanwise wavenumber k and opening bend ratio β. Figure 4.9 shows the

β	Re_c	k_c
0.2	125	3.00
0.5	278	2.05
1	397	1.98
2	387	1.93

TABLE 4.2: The onset of instability for $\beta = 0.2,\ 0.5,\ 1$ and 2.

predicted growth rates as a function of the Reynolds number and spanwise wavenumber k for $\beta = 0.2$, 0.5, 1 and 2. The primary linear spanwise instability is obtained via polynomial interpolation to determine the lowest Reynolds number that first produces $\sigma = 0$, and the wavenumber at which this occurs, which are tabulated in table 4.2. For $\beta > 0.2$, at very low wavenumber $k \lesssim 0.3$, a local maximum is observed, but the flow is always stable. Between this local maximum and the primary maximum, there is a small range of k for which the leading eigenvalues have a non-zero imaginary component. Larger wavenumbers than those shown in figure 4.9 were also studied. The leading eigenvalues at larger wavenumber are found to be stable and monotonically decrease with increasing k. This trend of the growth rate as a function of Re and k shows a good resemblance with those of backward facing step flow (Barkley *et al.* 2002). However, for all β, the critical Reynolds number for the flow to become three-dimensional are found to be much lower compared to the flow in backward facing step (Barkley *et al.* 2002; Armaly *et al.* 1983) and partially blocked channel (Griffith *et al.* 2007). This finding is expected as the two-dimensional flow around sharp bend becomes unsteady at much lower Reynolds number compared to those geometries.

Figure 4.9 shows that at $\beta = 0.2$ the first-occuring unstable mode is oscillatory, which means that the spanwise-periodic three-dimensional perturbation is time-dependent. Meanwhile, $\beta = 0.5$ becomes unstable through a synchronous dominant leading mode at $Re_c = 278$, which is surpassed at $Re > 400$, by an oscillatory mode. On the other hand, $\beta > 1$ always has a synchronous dominant leading mode.

To clarify the shift of the dominant leading mode from synchronous to oscillatory, several of the leading eigenvalues have been computed for $\beta = 0.5$ at each wavenumber and three different Reynolds numbers. The results are shown in figure 4.10. Again, the curves closely resemble those for the flow over a backward facing step (Barkley *et al.* 2002). They consist of two branches of real eigenvalues at low wavenumber which then coalesce into a single branch of non-real eigenvalues as k increases. This non-real

branch splits into a pair of real branches at further increases in wavenumber. The primary leading eigenvalues appear at higher wavenumbers with the real branch at high wavenumber being the first to become unstable. All branches shift to higher σ as Reynolds number increases. However, as Reynolds number increases further, it can be seen that an oscillatory mode becomes more pronounced (Figure 4.10(b)) and becomes dominant at $Re \approx 600$ as shown in figure 4.10(c). A similar observation was made by Natarajan & Acrivos (1993) in flow past spheres and disks, by Tomboulides & Orszag (2000) in the weak turbulent flow past a sphere, and by Johnson & Patel (1999) in a numerical and experimental study on flow past a sphere up to $Re_d = 300$. These studies found two eigenmodes, with the first underpinning a stationary bifurcation, and second justifying oscillatory bifurcation. Interestingly, in those cases, this shift from synchronous to oscillating dominant mode was echoed in the real three-dimensional flows, where the initially steady-state non-axisymmetric mode was replaced by a time-periodic non-axisymmetric state at higher Reynolds numbers. The corresponding three-dimensional behavior in the present 180-degree bend system is considered in § 4.5.

4.4.2 Structure of the eigenvalue spectra

Figure 4.11(a, b, c), (d, e, f) and (g, h, i) show the eigenvalue spectra for three different cases. Each has a different type of dominant leading eigenmode. The dashed curve is the unit circle marking the threshold for instability ($\sigma \geq 0$). Figure 4.11(a) depicts the eigenvalue spectrum for $\beta = 0.2$, $Re = 120$ and $k = 2.8$, which is near to the onset of instability. The four leading eigenvalues are two complex-conjugate pairs. The leading pair (e.g. figure 4.11(b)) exhibits a strong growth rate, with strong perturbation structure in the primary recirculation bubble, while the second pair (figure 4.11(c)) has perturbation structure mainly localised in the bulk flow near the secondary recirculation bubble.

In contrast to $\beta = 0.2$, larger β tends to favour synchronous leading modes. $\beta = 0.5$ is particularly interesting because this is the point of transition from synchronous ($Re = 400$ in figure 4.11(d)) to oscillatory ($Re = 600$ in figure 4.11(g)) leading mode is seen. The eigenvalue for $Re = 400$ is synchronous, while the second largest eigenmode is oscillatory. However, at higher Reynolds number, the oscillatory mode has higher growth rate compared to the synchronous mode, as can be seen in figure 4.11(g). These two modes are localised at the same location, in the primary recirculation bubble, near

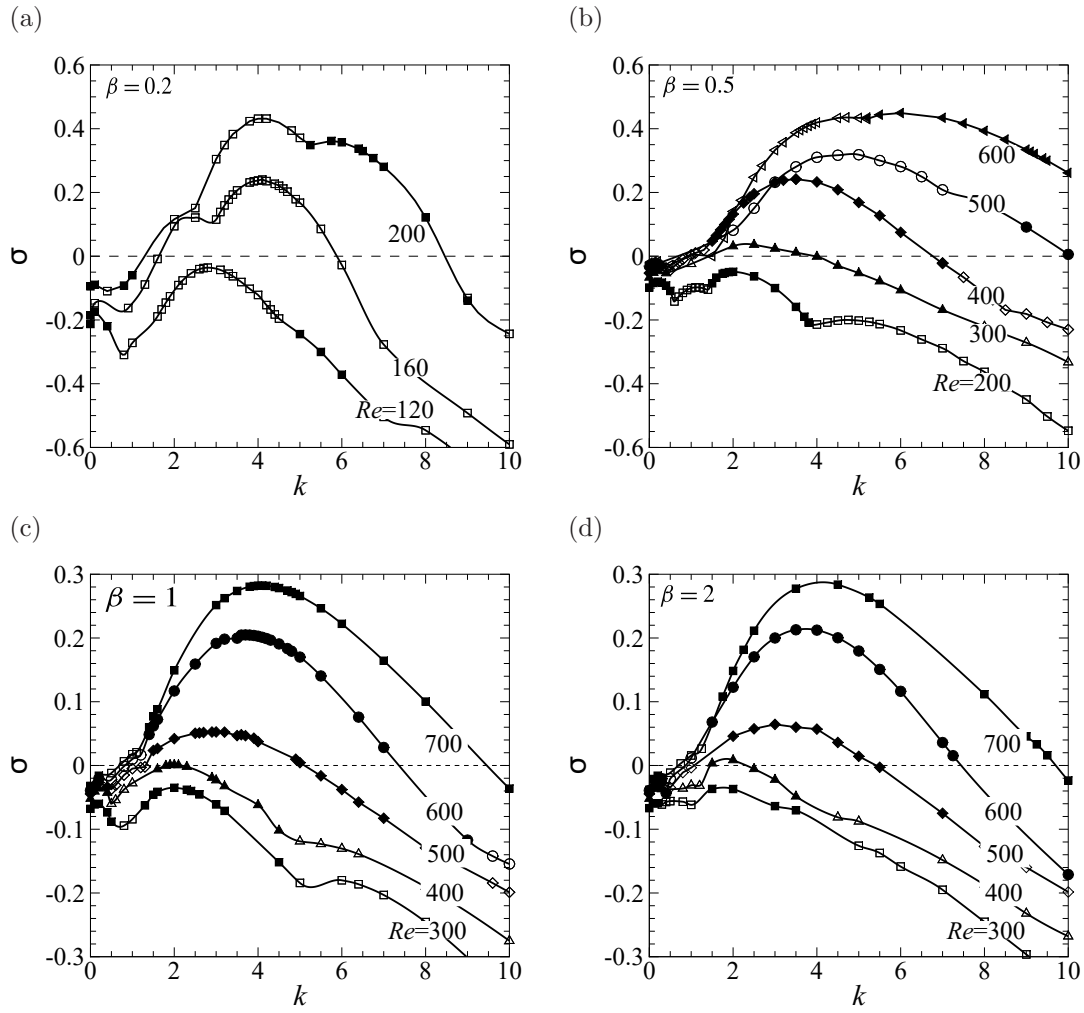

FIGURE 4.9: Growth rates of leading eigenmodes as a function of spanwise wavenumber k for (a)$\beta = 0.2$ and $Re \leq 200$, (b) $\beta = 0.5$ and $Re \leq 600$, (c) $\beta = 1$ and $Re \leq 700$, and (d) $\beta = 2$ and $Re \leq 700$. Solid symbols represent real leading eigenvalues, meanwhile hollow symbols represent complex-conjugate pair leading eigenvalues. Branches of these leading eigenvalues are connected by solid lines.

to the reattachment point. From the contours represented in figures 4.11(h,i), it can be seen that the contours in figure 4.11(b,e,i) have a similar synchronous eigenmode structure; meanwhile figure 4.11(c,f,h) have a consistent oscillatory eigenmode structure. The oscillatory mode structure is distinguished from the synchronous mode structure by the presence of an array of chevron-shaped vorticity structures following the core flow downstream from the aft end of the primary recirculation bubble.

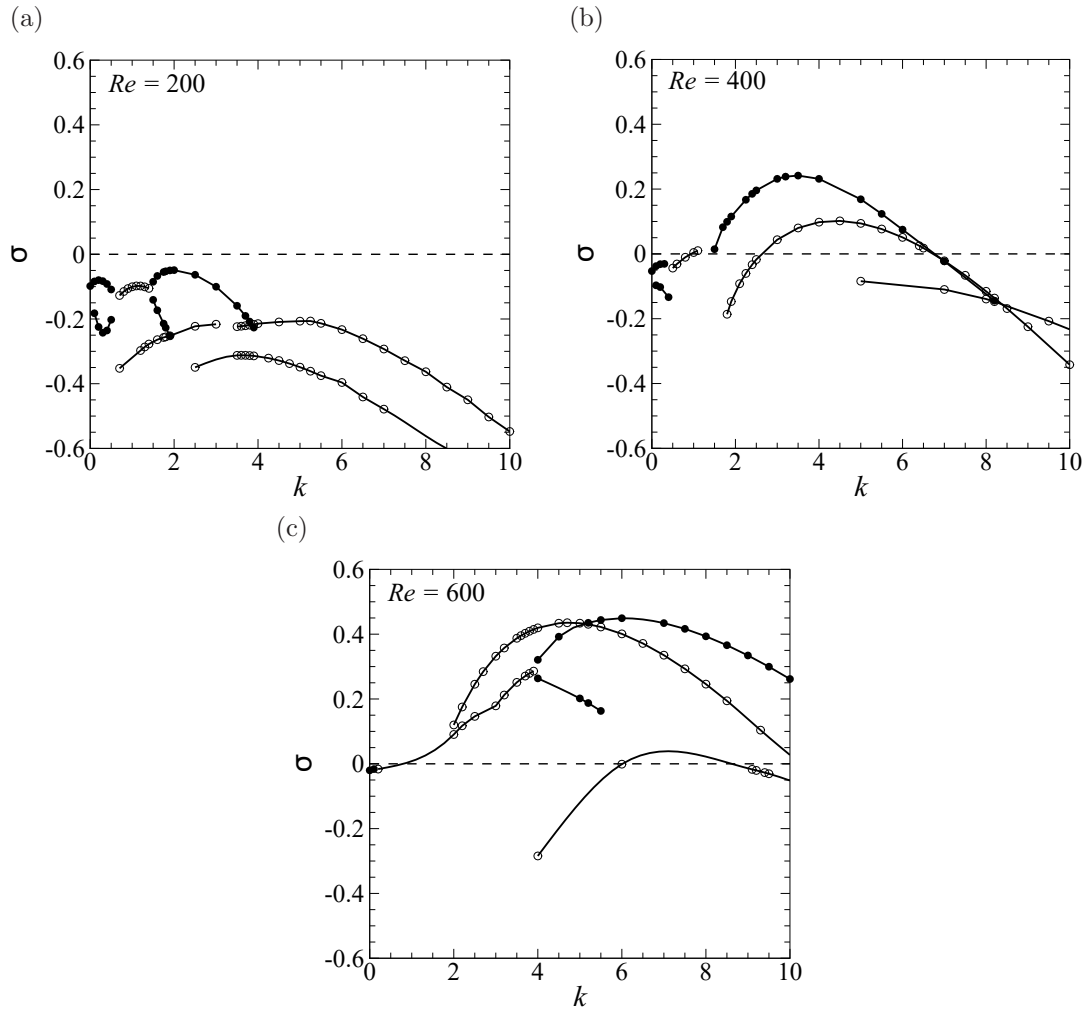

FIGURE 4.10: Growth rates of leading eigenmodes plotted against spanwise wavenumber at $\beta = 0.5$ for (a) $Re = 200$, (b) $Re = 400$ and (c) $Re = 600$. Solid symbols represent real leading eigenvalues, meanwhile hollow symbols represent complex-conjugate pair leading eigenvalues.

4.4.3 Dependence on β and analogy with related flows

From the known influence of the expansion ratio on the three-dimensional characteristics of the backward-facing step flow (Barkley *et al.* 2002; Lanzerstorfer & Kuhlmann 2012), the opening ratio in a partially blocked channel flow (Griffith *et al.* 2007) and the two-dimensional characteristics of 180-degree sharp bend flow (Zhang & Pothérat 2013), it is expected that the three-dimensional flow in a 180-degree sharp bend will also be dependent on the same physical parameter (here β).

Figure 4.12 illustrates the effect of β on the Re and k of the onset of three-dimensional instability. In the range of β studied, only $\beta = 0.2$ first becomes three-dimen-

(a) $\beta = 0.2$, $Re = 120$ and $k = 2.8$

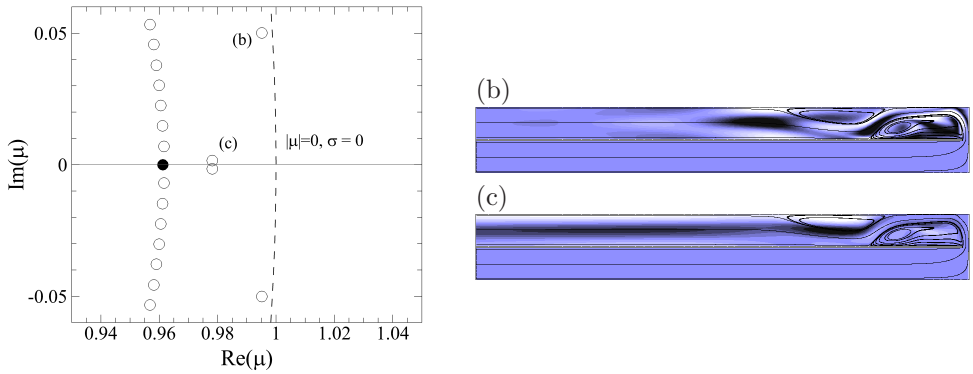

(d) $\beta = 0.5$, $Re = 400$ and $k = 3.5$

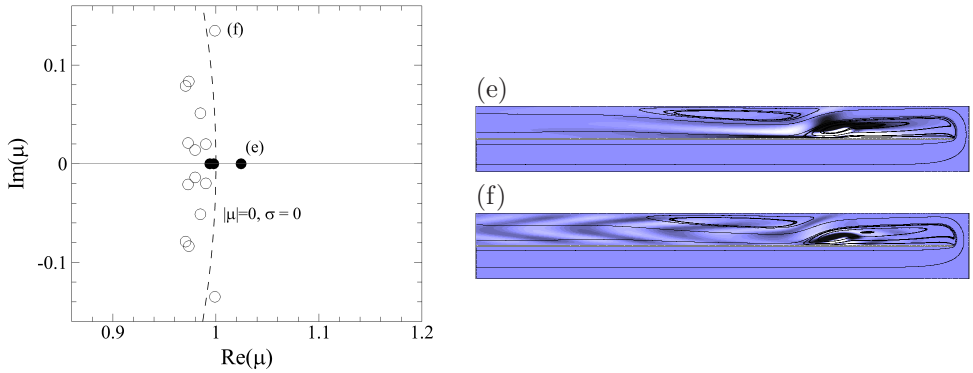

(g) $\beta = 0.5$, $Re = 600$ and $k = 4.5$

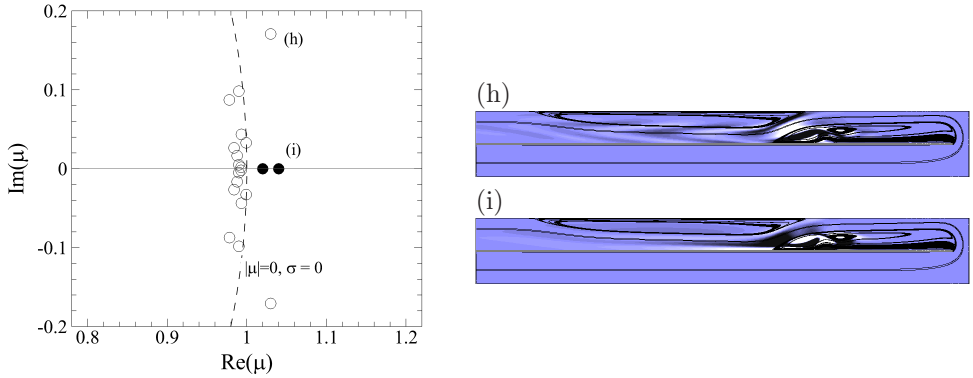

FIGURE 4.11: Eigenvalue spectra for (a) $\beta = 0.2, Re = 120, k = 2.8$, (d) $\beta = 0.5, Re = 400, k = 3.5$, and (g) $\beta = 0.5, Re = 600, k = 4.5$. (b), (e), and (h) show spanwise vorticity in the eigenvector field of the respective leading eigenvalues, while (c), (f) and (i) show the corresponding field for the second most dominant eigenmode. In these vorticity plots, zero vorticity is shown by the mid-level shading, while darker and lighter shading respectively show negative and positive shading. For complex eigenmodes, the perturbation field is shown at an arbitrary time.

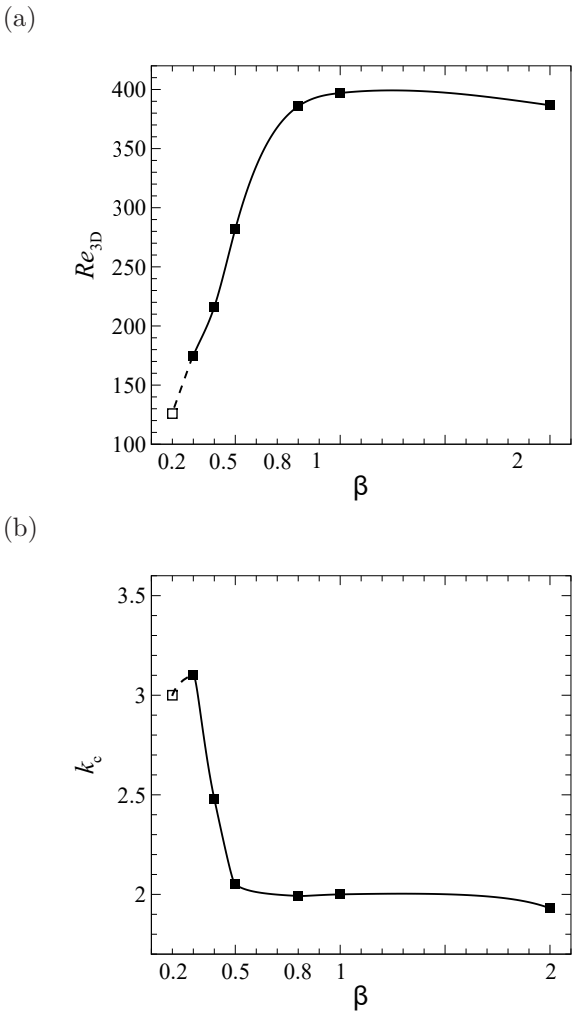

FIGURE 4.12: Critical (a) Reynolds number and (b) wavenumber as a function of bend opening ratio.

sional through the onset of an oscillatory mode; while all other cases transition through the onset of a non-oscillatory mode. Apparently, Re_{3D} increases steadily as the bend opening becomes larger until $\beta \approx 1$. Re_{3D} at $\beta = 2$ is slightly lower than $\beta = 1$ because of the appearance of the recirculation bubble at the far end of the bend wall that limits the width of the bulk flow in the bend, causing the flow to have a smaller effective β. Upon closer inspection, the value of Re_{3D} at $\beta = 2$ is almost the same as that of $\beta = 0.8$, which reflects the importance of β_{eff} in determining the stability of the flow.

The eigenvector fields at instability onset for all synchronous modes ($\beta \gtrsim 0.3$) have perturbation structure located in the recirculation bubble, similar to what was found in the backward facing step flow (Barkley *et al.* 2002; Alam & Sandham 2000),

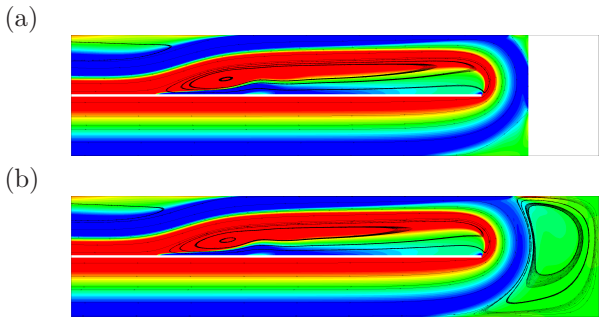

FIGURE 4.13: Contours of vorticity demonstrating steady flows and velocity streamlines for (a) $\beta = 2$ and (b) $\beta = 0.8$ at $Re = 700$.

partially blocked channel flow (Griffith *et al.* 2007) and separation flow (Hammond & Redekopp 1998). Barkley *et al.* (2002) concluded that the size and shape of the bubble directly affected the instability. Conversely, Hammond & Redekopp (1998) and Alam & Sandham (2000) confirmed in their studies that the onset of local absolute instability depended on the backflow of the bubble. Interestingly, as can be seen in the close up view of contours of vorticity and velocity streamlines of $\beta = 0.8$ and $\beta = 2$ in figure 4.13, qualitatively, both have very identical structure in the outlet channel. Quantitatively, both have comparable bubble size, peak backflow velocity and location of the peak backflow velocity (with errors of only 4.3%, 1.0% and 0.4%, respectively). Hence, supporting the view that for $\beta > 1$, the stability of the flow is characterised by β_{eff} rather than β, as both of these cases have $\beta_{\text{eff}} = 0.8$.

The dependence of k_c on β is also illustrated in figure 4.12. As β increases from 0.3 to 0.5, the dominant wavelength of the instability increases from $\lambda \approx 2\pi/3$ to $\approx \pi$. This is perhaps due to the transition from jet-like flow around the bend to a broader turning flow. k_c at $\beta = 0.2$ does not lie on the same trend as $\beta = 0.3$ to 0.5 due to the different mechanism. As $\beta \geq 0.5$, the critical wavenumber exhibits little dependence on β.

Figure 4.14 shows the marginal stability curves at several values of β. The marginal curves are obtained by interpolating $\sigma(k, Re)$ to zero growth rate for each Re from figure 4.9. For $\beta \leq 1$, with increasing β the neutral stability curve shifts to the right as expected, as the flow with wider bend opening ratio is more stable than those with smaller opening ratios. Beyond $\beta \approx 1$, the stability curve recesses slightly towards lower Reynolds numbers, occupying the region between the marginal stability curves

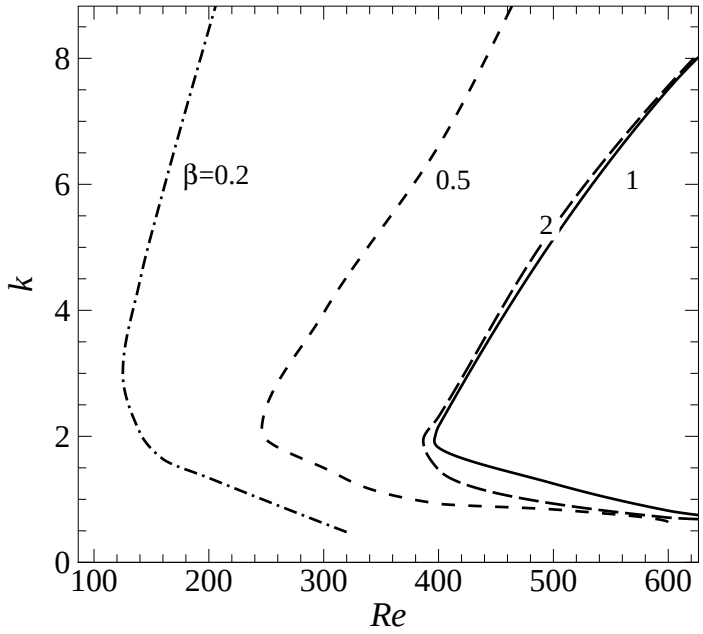

FIGURE 4.14: Marginal stability curves for sharp 180-degree bend flow with $\beta = 0.2$, 0.5, 1, and 2. Regions on the right of the curves represent flow conditions that are linearly unstable to three-dimensional perturbations for that particular β.

for $\beta = 0.5$ and 1. This is explained by the decrease in β_{eff} with β for $\beta > 1$ (See § 4.3). The stability curves also show a decrease in dominant wavenumber with increasing β. This is likely because the instability is scaled with bubble size as per the backward facing step flow discussed by Barkley & Henderson (1996). The length of the primary recirculation bubble as a function of critical Reynolds number and critical wavelength is depicted in figure 4.15. It can be seen from figure 4.15(a) that the flow becomes unstable at higher Re at bigger β. For the synchronous modes ($0.3 \lesssim \beta \lesssim 1$), the critical wavelength increases as the size of the primary recirculation bubble increases.

In order to consider the three-dimensional stability of these flows in the context of the underlying two-dimensional flows, figure 4.16 summarizes the (Re, β) parameter space explored in this thesis. Within this range, instability to three-dimensional perturbations always occurs in the regime where both primary and secondary recirculation bubbles exist. This agrees with Armaly *et al.* (1983), who found for the backward-facing step that three-dimensionality appeared in the flow after the secondary recirculation bubble had formed. In our study, $Re_{3\text{D}}$ increases monotonically with β before slightly reducing and becoming independent on β as β exceeds unity. The critical eigenvalue

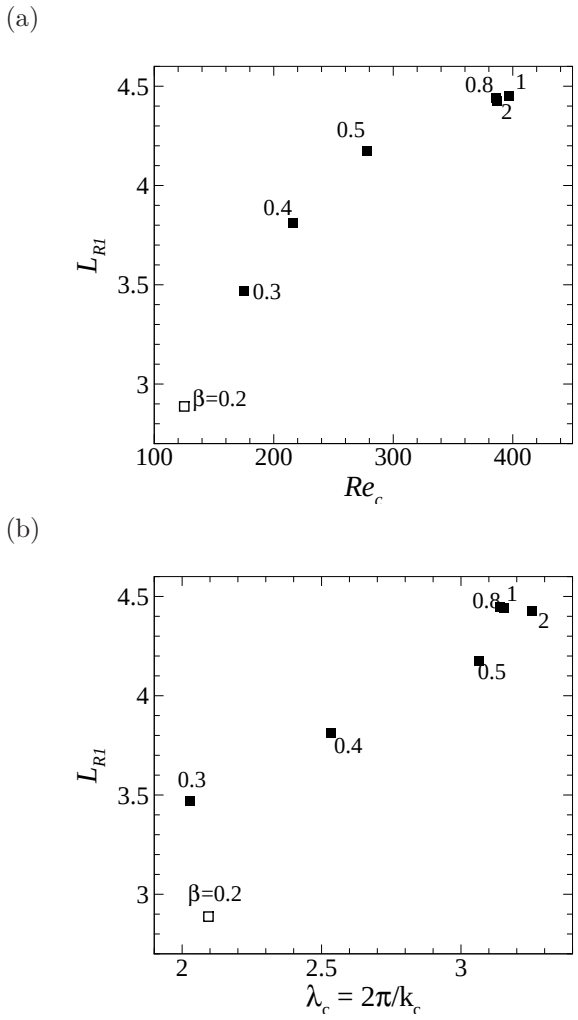

FIGURE 4.15: Length of primary recirculation bubble as a function of (a) critical Reynolds number and (b) critical wavelength.

for $\beta = 0.2$ is found to be non-real, while it is real for $\beta = 0.5$, 1 and 2. Across all considered Re studied at $\beta = 0.2$, the dominant eigenvalues are non-real. On the other hand, for $\beta \gtrsim 1$, the dominant eigenvalues are consistently real. A transition from real to complex occurs at $\beta = 0.5$ near the regime where the inside recirculation appears in the primary recirculation bubble.

4.4.4 Mechanism of instability

In this section, the mechanisms by which the three-dimensional infinitesimal perturbations are amplified are addressed. The obvious mechanism seen in the two-dimensional flow is Kelvin–Helmholtz instability. Zhang & Pothérat (2013) found that in regime IV, the shear layers around both bubbles are subject to it, and lead to unsteadiness. How-

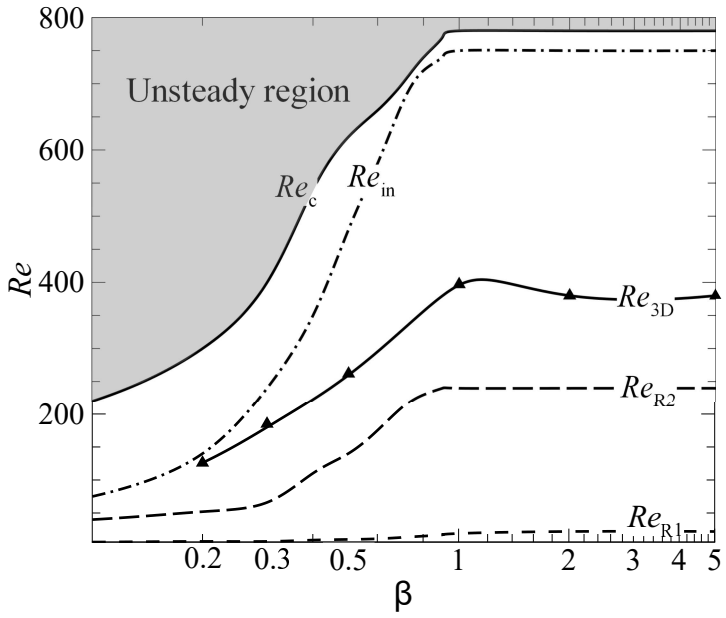

FIGURE 4.16: Parameter space for flow regimes and leading peak eigenvalues of three-dimensional stability. Solid and hollow symbols indicate leading real and complex eigenvalues, respectively. The onset of three-dimensional instability is represented by △. Lines are included for guidance, and the shaded region shows the parameter values exhibiting unsteady two-dimensional solutions.

ever, as this study demonstrates, absolute three-dimensional instabilities are found at $Re \ll Re_c$ involving different mechanisms.

As mentioned earlier, the structure of instability affecting the primary recirculation bubble bears a strong similarity to both the flow over a backward-facing step and in a partially blocked channel. Ghia *et al.* (1989) suggested that the appearance of the secondary bubble introduced a concave curvature in the streamlines of the bulk flow, thus inducing Taylor–Görtler instability. However, this scenario has been ruled out (Barkley *et al.* 2002; Griffith *et al.* 2007) because instability arises neither in the secondary recirculation bubble nor in the main bulk flow between the primary and secondary recirculation bubble zones. The leading instability mode from our analysis is also found in a different location; however, the second leading eigenmode at lower wavenumber is found to be located in these regions.

Three-dimensionality appears at the reattachment and separating points of the primary recirculation bubble as shown in spanwise velocity component in figure 4.17(b)(iii),

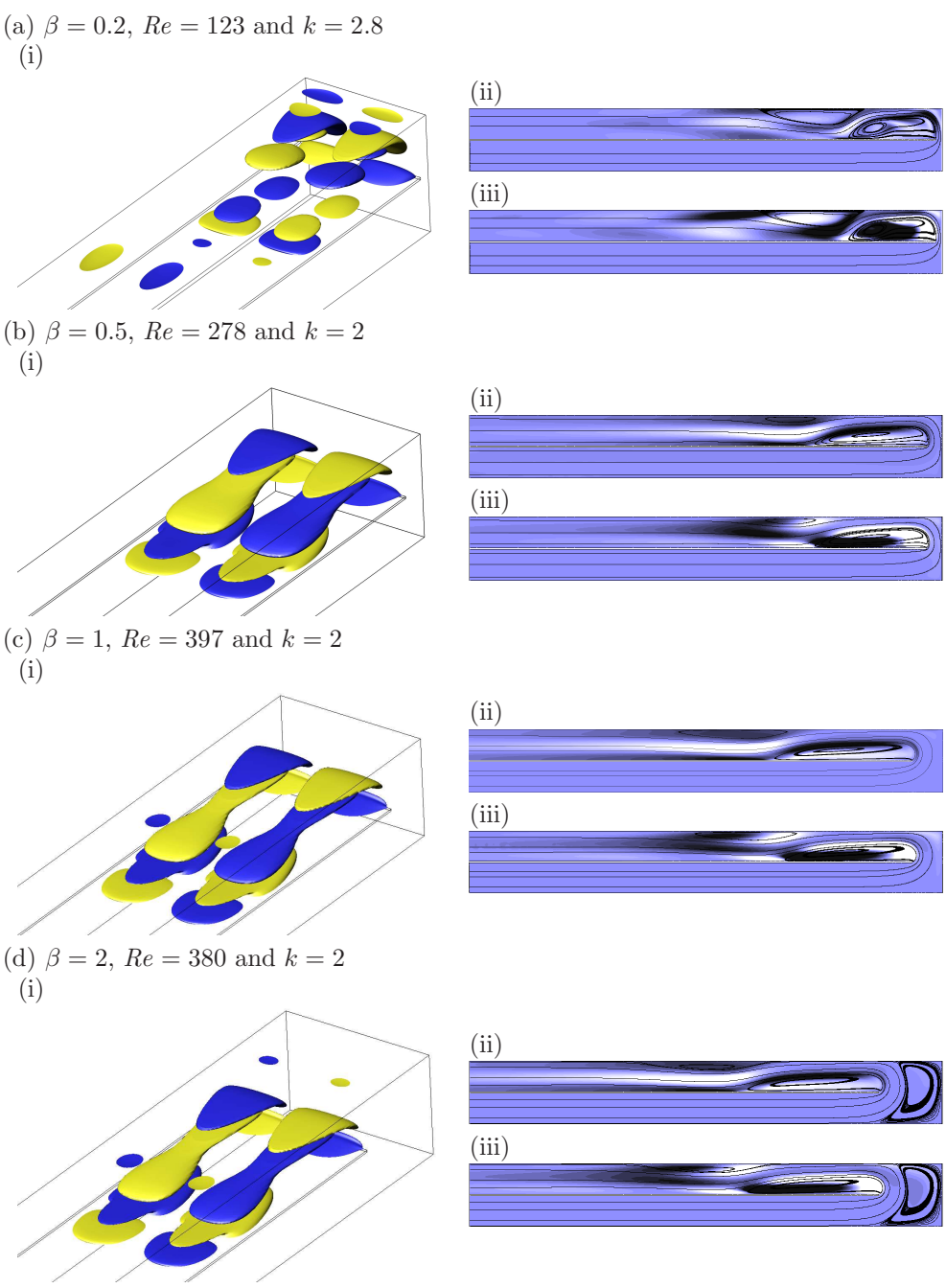

FIGURE 4.17: Visualisation of the real part of leading eigenmodes at (a) $\beta = 0.2$, (b) $\beta = 0.5$, (c) $\beta = 1$ and (d) $\beta = 2$, consisting of (i) a three-dimensional visualisation of the streamwise (x-component of) vorticity, (ii) spanwise (z-component of) vorticity and (iii) spanwise velocity contours overlaid with the base flow streamlines. Dark, mid and light shading represent negative, zero and positive levels, respectively, while (ii) and (iii) are plotted on the plane $z = 0$.

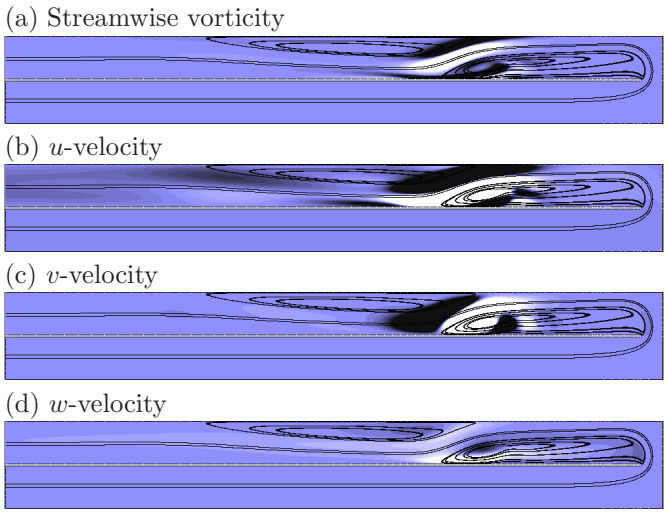

FIGURE 4.18: Structure of the eigenmode at $\beta = 0.5$, $Re = 400$ and $k = 0.2$: flooded contours of (a) streamwise vorticity and (b) u, (c) v and (d) w-velocity overlaid with the base flow streamlines. For clarity, only the vicinity of the bend is shown. Dark-mid-light shading denotes negative-zero-positive levels, respectively.

(c)(iii) and (d)(iii). The perturbation is confined within the closed streamlines of the primary recirculation bubble.

On the other hand, Griffith *et al.* (2007) and Lanzerstorfer & Kuhlmann (2012) suggested that at moderately large expansion ratio, the mechanism was elliptical rather than centrifugal due to the elliptical shape of the closed streamlines of the primary recirculation bubble. The elliptical recirculation tends to generate vorticity perpendicular to the basic vorticity. Their study also shows that the elliptical recirculation leads the flow to evolve toward a fine-scale structure through a small number of bifurcations, which agrees with the findings of Kerswell (2002). Spanwise perturbation vorticity contour plots shown in figure 4.19 exhibit perturbation vorticity structures that resemble those arising from an elliptic instability. The elliptic instability arises in strained vortex (Bayly 1986; Pierrehumbert 1986) due to an amplification of a pair of Kelvin waves that are coupled by the strain field when their characteristics satisfy a condition of resonance (Moore & Saffman 1975; Kerswell 2002). Note that the counter-rotating vortices occur at an angle to the strain direction and the recirculation bubble is highly elongated, resembling a strain vortex. A similar interaction of counter-rotating vortices in two-dimensional elliptic streamlines was seen in Thompson *et al.* (2001). Leweke & Williamson (1998) suggested that when two counter-rotating vortices bal-

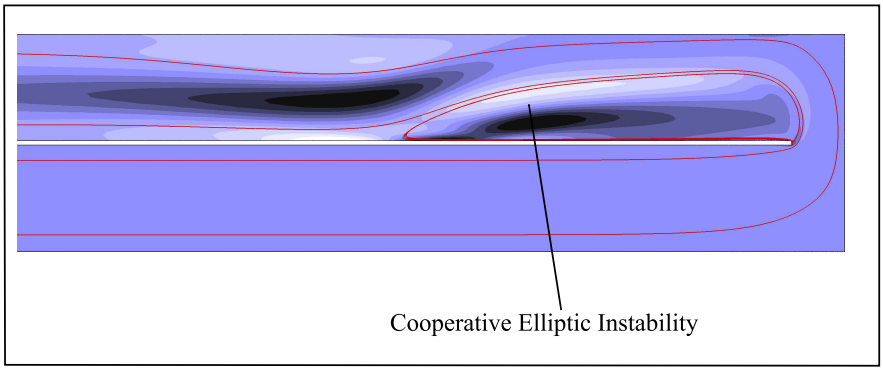

FIGURE 4.19: Contour plot of the perturbation spanwise vorticity and velocity streamlines at $\beta = 0.5$, $Re = 278$ and $k = 2$. Contour levels are as per figure 4.11.

ance each other, the radial component of the strain field leads the disturbance to grow exponentially.

Lanzerstorfer & Kuhlmann (2012) observed that the combination of the flow deceleration near the reattachment point, a lift up process on both sides of the bulk flow between the primary and the secondary recirculation bubbles, and an amplification due to streamline convergence near and in the separated flow regions is the cause of the flow instability in the flow over backward-facing step with expansion ratio of 0.5. The same observation was made by Wee *et al.* (2004) where they found that the backward-facing step flow was locally absolutely unstable near the middle of the primary recirculation bubble. The backflow was found to be high and the shear layer was sufficiently thick to support an absolutely unstable mode; hence, an absolute mode was more likely to originate in the middle of the bubble. By contrast, Marquillie & Ehrenstein (2003) studied a flow behind a bump and observed that the structural changes near the reattachment point of the primary recirculation bubble behind the bump triggered an abrupt local transition from convective to absolute instability. It is observed that for the flow around a 180-degree sharp bend, as Re increases, the location of the peak backflow in the primary recirculation bubble shifted towards the reattachment point. The close gap between the peak backflow and the reattachment point means that the flow is strongly decelerated upon approaching the reattachment point. Interestingly, the peak backflow at the onset of instability in this study for $0.3 \lesssim \beta \lesssim 2$ is consistently located about $0.22L_{\mathrm{R1}}/a$ from the reattachment point (as shown in figure 4.20) which is also the same location of the peak perturbation spanwise velocity from the linear stability analysis

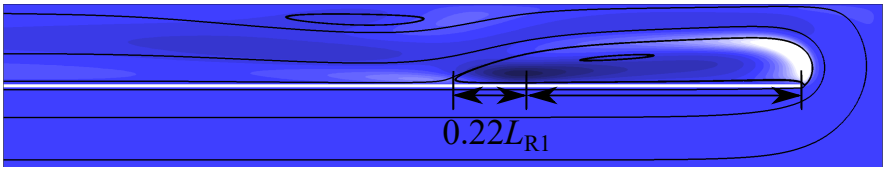

FIGURE 4.20: Contour of perturbation spanwise velocity with the the location of the peak backflow with respect to the length of the primary recirculation bubble for $\beta = 1$, $Re = 400$ and k=4.

(figure 4.17 biii, ciii, diii). This suggests that as in the other geometries mentioned, the instability in the 180-degree sharp bend for $\beta \geq 0.3$ is localised near the peak of back flow intensity.

The oscillatory critical mode at $\beta = 0.2$ exhibits strong spanwise velocities at the upstream end of the primary recirculation bubble and quite strong values around the intense vortex in the bubble. This is strongly consistent with a mechanism involving a centrifugal instability around the intense vortex. A similar mode was seen by Lanzerstorfer & Kuhlmann (2012) in the flow over a backward facing step with a very small opening. There, the perturbations were found to be a spanwise traveling wave that displaces the jet and the intense vortex periodically.

The structure of the mode that destabilizes the flow at $\beta = 0.5$, $Re = 278$ and $k = 2$ is shown in figure 4.17(b) in the isosurface plots of streamwise vorticity, spanwise vorticity and w velocity contours. The isosurface consists of positive (light) and negative (dark) vorticity contours located almost entirely in the primary recirculation bubble, near the separation and reattachment points. The spanwise vorticity contour plot shows that there is a pair of counter-rotating vortices in the primary recirculation bubble which resembles the flow in a partially blocked channel (Griffith *et al.* 2007). The spanwise velocity contours are also qualitatively similar to those of the unstable mode in the flow over a backward facing step (Barkley *et al.* 2002) where a "flat roll" (i.e. a roll in a horizontal plane about a vertical axis) mode structure exists in the bubble near the reattachment point. Across the opening ratios studied, the same mode structure has been found for all real primary leading eigenmodes indicated by the solid symbols in figure 4.16.

The same type of plots describing the dominant eigenmodes for $\beta = 0.2$, $Re = 123$ and $k = 2.8$ are shown in figure 4.17(a). The mode appears to grow in the primary re-

circulation bubble near the separation point and upstream of the intense vortex close to the reattachment point. Both of these modes have strong x-component of perturbation vorticity in the upstream part of the primary recirculation bubble which is where Zhang & Pothérat (2013) found secondary instability in their three-dimensional simulation of an unsteady flow at $Re = 2000$ and $\beta = 1$ with spanwise periodic domain of length 2 units (this is equivalent to the case of wavenumber $k = \pi$ in the present notations).

The structure of the most unstable eigenmode at very small wavenumber is shown in figure 4.18 as a plot of spanwise vorticity and (u, v, w) velocity contours. The structure consists of spanwise vortices in the main bulk flow located between the primary and secondary recirculation bubbles. The spanwise velocity contour in figure 4.18(d) clearly shows that the bifurcating mode is located in the main bulk flow near the closed streamlines of both bubbles.

4.4.5 Two-dimensional instability

§ 4.4.1 describes how for $Re < Re_{\mathrm{c}}$ at any β, the flow is stable to two-dimensional infinitesimal perturbations ($k = 0$). The linear stability analysis found that all eigenvalues for $k = 0$ are real and have negative growth rate. The two-dimensional flow around a sharp 180-degree bend becomes unsteady at small Re depending on β, which is almost twice the critical value for the onset of three-dimensional instability. From two-dimensional simulations, Zhang & Pothérat (2013) observed that two-dimensional instability starts in the shear layer between the two steady recirculation bubbles and sheds throughout the whole width of the channel. This agrees with the mechanism found for the two-dimensional leading eigenmode. As $k \to 0$, a leading real eigenmode splits into two complex-conjugate pairs. To aid in a determination of whether the onset of two-dimensionally unsteady flow is predicted by linear stability theory, figure 4.21 is plotted similarly to figure 13 in Barkley *et al.* (2002); whereby $\log(-\sigma)$ will approach $-\infty$ as $\sigma \to 0$ from below. However, the data here shows that the eigenmode growth rate remains negative as the critical Reynolds number of the rescaled steady base flow at a slightly lower Reynolds number is approached. This implies that the transition to unsteadiness of the steady-state two-dimensional solution branch does not appear to be due to a global linear instability. While it was not possible due to computing time limitations to obtain stability data closer to $Re_{c,\mathrm{upper}}$, this nevertheless suggests that the transition to unsteadiness of the steady-state two-dimensional solution branch is not due

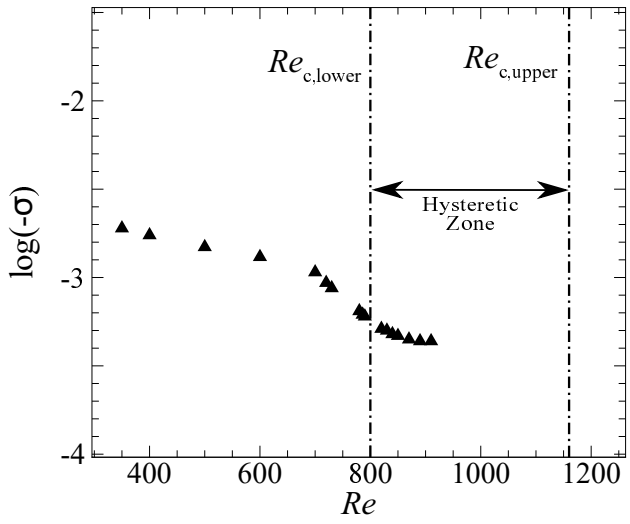

FIGURE 4.21: Leading two-dimensional ($k = 0$) eigenvalues for $\beta = 1$. Due to the hysteresis, there are two Re_c for this flow, $Re_{\mathrm{c,lower}}$ is the lowest Re the flow can become unsteady, meanwhile $Re_{\mathrm{c,upper}}$ is the highest Re the flow remains steady. The leading eigenvalues remain to have finite value of $\log(-\sigma)$ as $Re \to Re_{\mathrm{c}}$. Note that the flow will become two-dimensionally unstable when $\sigma \to 0^-$, $\log(-\sigma) \to -\infty$.

to a global linear instability. This is supported by our earlier observation that $Re_{c,\mathrm{upper}}$ was resolution-sensitive. Similar observations to that shown in figure 4.21 were made for flow behind a backward-facing step (Barkley *et al.* 2002) and through a partially blocked channel (Griffith *et al.* 2007). The data exhibit a kink at $Re = 700$, where a sudden steepening in gradient is observed before the data reverts to a nearly horizontal trend to higher Reynolds number. Barkley *et al.* (2002) saw a similar behaviour for the backward facing step flow (in that case occurring at $Re = 1250$), and found by inspection of secondary eigenvalues that the kink occurred due to an "avoided crossing" of the two eigenmode branches.

4.5 Non-linear analysis of the bifurcation to three-dimensional state

In this section, three-dimensional direct numerical simulation (DNS) is performed to assess the linear stability analysis predictions and to understand the nature of the bifurcation arising from the predicted linear instability modes. The three-dimensional algorithms exploit the spanwise homogeneity of the geometry, combining the two-di-

mensional spectral-element discretisation in the $x-y$ plane with a Fourier spectral method in the out-of-plane z-direction (for more details see Ryan *et al.* (2012); Sheard (2009)).The span of the domain in z may be specified, and periodic boundary conditions are naturally enforced in the z-direction.

Tests were conducted to determine the dependence of computed three-dimensional solutions on the number of Fourier modes N_f included in the simulations. In these tests, the spanwise wavenumber was selected to match a predicted linear instability mode above the critical Reynolds number, and a superposition of the two-dimensional base flow and three-dimensional eigenvector field of the predicted linear instability was used as an initial condition. The three-dimensional flow was then evolved in time until it saturated, at which point measurements of the domain integral of $|w|$ and a point-measurement of w-velocity were taken. Results are shown in table 4.3, demonstrating that the solution having 8 Fourier modes is converged to within at least 2 and 3 significant figures to the result obtained with 16 modes. This is deemed sufficient to capture the non-linear growth behaviour and the saturated state of the mode, so 8 Fourier modes are employed hereafter.

4.5.1 Non-linear evolution of the unstable modes

Three-dimensional simulations were subsequently performed at selected β and Re combinations. The spanwise wavenumber in each case is deliberately set to match the corresponding linear instability eigenmode. It is acknowledged that this choice excludes long-wavelength features that may or may not arise. However, it facilitates an isolation of the instability mode under scrutiny. Figure 4.22 shows the time history of the spanwise velocity in these three-dimensional simulations for (a) $\beta = 0.2$, $Re = 160$, $k = 4$ and (b) $\beta = 1$, $Re = 600$, $k = 4.5$. The oscillatory and the synchronous behavior in figure 4.22 (a) and (b), respectively, agree well with the behavior of the leading eigenmodes predicted using linear stability analysis (ref. figure 4.9). From the time history of w-velocity, the growth rate of the perturbation can be calculated. Table 4.3 shows strong agreement between the growth rates of perturbation field obtained from the linear stability analysis and three-dimensional DNS simulation for five different cases. $\beta = 2$ and $k = 4.5$ is chosen to demonstrate the accuracy of the predictions on flow with fast growing perturbations. Figure 4.23 shows the three-dimensional isosurface plots of streamwise vorticity for the same parameters as employed in fig-

β	Re/Re_{3D}	k	σ(LSA)	σ(3D DNS)	Percentage difference
0.2	1.12	3	0.06648	0.06667	0.27%
0.4	1.16	3.2	0.09877	0.09909	0.3%
0.5	1.22	2	0.03131	0.03133	0.011%
0.8	1.03	2	0.01454	0.01455	0.043%
2	1.55	4.5	0.20032	0.20102	0.35262%

TABLE 4.3: Comparison between the growth rates calculated from linear stability analysis (LSA) and three-dimensional DNS simulations.

ure 4.22, respectively, comparing the predicted three-dimensional eigenmode with the actual three-dimensional state produced once the flow saturates following instability growth. The streamwise vorticity from the linear stability analysis (figure 4.23(a-b)(i)) has a strong resemblance to those of three-dimensional DNS simulations (figure 4.23(a-b)(ii)). The strong agreement is seen between the predicted eigenmode structure and the resulting saturated three-dimensional structure. This verifies that the linear stability analysis provides meaningful predictions of the three-dimensional nature of the flow. The Reynolds numbers in figure 4.23(a) and (b) are 28% and 51% higher than the critical Reynolds numbers for $\beta = 0.2$ and 1, respectively. Both cases produce non-zero Fourier mode energy at saturation having a magnitude of order 10^{-2} relative to the base flow energy which is very small. The smaller the disturbance energy compared to the base flow energy, the closer the saturated state will be to the predicted infinitesimal eigenmode because the contribution of nonlinear terms is weaker.

From the DNS simulations, it was found that the unsteady saturated state for $\beta = 0.2$ persists to at least $Re = 160$, though it might be anticipated, based on the close agreement between the saturated three-dimensional flow structure and the corresponding predicted linear instability mode, that a similar behaviour would extend to higher Reynolds numbers: linear stability analysis was performed up to $Re = 200$, continuing to capture this mode. Meanwhile, for $\beta = 0.5$, as Reynolds number increases, the saturated state changed from a steady state at $Re = 300$ and 400 to an unsteady saturated state at $Re = 500$ with $k = 4.5$. The same behaviour is predicted in figure 4.9, demonstrating the applicability of linear stability analysis to this flow, and the rich tapestry of flow regimes across the $Re - \beta$ parameter space.

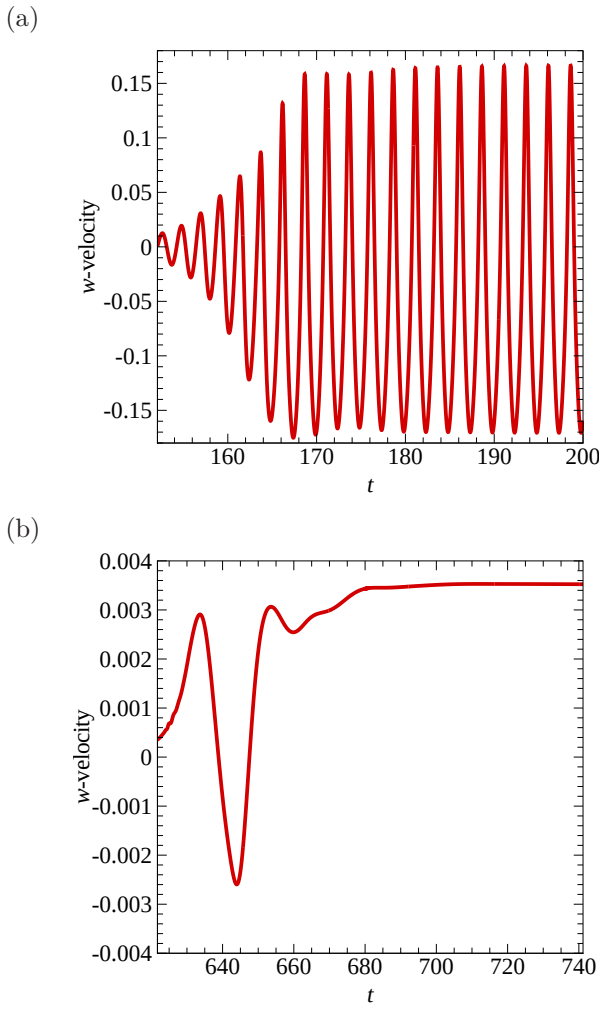

FIGURE 4.22: The time history of w-velocity when two-dimensional base flows (w-vel= 0) of (a) $\beta = 0.2$, $Re = 160$, $k = 4$ and (b) $\beta = 1$, $Re = 600$, $k = 4.5$ evolved into three-dimensional flows.

4.5.2 Stuart–Landau model analysis

In this subsection, the Stuart–Landau model analysis of the nonlinear features of the instability mode evolution is performed. The nonlinear mode evolution theory pertaining to the Stuart–Landau model described in § 3.1.5 provides a way to study the nonlinear behavior near the transition Reynolds number.

Figure 4.24 plots the time derivative of mode amplitude logarithm plotted against the square of the amplitude for two different cases (a) $\beta = 0.2$, $Re = 160$, $k = 4$ which grows from an oscillatory mode and (b) $\beta = 0.5$, $Re = 400$, $k = 3.5$ which grows from a synchronous mode. The behaviour shown for $\beta = 0.5$ is consistent with that found

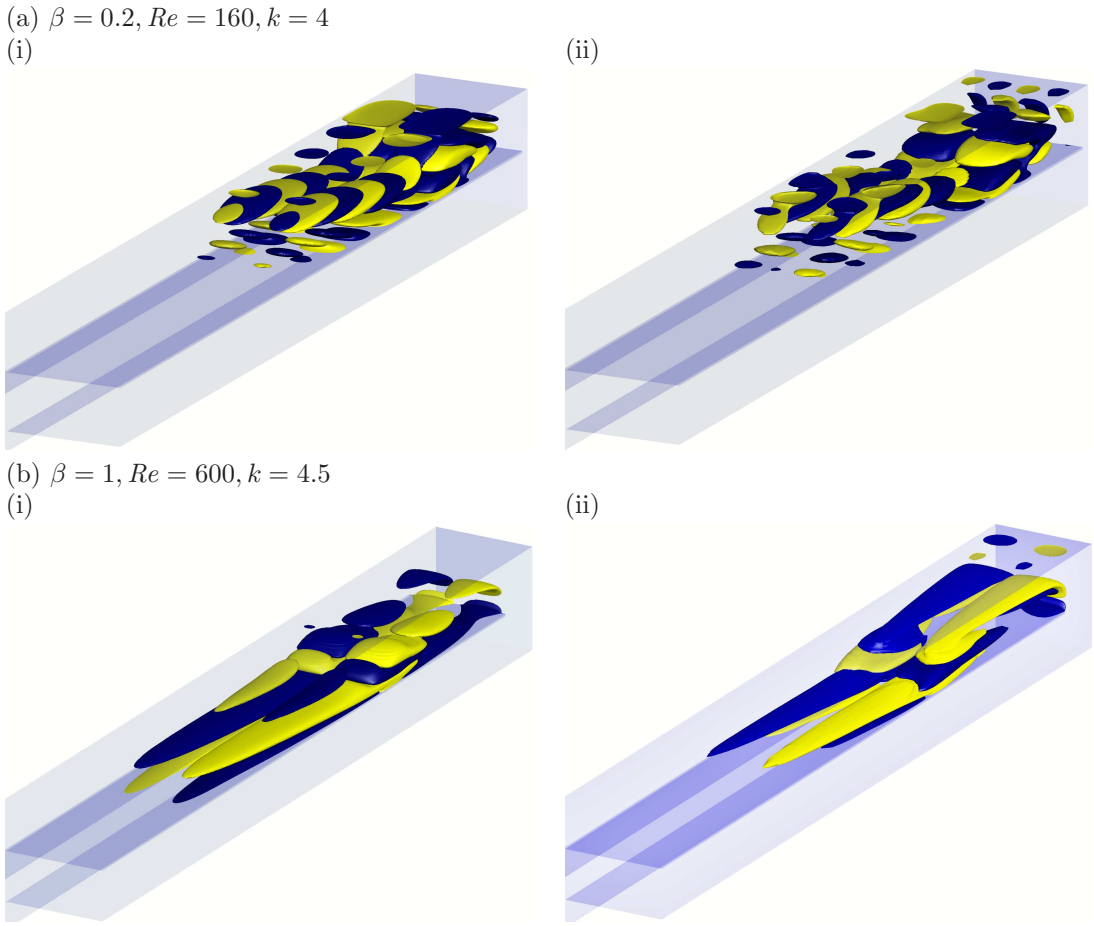

FIGURE 4.23: The three-dimensional visualisation of the x-component of perturbation vorticity for (a) $\beta = 0.2, Re = 160, k = 4$ and (b) $\beta = 1, Re = 600, k = 4.5$ obtained from (i) linear stability analysis and (ii) three-dimensional DNS simulation.

at larger β. The near linear variations with negative slope of $\mathrm{d}\log|A|\mathrm{d}t$ vs $|A|^2$ in the limit of small amplitudes in the vicinity of the vertical axis shown in both plots indicate that the transition in both cases occurs through a supercritical bifurcation. This is consistent with other confined flow featuring recirculation bubbles such as the flow past a backward facing step (Kaiktsis *et al.* 1991), through a sudden expansion in a circular pipe (Mullin *et al.* 2009), and past a sphere (Tomboulides & Orszag 2000). The oscillatory and synchronous behavior of the modes in (a) and (b) reveal them to occur through supercritical Hopf bifurcation and pitchfork bifurcations, respectively.

In addition to the aforementioned sub- and supercritical bifurcation scenarios, another possibility is that a transcritical bifurcation. A dynamical system producing transcritical behavior takes the form

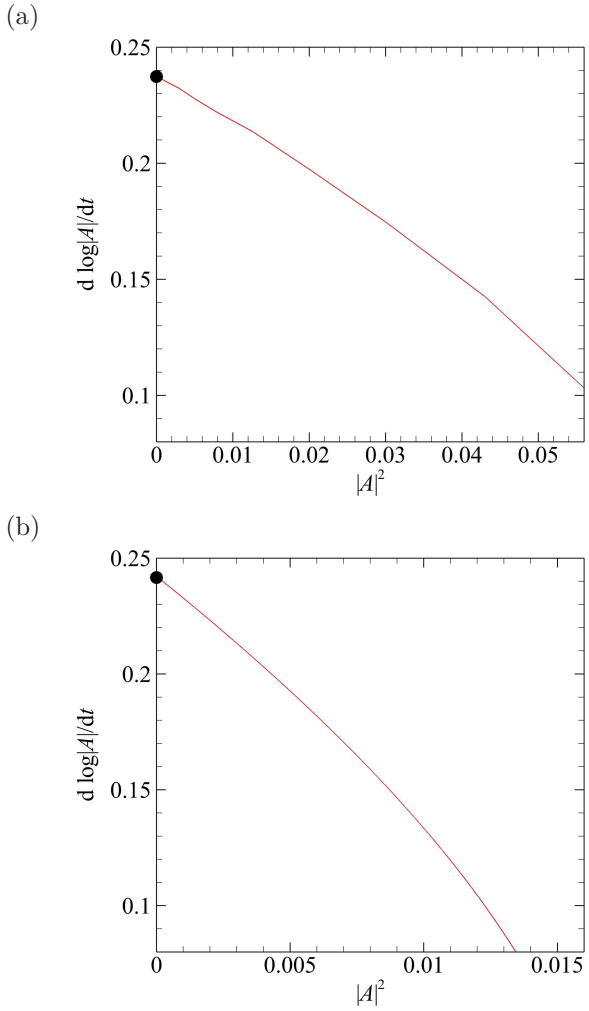

FIGURE 4.24: The time derivative of mode amplitude logarithm plotted against the square of the amplitude for (a) $\beta = 0.2$, $Re = 160$, $k = 4$ and (b) $\beta = 0.5$, $Re = 400$, $k = 3.5$ demonstrating supercritical behaviour. The solid circle symbol represents the linear stability analysis predicted growth rate.

$$\frac{\mathrm{d}\rho}{\mathrm{d}t} = \sigma\rho - l\rho^2, \tag{4.3}$$

which differs from the amplitude part of the Stuart–Landau model equation (3.24) by the replacement of ρ^3 with ρ^2 in the non-linear term on the right hand side. Under an analogous manipulation,

$$\frac{\mathrm{d}\log\rho}{\mathrm{d}t} = \sigma - l\rho = \sigma - l\sqrt{\rho^2}. \tag{4.4}$$

The $\sqrt{\rho^2}$ term indicates that an infinite gradient would present at $|A|^2 = 0$ in a plot of $\mathrm{d}(\log|A|)/dt$ against $|A|^2$. The absence of such a behaviour in figure 4.24 rules out a

transcritical bifurcation. Similarly, a transcritical dynamical system expressed in terms of the complex amplitude A,

$$\frac{\mathrm{d}A}{\mathrm{d}t} = (\sigma + i\omega)A - l(1 + ic)A^2, \tag{4.5}$$

features a real component that simplifies to

$$\frac{\mathrm{d}(\log \rho)}{\mathrm{d}t} = \sigma - l\sqrt{\rho^2}[\cos\phi - c\sin\phi]. \tag{4.6}$$

In the limit $|A| = \rho \to 0$, the oscillation described by the trigonometric term produces gradients in $\mathrm{d}(\log|A|)/\mathrm{d}t$ as a function of $|A|^2$ that approach infinity; the absence of this behavior in figure 4.24 again supports the present classification of these bifurcations as being supercritical.

4.6 Conclusions

A linear stability analysis was conducted to characterise the onset of unsteadiness in the flow around a 180^o sharp bend. A range of opening ratios β was considered spanning all regimes from a jet-like flow through a small aperture to flow topologies involving a recirculation within the turning part (Zhang & Pothérat 2013). In all cases, the two-dimensional base flow exhibited a steady bubble in the outlet that was found to become unstable to infinitesimal two-dimensional perturbations at a finite critical Reynolds number Re_{c}, which increases monotonically with the effective opening ratio β_{eff}. β_{eff} measures the actual width of the main stream in the turning part. Consequently, Re_{c} increases monotonically with the geometric opening ratio β so long as the mean stream occupies the whole turning part (up to $\beta \sim 1$). By contrast, for high opening ratios, $Re_c(\beta)$ decreases asymptotically to $Re_c(\beta_{\mathrm{eff}} \simeq 0.8)$, because the recirculation in the turning part reduce the effective width available to the main stream.

The linear stability analysis revealed three types of leading eigenmodes. In the subcritical range, the leading eigenmode is reminiscent of long-wave Taylor–Götler vortices localised in the main stream between the two recirculation bubbles attached to either outlet walls. This mode was, however, never found to become unstable. As Reynolds number was increased, two unstable branches emerged that were respectively associated a real eigenvalue and a complex conjugate pair of eigenvalues. The former dominates for $\beta \geq 0.3$. The corresponding perturbation has a spanwise wavenumber $k \simeq 2$ and is

confined to the first recirculation region, with maximum intensity where the back flow is most intense. For $\beta = 0.2$, by contrast, unsteadiness sets in via the second branch under the form of a spanwise oscillating mode, akin to that found in backward facing step flows with small opening ratios (Lanzerstorfer & Kuhlmann 2012).

In all cases, critical modes were three-dimensional. Accordingly, locally unstable two-dimensional modes (*i.e. having zero spanwise wavenumber*) are only found at higher Reynolds numbers than three-dimensional modes but do not grow through a global instability. They drive a Kelvin–Helmholtz instability in the main stream between the two recirculating bubbles that is consistent with the DNS of Zhang & Pothérat (2013).

Analysis of the non-linear evolution of dominant instability modes using three-dimensional DNS and the Stuart–Landau equation demonstrated that transition from two-dimensional to three-dimensional flow consistently occurred through a supercritical bifurcation: a supercritical Hopf bifurcation at small β and a supercritical pitchfork bifurcation at larger β. In the next chapter, the two-dimensional stability of the flow will be further investigated using a transient growth analysis.

Chapter 5

Optimal transient perturbations leading to two-dimensional unsteady flow

5.1 Introduction

This chapter focuses on the role of linear transient growth and its consequences for the effective transition to unsteady flow in the two-dimensional solution branch. Although some of the flows in this study are linearly stable, perturbations may still display a significant transient response. The onset of two-dimensional unsteadiness of the flow, Re_c is low, and the onset of three-dimensional global linear instability, $Re_{3\mathrm{D}}$, is about half of Re_c. Understanding the non-modal growth properties of the flow is important because the mechanism may cause it to become unsteady at Reynolds number lower than those two onsets mentioned earlier.

In the present investigation, an optimal transient energy growth analysis is performed with two-dimensional perturbations over a range of opening ratios. The aim of this study is to understand the sensitivity of the two-dimensional bend flow to non-modal short-timescale amplifications which is common to many shear flows. These are important as the amplifications may be strong enough to invoke the bypass transition in the flow, in the absence of a global linear instability. The analysis does not consider the three-dimensional perturbations. The intention of this chapter is to elucidate the transient two-dimensional perturbations growth in the two-dimensional flow because it is the most pertinent to the corresponding quasi-two-dimensional MHD flow.

5.2 Problem setup

The configuration of the system is a channel with a 180-degree sharp bend as presented earlier in Figure 3.2. The type of flow studied is a hydrodynamic flow with a smaller range of Reynolds number compared to range investigated in the previous chapter (Chapter 4) because the present interest is in the prospect of non-modal energy amplification *below* Re_{3D} (Blackburn *et al.* 2008a; Griffith *et al.* 2008).

For the mesh, many elements are concentrated in areas of the domain that experience high velocity gradients (i.e. especially at low bend opening ratio) and at the abrupt geometry change (i.e. at the sharp corner of the bend). From previous studies, the optimal instability tends to start from those locations (Sherwin & Blackburn 2005; Blackburn *et al.* 2008a,b; Griffith *et al.* 2008; Hussam *et al.* 2012b). The upstream and downstream lengths chosen for this study are 15 and 40, respectively.

For the basic flow, the fluid enters from the inlet and flows downstream counterclockwise around the sharp bend and down the outlet channel. Boundary conditions are imposed as follows: at the inlet ($x = b-d, -1.02 \leq y \leq -0.02$), a Poiseuille velocity profile $u_x = 1 - 4(y + 0.052)^2, u_y = 0, u_z = 0$ is imposed. A no slip boundary condition ($u = 0$) is imposed at all solid walls. At the outlet ($x = b - e, 0.02 \leq y \leq 1.02$), a standard outflow boundary is enforced with a Dirichlet reference pressure ($p = 0$) and a weakly enforced zero normal velocity gradient (Barkley *et al.* 2008; Griffith *et al.* 2010; Blackburn *et al.* 2008a).

For the transient growth analysis, a zero-velocity Dirichlet condition (Equation (3.49)) is imposed during solution of the linearised equations (3.7)–(3.8) on all boundaries (wall, inlet and outlet) during integration of the forward and adjoint equations so that the time integration of the adjoint equations backwards in time did not produce numerical instability due to inflow at the outlet (Blackburn *et al.* 2008a; Barkley *et al.* 2008).

5.2.1 Validation

To gain confidence in the result of this analysis, the energy amplification in arbitrary geometries, independent of the adjoint system has been checked. The computed leading eigenvector of $\mathscr{A}^*(\tau)\mathscr{A}(\tau)$ is used as an initial condition for the integration of the linearized Navier–Stokes equations over interval τ. The ratio of the integrals of the energies at $t = \tau$ and $t = 0$ should be the same as the leading eigenvalue of $\mathscr{A}^*(\tau)\mathscr{A}(\tau)$.

N	$G(1.6)$	% Error
3	77.86149	1.4987
4	76.71178	1.6302
5	77.98307	0.0405
6	78.01463	0.0014
7	78.01574	0.0007
8	78.01523	-

TABLE 5.1: Dependence of energy growth on polynomial order for $\beta = 1$, $Re = 400$ and $\tau = 1.6$. Parameter N indicates the independent polynomial order used for the transient growth analysis. Errors in energy growth at each N relative to the highest N are also provided, demonstrating a rapid convergence with increasing N

The energy amplification for $\tau = 12.8$ for the 180-degree sharp bend at $\beta = 1$ and $Re = 400$ is

$$\frac{E(12.8)}{E(0)} = \frac{0.851907495}{1.59E-05} = 52746 \tag{5.1}$$

The eigenvalue of $\mathscr{A}^*(\tau)\mathscr{A}(\tau)$ obtained from the transient growth analysis is 52743 which is only 0.006% different from the calculation using the ratio of the integrals of the energies.

5.2.2 Convergence

This subsection seeks to determine the suitable polynomial N to be used and the upstream length of the channel in the present study to ensure optimal numerical accuracy while minimising computing cost. Table 5.1 shows a convergence study involving transient growth performed on a base flow having $\beta = 1$ and $Re = 400$. A nominal value of $\tau = 1.6$ was used to verify the suitable polynomial degree to be employed in this study. The relative error is calculated about each incrementally larger polynomial degree. The polynomial degree of $N = 5$ gives small percentage error for $G(1.6)$ which is only 0.041%. It is in agreement with the result of the convergence study on the polynomial degree for linear global stability analysis in § 4.2.1. Hence, polynomial degree $N = 5$ will be used throughout this chapter.

The suitable upstream length is determined from the calculation of the dependence of energy amplification at a fixed time span of $\tau = 1.6$. The upstream domain length can be important in transient growth calculations as the reversed-time evolution of disturbances upstream of the bend needs to be accommodated by the domain. The error calculated in table 5.2 uses the longest upstream length employed in the validation

x_u	$G(1.6)$	% Error
5	77.961635	0.00059
10	77.982948	0.02675
15	77.983639	0.02764
20	77.962454	0.00046
25	77.962094	-

TABLE 5.2: The effect of upstream domain length, x_u, on energy amplification of the perturbations at $\tau = 1.6$ for opening ratio $\beta = 1$, $Re = 400$ with $N = 5$.

which is $x_u = 25$ as the reference. In general, all upstream lengths give percentage error much smaller than 0.1%. Hence, an upstream length of 15 will be used throughout this chapter.

5.3 Two-dimensional base flows

This section discusses two-dimensional base flow in detail, especially the steady base flow as the transient energy growth can be triggered at very low Reynolds number in the steady flow regime. The effect of the bend opening ratio and Reynolds number on the size of the primary recirculation bubble is briefly investigated because it plays very important role in amplifying the transient perturbations energy in the flow.

5.3.1 Steady base flow

The steady base flow is characterized by the formation of recirculation bubbles near the wall at the downstream of the bend as discussed in § 4.3. The length of the wake is of interest from the perspective of transient perturbations in the flow. Recent studies have shown that separated shear layers are particularly susceptible to transient amplification in energy in perturbations (Blackburn *et al.* 2008a,b; Barkley *et al.* 2008; Cantwell *et al.* 2010; Hussam *et al.* 2012b). As the Reynolds number increases, the length of the recirculation bubbles also increases, especially the primary recirculation bubble. It is also found that at a fixed Reynolds number, as the bend opening ratio increases, the length of the bubbles decreases.

To investigate these relationship more closely, the length of the primary recirculation bubble is recorded at a range of points in the $Re - \beta$ parameter space. Bubble length was assumed to scale as $L_{\mathrm{R1}}/a \sim Re^A \beta^B$, and an optimisation analysis was performed seeking the combination of exponents A and B maximising the square of the correlation coefficient R^2. Figure 5.1(a) shows the collapse of the primary recirculation bubble

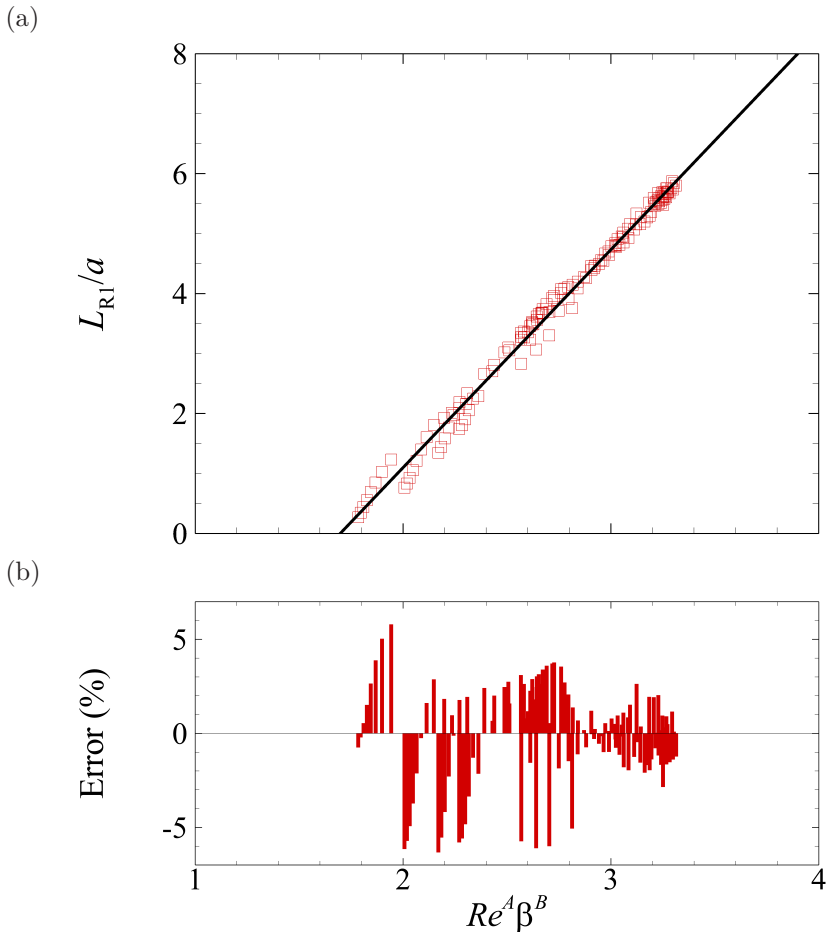

FIGURE 5.1: Collapse of the primary recirculation bubble length over ranges of bend opening ratio $0.2 < \beta < 1$ and Reynolds number $25 < Re < 780$ when plotted against $Re^{0.178}\beta^{-0.0566}$ with $R^2 = 0.9917$ is shown in (a). The error between the individual actual data and the fit is presented in (b).

length against $Re^A\beta^B$. The length of the primary recirculation bubble increases almost linearly with $Re^{0.178}\beta^{-0.0566}$ with the square of the correlation coefficient $R^2 = 0.9917$. The positive value of a indicates that the length of the bubble increases as Reynolds number increases when β is constant, while the negative value of b indicates that the length of the bubble increases as β decreases when Re is constant. The error between the individual actual data with the fitting is shown in Figure 5.1(b). Many points have percentage difference more than 5% compared to the predicted value from the fitting. It is found that those points corresponded to Re and β values for which the secondary recirculation bubble had already formed at the upper wall downstream.

By removing the points corresponding to the existence of the secondary bubble, a superior linear correlation of the data can be obtained. This is where the linear

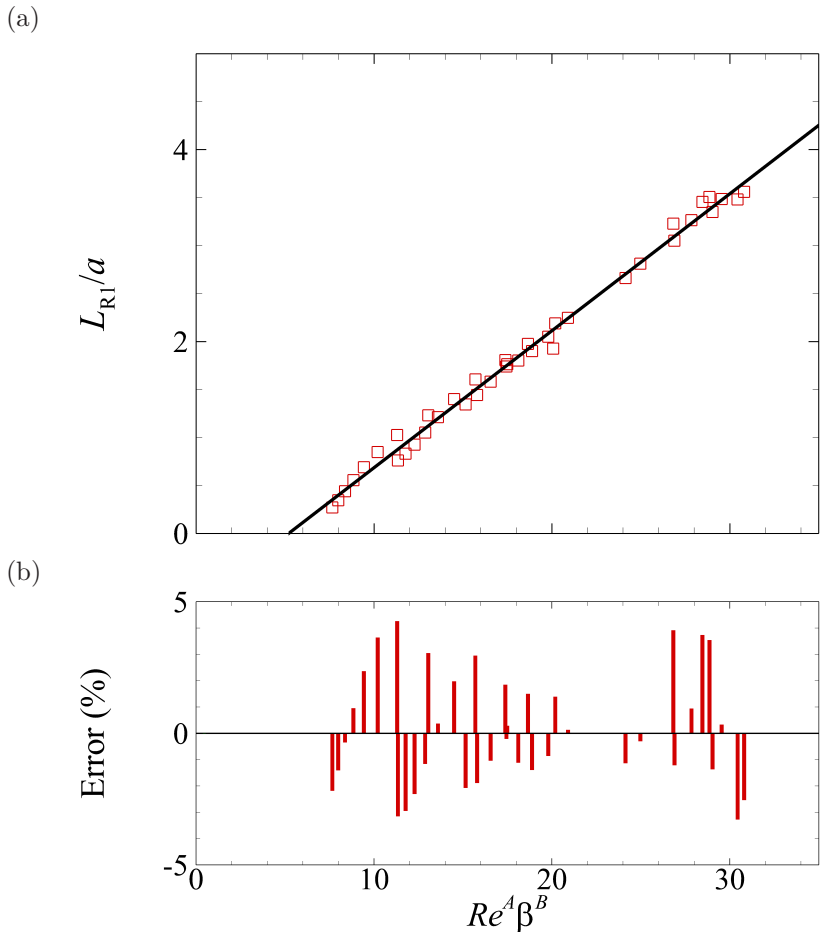

FIGURE 5.2: Collapse of the primary recirculation bubble length over ranges of bend opening ratio $0.2 < \beta < 1$ and Reynolds number $25 < Re < 225$ when plotted against $Re^{0.6208}\beta^{-0.3544}$ with the correlation of coefficient of $R^2 = 0.9931$. The error between the individual actual data and the fit is presented in (b).

region of the primary recirculation (as presented in Figure 4.6), lies before entering the first bifurcation region. Figure 5.2(a) shows a new linear fitting that gives a higher square of the correlation coefficient which is $R^2 = 0.9931$ and with a smaller individual error for each data as illustrated in Figure 5.2(b). The universal relationship between recirculation length, Reynolds number and bend opening ratio is approximated by

$$L_R = 0.1427 Re^{0.6208}\beta^{-0.3544} - 0.7415. \tag{5.2}$$

The proportional relationship between the length of the primary recirculation bubble and Reynolds number in the steady regime was also seen in the previous studies on steady and laminar flow regime in the backward facing step flow (Blackburn *et al.*

2008a; Barkley *et al.* 2002), and expansion ratio in a circular pipe, both experimentally (Back & Roschke 1972; Furuichi *et al.* 2003; Hammad *et al.* 1999) and numerically (Pollard 1981; Cantwell *et al.* 2010).

5.4 Transient growth analysis

This section presents the dependence of the optimal growth for two-dimensional perturbations (zero-wavenumber) on Reynolds number and the bend opening ratio. Subsequently, the relationship between the optimal growth, Reynolds number and evolution time is also discussed.

5.4.1 Reynolds number dependence

Figures 5.3 and 5.4 summarize the two-dimensional optimal growth computation results over a range of time interval and Reynolds number in this analysis. It also makes sense to define the critical parameter ratio

$$C_{Re} = (Re - Re_c)/Re_c, \tag{5.3}$$

since transient growth is relevant to critical Reynolds number.

Figure 5.3 shows only the optimal curve $G(\tau)$ at $Re > Re_{\mathrm{TG}}$, where all curves have positive slope at $\tau = 0$. As τ increases, the curves eventually adopts a monotonically decreasing trends; hence, there is a finite range of τ with $G(\tau) > 1$. This is the range where the energy of an optimal perturbation increases from its initial value.

As the Reynolds number increases, perturbations can be significantly amplified. For example, in Figure 5.4(c,d) at $Re = 300$ for $\beta = 1$ and 2, perturbations are amplified by factors of over 10^3. Even though the flow is linearly stable at $Re = 300$, it can amplify small perturbations to strong level through strictly linear growth.

Figure 5.3(a) shows optimal envelope curves, $G(\tau)$, for a set of Reynolds numbers from $Re = 60$ to $Re = 200$ for $\beta = 0.2$ that corresponds to the range of $-0.80 \lesssim C_{Re} \lesssim -0.33$. Meanwhile figure 5.3(b-d) show the set of Reynolds number from $Re = 80$ to $Re = 600$ for $\beta = 0.5, 1$ and 2 that correspond to $-0.90 \lesssim C_{Re} \lesssim -0.03$, $-0.92 \lesssim C_{Re} \lesssim -0.23$ and $-0.92 \lesssim C_{Re} \lesssim -0.23$, respectively.

The intersection of the unit amplification $G = 1$ contour with the Reynolds number axis is a saddle-point of the growth function in the $Re - \tau$ plane and indicates the onset of the transient energy growth, Re_{TG}. Table 5.3 records the value of Re_{TG} for a range

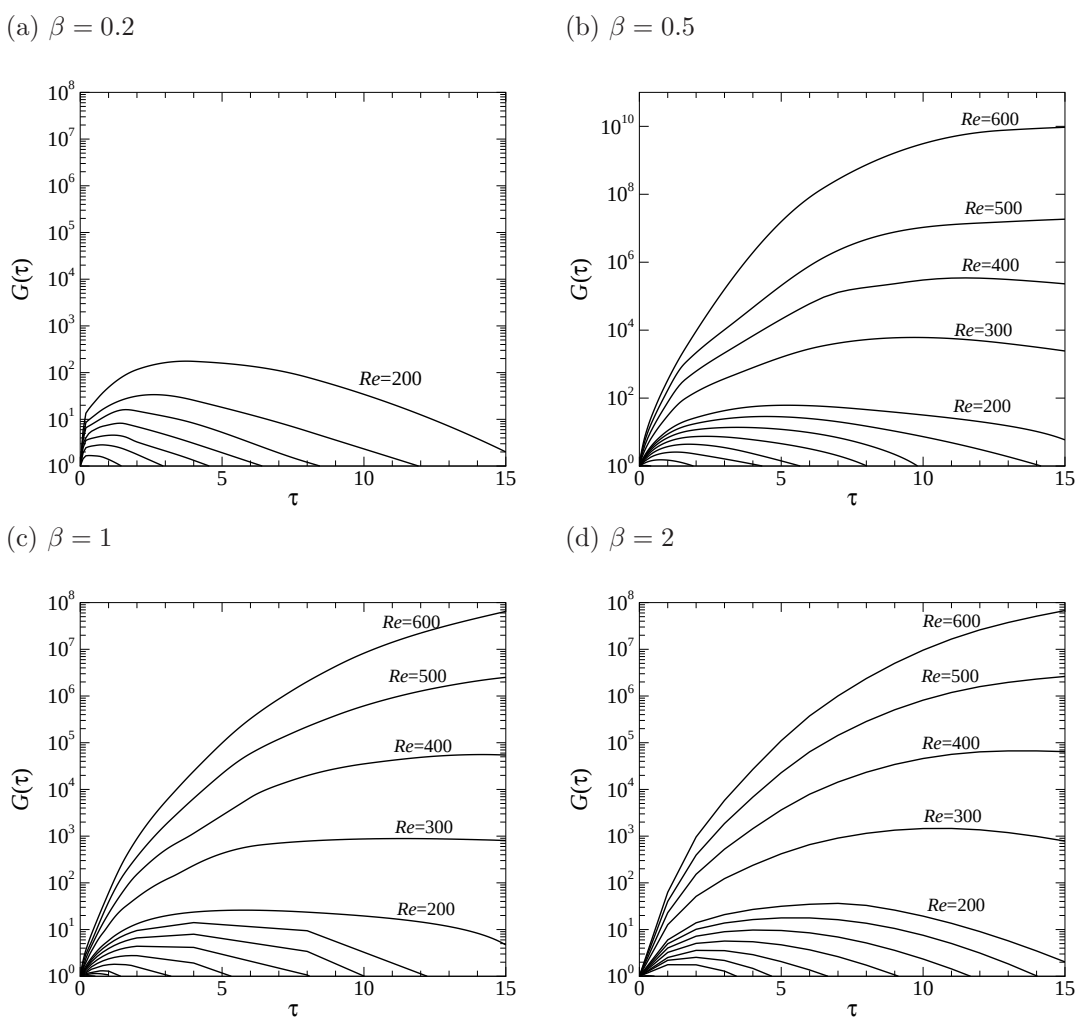

FIGURE 5.3: Two-dimensional optima as functions of τ for Reynolds numbers up to 600 for (a) $\beta = 0.2$,(b) $\beta = 0.5$, (c) $\beta = 1$ and (d) $\beta = 2$.

of bend opening ratio, $0.2 \leq \beta \leq 2$. For the flow with Reynolds number lower than Re_{TG}, there is no energy amplification over any time interval. Re_{TG} can be determined by finding the Reynolds number at which the gradient $\mathrm{d}G/\mathrm{d}t = 0$ as $\tau \to 0$. This is because at $Re < Re_{\mathrm{TG}}$, $G(\tau)$ decreases monotonically with increasing τ. The gradient $\mathrm{d}G/\mathrm{d}t$ were obtained using linear interpolation between $\tau = 0$ and a very small τ (i.e. $\tau = 0.1$). The gradients were then used to interpolate for the Reynolds number having $\partial G(\tau)/\partial\tau = 0$. Thus, for $Re > Re_{\mathrm{TG}}$, the growth envelope $G(\tau)$ has positive slope at $\tau = 0$, and $G(\tau) > 1$ for at least some values of τ. It can be seen in Table 5.3 that the critical Reynolds numbers, Re_{TG}, separating where G first exceeds unity, are very small for all β.

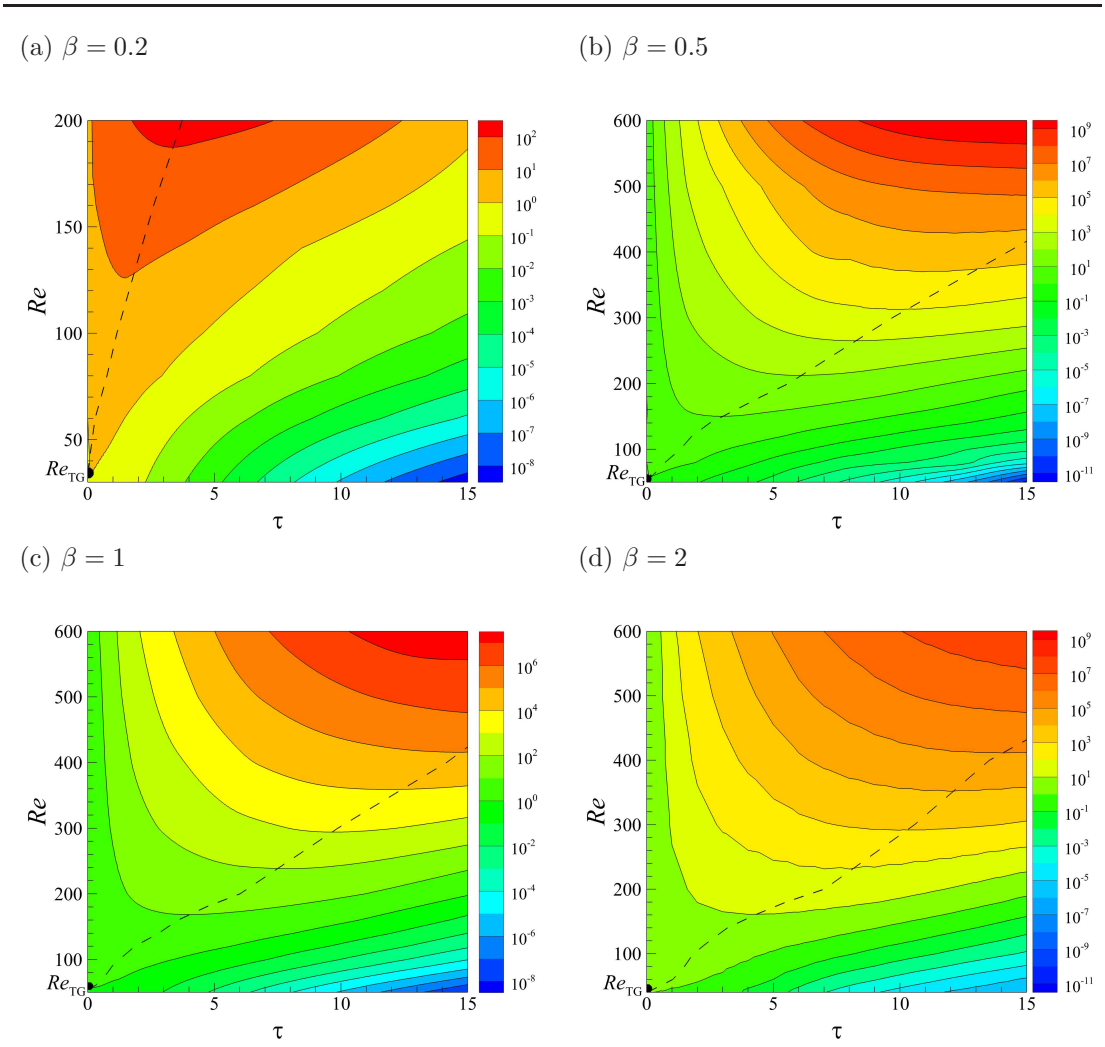

FIGURE 5.4: Contour plot for two-dimensional growth G as a function of τ and Re for (a) $\beta = 0.2$,(b) $\beta = 0.5$,(c) $\beta = 1$ and (d) $\beta = 2$. The dashed line shows the locus of global maximum growth as a function of τ. The solid lines indicate the growth G at decade intervals. Dark-to-light contour denotes the increase of G from very stable to highly unstable.

Figure 5.4 presents G as a contour plot in the (Re–τ)-plane. Re_{TG} is indicated in Figure 5.4 at $\tau \approx 0$. Peak growth and the time at which it occurs increases monotonically with Reynolds number as can be seen in Figure 5.5.

From both figures 5.4 and 5.5, for $\beta = 0.2, 0.5, 1$ and 2, there are perturbations that grow in energy at Reynolds number as low as $Re = 80$ which are well below the onset of linear global instability $Re_{3\mathrm{D}} = 125, 278, 397$ and 387, respectively, as discussed in the previous chapter. It can be seen that the perturbations grow at Reynolds number well below Re_c, at a critical parameter ratio as low as $C_{Re} = -0.8$.

Figure 5.5 shows the dependence of $G_{\max}$ and $\tau_{\max}$ on Re for different β. For all

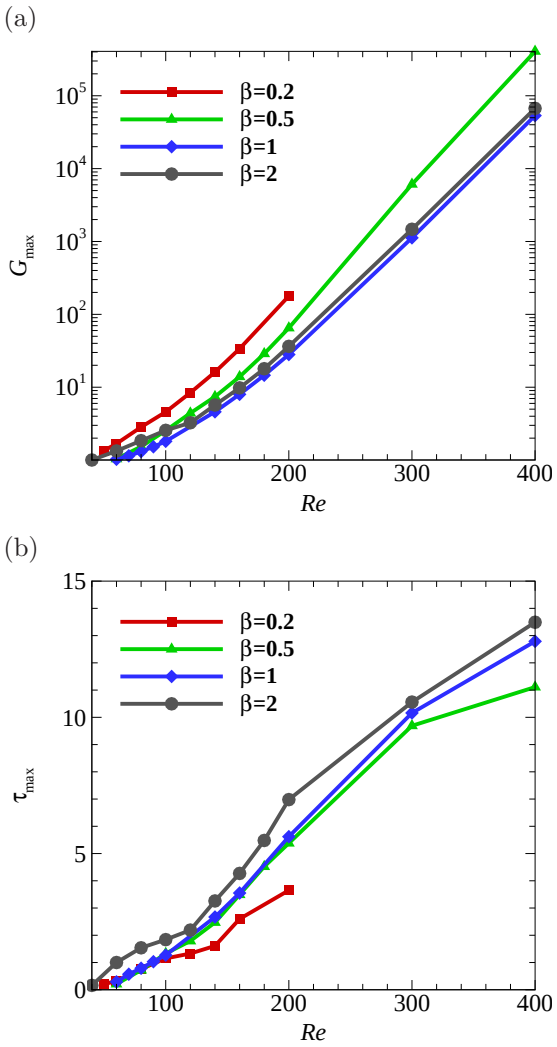

FIGURE 5.5: Graphs showing (a) the maximum energy amplification $G_{\max}$ and (b) the time of the energy maximum as a function of Reynolds number for different opening ratio β. Exponential relationship in (a) signified by linear trends in the data. The values of Re displayed include both below and beyond the critical Reynolds numbers for global instability.

β, it transpired that $G_{\max}$ grows exponentially with Reynolds number similar to the observation seen by Blackburn *et al.* (2008a) in the backward facing step flow and by Griffith *et al.* (2010) in the flow past a stenotic geometry. At very small Reynolds number in Figure 5.5(a), $\beta = 0.2$ and 2 are first to have G exceeding unity, followed by $\beta = 0.5$ and 1. This is consistent with the Re_{TG} data in table 5.3. As Reynolds number exceeds $Re = 100$, the amplification of the perturbation energy for $\beta = 0.5$ becomes more pronounced compared to $\beta = 2$. As Reynolds number increases beyond $Re \approx 140$, the maximum energy amplification at $\beta = 1$ and 2 increases monotonically in parallel

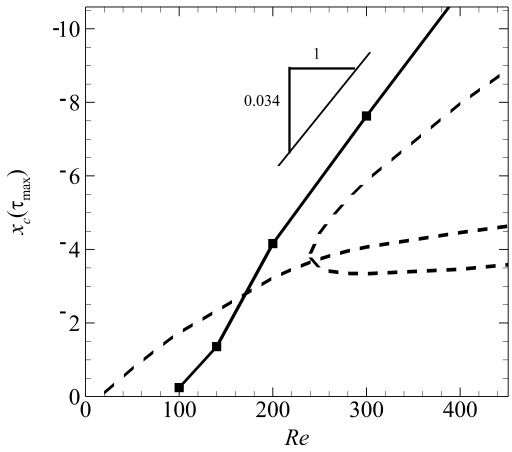

FIGURE 5.6: The centroid location x_c for $\beta = 1$ is represented by the solid line, with separation and reattachment points of the base flow represented by dashed curves. x_c has negative sign because $x = 0$ is the location of the sharp bend, and the flow is moving in $-x$-direction.

to each other. The coexistence of both primary and secondary recirculation bubbles in the channel causes the main bulk flow passing between them to be accelerated; hence, contributing to a higher kinetic energy into the advected perturbations and extending the unstable region in the flow. This causes the growth of the value $G_{\max}$ on Re to become more rapid as Re goes beyond the onset of the formation of the secondary recirculation bubble.

Figure 5.6 shows the dependence of the location of the centroid of the energy distribution for maximum transient growth at $\tau_{\max}$ with Reynolds number. For Reynolds number below $Re \approx 170$, the centroid $x_c(\tau_{\max})$ lies upstream of the reattachment point of the primary recirculation bubble. For larger Reynolds number, the centroid lies downstream of the primary and secondary recirculation bubbles which formed at $Re \approx 275$. For large Re, the data exhibits $\partial x_c/\partial Re \approx -0.034$.

5.4.2 Bend opening ratio dependence

The significant effect of bend opening ratio on the perturbation energy amplification is also revealed. The same effect of bend opening ratio on global linear instability in the previous chapter is expected in the amplification of transient perturbation energy in the flow. For $Re = 200$, at $\beta = 0.2$, the energy amplification is 175.88 which is higher compared to those for $\beta = 0.5, 1$ and 2 that have energy amplification factors of 64.07, 28.12 and 36.36, respectively. The difference is more pronounced at smaller critical

β	Re_{TG}	C_{Re}
0.2	34.52	-0.8849
0.5	56.34	-0.9091
0.7	65.20	-0.9068
1	56.66	-0.9273
1.5	45.64	-0.9414
2	39.52	-0.9493

TABLE 5.3: The onset of transient energy growth Re_{TG} and the respective critical parameter ratio.

parameter ratio, for example at $Re = 600$, where it gives $\beta = 0.5, 1$ and 2 the growth of energy by the factor of $1.66 \times 10^9, 1.23 \times 10^8$ and 1.58×10^8, respectively, with the respective critical parameter ratios $C_{Re} = -0.0323, -0.2307$ and -0.2307.

Figure 5.7 shows further elucidation of the dependence of the onset of the transient energy growth Re_{TG} on β compared to the data provided in table 5.3. The emergence of the transient energy growth (Re_{TG}) is found to be much lower compared to the threshold of global linear instability (Re_{3D}) and the onset of two-dimensional unsteadiness (Re_{c}) of the flow. The flow is found to be least sensitive to the transient disturbance at $\beta = 0.7$ where the growth of the disturbance only occurs at $Re \gtrsim 65$. On the other hand, Re_{TG} decreases with decreasing β further from $\beta = 0.7$ and increasing β beyond $\beta = 0.7$.

The base flows near the onset of transient growth $Re/Re_{\mathrm{TG}} \approx 1$ are shown in figure 5.8 for (a) $\beta = 0.3$ at $Re/Re_{\mathrm{TG}} = 1.48$, (b) $\beta = 0.7$ at $Re/Re_{\mathrm{TG}} = 1.23$, (c) $\beta = 0.9$ at $Re/Re_{\mathrm{TG}} = 1.18$, (d) $\beta = 1.5$ at $Re/Re_{\mathrm{TG}} = 1.38$, and (e) $\beta = 1.8$ at $Re/Re_{\mathrm{TG}} = 1.21$. It can be seen that at very small bend opening ratio (i.e. $\beta = 0.3$), a jet-like flow behind the bend creates a thin shear layer. As bend opening ratio increases, the jet becomes wider cause the jet-like effect disappears. However, as bend opening ratio increases beyond $\beta = 0.7$, the bend opening is wide enough for a separation caused by the sharp edge of the inner bend wall which may causes the energies of perturbation to be concentrated at the vicinity. A similar observation was seen in the backward facing step flow (Blackburn *et al.* 2008a), where for both two-dimensional and three-dimensional perturbations, the optimal initial disturbances were concentrated around the sharp edge of the step. More details on the effect of β at the onset of the transient growth will be discussed in § 5.4.4.

This study has shown simulations up to $Re = 700$ for $\beta = 0.5, 1$ and 2 but due

(a)

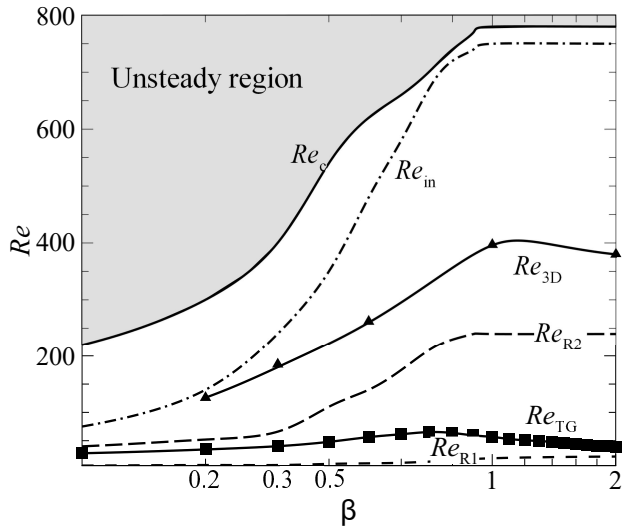

(b)

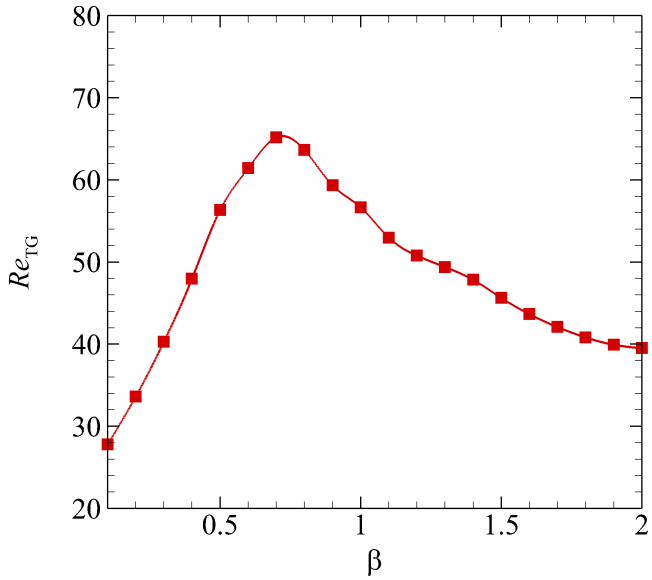

FIGURE 5.7: Reynolds number where primary recirculation bubble Re_{R_1}, secondary recirculation bubble Re_{R_2} and inside recirculation bubble Re_{in} regimes appear in the two-dimensional flow with Re_{c}, $Re_{3\mathrm{D}}$ and Re_{TG} are the onset of two-dimensional unsteadiness, global instability and transient energy growth, respectively, are shown in (a). A more detailed plot of $Re_{\mathrm{TG}}(\beta)$ is shown in (b) which also corresponds to table 5.3.

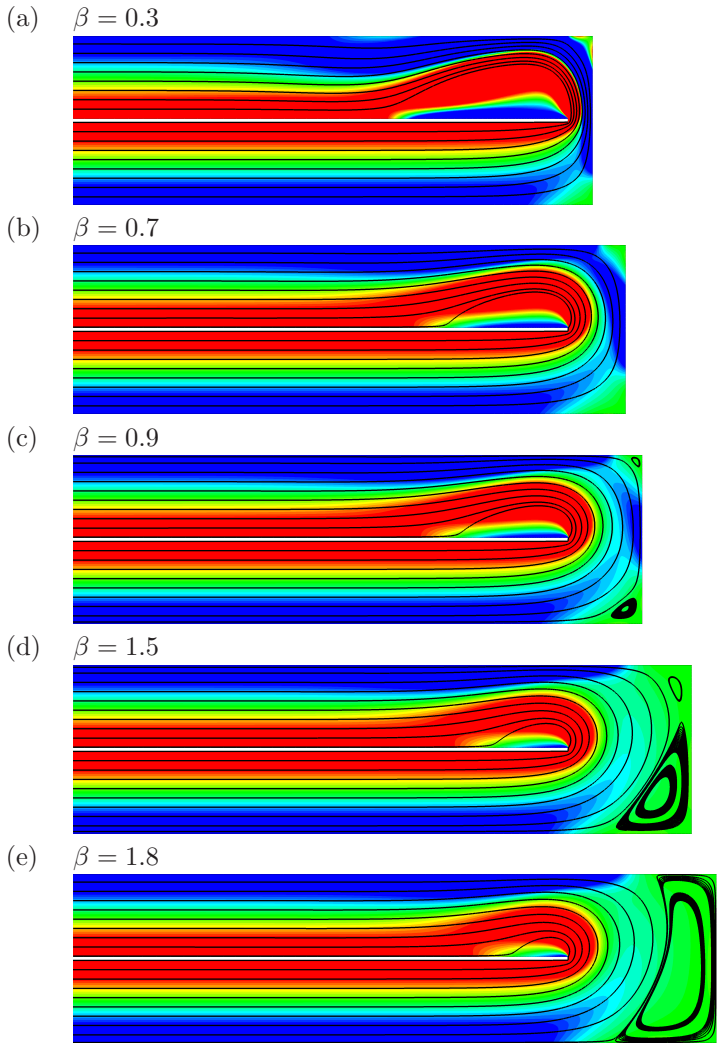

FIGURE 5.8: Contours of spanwise vorticity and velocity streamlines for (a) $\beta = 0.3$ at $Re/Re_{\mathrm{TG}} = 1.48$, (b) $\beta = 0.7$ at $Re/Re_{\mathrm{TG}} = 1.23$, (c) $\beta = 0.9$ at $Re/Re_{\mathrm{TG}} = 1.18$, (d) $\beta = 1.5$ at $Re/Re_{\mathrm{TG}} = 1.38$, and (e) $\beta = 1.8$ at $Re/Re_{\mathrm{TG}} = 1.21$.

to the very demanding computing time and the very slow convergence rate, this study only covers time intervals up to $\tau = 25.6$ where their respective energy amplification is denoted by empty symbols in figure 5.9. At $Re = 600$, for $\beta = 0.5$, it could be confirmed that $\tau_{\max} < 25.6$ because $G(\tau)$ exhibits a maximum turning point in this range of τ. However, for $\beta = 1$ and 2, no $G(\tau)$ turning point was detected which is expected from Figure 5.5(b) where the curves of $\tau_{\max}$ for both β are always above that of $\beta = 0.5$. From the value of $G(25.6)$ for $\beta = 1$ and 2, it can be expected that $G_{\max}$ can exceed 10^{10} in this system at $Re = 700$, where the base flow is still two-dimensionally steady.

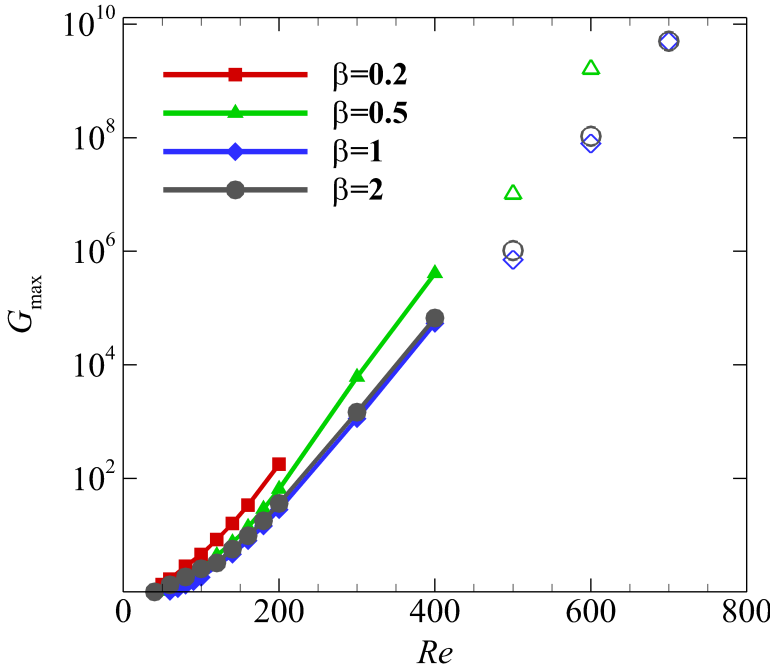

FIGURE 5.9: Energy amplification G for four different bend opening ratios. The solid symbols represent $G_{\max}$, whereas empty symbols represent energy amplification for the highest τ captured for $Re > 400$ in the present study.

5.4.3 Time evolution of optimal perturbations

Here consideration is given to the time evolution of selected optimal perturbations at $Re = 400$ and $\beta = 1$. Figure 5.10 shows the optimum envelope of the optimal growth at $Re = 400$, together with three transient responses. The three transients come from the initial conditions that produce optimal energy amplification at $\tau = 6.4, 12.8$ and 26. It is necessary for these curves to tangentially contact the optimum envelope at the corresponding time as can be seen in the figure. Figure 5.10 emphasizes the idea that the optimal curves (such as those shown in Figure 5.3), represent envelopes of individual transient responses. Nevertheless, practically, many of the individual transients which follow from optimal initial conditions correspond qualitatively and approximately quantitatively to the envelope. Particularly, for $Re = 400$, transient responses starting from the optimal perturbation corresponding to $\tau = 12.8$ are nearly indistinguishable from the optimal envelope $G(\tau)$ shown in Figure 5.10. However, according to Corbett & Bottaro (2000), for a flow with more than one instability mechanism, the responses may be different compared to what is seen in Figure 5.10.

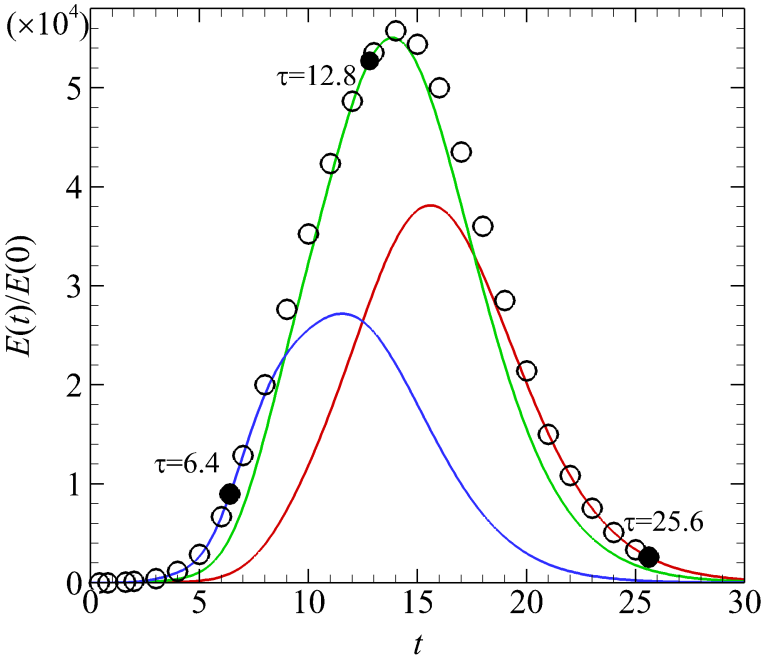

FIGURE 5.10: The envelope of two-dimensional optima (circles) at $Re = 400$ for $\beta = 1$ along with the linear energy evolution from three optimal initial conditions of $\tau = 6.4, 12.8$ and 25.6. Solid circles mark the points at which the curves of linear growth osculate the envelope.

5.4.4 Perturbation fields

This section discusses the perturbation fields associated with optimal growth. Figure 5.11 illustrates the vorticity of the global optimum perturbation initial condition at τ_{max} for the four opening ratios presented in Figure 5.3. The perturbation fields are found to be localized in the region of the boundary layer separation around the sharp inner bend. Same observation was also found for backward facing step (Blackburn *et al.* 2008a), cylinder wake (Hussam *et al.* 2012b; Giannetti & Luchini 2007) and wake behind turbine blade (Abdessemed *et al.* 2009). The structure of the perturbation is predominant in the jet downstream at small bend opening ratio $\beta = 0.2$. As the opening ratio increased, the initial optimal perturbation field is most pronounced in overlapping slanted bends upstream and around the bend.

The kinetic energy contours of the initial perturbation in the flow at the onset of transient growth $Re/Re_{\mathrm{TG}} \approx 1$ for several bend opening ratios are shown in figure 5.12. This figure explains and supports the value of Re_{TG} as a function of β in figure 5.7. At small bend opening ratio (Figure 5.12(a)), the optimal energy of the initial perturbation

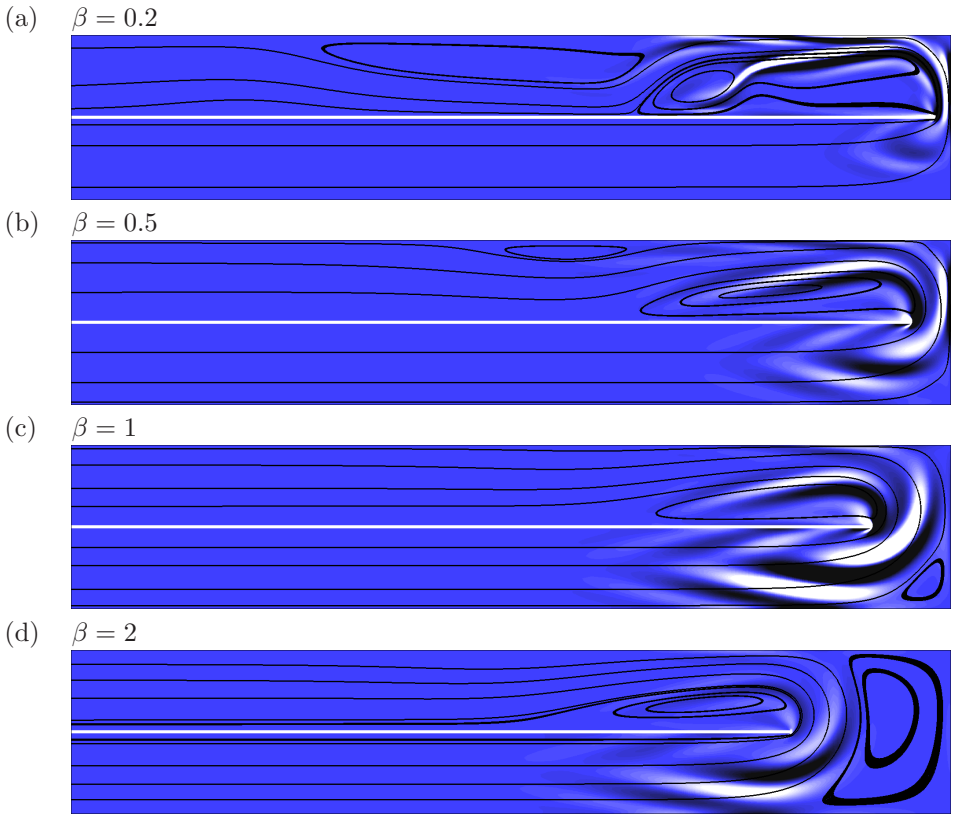

FIGURE 5.11: Plots of vorticity of the optimal initial perturbation at τ_{max} and $Re = 200$ for (a) $\beta = 0.2$, (b) $\beta = 0.5$, (c) $\beta = 1$ and (d) $\beta = 2$. The light-mid-dark contours indicate positive-zero-negative spanwise vorticity. The streamlines of the stable base flow are overlaid in the plots.

is located in the very thin shear layer produced by the jet-like flow caused by the narrow opening, similar to what was seen in a flow around a solid circular cylinder with very small opening ratio (Hussam *et al.* 2012b). As the bend opening ratio becomes larger, the location of the optimal energy of the initial perturbation shifted towards upstream of the channel indicating the diminishing of the jet-like flow due to the wider bend opening. For $\beta > 0.7$ (Figure 5.12(c)-(e)), the kinetic energy of the initial perturbation is concentrated at the first sharp corner of the bend.

The change of location of the initial optimal perturbation at different β varies because of the difference in separating shear flow at the bend. In each of the cases with different β, the maximum energy of the perturbation is located in the vicinity of the separation point of the sharp corner. The perturbation then travels along the separating shear layer, where it amplified. It indicates that the width of the bend opening does not affect the nature of the perturbation. However, the width plays a significant role

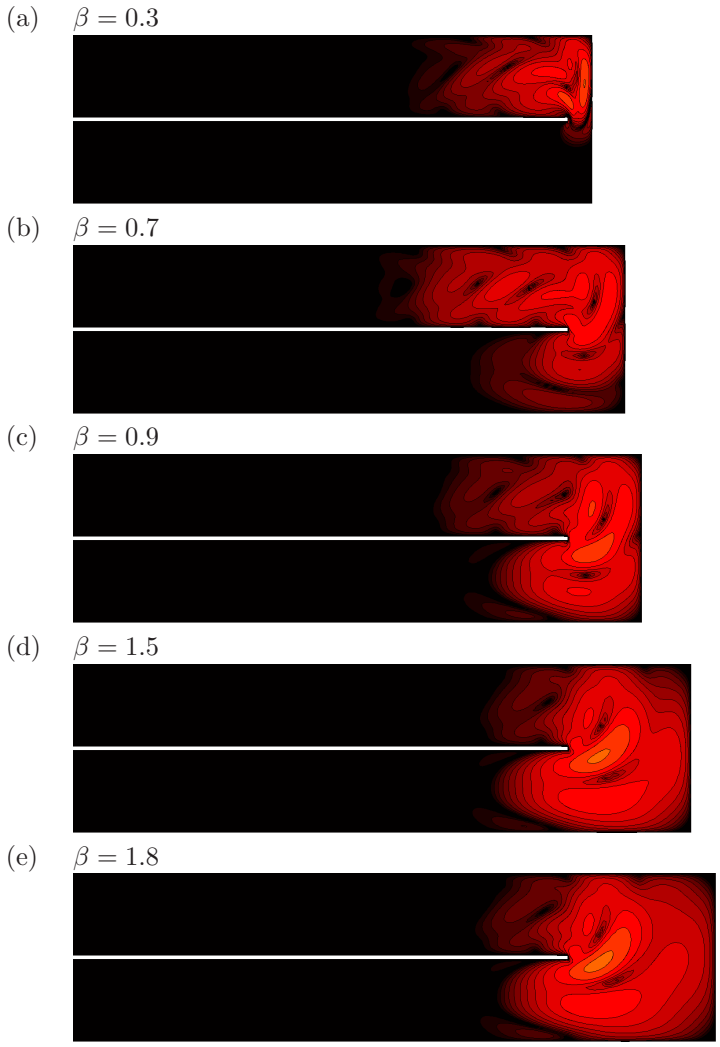

FIGURE 5.12: Contours of the logarithm of kinetic energy in the two-dimensional optimal perturbation initial condition for (a) $\beta = 0.3$ at $Re/Re_{\mathrm{TG}} = 1.48$, (b) $\beta = 0.7$ at $Re/Re_{\mathrm{TG}} = 1.23$, (c) $\beta = 0.9$ at $Re/Re_{\mathrm{TG}} = 1.18$, (d) $\beta = 1.5$ at $Re/Re_{\mathrm{TG}} = 1.38$, and (e) $\beta = 1.8$ at $Re/Re_{\mathrm{TG}} = 1.21$. The light-mid-dark contour colours represent high-moderate-zero kinetic energy.

in shaping the shear layers that lead to the different location of the maximum kinetic energy of the initial perturbations.

Figure 5.13 shows a sequence of perturbation vorticity contours that evolve from the two-dimensional global optimum perturbation initial condition for $\beta = 1$, $Re = 400$, $\tau = 12.8$ (shown in Figure 5.14). This evolution corresponds to the transient energy trajectory drawn in Figure 5.10. The characteristic of a locally convectively unstable flow is evident: the maximum energy amplification occurs when the perturbation passes through the thinnest part of the shear layer near the sharp corner. The evolved roller

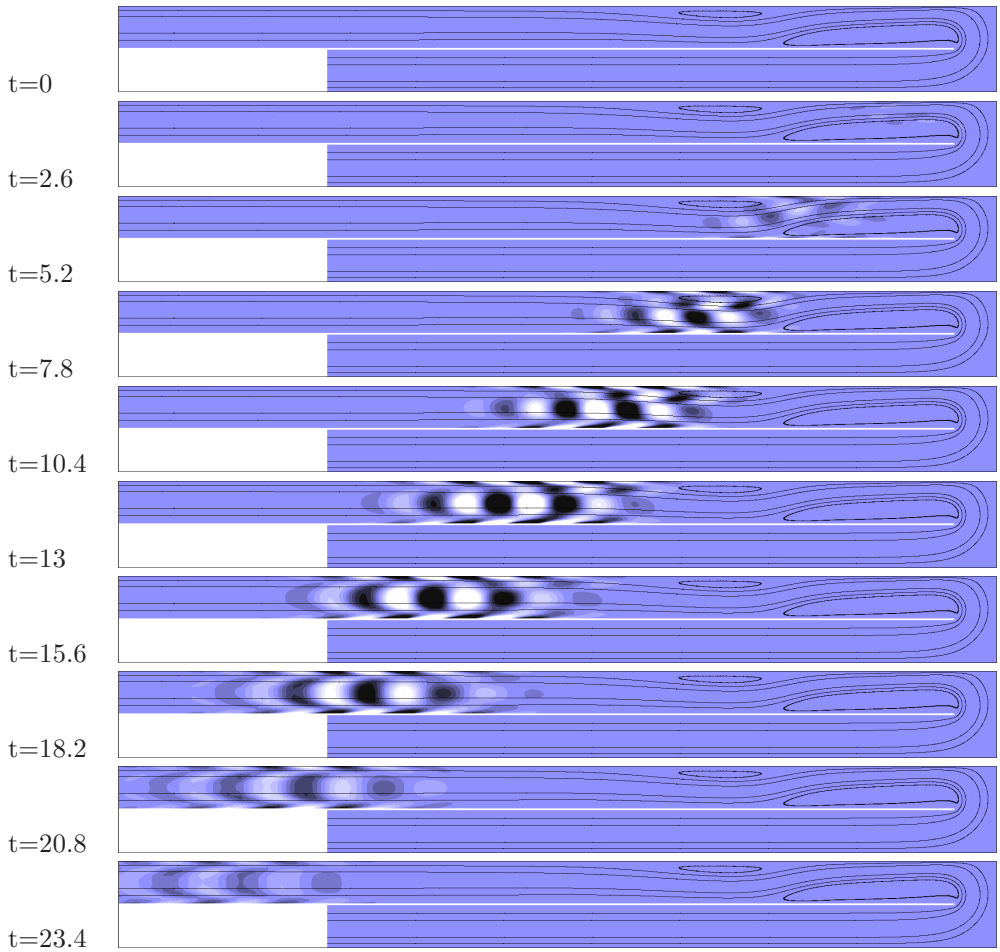

FIGURE 5.13: Sequence of linear perturbation vorticiy contours developed from the two-dimensional global optimum perturbation initial condition for $\beta = 1$ and $Re = 400$ (maximum energy amplification occurs for $t = \tau = 12.8$. Separation streamlines of the base flow are also shown. The characteristic space-time dynamics of a local convective instability is clearly evident.

structures are seen precisely for times between 10.4 and 15.6, and for x in the range -8 to -14. After this point, the energy in the perturbation passes into a less unstable region where the structures decay due to the distortion by the mean strain field. This spatial pattern shows that the energetic amplification is similar to convective instability, where the amplitude of maximum energy amplification moves in a frame convecting with the perturbation, and the energy at the initial perturbation location and downstream decays as the perturbation convects away.

Figure 5.14(a) presents the contours of the initial condition of the energy in the global optimum two-dimensional perturbation for $\beta = 1$ at $Re = 400$ and $\tau = 12.8$. The kinetic energy of the eigenfunction is concentrated near the sharp edge. Figure

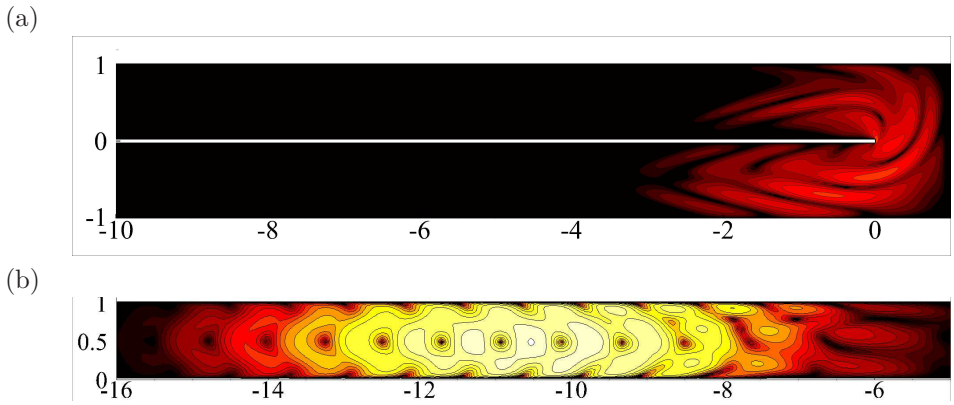

FIGURE 5.14: Contours of the logarithm of energy in the two-dimensional (a) optimal perturbation initial condition for $\beta = 1$ at $Re = 400$ and (b) in the corresponding linear growth outcomes at $\tau = 12.8$.

5.14(b) shows the contours of energy in the perturbation solutions that linearly evolved at $t = 12.8$ when the amplification of the perturbation's energy is maximum. The flow structures that give rise to these energy contours are similar to those found for the backward facing step (Blackburn *et al.* 2008a). The structures are a series of counter-rotating spanwise rollers. The energy maxima at the centreline of the channel correspond to the centre of the spanwise rollers. The energetic spanwise rollers are produced through tilting of initially highly strained and backward-leaning structures that arise near the walls, which is similar to what was observed for two-dimensional optimal growth in plane Couette and Poiseuille flows (Schmid & Henningson 2001; Farrell 1988).

Figure 5.15 illustrates the profiles of the vertical velocity component that evolved from the optimal initial condition for the same case as shown in Figure 5.13. The vertical velocity component is extracted along the centreline of the downstream channel ($y = c+a/2 = 0.52$). The profiles are normalized to have an absolute maximum value of $|v|' = 1$. As in figure 5.13, the characteristic of the 'generic' local convective instability is apparent. The perturbation at the initial location decays as the perturbation convects away. The extremely sharp fluctuations in the optimal perturbation at the sharp bend can be seen in Figure 5.15 at $t = 0$. By using zero-crossing analysis-estimation, the average streamwise wavelength of the fluctuations of the vortical structure at the optimal time is $L_x \approx 1.8$. The wavelength is larger than the channel height which is expected for a pair of circular counter-rotating vortices to appear in the channel as

shown in Figure 5.14(b). The energy in the initial perturbation condition is shown in Figure 5.14(a) where the maximum energy amplification is at the upstream of the sharp bend.

Figure 5.16(a) and (b) show the contours of the logarithm of optimal energy for $\beta = 0.2$ and $Re = 200$ at its initial condition ($t = 0$) and when the energy perturbation is at its peak ($t \approx \tau_{\max} = 4$), respectively. The vortical structure at the optimal time is slightly different with those of at larger bend opening ratio and in backward-facing step flow. The small $\tau_{\max}$ at small bend opening ratio causes the perturbation to reach its peak amplification earlier compared to the larger opening ratio case. The local source of the perturbation is advected a shorter distance, causing the energy amplification of the perturbation to reach its peak value in the main bulk flow below the secondary recirculation bubble. Thus, the vortical structure when the energy is maximum is smaller and displaced towards the lower wall compared to those of at larger bend opening ratio because of the restriction caused by the secondary recirculation bubble.

Based on the same approach as used across in figures 5.13 and 5.15, the centroidal locations of energy were obtained in a perturbation that grows from the two-dimensional global optimum perturbation at $Re = 400$ and $\beta = 1$ which is shown in Figure 5.17. The multiple lines indicate the centroid with the highest energy as the perturbation evolves with time. The centroid of perturbation energy that appears at the beginning eventually decays and a new centroid appears at its downstream and grows. This repeats until $t \approx \tau_{\max}$ where no new centroid with growing E_k appears. According to Chomaz (2005), for weakly nonparallel flows, which are stable or unstable everywhere, an artificially introduced perturbation grows while it is traveling in the convectively unstable region, but decays when it reaches the stable region. This is why globally stable open flows exhibit large transient growth associated with downstream propagation of perturbations. This means that for the case of $Re = 400$ and $\beta = 1$, the convectively unstable region is at $0 \leq -x \lesssim 10.42$. At $x \lesssim -10.42$, the region is stable, hence without any continuous external forcing or feedback, the flow returns to its basic state. It is of interest to know the location of this regions because for applications that need the perturbation to remain in the flow, the perturbation can be sustained by adding vortex promoter before the location where the perturbation will have completely decayed. As for the repetitive 180-degree sharp bend in fusion blanket application as proposed by Boccaccini *et al.* (2004), the length of the outlet before the next sharp bend can be

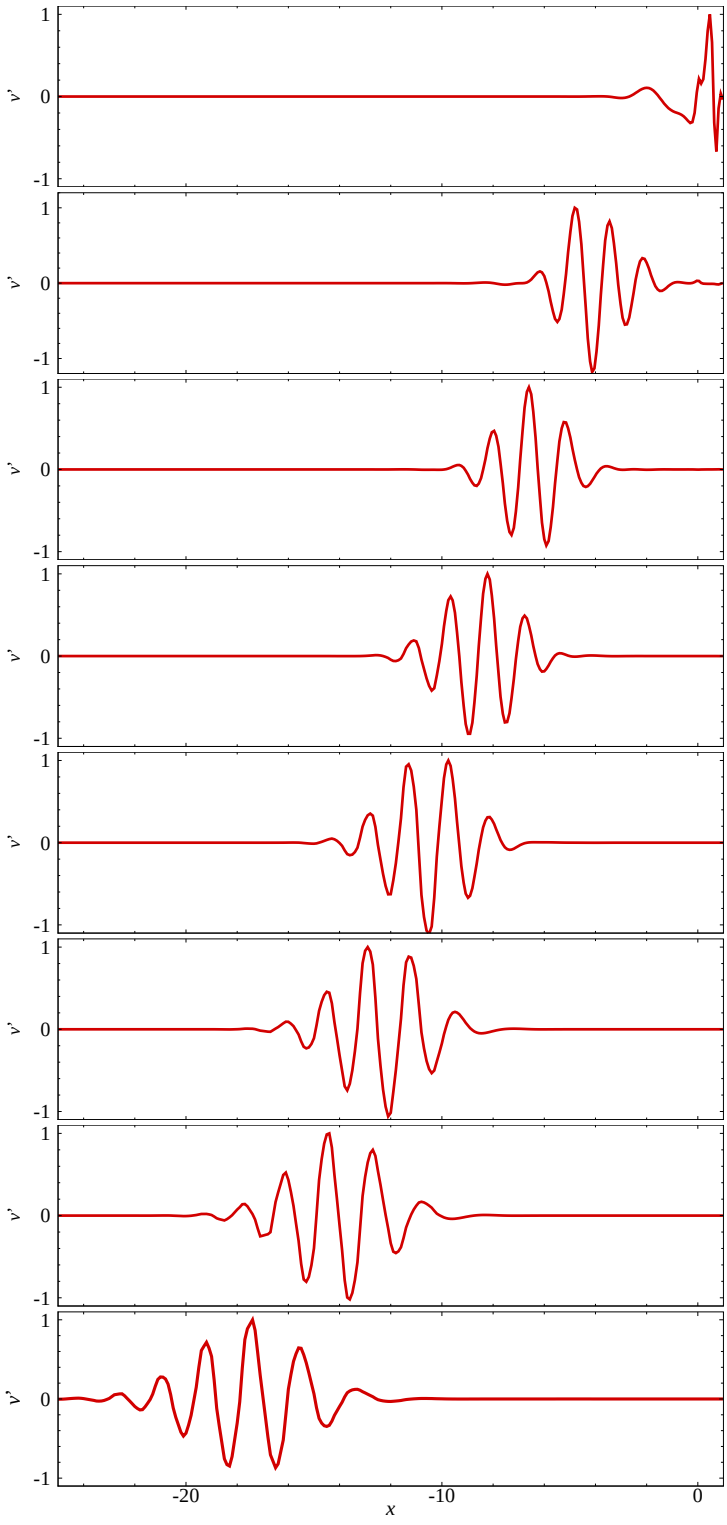

FIGURE 5.15: Time sequence of the vertical component of the perturbation velocity (v') profile along the outlet channel centreline obtained at $Re = 400$, $\beta = 1$. The sequence evolves from the optimal perturbation achieving energy amplification, which had an evolution time $\tau_{\max} = 12.8$. Note that $x = 0$ is the location of the sharp corner and the flow is moving leftward in this outlet channel.

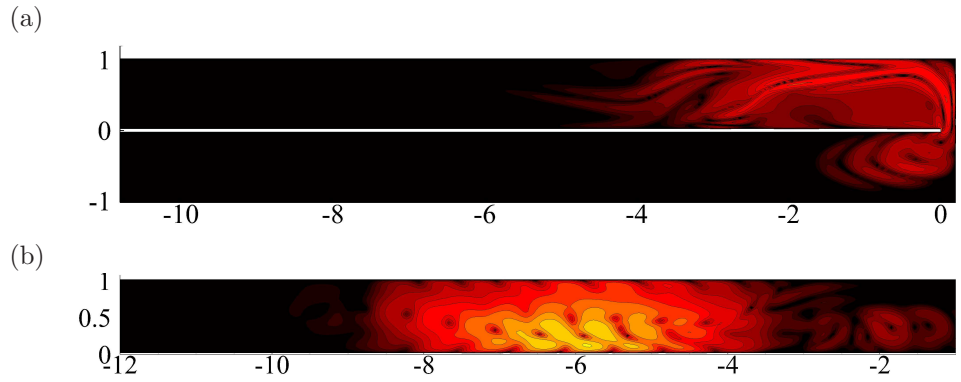

FIGURE 5.16: Contours of the logarithm of energy in the two-dimensional (a) optimal perturbation initial condition for $\beta = 2$ at $Re = 200$ and (b) in the corresponding linear growth outcomes at $\tau = 4$.

adjusted depending on the amplification of the perturbation required.

The line slope $-3/5$ in Figure 5.17(a) indicates the streamwise velocity of the centroids which is very close to the asymptotic average dimensionless flow speed in the downstream channel, $u_{avg} = 2/3$. This shows that the perturbation advected downstream along with the main bulk flow, as what should be expected from any hydrodynamic flow. The slope, or the gradient $\partial x_c/\partial \tau_{\max}$, can be related to the variation of the optimal time $\tau_{\max}$ with Reynolds number from Figure 5.5(b), $\partial \tau_{\max}/\partial Re \approx 0.0396$ and the gradient $\partial x_c(\tau_{\max})/\partial Re = -0.034$ from figure 5.6. A value of $\partial x_c/\partial \tau_{\max} \approx \partial x_c/\partial Re \times \partial Re/\partial \tau_{\max} \approx -0.034 \times 1/0.0396 \approx -0.85$ is obtained. It is slightly large because it does not consider the transfer of the optimal centroid from one centroid to another in its downstream as seen in Figure 5.17(a,b). A dashed line with a slope of -0.85 in figure 5.17(a) can be seen to match very well with the overall convection speed of disturbance.

5.4.5 Response of the flow to continuous inflow perturbations

Direct numerical simulations have been performed to demonstrate the relevance of the computations of the linear growth of perturbation to a real flow in the presence of inflow noise. This demonstration is relevant because, in any real flow, inflow noise is always available to trigger shear-layer instabilities (Blackburn *et al.* 2008b).

The initial state chosen is the steady-state flow at $Re = 400$ and $\beta = 1$ because it exhibits large transient energy amplification amplitude, while being well below the critical Reynolds number for the onset of unsteady flow. The velocity field of the flow

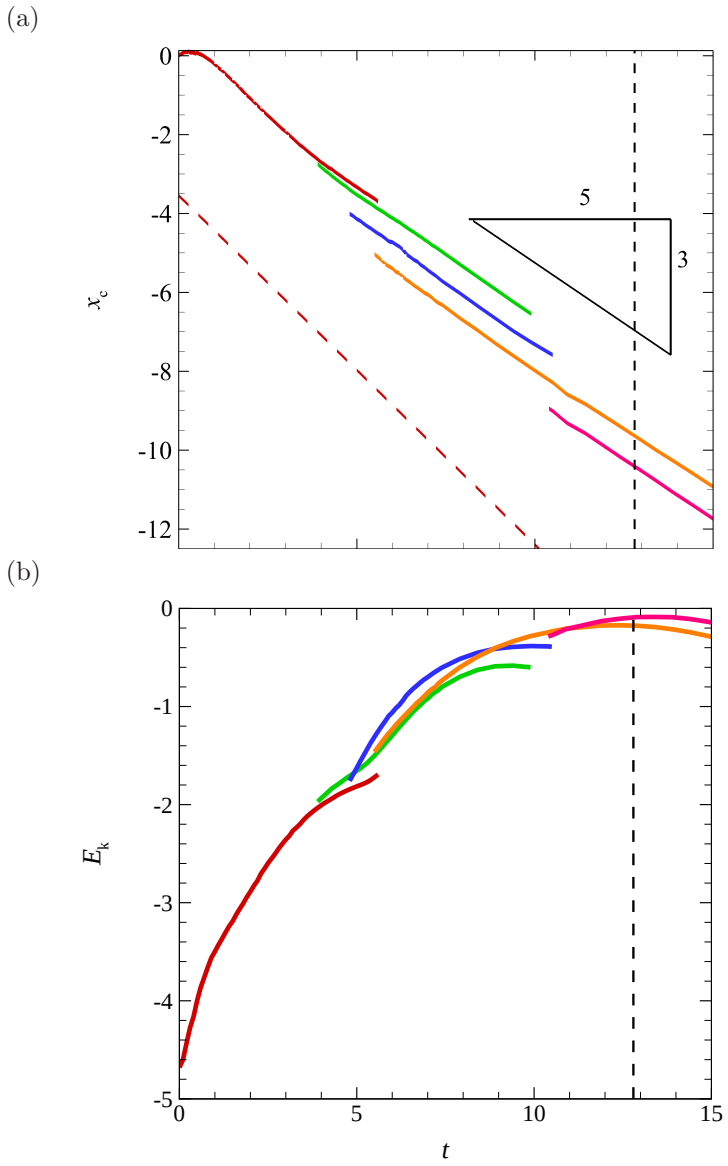

FIGURE 5.17: The location of the centroids of perturbation energy (x_c) evolving from the two-dimensional optimal initial perturbation as a function of time for $Re = 400$ and $\beta = 1$ is shown in (a). The corresponding centroid energies are shown in (b) which indicates that E_k is at maximum when $t \approx \tau_{max} = 12.8$ (represented by the vertical dashed line). The line slope -3/5 indicates the asymptotic average dimensionless flow speed in the downstream channel. The red dashed slanted line in (a) indicates a slope of -0.85 which represents the overall convection speed of the disturbance.

at the inlet is invoked with a random white noise with small amplitude. In Kaiktsis *et al.* (1996) study, the authors found that both monochromatic and random inflow excitations result in an oscillatory flow. Here it was anticipated that significant growth of perturbations to non-linear levels would be seen as the base flow is excited with

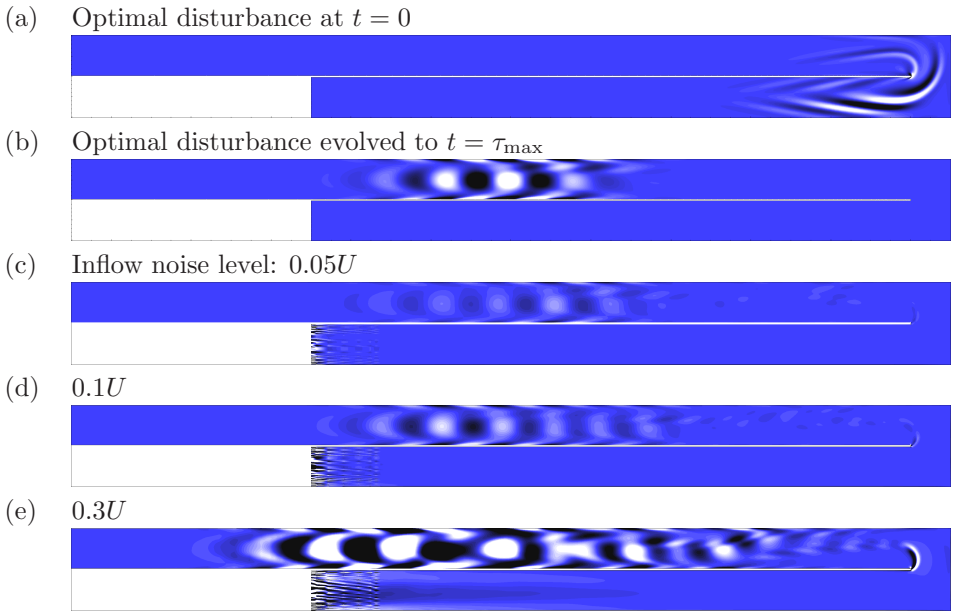

FIGURE 5.18: Perturbation vorticity contours obtained for $Re = 400$ and $\beta = 1$. The optimal initial disturbance at $\tau = 13$ is shown in (a), and the evolved disturbance at $t = \tau_{\max} = 12.8$ is shown in (b). The perturbation velocity field obtained by subtracting the unperturbed steady-state solution from a snapshot of the simulations perturbed by white noise with amplitudes of (c) $0.05U$, (d) $0.1U$ and (e) $0.3U$ are presented.

noise. Naturally, the inflow noise represents a continuous forcing while the transient growth analysis examines the growth of discrete wavepackets, so the interpretation of the results need to be considered carefully.

In a hydrodynamic flow, an introduced perturbation decays only because of the effect of viscosity. Figure 5.18 shows the vorticity of perturbation from the transient growth analysis (a)–(b) and from a steady-state base flow excited by the addition of the white noise to the flow from the inlet. Three amplitudes of white noise were imposed at the inlet, (c) $0.05U$, (d) $0.1U$ and (e) $0.3U$. Figure 5.18(a) and (b) show the optimal initial disturbance at $\tau_{\max} = 12.8$ and the evolved disturbance in the flow at $t = 12.8$. The imposed noise can be seen to rapidly decay below the plotted contour levels near the inlet, before the transient growth mechanism acts to amplify the remaining low-level noise to visible levels. The location and structure where the disturbance structures are strongest in the downstream channel bears a close resemblance to the optimal disturbance when evolved to $\tau_{\max}$.

5.5 Conclusions

A study has been conducted on the transient growth of optimal linear two-dimensional perturbations in a fluid flow around a 180-degree sharp bend. The numerical simulations have been performed over the range of $1 \leq Re \leq 600$ and opening ratios $0.2 \leq \beta \leq 2$. The underlying base flow is two-dimensional and steady, and the linearised Navier–Stokes and adjoint equations are solved in a two-dimensional domain. Only a zero-wavenumber perturbation was considered because it is the most relevant to quasi-two-dimensional MHD flow. It is also of interest to understand the effect of transient energy growth from two-dimensional perturbation on the flow because global linear stability could not predict the onset of two-dimensional unstable flow.

The relationship between the primary recirculation bubble length with the bend opening ratio and Reynolds number can be described as $L_{\mathrm{R1}} \propto Re^{0.6208}\beta^{-0.3544}$. The correlation indicates that the influence of the bend opening ratio is more significant compared to Reynolds number in determining the flow structure for $\beta \leq 1$.

A very appreciable transient energy growth was found in the range of opening ratio and Reynolds number in this study. This suggests a design of actuation mechanisms introducing vortex shedding and enhancing heat transfer in the duct. The energy amplification of the perturbations was found to increase significantly with decreasing bend opening ratio, and the growth peak at shorter time intervals. The global maxima were found to change with the opening ratio, being longer at a larger opening ratio. At small bend opening ratio $\beta \leq 0.4$, the perturbation predominantly in jet downstream of the bend gap; at higher bend opening ratio, the perturbation seems to be quite pronounced in overlapping slanted bends upstream and around the bend.

The critical Reynolds number of the onset of the transient growth increased as the bend opening ratio increases over $\beta \leq 0.7$ but decreased beyond $\beta > 0.7$. The jet-like flow at $\beta \leq 0.7$ creates a long thin shear layer behind the bend opening. Meanwhile, at $\beta \geq 0.7$, the bend opening is sufficiently wide for the flow to experience separation that causes the energies of the perturbation to be concentrated in the vicinity.

Direct numerical simulations with the inflow were perturbed by white noise demonstrated that the optimal transient growth properties of the flow could be activated by continuous upstream random perturbations. This resulted in a significant amplification of the perturbations as they passed around the 180-degree sharp bend. The low-amplitude noise was sufficient to destabilize the wake through the global instability

responsible for producing the Kelvin–Helmholtz instability, despite the simulation being run at conditions below the critical Reynolds number for the onset of two-dimensional unsteadiness.

Chapter 6

Magnetohydrodynamic flow around a 180-degree sharp bend

6.1 Introduction

This chapter considers the effect of a strong magnetic field in the spanwise direction on an electrically conducting liquid metal flow around a 180-degree sharp bend in a duct as shown in figure 6.1. Parameters like Re, H and β are systematically varied to investigate their influences on the stability of the quasi-two-dimensional flow. These three parameters are of interest because they play a major role in determining the state of the flow downstream of the bend. This study provides the relationship of the length of the primary recirculation bubble with Reynolds number, Hartmann friction parameter and bend opening ratio quantitatively, similar to the analysis by Dousset & Pothérat (2008) and Hussam *et al.* (2012b) for flow around a bluff body. A mapping of flow regimes is also discussed to provide a better understanding of the effect these parameters have on the characteristics of the flow.

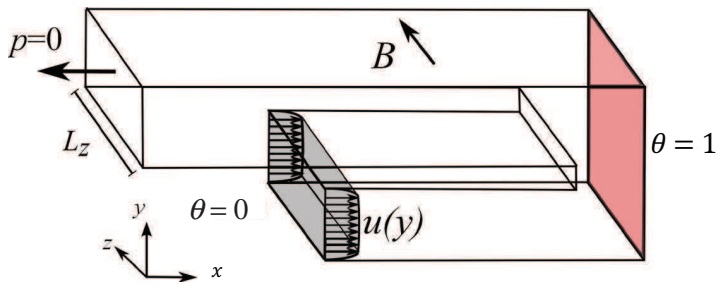

FIGURE 6.1: Flow geometry for the 180-degree sharp bend. The dimension used in this problem is the same as discussed in figure 3.2 in § 3.4.

This is followed by an analysis of the effect of the parameters on the convective heat transportation in the system. The rate of heat transfer on a heated bend end wall and the flow pressure difference are considered to analyse the condition for the heat transport to be optimal. The computations are made over a wide range of Reynolds number $1 \leq Re \leq 2000$ and Hartmann friction parameter $0 \leq H \leq 1000$ in a 180-degree sharp bend duct with bend opening ratio $0.2 \leq \beta \leq 2$.

Firstly, a brief description of the problem setup is given in § 6.2. The influence of magnetic field on the flow structure and the phase state diagram of the flow are presented in § 6.3.1 and § 6.3.2, respectively. And finally, the effect of Hartmann friction parameter and bend opening ratio is discussed in § 6.4.1.

6.2 Problem setup

Figure 6.1 shows the domain considered in this study. Viscous electrically conducting fluid is considered flowing in a duct with a sharp 180-degree bend with the origin of the Cartesian coordinate system located at the center of the inner vertical wall of the bend. The upstream and downstream ducts are parallel to each other. The flow is incompressible.

The dimension of the domain is the same used in the previous two Chapters, 4 and 5. In this chapter, some additional parameters have been added, a spanwise (z-direction) magnetic field of strength B, L_z the width of the duct in the spanwise direction. Hartmann friction parameter is defined by Pothérat (2007) as $H = n(a^2/L_z^2)aB\sqrt{\sigma_e/(\rho\nu)}$ where σ_e, ρ and ν are the electrical conductivity, mass density and kinematic viscosity of the fluid, respectively. The parameter H is a modified Hartmann number and is a measure of the friction due to the Lorentz force effect on the flow, n represents the number of Hartmann layers in any given cross-section of the duct, which is, in this case, $n = 2$. The range of Hartmann friction parameter considered in this chapter is $0 \leq H \leq 1000$.

The current study uses a quasi-two-dimensional model for the MHD flow, developed by Sommeria & Moreau (1982) and extended by Pothérat *et al.* (2000b, 2005). The model is valid for flows with interaction parameter $N \gg 1$ and Hartmann number $Ha \gg 1$.

For the heat transfer study, the end wall of the bend is considered to be heated, and the fluid is considered to be cold and enters the inlet with a fully developed Hartmann

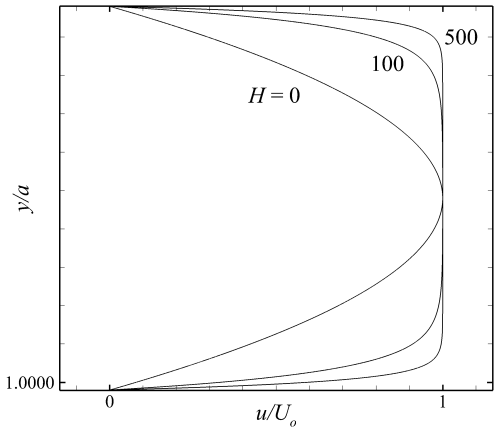

FIGURE 6.2: Quasi-two-dimensional velocity profile at H as indicated normalized with maximum inlet velocity for fully developed duct flow as described by equation (6.1).

flow as shown in figure 6.2 that is analytically described for a straight channel as

$$\left.\begin{array}{ll} u & = \frac{\cosh\sqrt{H}}{\cosh\sqrt{H}-1}\left(1-\frac{2\cosh\sqrt{H}(y+0.52)}{\cosh\sqrt{H}}\right) \\ v & = 0 \end{array}\right\}. \tag{6.1}$$

All walls other than the heated wall are treated as thermally insulating; hence, no energy is released through the walls. The electrically conducting fluid metal considered in this study is $Ga^{68}In^{20}Sn^{12}$ which at 20°C has the properties of density $\rho = 6.3632 \times 10^3$ kg m^{-3}, electrical conductivity $\sigma = 3.30737 \times 10^6\ \Omega^{-1}\mathrm{m}^{-1}$, kinematic viscosity $\nu = 3.4809 \times 10^{-7}\mathrm{m}^2\mathrm{s}^{-1}$ and Prandtl number Pr = 0.022 (Lyon 1952). $Ga^{68}In^{20}Sn^{12}$ is also liquid at this temperature.

6.3 Quasi-two-dimensional flow

In this section, the numerical simulations covering the effects of the magnetic field on the recirculation bubble length and the stability of the flow is considered.

6.3.1 Influence of magnetic field on the flow structure

In this study, the magnetic Reynolds number is significantly small $R_m \ll 1$ making the magnitude of the induced magnetic field negligible resulting to the total magnetic field imposed on the flow as $\mathbf{B} = B\hat{\mathbf{z}}$ as shown in figure 6.1. This resulting magnetic field induces Lorentz force in the core region that balances the driving pressure gradient. The ratios of Lorentz forces to inertia $N = \sigma L_z B^2/(\rho U_0)$ and to viscous forces $Ha^2 =$

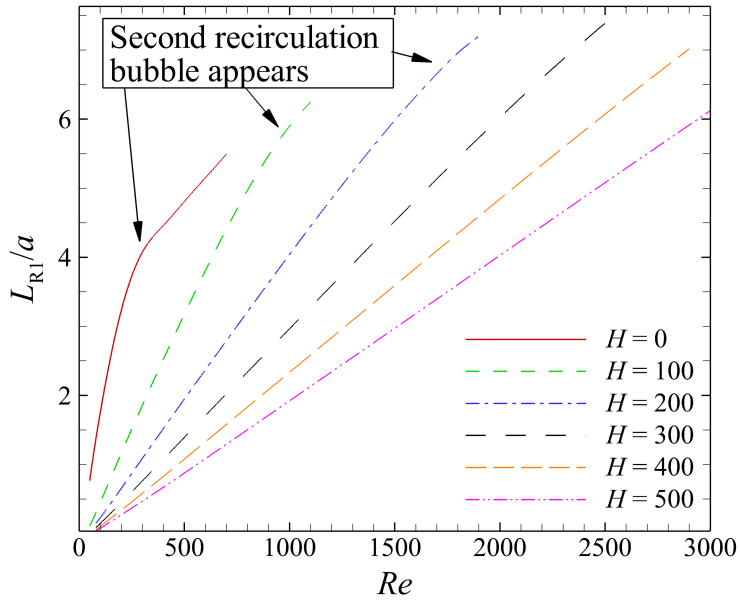

FIGURE 6.3: Primary recirculation bubble length in the function of Re.

$L_z^2 B^2 \sigma/(\rho\nu)$ are large, causing the velocity variations parallel to the direction of the magnetic field to be damped strongly by the Lorentz forces, except in the vicinity of the walls normal to the magnetic field.

The steady base flow is characterised by a recirculation bubble at the downstream of the sharp bend, immediately behind the sharp corner of the inner bend. Figure 6.3 shows the length of the primary recirculation bubble L_{R1}/a as a function of Reynolds number for $\beta = 1$ and for various Hartmann friction parameter. L_{R1}/a increases linearly with increasing Reynolds number at a constant Hartmann friction parameter, and decreases with Hartmann friction parameter when Reynolds number is fixed. When the secondary recirculation bubble starts to form further downstream, the growth of the primary recirculation bubble is reduced. This is visible at $H = 0$, where at $Re \simeq 300$, the gradient decreases. Similar gradient decreases are seen for $H = 100$ $Re = 700$, the increase of friction parameter from 0 to 500 leads to a decrease in L_{R1}/a of approximately 20%, 49%, 63%, 71% and 76% for $H = 100$, 200, 300, 400 and 500, respectively.

Figure 6.4 shows the property of the streamwise velocity for $Re = 700$ and friction parameter ranging from 0 (non-MHD) to 500 at two channel sections: $x = -a$ (at the

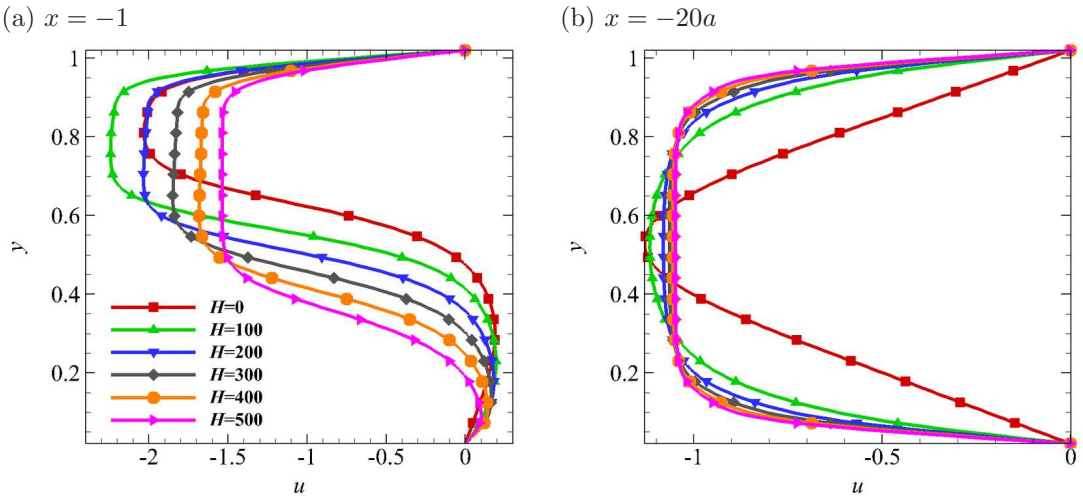

FIGURE 6.4: Streamwise velocity profile at (a) $x = -1$ and (b) $x = -20a$ in the outlet channel under the effect of Hartmann friction parameter, $0 \leq H \leq 500$.

primary recirculation bubble) and $x = -20a$ (further downstream where the flow has recorded its fully developed state). Figure 6.4(a) shows u-velocity at $x = -a$, where the velocity is positive at the bottom representing the backflow in the primary recirculation bubble and negative at the top representing the main bulk flow. As the friction parameter is increased, the damping effect is observed to be more profound. The magnitude of the main bulk flow is lowest at $H = 0$ compared to the rest is because of the appearance of the secondary recirculation bubble which inhibiting the direction of the flow in x-direction. For $H \geq 100$, the secondary recirculation bubble fails to formed causing the flow in x-direction to be larger. For $H > 0$, streamwise velocity component is damped due to the conservation of mass flow. Figure 6.4(b) represents the numerical fully developed velocity profile that agrees well with the analytical velocity profile discussed in equation (6.1) and figure 6.2. The flow at the channel core experienced intense velocity damping, whereas the flow near the wall accelerates significantly.

Dousset & Pothérat (2008), in their study of flow around a cylinder under a strong axial magnetic field with blockage ratio $\beta = 0.25$, found that the recirculation bubble length behind the cylinder (L_R/d) collapsed when plotted against $Re/H^{4/5}$, meanwhile Hussam *et al.* (2012b) proposed a more general relationship incorporating the blockage ratio against scaling $Re^{0.844}H^{-0.711}B^{0.166}$. A similar analysis is conducted here to find a general relationship for L_{R1}/a against control parameters Re, H and β. A non-linear optimization was performed to obtain exponents A, B and C maximizing the square

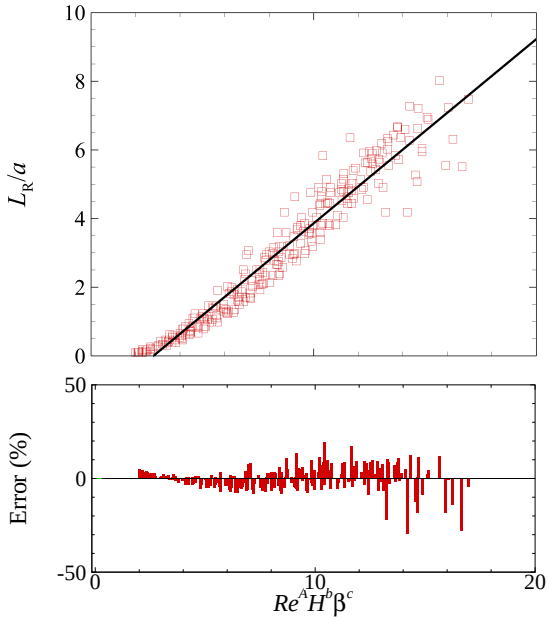

FIGURE 6.5: Collapse of primary recirculation bubble over ranges of Hartmann friction parameter $25 \leq H \leq 500$, Reynolds number $10 \leq Re \leq 2000$ and bend opening ratio $0.2 \leq \beta \leq 1$ when plotted against $Re^{0.9568} H^{-0.6480} \beta^{-0.6005}$. The error of the predicted equation with the actual recirculation length is shown in the second figure. The correlation coefficient is $R^2 = 0.9963$.

of the correlation coefficient (R^2) of a linear least-squares fit to the L_{R1}/a data when plotted against $Re^A H^B \beta^C$. For $Re < Re_{\mathrm{c,u}}$, the optimal exponents were determined to be $A = 0.9568$, $B = -0.6480$ and $C = -0.6005$ with $R^2 = 0.9963$. This reveals a nearly linear increase in L_{R1}/a with increasing Re, while increasing either H or β serve to reduce the bubble length. Hence, decreasing H has a similar effect of increasing Re in primary bubble formation which may affect the tendency of the flow to destabilise. Here, the universal relationship between the primary recirculation bubble length, Re, H and β is approximated by

$$L_{R1}/a = 0.1713 Re^{0.9568} H^{-0.6480} \beta^{-0.6005} - 0.2367, \tag{6.2}$$

and the agreeable collapse of the data obtained is shown in figure 6.5.

It is noted that a non-asymptotic region appears at very small L_{R1}/a that might not be accurate due to a numerical artefact caused by the size of the mesh that is not small enough to capture very small sized bubble. The collapse of data in equation (6.2) and figure 6.5 can be further improved by removing the non-asymptotic region and the

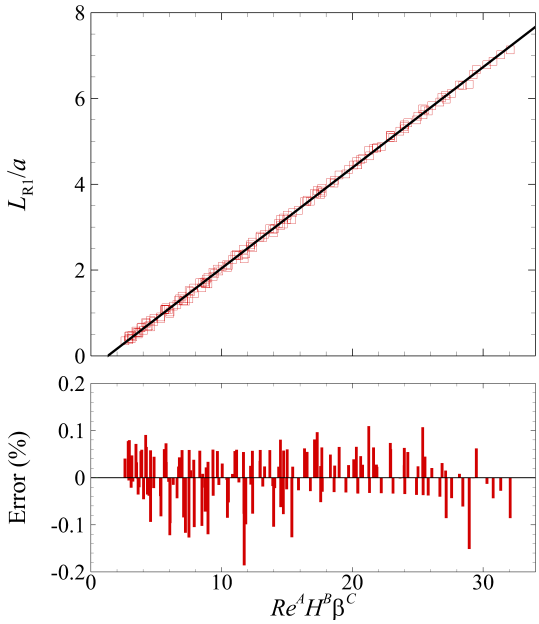

FIGURE 6.6: Collapse of primary recirculation bubble over ranges of Hartmann friction parameter $25 \leq H \leq 500$, Reynolds number $10 \leq Re \leq 1800$ and bend opening ratio $0.2 \leq \beta \leq 1$ when plotted against $Re^{0.9726} H^{-0.7192} \beta^{-0.6350}$. Only regime before the onset of the formation of the secondary recirculation bubble is considered. The error of the predicted equation with the actual recirculation length is shown in the second figure. The correlation coefficient is $R^2 = 0.9917$.

regime where the second bubble exists because the growth of the primary recirculation bubble concerning Reynolds number is entirely linear before the appearance of the second bubble. Thus, by limiting the range of Reynolds numbers $Re < Re_{\mathrm{R2}}$ and $Re \gtrsim Re_{\mathrm{R1}}$, a linear trend line with a better correlation with the data of L_{R1} can be achieved. The new optimum exponents are, $A = 0.9726$, $B = -0.7192$ and $C = -0.6350$ with improved $R^2 = 0.999$. The universal relationship can be estimated by

$$L_{R1}/a = 0.0.2344 Re^{0.9726} H^{-0.7192} \beta^{-0.6350} - 0.3014, \tag{6.3}$$

which is depicted in figure 6.6. Notice in figure 6.6 the significant reduction in error for each data point for this revised correlation (6.3) compared to that in (6.2) shown in figure 6.5.

Equation 6.3 indicates that at constant Hartmann friction parameter and bend opening ratio, the length of the primary recirculation bubble is linearly proportional to Reynolds number. On the other hand, the increase in Hartmann friction parameter and bend opening ratio makes the length of the bubble decrease and vice versa.

6.3.2 Phase state diagram

This subsection discusses the regimes that exist in the MHD flow for bend opening ratio $\beta = 1$. Figure 6.7 categorizes the flow in a range of Re with the effect of H into several regimes. The threshold Reynolds numbers for the formation of first and second bubbles captured by the numerical simulations are represented by Re_{R1} and Re_{R2}, respectively. The critical Reynolds number at the onset of unsteadiness is denoted by Re_{c}. The finite value of Re_{R1} seen in this study is a numerical artefact of finite spatial resolution behind the sharp corner. Theoretically, a sharp edge always creates separation in a flow, even at $Re \approx 0$ (Taneda 1979). The curves of $N = 1$ and $N = 10$ in the figure represent the interaction parameter for a square cross section duct (aspect ratio, $\alpha = 1$). The SM82 model is only valid in the region on the right side of the curve of $N = 1$. Larger N gives more accurate numerical solution for MHD flow. Ducts with larger depth in the spanwise (z-direction) would scale the curves to lower Hartmann numbers.

Similar to what was seen in the hydrodynamic case in § 4.3, due to the hysteretic behaviour caused by the 180-degree sharp corner, the flow has two critical Reynolds numbers to define the transitions between the steady and unsteady regions. These are the lower critical Reynolds number $Re_{\mathrm{c,l}}$ and upper critical Reynolds number $Re_{\mathrm{c,u}}$. Both critical Reynolds numbers are recorded in figure 6.7.

As with the hydrodynamic case considered in chapter 4, the onset of unsteadiness of this flow strongly depends on the initial state of the base flow. Lower critical Reynolds number is reached when the simulation is started from scratch or at much lower Reynolds number than the targeted Reynolds number. On the other hand, a steady flow transitions to unsteady at $Re = Re_{\mathrm{c,u}}$ if the Reynolds number is increased incrementally. Similarly to the hydrodynamic flow, this hysteresis most probably occurs because of the sharp edge of the inner bend wall. A transient change in the velocity in the inlet occurred when the Reynolds number of a simulation is changed. The magnitude of the perturbation is proportional to the difference between the new Reynolds number and the previous. This creates a perturbation at the upstream of the bend, which if the perturbation is large enough, it will be amplified near the sharp corner (as discussed in Chapters 4 and 5) and causes the downstream flow to be unsteady. However, a stable steady-state solution can be preserved by incrementally increasing Reynolds number to an unsteady threshold $Re_{\mathrm{c,u}}$ well above the threshold $Re_{\mathrm{c,l}}$. These two critical Reynolds numbers are depicted in figure 6.7 with the striped region denot-

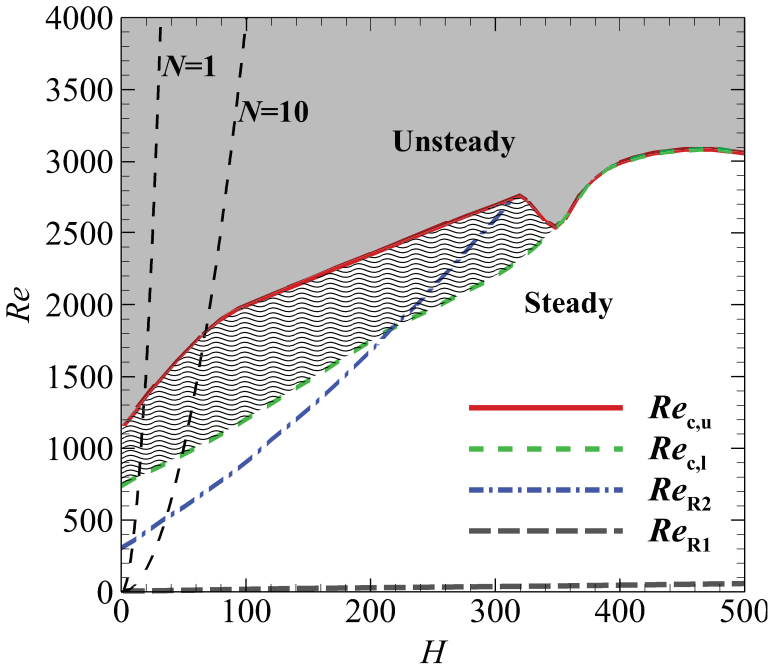

FIGURE 6.7: Critical Reynolds number where transitions from steady to unsteady, and Re where the secondary recirculation bubble starts to appear for $0 \leq H \leq 500$. The grey region indicates unsteady regime, the regions below the dashed green line is steady regimes, while the yellow region is where the primary and secondary recirculation bubbles coexist in the downstream duct. For guidance in relation to the applicability of the SM82 model (requiring high N), $N = 1$ and $N = 10$ dashed curves representing the interaction parameters for a square cross section duct have been included on the plot.

ing the range of Reynolds numbers over which hysteretic behaviour was observed. A representative flow within this region is shown in figure 6.8.

The gap between $Re_{\mathrm{c,u}}$ and $Re_{\mathrm{c,l}}$ increases as H increased from $H = 0$ to 100. Beyond $H = 100$, both critical Reynolds numbers increase almost parallel with increasing Hartmann friction parameter. Although at low Hartmann friction parameter, Re_{R2} is lower than both critical Reynolds numbers, due to its quadratic relationship with H, there is a point it overlaps with the critical Reynolds numbers. The uninterrupted trends at the intercept of $Re_{\mathrm{R2}}(H)$ with $Re_{\mathrm{c,l}}(H)$ shows that the secondary recirculation bubble does not affect the mechanism that causes the flow to become unsteady. However, as $Re_{\mathrm{c,u}}(H)$ and $Re_{\mathrm{c,l}}(H)$ intersect, $Re_{\mathrm{c,u}}(H)$ starts to sharply decrease with H. The reason for this decrease is that the absence of the secondary recirculation bubble causes the shear layer of the primary recirculation to become longer and thinner; hence, making it susceptible to Kelvin–Helmholtz instability as seen in backward-facing step

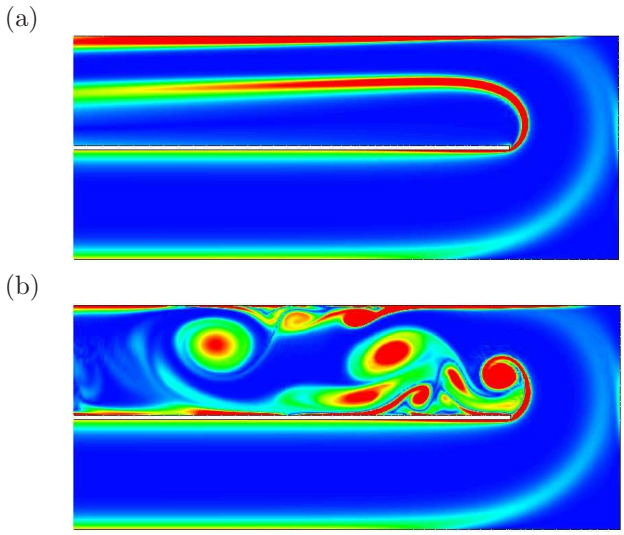

FIGURE 6.8: Vorticity magnitude contour plots for the flow at $Re = 2000$, $H = 200$ obtained by initializing the flow with a solution from (a) a steady solution at lower Re and (b) an unsteady solution at higher Re. The contours were plotted using red-blue color scheme which indicates maximum-zero magnitude of the vorticity, respectively.

flows with large expansion ratios (Lanzerstorfer & Kuhlmann 2012; Gautier & Aider 2014). Kelvin–Helmholtz instability is two-dimensional; thus, it may occur in the Q2D MHD flow.

Figure 6.9 shows contours of the magnitude of vorticity for $Re = 1500$ across a range of H. The flow is strongly unsteady when there is no magnetic field effect (Figure 6.9(a)). As the intensity of applied magnetic field increases, the vortex shedding formed in the channel becomes weaker, similar with the observation in a confined jet flow by Lee *et al.* (2005). Figure 6.9(b) shows the dampened vortices in the downstream duct when H is increased to 100. As H increases to 200 and beyond, the flow becomes steady with decreasing size of bubbles as per equation (6.3).

The effect of the bend opening ratio on the unsteady flow regime is now considered. From the magnitude of the vorticity contours in the unsteady flow shown in Figure 6.10, $\beta = 0.2$ produces very strong vortices behind the sharp bend compared to $\beta = 0.5, 1$ and 2. This smallest gap ratio shows that vorticity from both the inner and outer sides of the gap interact, vorticity from the shear layers is rolled into vortices which initiate unsteady flow immediately behind the bend. The flow at smaller opening ratio can sustain the high magnitude of vorticity further downstream compared to the larger opening ratio. However, the unsteady flow in $\beta = 2$ can sustain the vorticity further

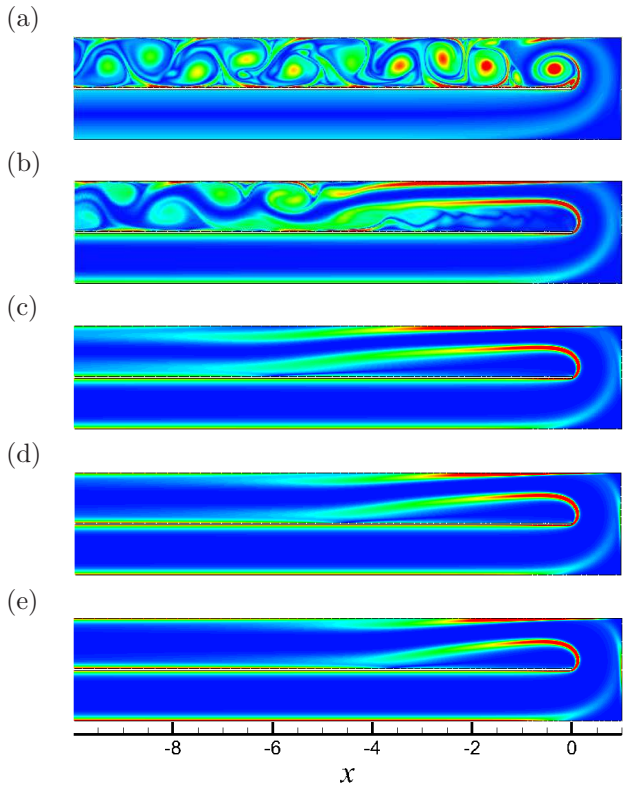

FIGURE 6.9: Magnitude of vorticity contours for $Re = 1500$ in unsteady-state flow regime at (a) $H = 0$, (b) $H = 100$, and steady flow regime at (c) $H = 200$, (d) $H = 300$, and (e) $H = 400$. The contours were plotted using red-blue color scheme which indicates maximum-zero magnitude of the vorticity, respectively.

compared to $\beta = 1$. This might be due to the effective opening ratio for $\beta = 2$ being smaller compared to 1 as a consequence of the formation of a large recirculation bubble in the bend near the outer wall. Figure 6.11 demonstrates the presence of the large recirculation bubble for $\beta > 1$ which delimits the motion of the bulk flow from moving further horizontally, forcing it to move upward earlier than $\beta = 1$. This bubble also narrows the opening for the bulk flow to pass through, acting as a slip wall instead of a non-slip condition on the actual wall, which sees the bulk flow accelerates at the bend, hence creating a more unstable flow compared to $\beta = 1$. However, as Hartmann friction parameter increases, the bend recirculation bubble is also damped significantly. This result is because the magnetic field prohibits the boundary layer to travel far from the wall; hence, inhibiting flow separation at the walls upstream of the bend at high Hartmann friction parameter.

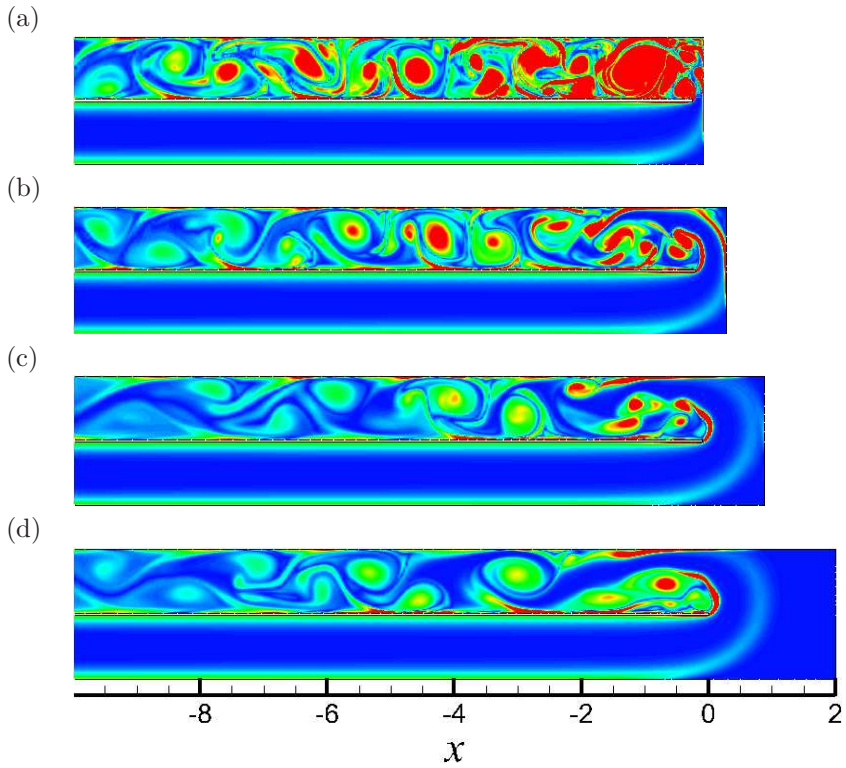

FIGURE 6.10: The structure of the unsteady flow at $Re = 1200$ and $H = 100$ for (a) $\beta = 0.2$, (b) $\beta = 0.5$,(c) $\beta = 1$ and (d) $\beta = 2$ started from scratch. The contours were plotted using red-blue color scheme which indicates maximum-zero magnitude of the vorticity, respectively.

6.4 Quasi-two-dimensional flow with heated side wall

This section discusses the effect of the strong external imposed magnetic field onto the heat transfer efficiency from the heated side wall of the 180-degree sharp bend.

6.4.1 Heat transfer efficiency and pressure drop

Figure 6.12 shows the temperature field for three different bend opening ratios: (a) $\beta = 0.2$, (b) $\beta = 1$ and (c) $\beta = 2$ at $Re = 600$ and $H = 300$. The temperature field in the figures is represented by dark-light contours indicating cold-hot fluid, respectively. The inlet channel is filled with cold fluid in all three conditions until the side wall transfers heat into the cold fluid to be convected to the outlet. From the temperature field contour in the figure, it can be seen that smaller bend opening ratio has thinner thermal boundary layer at the heated side wall and convects more heat to the outlet.

The heat transfer from the heated wall within the fluid is determined by the Nusselt number Nu, which represents the ratio of convective to conductive heat transfer. The

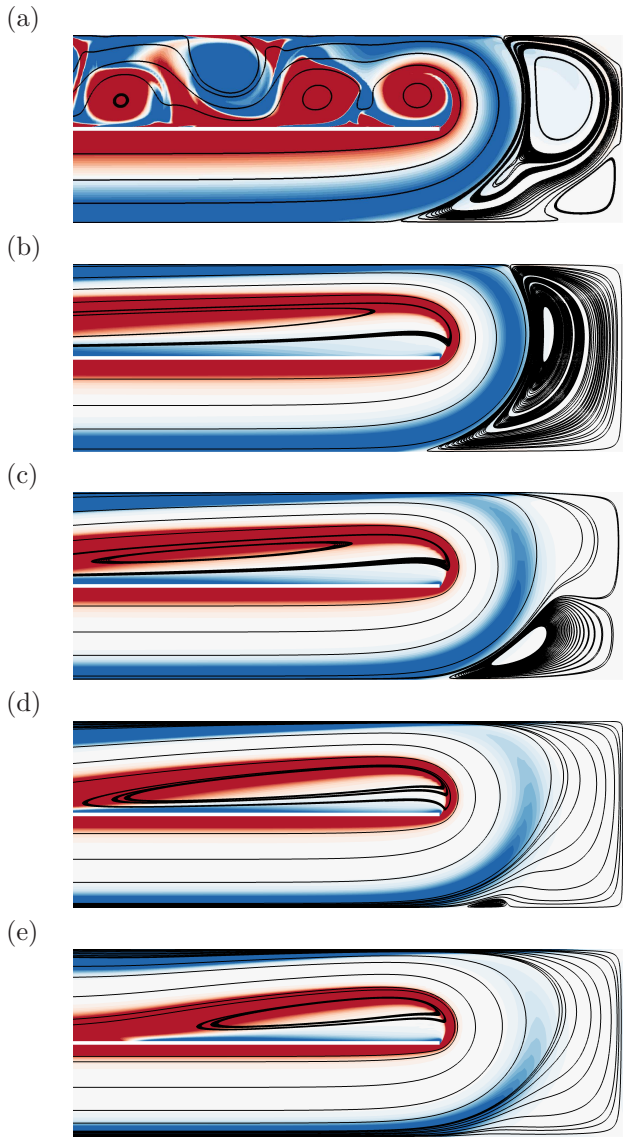

FIGURE 6.11: The influence of Hartmann friction parameter to the bend at the far end of the bend wall for the flow at $Re = 1500$, $\beta = 2$ with (a) $H = 0$, (b) $H = 100$, (c) $H = 200$, (d) $H = 300$, and (e) $H = 400$.

effect of the bend opening ratio and Hartmann friction parameter on heat transfer at the heated side wall is presented in figure 6.13. It can be seen that at very small bend opening ratio, the effect of Hartmann friction parameter is insignificant. However, as the bend width becomes larger, the heat transfer becomes more efficient, especially at higher Reynolds number. It is evident that as Hartmann friction parameter increased, the rate of heat transfer is also increased, the same observation was also seen in studies done numerically by Nigam & Singh (1960); Lahjomri *et al.* (2002) for MHD flow through a parallel-plate channel and experimentally by Sukoriansky *et al.* (1989)

FIGURE 6.12: Instantaneous temperature contour plots for $Re = 600$, $H = 300$ at (a) $\beta = 0.2$, (b) $\beta = 1$ and (c) $\beta = 2$. Temperature field level contours are represented by dark and light for cold and hot fluid, respectively.

for MHD flow in straight rectangular channels. Sukoriansky *et al.* (1989) found that the heat transfer coefficient dropped as the magnetic field strength increased before it reached its minimum and then went up. In the present study, in a fully developed velocity profile in an empty duct channel, the higher the magnetic field strength, the thinner the Shercliff and Hartmann layers. The thinner layers cause the flow to have higher velocity near the electrically insulated walls as shown in figure 6.4(b). Hence, this improves the heat transfer efficiency between the heated electrically insulated walls and the liquid metal. In the present study, the increase in Nu with H was not seen at low Re (i.e. $Re = 200$), but was detected at $Re \geq 600$. Also, in all cases, the H-dependence was stronger at larger β, presumably because of the significant effect that H had on the end-wall flow at these β values. It is noted that the strongest relationship for Nu was against Re, with Nu increasing from $\simeq 1.8$ to $\simeq 6.5$ from $Re = 200$ to $Re = 1500$ at $\beta = 0.2$.

Figure 6.14 shows the effect of the bend opening ratio and Hartmann friction parameter on the pressure drop in the flow. At any constant Reynolds number and bend opening ratio, the pressure drop is consistently increased as Hartmann friction parameter is increased (Dousset & Pothérat 2008). The Lorentz force produced by the interaction of the induced current in the flow with the external magnetic field is opposite to the applied external pressure gradient driving the flow (Barleon *et al.* 1996). The increase of the pressure drop at all four Reynold numbers varies almost linearly with the increase in Hartmann friction parameter, as was observed by Hunt & Stewartson

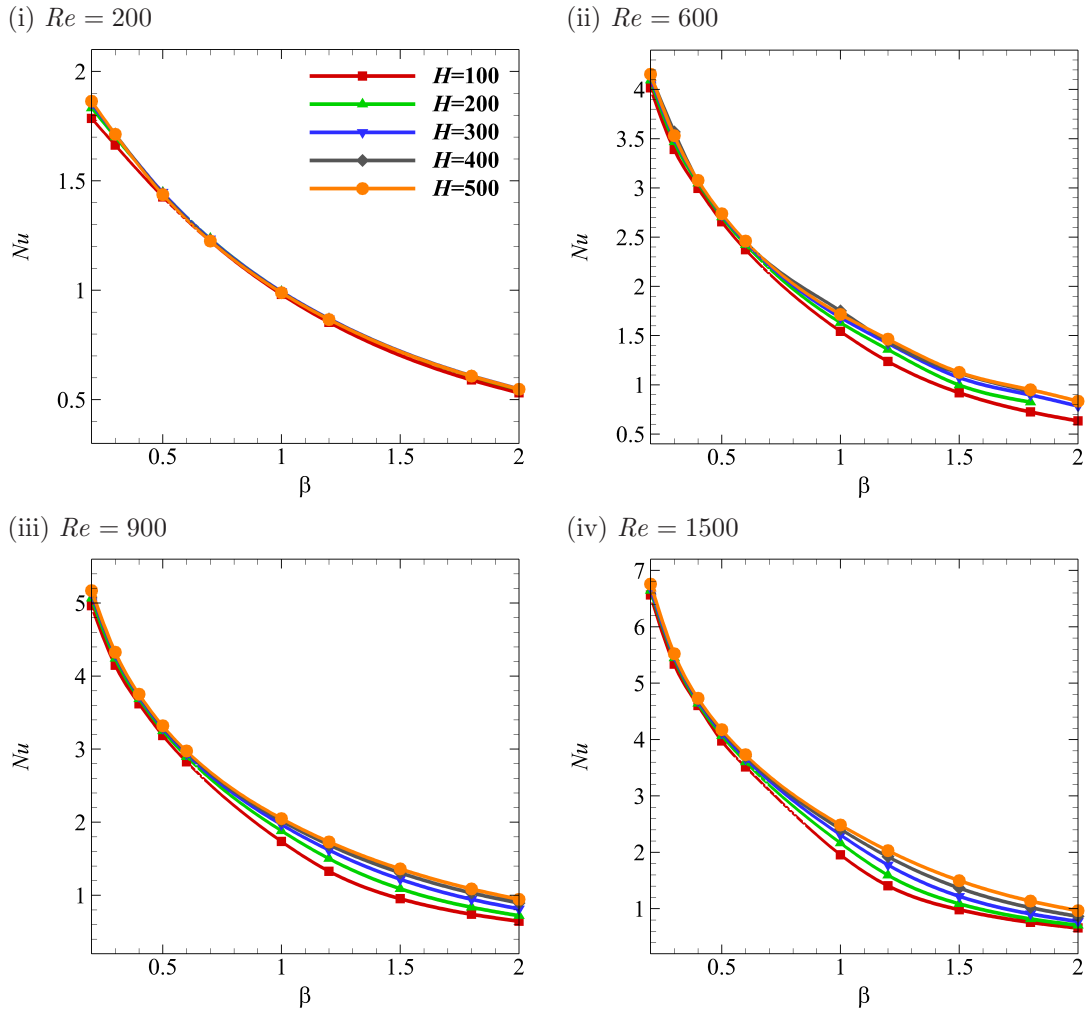

FIGURE 6.13: Plots of Nu against β for various H and Re as shown, revealing the effect of the bend opening ratio on the heat transfer at the side wall.

(1965); Barleon *et al.* (1991); Bühler & Molokov (1995) and Hong-yan *et al.* (2002) for MHD flows in a duct with electrically insulating walls. This is, however, an advantage of using electrically insulating walls compared to conducting walls which the pressure drop is linearly increased with the increase of square of Hartmann friction parameter (Barleon *et al.* 1991, 1996).

To gain a better understanding on the behaviour of the total pressure drop throughout the channel, the measurement of the pressure drop is divided into three parts: along the inlet channel, the bend part and the outlet channel as shown in figure 6.15. The pressure drop of these parts is recorded in figure 6.16. For the inlet and outlet channels, the bend opening ratio does not significantly affect the pressure drop as can be seen from figure 6.16(a) and (b), respectively. The total pressure drop in the inlet and

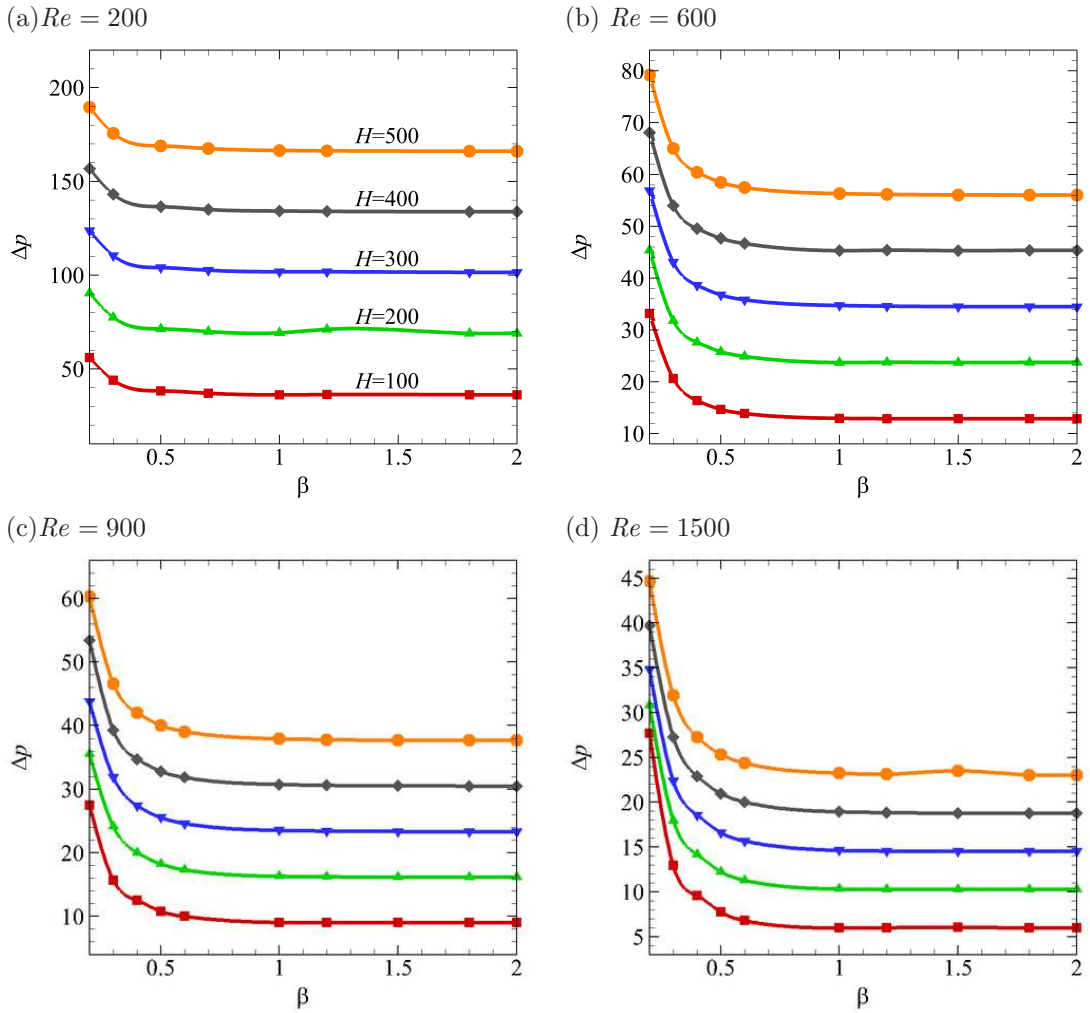

FIGURE 6.14: The effect of the bend opening ratio and Hartmann friction parameter on the pressure drop Δp that is computed with the reference pressure taken at the inlet of the channel.

outlet channels in figure 6.16(c) is almost constant at all Hartmann friction parameters studied. Meanwhile, the pressure drop in the bend shows that the pressure drop is increased as the bend opening ratio decreases at $\beta \leq 0.5$. This clearly indicates that the main factor affecting the pressure drop in the flow is the valve effect in the bend.

Figure 6.17 shows the evolution of pressure drop against Reynolds number and Hartmann friction parameter. The relationship between the pressure drop and the ratio of H/Re is almost linear for most of the bend opening ratio studied between $0.1 \leq H/Re \leq 10$. Some outliers are due to the effect of the significant pressure drop in the bend at $\beta \leq 0.5$. The overall pressure drop appears to be governed by parameter H/Re. The gradient of the linear region round off to three decimal places is ~ 1.002.

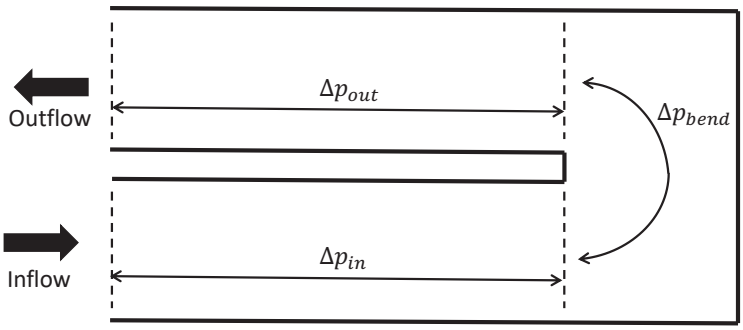

FIGURE 6.15: Diagram showing separate part of the channel where the pressure drops are calculated.

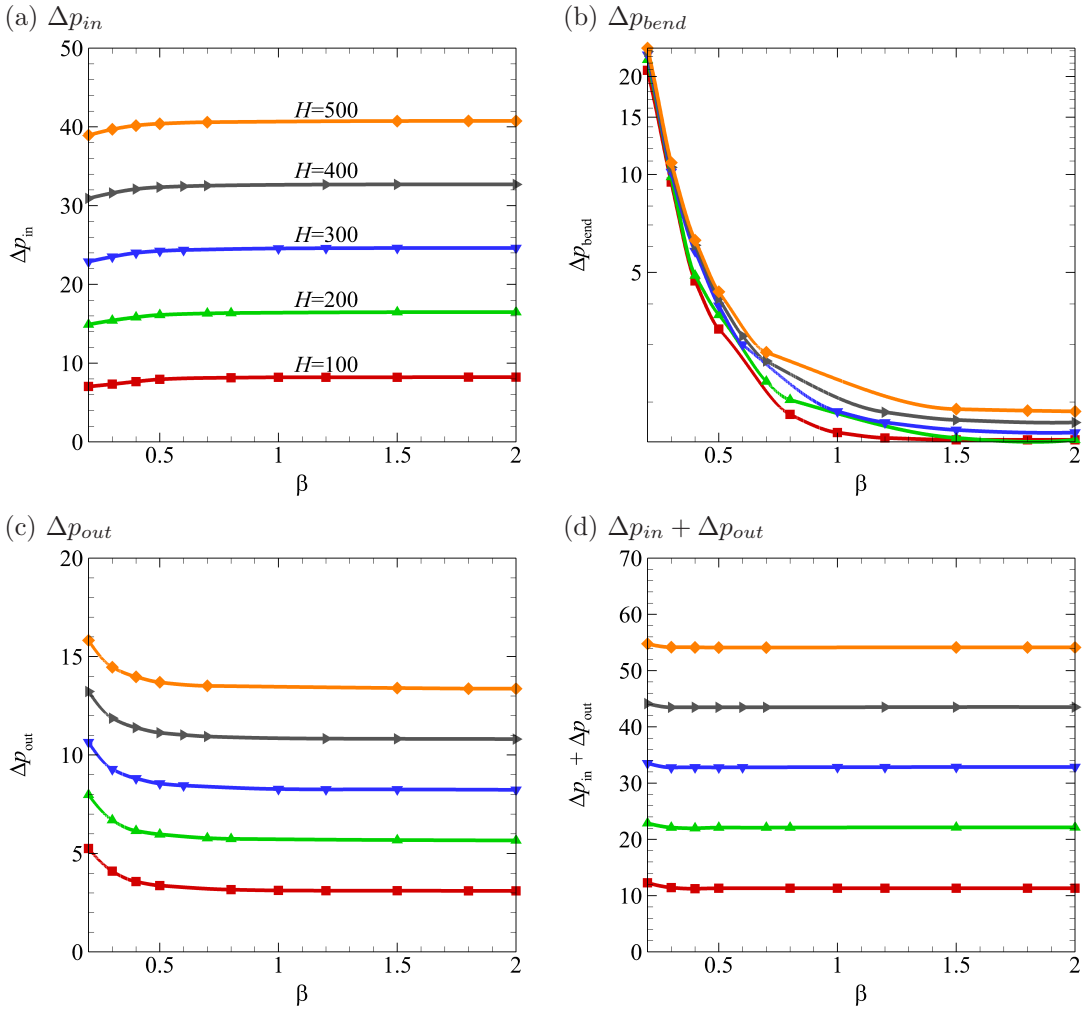

FIGURE 6.16: Pressure drop at different parts of the channel: (a) Inlet channel, (b) bend part, and (c) outlet channel for $Re = 600$. Meanwhile, (d) represents the total pressure drop in both inlet and outlet channels.

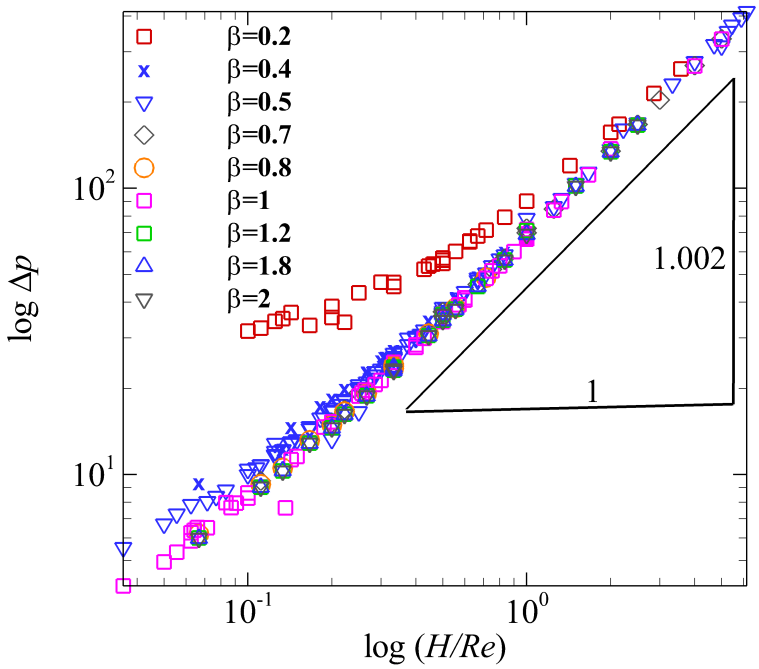

FIGURE 6.17: Streamwise averaged total pressure drop against H/Re at various bend opening ratio.

The relationship between Δp and H/Re can be written as $\Delta p \sim (H/Re)^{1.002}$. A similar correlation was seen in a study on MHD flow past a square cylinder by Dousset (2009), where they found that the base pressure coefficient scales with $(Re/H)^{-1}$ at $Ha \gg 1$. Similarly, in both Dousset (2009) and present studies, the correlation between Δp with H/Re becomes more linear at high H/Re.

6.5 Conclusions

The liquid metal flow past a 180-degree sharp bend under a strong spanwise homogeneous magnetic field has been studied. Due to the high values of the interaction parameter and Hartmann friction parameter ($N \gg 1$ and $Ha \gg 1$), the flow can be assumed to be quasi-two-dimensional. Thus SM82 model can be applied for the numerical simulations (Sommeria & Moreau 1982).

The recirculation bubbles created from the separation and reattachment flow caused by the abrupt change in the geometry of the sharp bend are damped as Hartmann friction parameter increased because of the induced Hartmann braking effect. The length of the primary recirculation bubble, Reynolds number, Hartmann friction parameter

and the bend opening ratio were related as $L_{R1}/a = 0.0.2344Re^{0.9726}H^{-0.7192}\beta^{-0.6350} - 0.3014$.

The thresholds of Reynolds number for the formation of primary recirculation bubble and secondary recirculation bubble is delayed as Hartmann friction parameter is increased. The same trend has been seen for the onset of two-dimensional unseteadiness. Similar to the hydrodynamic flow presented in Chapter 4, hysteretic behavior also was seen in MHD flow. At the onset of the upper critical Reynolds number, vortex shedding seems to appear at far downstream behind the primary recirculation bubble, however at the onset of the lower critical Reynolds number, vortex shedding starts at the sharp bend. However, the behaviour was seen only up to a certain H at when the onset of formation of the secondary recirculation bubble with the upper critical Reynolds number. This shows that the secondary recirculation bubble plays an important role in the flow transition from steady to unsteady.

The effect of the magnetic field to the structure of the flow for different opening ratio, in particular on the thresholds Reynolds number between steady-state and unsteady flow regimes discussed in this study may be very useful for the optimization of heat transfer efficiency for MHD applications.

Chapter 7

Conclusions

This thesis has presented a numerical investigation of the hydrodynamic and MHD flows around a 180-degree sharp bend. The stability of the flow to two- and three-dimensional infinitesimal perturbations and the characteristics of the liquid metal flow subjected to a uniform magnetic field and without magnetic field are considered. The numerical study has been conducted using a spectral-element method. The hydrodynamic flow was simulated two-dimensionally using the Navier–Stokes equations. The linear stability analysis has been employed to predict the three-dimensional characteristics of the hydrodynamic flow. The liquid metal flow under a uniform magnetic field is, however, quasi-two-dimensional in nature. Three main governing parameters in the current quasi-two-dimensional study are the Reynolds number, bend opening ratio and friction parameter. A model for the quasi-two-dimensional MHD flows known as the SM82 model which augments the Navier–Stokes equations with a friction parameter is solved in a two-dimensional domain. The present study provides the fundamental understanding of the flow around a 180-degree sharp bend, and the effect of the geometry and the friction parameter on the heat transfer efficiency.

The following sections concludes the overall findings from Chapters 4, 5 and 6, which are divided into three main areas; global linear stability, convective linear stability and magnetohydrodynamic flow charaterisation.

7.1 Global linear instability

The onset of three-dimensionality of the flow ($Re_{3\mathrm{D}}$) at different bend opening ratio was determined. It was found that $Re_{3\mathrm{D}}$ increases with increasing bend opening ratio until $\beta \approx 1$ where it slightly decreases as β slightly over 1 and remains almost constant until $Re = 2$. The pattern is almost similar to the onset of two-dimensional unsteadiness

where Re_c was found to be steadily increased from $\beta = 0.0125$ until 1 and remained almost constant between $\beta = 1$ until 5.

In the two-dimensional characterisation analysis of the flow, hysteretic behavior has been observed when the simulation is started from different initial conditions. The flow tends to become unsteady at low Reynolds number ($Re = Re_{c,l}$) if a large increment of Reynolds number is imposed into the numerical simulation. However, if Reynolds number is increased gradually with very small increment, the flow could maintain its steady state until $Re_{c,u}$ which is significantly larger than $Re_{c,l}$. It is also observed that the shedding of both conditions is located at the different location; the shedding of the unsteady flow that triggered at $Re = Re_{c,l}$ is started from the sharp bend, whereas for that triggered at $Re = Re_{c,u}$, the shedding originated behind the secondary recirculation bubble.

The linear stability analysis predicted two types of leading eigenmodes that make the steady two-dimensional flow to become three-dimensionally unstable. For $\beta = 0.2$, unsteadiness is via the branch in the form of a spanwise oscillating mode similar to that found in backward-facing step flows with small opening ratios (Lanzerstorfer & Kuhlmann 2012). Meanwhile, for $\beta \geq 0.3$, the unsteadiness sets in via the branch in the form of a stationary mode that is confined in within the primary recirculation bubble which also agrees well with the findings of Barkley *et al.* (2002) and Lanzerstorfer & Kuhlmann (2012) in backward-facing step flows with large opening ratios. Only three-dimensional critical modes were found in the present study. From the non-linear analysis, the critical modes are consistently occurred through a supercritical bifurcation. On the other hand, two-dimensional perturbations (zero wavenumber perturbations) in this flow do not grow through a global instability.

7.2 Transient energy growth

For all bend opening ratio, very substantial transient energy growths were found below the onset of three-dimensional global instability. The optimal initial disturbance fields were typically concentrated near the sharp corner of the inner wall of the bend; behind the bend at small β, and before the bend at large β.

At the onset of transient growth Re_{TG}, the flow is found to be least sensitive to transient amplifications at $\beta = 0.7$. The thin shear layer behind the sharp bend due to the jet-like flow at very small bend opening ratios contributes to the energy amplification

of the disturbance. Meanwhile, for large bend opening ratio, a separation at the first corner of the sharp bend causes the disturbance tends to be amplified starting from the upstream of the bend. However, as Re increases beyond $Re = 100$, the amplification of disturbance at $\beta = 1$ seems to be the smallest in the range of bend opening ratios studied.

The maximum energy amplification factor $G_{\max}$ obtained may reach up to the order of $\sim 10^5$ for $Re \leq 400$. Due to the limitation in computing cost, the present study could only compute G up to $\tau = 25.6$ which is from the trend of G–τ, $\tau_{\max}$ is expected to be larger than 25.6 for $Re > 400$. Although $G(25.6)$ for $Re > 400$ is lower than $G_{\max}$, it almost reaches 10^{10} at $Re = 700$ (steady-state condition) for $\beta = 1$ and 2. This amplification factor is significantly higher than those seen in steady stenotic flow Griffith *et al.* (2010) that is approximately five orders of magnitude and about the same as seen in pulsatile stenotic flow at $Re = 700$ that is about ten orders of magnitude (Blackburn *et al.* 2008b).

Two-dimensional direct numerical simulations where the inflow was perturbed by white noise showed predominantly two-dimensional wave packets that are similar to the optimal disturbances. This means that the optimal transient growth of the flow could be triggered by continuous random perturbations at the upstream of the unstable region. A pronounced amplification in the perturbations energy occurred when the perturbations convected past the amplifying region which is around the sharp corner of the bend. This suggests that the flow can potentially be driven into an unsteady state, despite the flow being run at conditions well below the critical Reynolds number for two-dimensional unsteadiness. This phenomenon could potentially be used to improve the efficiency of heat transfer in heat exchangers designs.

7.3 Magnetohydrodynamic flow

The characteristics of quasi-two-dimensional MHD flows with both interaction parameter N and Hartmann number Ha much greater than unity have been studied using SM82 model for flow simulation. It was found that the critical Reynolds number or the transition from steady to unsteady flow increases with increasing Hartmann number.

In the steady-state flow regime, the effect of Hartmann number on the size of the recirculation bubble is found to be significant. For $\beta = 1$, the secondary recirculation bubble is suppressed completely at $H \gtrsim 220$. This was due to the Lorentz force

which produces a force opposing the flow. The variation in the length of the primary recirculation bubble is determined as a function of Reynolds number, Hartmann friction parameter and bend opening ratio, which results in a universal scaling law $L_{R1}/a = 0.0.2344Re^{0.9726}H^{-0.7192}\beta^{-0.6350} - 0.3014$.

The effect of Hartmann number on heat transfer from the heated side wall is found to be insignificant. However, the heat flux is highly dependent on Re, with heat flux increasing from $\simeq 1.8$ to $\simeq 6.5$ from $Re = 200$ to 500 at $\beta = 0.2$. At constant Ha and Re, the heat flux decreases asymptotically with increasing β.

The overall pressure drop throughout the domain is found to be linearly dependent on the ratio of H/Re. At constant Re, the overall pressure drop reduces asymptotically until $\beta \approx 0.5$. The pressure drop along the inlet and outlet channel are found to be almost constant, meaning that the varying overall pressure drop is found to be due to the valve effect caused by the narrow opening of the bend.

7.4 Suggestion for future works

This thesis has presented in detail the characteristics of the global and convective stability of flow around a 180-degree sharp bend. It has also explored the effect of the strong uniform magnetic field on the stability of the flow and the heat transfer efficiency. However, there are still opportunities to extend the current study in several ways.

The main geometrical features that play important role in 180-degree sharp bend and backward facing step flows is the sharp corner. Another geometrical configuration that has a sharp bend that is widely used in engineering applications is 90-degree bend. The flow in the geometry has been studied experimentally (Taylor *et al.* 1982; Sudo *et al.* 1998, 2001) and numerically (Yeo *et al.* 1991; Spedding *et al.* 2004; Niu & Dou 2013), however, the instabilities in the flow and the nature of the instabilities are not yet understood. It would be beneficial to do a similar analysis as in the present study on 90-degree sharp bend flow to gain better fundamental understanding of the effect of the sharp bend to the flow.

In the present study, the transient growth analysis only considered two-dimensional perturbation fields in hydrodynamic flow because the focus of this study is to relate it to the quasi-two-dimensional MHD flow. Furthermore, the computing cost required to do this analysis is currently prohibitive due to the complicated structure of the flow

around the sharp corner. Thousands of computing hours were dedicated in the present study to study only zero-wavenumber perturbation fields up to $\tau = 25.6$ and $Re = 700$. In the future it will eventually possible with advancing computing power for a wider range of parameters to be conducted including non-zero wavenumbers.

A separate study also can be done to investigate the optimal transient disturbance in quasi-two-dimensional MHD flow around a 180-degree sharp bend. The same approach as used in Chapter 5 and also used in (Hussam *et al.* 2012b) can be applied in the study. From the study, the effect of the additional control parameter, Hartmann parameter, could be elucidated.

Another work that could be done in the future is to investigate a three-dimensional phenomena that have potential to take place around the sharp corner because of the existence of a very large inertia. The three-dimensional phenomena could happen even in MHD flow despite the very high magnetic field. This is a very important open question.

References

Abdessemed, N., Sherwin, S. & Theofilis, V. 2009 Linear instability analysis of low-pressure turbine flows. *J. Fluid Mech.* **628**, 57–83.

Abu-Nada, E. 2008 Application of nanofluids for heat transfer enhancement of separated flows encountered in a backward facing step. *Int. J. Heat Fluid Flow* **29** (1), 242–249.

Airiau, C. & Castets, M. 2004 On the amplification of small disturbances in a channel flow with a normal magnetic field. *Phys. Fluids* **16** (8), 2991–3005.

Alam, M. & Sandham, N. D. 2000 Direct numerical simulation of 'short'laminar separation bubbles with turbulent reattachment. *J. Fluid Mech.* **403**, 223–250.

Albarède, P. & Provansal, M. 1995 Quasi-periodic cylinder wakes and the Ginzburg–Landau model. *J. Fluid Mech.* **291**, 191–222.

Alfvén, H. 1942 On the cosmogony of the solar system. *Stockholms Observatoriums Annaler* **14**, 2–1.

Anderson, Jr., J. 2010 *Fundamentals of Aerodynamics*. Tata McGraw-Hill Education.

Andersson, P., Berggren, M. & Henningson, D. S. 1999 Optimal disturbances and bypass transition in boundary layers. *Phys. Fluids* **11** (1), 134–150.

Armaly, B. F., Durst, F., Pereira, J. & Schönung, B. 1983 Experimental and theoretical investigation of backward-facing step flow. *J. Fluid Mech.* **127**, 473–496.

Astarita, T. & Cardone, G. 2000 Thermofluidynamic analysis of the flow in a sharp 180 turn channel **20** (3), 188–200.

Back, L. & Roschke, E. 1972 Shear-layer flow regimes and wave instabilities and reattachment lengths downstream of an abrupt circular channel expansion. *J. Appl. Mech.* **39** (3), 677–681.

Barkley, D. 1992 Linear stability analysis of rotating spiral waves in excitable media. *Phys. Rev. Lett.* **68** (13), 2090–2093.

Barkley, D., Blackburn, H. & Sherwin, S. 2008 Direct optimal growth analysis for timesteppers. *Int. J. Numer. Methods Fluids* **57** (9), 1435–1458.

Barkley, D., Gomes, M. G. M. & Henderson, R. D. 2002 Three-dimensional instability in flow over a backward-facing step. *J. Fluid Mech.* **473**, 167–190.

Barkley, D. & Henderson, R. D. 1996 Three-dimensional floquet stability analysis of the wake of a circular cylinder. *J. Fluid Mech.* **322**, 215–242.

Barleon, L., Casal, V. & Lenhart, L. 1991 MHD flow in liquid-metal-cooled blankets. *Fusion Eng. Des.* **14** (3), 401–412.

Barleon, L., Mack, K. J. & Stieglitz, R. 1996 The MEKKA-facility: A flexible tool to investigate MHD-flow phenomena. Tech. rep. Institute of Applied Thermo- and Fluid Dynamics, Research Centre Karlsruhe.

Barton, I. 1997a The entrance effect of laminar flow over a backward-facing step geometry. *Int. J. Numer. Methods Fluids* **25** (6), 633–644.

Barton, I. 1997b Laminar flow over a backward-facing step with a stream of hot particles. *Int. J. Heat Fluid Flow* **18** (4), 400–410.

Batchelor, G. 1967 An introduction to fluid mechanics, 615 pp. *Cambridge University Press, New York* .

Bayly, B. 1986 Three-dimensional instability of elliptical flow. *Phys. Rev. Lett.* **57** (17), 2160.

Bergman, T. L. & Incropera, F. P. 2011 *Introduction to heat transfer*. John Wiley & Sons.

Bers, A. 1975 Linear waves and instabilities. In *Plasma Physics–Les Houches 1972*.

Biau, D., Soueid, H. & Bottaro, A. 2008 Transition to turbulence in duct flow. *J. Fluid Mech.* **596**, 133–142.

Blackburn, H., Barkley, D. & Sherwin, S. J. 2008a Convective instability and transient growth in flow over a backward-facing step. *J. Fluid Mech.* **603**, 271–304.

Blackburn, H., Sherwin, S. J. & Barkley, D. 2008b Convective instability and transient growth in steady and pulsatile stenotic flows. *J. Fluid Mech.* **607**, 267–277.

Blackburn, H. M. & Sherwin, S. 2007 Instability modes and transition of pulsatile stenotic flow: pulse-period dependence. *J. Fluid Mech.* **573**, 57–88.

Boccaccini, L., Giancarli, L., Janeschitz, G., Hermsmeyer, S., Poitevin, Y., Cardella, A. & Diegele, E. 2004 Materials and design of the european demo blankets. *J. Nucl. Mater.* **329**, 148–155.

Boeck, T., Krasnov, D., Rossi, M. & Zikanov, O. 2009 Transient growth in MHD duct flow. *Advances in Turbulence XII* pp. 829–832.

Boeck, T., Krasnov, D., Thess, A. & Zikanov, O. 2008 Large-scale intermittency of liquid-metal channel flow in a magnetic field. *Phys. Rev. Lett.* **101** (24), 244501.

Branover, H. 1978 *Magnetohydrodynamic flow in ducts*. Halsted Press, New York, NY.

Branover, H., Eidelman, A. & Nagorny, M. 1995 Use of turbulence modification for heat transfer enhancement in liquid metal blankets. *Fusion Eng. Des.* **27**, 719–724.

Branover, H., Mond, M. & Lykoudis, P. 1985 Single- and multi-phase flows in an electromagnetic field: Energy, metallurgical, and solar applications((book)). *New York, American Institute of Aeronautics and Astronautics, Inc.(Progress in Astronautics and Aeronautics.* **100**.

Brede, M., Eckelmann, H. & Rockwell, D. 1996 On secondary vortices in the cylinder wake. *Phys. Fluids* **8** (8), 2117–2124.

Briggs, R. J. 1964 *Electron-stream interaction with plasmas*. MIT.

Bühler, L. 1996 Instabilities in quasi-two-dimensional magnetohydrodynamic flows. *J. Fluid Mech.* **326**, 125–150.

Bühler, L. & Molokov, S. 1995 Magnetohydrodynamic flows in ducts with insulating coatings. *Magnetohydrodynamics (New York)* **30** (4).

Burr, U., Barleon, L., Müller, U. & Tsinober, A. 2000 Turbulent transport of momentum and heat in magnetohydrodynamic rectangular duct flow with strong sidewall jets. *J. Fluid Mech.* **406**, 247–279.

Cantwell, C., Barkley, D. & Blackburn, H. 2010 Transient growth analysis of flow through a sudden expansion in a circular pipe. *Phys. Fluids* **22** (3), 034101.

Carmo, B. S., Sherwin, S. J., Bearman, P. W. & Willden, R. H. 2008 Wake transition in the flow around two circular cylinders in staggered arrangements. *J. Fluid Mech.* **597**, 1–29.

Cassells, O. G., Hussam, W. K. & Sheard, G. J. 2016 Heat transfer enhancement using rectangular vortex promoters in confined quasi-two-dimensional magnetohydrodynamic flows. *Int. J. Heat Mass Tran.* **93**, 186–199.

Chatterjee, D., Chatterjee, K., Mondal, B. & Hui, N. B. 2014 Wall-confined flow and heat transfer around a square cylinder at low reynolds and hartmann numbers. *Heat Tran. Asian Res.* **43** (5), 459–475.

Chatterjee, D. & Gupta, S. K. 2015 MHD flow and heat transfer behind a square cylinder in a duct under strong axial magnetic field. *Int. J. Heat Mass Tran.* **88**, 1–13.

Chomaz, J., Huerre, P. & Redekopp, L. 1988 Bifurcations to local and global modes in spatially developing flows. *Phys. Rev. Lett.* **60** (1), 25.

Chomaz, J.-M. 2005 Global instabilities in spatially developing flows: non-normality and nonlinearity. *Annu. Rev. Fluid Mech.* **37**, 357–392.

Chun, K.-B. & Sung, H. 1996 Control of turbulent separated flow over a backward-facing step by local forcing. *Exp. Fluids* **21** (6), 417–426.

Chung, Y. M., Tucker, P. G. & Roychowdhury, D. 2003 Unsteady laminar flow and convective heat transfer in a sharp 180 bend. *Int. J. Heat Fluid Flow* **24** (1), 67–76.

Corbett, P. & Bottaro, A. 2000 Optimal perturbations for boundary layers subject to stream-wise pressure gradient. *Phys. Fluids* **12** (1), 120–130.

Cruchaga, M. A. 1998 A study of the backward-facing step problem using a generalized streamline formulation. *Int J Numer Method Biomed Eng.* **14** (8), 697–708.

Davidson, P. 1995 Magnetic damping of jets and vortices. *J. Fluid Mech.* **299**, 153–186.

Davidson, P. 1999 Magnetohydrodynamics in materials processing. *Annu. Rev. Fluid Mech.* **31** (1), 273–300.

Davidson, P. A. 2001 *An introduction to magnetohydrodynamics*, , vol. 25. Cambridge University Press.

Dobran, F. 2012 Fusion energy conversion in magnetically confined plasma reactors. *Prog. Nucl. Energ.* **60**, 89–116.

Dousset, V. 2009 Numerical simulations of mhd flows past obstacles in a duct under externally applied magnetic field. PhD thesis, Coventry University, UK.

Dousset, V. & Pothérat, A. 2008 Numerical simulations of a cylinder wake under a strong axial magnetic field. *Phys. Fluids* **20** (1), 017104.

Drake, D. G. & Abu-Sitta, A. M. 1966 Magnetohydrodynamic flow in a rectangular channel at high hartmann number. *Zeitschrift für Angewandte Mathematik und Physik (ZAMP)* **17** (4), 519–528.

Drazin, P. G. & Reid, W. H. 2004 *Hydrodynamic stability*. Cambridge University Press.

Dušek, J., Le Gal, P. & Fraunié, P. 1994 A numerical and theoretical study of the first hopf bifurcation in a cylinder wake. *J. Fluid Mech.* **264**, 59–80.

Ellingsen, T. & Palm, E. 1975 Stability of linear flow. *Phys. Fluids* **18** (4), 487–488.

Erturk, E. 2008 Numerical solutions of 2-D steady incompressible flow over a backward-facing step, part i: High Reynolds number solutions. *Comput. Fluids* **37** (6), 633–655.

Farrell, B. F. 1988 Optimal excitation of perturbations in viscous shear flow. *Phys. Fluids* **31** (8), 2093.

Frank, M., Barleon, L. & Müller, U. 2001 Visual analysis of two-dimensional magnetohydrodynamics. *Phys. Fluids* **13** (8), 2287–2295.

Furuichi, N., Takeda, Y. & Kumada, M. 2003 Spatial structure of the flow through an axisymmetric sudden expansion. *Exp. Fluids* **34** (5), 643–650.

Gardner, R. & Lykoudis, P. 1971 Magneto-fluid-mechanic pipe flow in a transverse magnetic field. part 1. Isothermal flow. *J. Fluid Mech.* **47** (04), 737–764.

Gautier, N. & Aider, J.-L. 2014 Upstream open loop control of the recirculation area downstream of a backward-facing step. *Comptes Rendus Mécanique* **342** (6), 382–388.

Gerard-Varet, D. 2002 Amplification of small perturbations in a hartmann layer. *Phys. Fluids* **14** (4), 1458–1467.

Ghia, K., Osswald, G. & Ghia, U. 1989 Analysis of incompressible massively separated viscous flows using unsteady navier–stokes equations. *Int. J. Numer. Methods Fluids* **9** (8), 1025–1050.

Giannetti, F. & Luchini, P. 2007 Structural sensitivity of the first instability of the cylinder wake. *J. Fluid Mech.* **581**, 167–197.

Griffith, M., Leweke, T., Thompson, M. & Hourigan, K. 2008 Steady inlet flow in stenotic geometries: convective and absolute instabilities. *J. Fluid Mech.* **616**, 111–133.

Griffith, M., Thompson, M., Leweke, T. & Hourigan, K. 2010 Convective instability in steady stenotic flow: optimal transient growth and experimental observation. *J. Fluid Mech.* **655**, 504–514.

Griffith, M., Thompson, M., Leweke, T., Hourigan, K. & Anderson, W. 2007 Wake behaviour and instability of flow through a partially blocked channel. *J. Fluid Mech.* **582**, 319–340.

Hamid, A. H., Hussam, W. K., Pothérat, A. & Sheard, G. J. 2015 Spatial evolution of a quasi-two-dimensional Kármán vortex street subjected to a strong uniform magnetic field. *Phys. Fluids* **27** (5), 053602.

Hamid, A. H., Hussam, W. K. & Sheard, G. J. 2016 Combining an obstacle and electrically driven vortices to enhance heat transfer in a quasi-two-dimensional mhd duct flow. *J. Fluid Mech.* **792**, 364–396.

Hammad, K. J., Ötügen, M. V. & Arik, E. B. 1999 A PIV study of the laminar axisymmetric sudden expansion flow. *Exp. Fluids* **26** (3), 266–272.

Hammond, D. A. & Redekopp, L. G. 1998 Local and global instability properties of separation bubbles. *Eur. J. Mech. B-Fluid* **17** (2), 145–164.

Hartmann, J. & Lazarus, F. 1937 *Hg-dynamics II: Experimental investigations on the flow of mercury in a homogeneous magnetic field*. Levin & Munksgaard, Copenhagen.

Heilbron, J. L. 1979 *Electricity in the 17th and 18th centuries: A study of early modern physics*. Univ of California Press.

Henderson, R. D. 1997 Nonlinear dynamics and pattern formation in turbulent wake transition. *J. Fluid Mech.* **352**, 65–112.

Henderson, R. D. & Barkley, D. 1996 Secondary instability in the wake of a circular cylinder. *Phys. Fluids* **8** (6), 1683–1685.

Henningson, D. S., Lundbladh, A. & Johansson, A. V. 1993 A mechanism for bypass transition from localized disturbances in wall-bounded shear flows. *J. Fluid Mech.* **250**, 169–207.

Hirota, M., Fujita, H., Syuhada, A., Araki, S., Yoshida, T. & Tanaka, T. 1999 Heat/mass transfer characteristics in two-pass smooth channels with a sharp 180-deg turn. *Int. J. Heat Mass Tran.* **42** (20), 3757–3770.

Hong-yan, W., Yi-can, W. & Xiao-xong, H. 2002 Preliminary analysis of liquid metal MHD pressure drop in the blanket for the FDS. *Plasma Sci. Technol* **4** (5), 1497.

Huang, H. & Li, B. 2010 Heat transfer enhancement of free surface MHD-flow by a protrusion wall. *Fusion Eng. Des.* **85** (7), 1496–1502.

Huerre, P. & Monkewitz, P. A. 1985 Absolute and convective instabilities in free shear layers. *J. Fluid Mech.* **159**, 151–168.

Hughes, M., Pericleous, K. & Cross, M. 1995 The numerical modelling of DC electromagnetic pump and brake flow. *Appl. Math. Modell.* **19** (12), 713–723.

Hunt, J. & Stewartson, K. 1965 Magnetohydrodynamic flow in rectangular ducts. ii. *J. Fluid Mech.* **23** (03), 563–581.

Hussam, W. K., Thompson, M. C. & Sheard, G. J. 2011a Dynamics and heat transfer in a quasi-two-dimensional MHD flow past a circular cylinder in a duct at high Hartmann number. *Int. J. Heat Mass Tran.* **54** (5), 1091–1100.

Hussam, W. K., Thompson, M. C. & Sheard, G. J. 2011b Dynamics and heat transfer in a quasi-two-dimensional mhd flow past a circular cylinder in a duct at high hartmann number. *Int. J. Heat Mass Tran.* **54** (5), 1091–1100.

Hussam, W. K., Thompson, M. C. & Sheard, G. J. 2012a Enhancing heat transfer in a high Hartmann number magnetohydrodynamic channel flow via torsional oscillation of a cylindrical obstacle. *Phys. Fluids* **24** (11), 113601.

Hussam, W. K., Thompson, M. C. & Sheard, G. J. 2012b Optimal transient disturbances behind a circular cylinder in a quasi-two-dimensional magnetohydrodynamic duct flow **24**, 024105.

Johnson, T. & Patel, V. 1999 Flow past a sphere up to a reynolds number of 300. *J. Fluid Mech.* **378**, 19–70.

Kaiktsis, L., Karniadakis, G. E. & Orszag, S. A. 1991 Onset of three-dimensionality, equilibria, and early transition in flow over a backward-facing step. *J. Fluid Mech.* **231**, 501–528.

Kaiktsis, L., Karniadakis, G. E. & Orszag, S. A. 1996 Unsteadiness and convective instabilities in two-dimensional flow over a backward-facing step. *J. Fluid Mech.* **321**, 157–187.

Kanaris, N., Albets, X., Grigoriadis, D. & Kassinos, S. 2013 Three-dimensional numerical simulations of magnetohydrodynamic flow around a confined circular cylinder under low, moderate, and strong magnetic fields. *Phys. Fluids* **25** (7), 074102.

Karcher, C., Kocourek, V. & Schulze, D. 2003 Experimental investigations of electromagnetic instabilities of free surfaces in a liquid metal drop. In *International Scientific Colloquium, Modelling for Electromagnetic Processing*, pp. 105–110.

Karniadakis, G. & Sherwin, S. 2013 *Spectral/hp element methods for computational fluid dynamics*. Oxford University Press.

Karniadakis, G. E., Israeli, M. & Orszag, S. A. 1991 High-order splitting methods for the incompressible navier-stokes equations. *J. Comput. Phys.* **97** (2), 414–443.

Kendall, J. 1985 Experimental study of disturbances produced in a pre-transitional laminar boundary layer by weak freestream turbulence. In *18th Fluid Dynamics and Plasmadynamics and Lasers Conference*, p. 1695.

Kerrebrock, J. L. 1965 Magnetohydrodynamic generators with nonequilibrium ionization. *AIAA J* **3** (4), 591–601.

Kerswell, R. R. 2002 Elliptical instability. *Annu. Rev. Fluid Mech.* **34** (1), 83–113.

Kharicha, A., Wu, M., Ludwig, A. & Karimi-Sibaki, E. 2016 Simulation of the electric signal during the formation and departure of droplets in the electroslag remelting process. *Metall. Mater. Trans. B* **47** (2), 1427–1434.

Koch, W. 2002 On the spatio-temporal stability of primary and secondary crossflow vortices in a three-dimensional boundary layer. *J. Fluid Mech.* **456**, 85–111.

Kolesnikov, Y. B. & Tsinober, A. 1974 Experimental investigation of two-dimensional turbulence behind a grid. *Fluid Dyn.* **9** (4), 621–624.

Krall, K. & Sparrow, E. M. 1966 Turbulent heat transfer in the separated, reattached, and redevelopment regions of a circular tube. *J. Heat Transf.* **88** (1), 131–136.

Krasnov, D., Zienicke, E., Zikanov, O., Boeck, T. & Thess, A. 2004 Numerical study of the instability of the Hartmann layer. *J. Fluid Mech.* **504**, 183–211.

Krasnov, D., Zikanov, O. & Boeck, T. 2012 Numerical study of magnetohydrodynamic duct flow at high Reynolds and Hartmann numbers. *J. Fluid Mech.* **704**, 421–446.

Krasnov, D., Zikanov, O., Rossi, M. & Boeck, T. 2010 Optimal linear growth in magnetohydrodynamic duct flow. *J. Fluid Mech.* **653**, 273–299.

Lahjomri, J., Oubarra, A. & Alemany, A. 2002 Heat transfer by laminar Hartmann flow in thermal entrance region with a step change in wall temperatures: the Graetz problem extended. *Int. J. Heat Mass Tran.* **45** (5), 1127–1148.

Landahl, M. 1977 Dynamics of boundary layer turbulence and the mechanism of drag reduction. *Phys. Fluids* **20** (10), S55–S63.

Landahl, M. 1980 A note on an algebraic instability of inviscid parallel shear flows. *J. Fluid Mech.* **98** (02), 243–251.

Landau, L. & Lifshitz, E. 1976 Mechanics pergamon press. *New York* p. 93.

Lanzerstorfer, D. & Kuhlmann, H. C. 2012 Global stability of the two-dimensional flow over a backward-facing step. *J. Fluid Mech.* **693**, 1–27.

Larson, H. K. 1959 Heat transfer in separated flows. *J. Aerospace Sci.* **26** (11), 731–738.

Le, H., Moin, P. & Kim, J. 1997 Direct numerical simulation of turbulent flow over a backward-facing step. *J. Fluid Mech.* **330**, 349–374.

Le Gal, P., Nadim, A. & Thompson, M. 2001 Hysteresis in the forced stuart–landau equation: application to vortex shedding from an oscillating cylinder. *J. Fluids Struct.* **15** (3), 445–457.

Lee, H., Ha, M. & Yoon, H. 2005 A numerical study on the fluid flow and heat transfer in the confined jet flow in the presence of magnetic field. *Int. J. Heat Mass Tran.* **48** (25), 5297–5309.

Lehoucq, R. B., Sorenson, D. C. & Yang, C. 1998 *ARPACK Users' Guide: Solution of Large-Scale Eigenvalue Problems with Implicitly Restarted Arnoldi Methods*. SIAM.

Leweke, T. & Williamson, C. 1998 Cooperative elliptic instability of a vortex pair. *J. Fluid Mech.* **360**, 85–119.

Liou, T.-M., Chen, C.-C., Tzeng, Y.-Y. & Tsai, T.-W. 2000 Non-intrusive measurements of near-wall fluid flow and surface heat transfer in a serpentine passage. *Int. J. Heat Mass Tran.* **43** (17), 3233–3244.

Liou, T.-M., Tzeng, Y.-Y. & Chen, C.-C. 1999 Fluid flow in a 180 deg sharp turning duct with different divider thicknesses. *J. Turbomach.* **121** (3), 569–576.

Lyon, R. N. 1952 Liquid-metals handbook. *Tech. Rep.*. Committee on the Basic Properties of Liquid Metals, Office of Naval Research.

Malang, S., Tillack, M., Barleon, L., Baumgärtner, S., Borgstedt, H., Bühler, L., Dammel, F., Feuerstein, H., Fischer, U., Gabel, K. *et al.* 1995 Development of self-cooled liquid metal breeder blankets. *EUR(Luxembourg)* .

Malghan, V. 1996 History of mhd power plant development. *Energ. Convers. Manage.* **37** (5), 569–590.

Marquillie, M. & Ehrenstein, U. 2003 On the onset of nonlinear oscillations in a separating boundary-layer flow. *J. Fluid Mech.* **490**, 169–188.

Metzger, D. E. & Sahm, M. K. 1986 Heat transfer around sharp 180-deg turns in smooth rectangular channels. *J. Heat Transfer* **108** (3), 500–506.

Moffatt, H. 1967 On the suppression of turbulence by a uniform magnetic field. *J. Fluid Mech.* **28** (03), 571–592.

Monkewitz, P. A., Huerre, P. & Chomaz, J.-M. 1993 Global linear stability analysis of weakly non-parallel shear flows. *J. Fluid Mech.* **251**, 1–20.

Moore, D. & Saffman, P. 1975 The instability of a straight vortex filament in a strain field. In *Proceedings of the Royal Society of London A: Mathematical, Physical and Engineering Sciences*, , vol. 346, pp. 413–425. The Royal Society.

Moreau, R. 1990 *The equations of magnetohydrodynamics*. Springer.

Morkovin, M. V. 1985 Bypass transition to turbulence and research desiderata .

Morley, N., Burris, J., Cadwallader, L. & Nornberg, M. 2008 Gainsn usage in the research laboratory. *Rev. Sci. Instrum.* **79** (5), 056107.

Morley, N. B., Smolentsev, S., Barleon, L., Kirillov, I. R. & Takahashi, M. 2000 Liquid magnetohydrodynamicsrecent progress and future directions for fusion. *Fusion Eng. Des.* **51**, 701–713.

Mück, B., Günther, C., Müller, U. & Bühler, L. 2000 Three-dimensional mhd flows in rectangular ducts with internal obstacles. *J. Fluid Mech.* **418**, 265–295.

Müller, U. & Bühler, L. 2001 *Magnetofluiddynamics In Channels And Containers*. Springer.

Mullin, T., Seddon, J., Mantle, M. & Sederman, A. 2009 Bifurcation phenomena in the flow through a sudden expansion in a circular pipe. *Phys. Fluids* **21** (1), 014110.

Mutschke, G., Gerbeth, G., Shatrov, V. & Tomboulides, A. 1997 Two-and three-dimensional instabilities of the cylinder wake in an aligned magnetic field. *Phys. Fluids* **9**, 3114.

Nait Bouda, N., Schiestel, R., Amielh, M., Rey, C. & Benabid, T. 2008 Experimental approach and numerical prediction of a turbulent wall jet over a backward facing step. *Int. J. Heat Fluid Flow* **29** (4), 927–944.

Natarajan, R. & Acrivos, A. 1993 The instability of the steady flow past spheres and disks. *J. Fluid Mech.* **254**, 323–344.

Nigam, S. & Singh, S. 1960 Heat transfer by laminar flow between parallel plates under the action of transverse magnetic field. *Quart. J. Mech. Appl. Math.* **13** (1), 85–97.

Niu, L. & Dou, H.-S. 2013 Stability study of flow in a 90 bend based on the energy gradient theory. In *IOP Conference Series: Materials Science and Engineering*, , vol. 52, p. 022006. IOP Publishing.

Park, G. S. & Seo, K. 2003 A study on the pumping forces of the magnetic fluid linear pump. *Magnetics, IEEE Transactions on* **39** (3), 1468–1471.

Pauley, L. L., Moin, P. & Reynolds, W. C. 1990 The structure of two-dimensional separation. *J. Fluid Mech.* **220**, 397–411.

Pierrehumbert, R. 1984 Local and global baroclinic instability of zonally varying flow. *J. Atmos. Sci.* **41** (14), 2141–2162.

Pierrehumbert, R. 1986 Universal short-wave instability of two-dimensional eddies in an inviscid fluid. *Phys. Rev. Lett.* **57** (17), 2157.

Pollard, A. 1981 A contribution on the effects of inlet conditions when modelling stenoses using sudden expansions. *J. Biomech.* **14** (5), 349–355.

Pothérat, A. 2007 Quasi-two-dimensional perturbations in duct flows under transverse magnetic field. *Phys. Fluids* **19**, 074104.

Pothérat, A. & Klein, R. 2014 Why, how and when MHD turbulence at low Rm becomes three-dimensional. *J. Fluid Mech.* **761**, 168–205.

Pothérat, A. & Schweitzer, J.-P. 2011 A shallow water model for magnetohydrodynamic flows with turbulent hartmann layers. *Phys. Fluids* **23** (5), 055108.

Pothérat, A., Sommeria, J. & Moreau, R. 2000a 2D models for MHD flows. *Comptes Rendus de l'Académie des Sciences-Series IIB-Mechanics-Physics-Astronomy* **328** (2), 129–134.

Pothérat, A., Sommeria, J. & Moreau, R. 2000b An effective two-dimensional model for MHD flows with transverse magnetic field. *J. Fluid Mech* **424**, 75–100.

Pothérat, A., Sommeria, J. & Moreau, R. 2002 Effective boundary conditions for magnetohydrodynamic flows with thin hartmann layers. *Phys. Fluids* **14**, 403.

Pothérat, A., Sommeria, J. & Moreau, R. 2005 Numerical simulations of an effective two-dimensional model for flows with a transverse magnetic field. *J. Fluid Mech* **534**, 115–143.

Provansal, M., Mathis, C. & Boyer, L. 1987 Bénard-von kármán instability: transient and forced regimes. *J. Fluid Mech.* **182** (1), 1.

Purrington, R. D. 1997 *Physics in the nineteenth century*. Rutgers University Press.

Reddy, S. C., Schmid, P. J., Baggett, J. S. & Henningson, D. S. 1998 On the stability of streamwise streaks and transition thresholds in plane channel flows. *J. Fluid Mech.* **365**, 269–303.

Roberts, P. H. 1967 An introduction to magnetohydrodynamics. *An Introduction to Magnetohydrodynamics, by PH Roberts. Textbook published by Longmans, Green and Co ltd, London, 1967* **1**.

Ryan, K., Butler, C. J. & Sheard, G. J. 2012 Stability characteristics of a counter-rotating unequal-strength batchelor vortex pair. *J. Fluid Mech.* **696**, 374–401.

Sapardi, A. M., Hussam, W. K., Pothérat, A. & Sheard, G. J. 2017 Linear stability of confined flow around a 180-degree sharp bend. *J. Fluid Mech.* **822**, 813–847.

Schäfer, F., Breuer, M. & Durst, F. 2009 The dynamics of the transitional flow over a backward-facing step. *J. Fluid Mech.* **623**, 85–119.

Schmid, P. J. & Henningson, D. S. 2001 *Stability and transition in shear flows*, , vol. 142. Springer.

Schumann, U. 1976 Numerical simulation of the transition from three-to two-dimensional turbulence under a uniform magnetic field. *J. Fluid Mech.* **74** (01), 31–58.

Schumm, M., Berger, E. & Monkewitz, P. A. 1994 Self-excited oscillations in the wake of two-dimensional bluff bodies and their control. *J. Fluid Mech.* **271**, 17–53.

Shah, R. 1972 Laminar flow forced convection heat transfer and flow friction in straight and curved ducts: A summary of analytical solutions(Application of laminar flow solutions for heat transfer and flow friction to design of heat exchangers).

Sheard, G., Thompson, M. & Hourigan, K. 2003a A coupled Landau model describing the Strouhal–Reynolds number profile of a three-dimensional circular cylinder wake. *Phys. Fluids* **15**, L68.

Sheard, G., Thompson, M. & Hourigan, K. 2003b From spheres to circular cylinders: the stability and flow structures of bluff ring wakes. *J. Fluid Mech.* **492**, 147–180.

Sheard, G. J. 2009 Flow dynamics and wall shear-stress variation in a fusiform aneurysm. *J. Eng. Math.* **64** (4), 379–390.

Sheard, G. J. 2011 Wake stability features behind a square cylinder: focus on small incidence angles. *Journal of Fluid Structure* **27** (5), 734–742.

Sheard, G. J., Fitzgerald, M. J. & Ryan, K. 2009 Cylinders with square cross-section: wake instabilities with incidence angle variation. *J. Fluid Mech.* **630**, 43–69.

Sheard, G. J., Thompson, M. C. & Hourigan, K. 2004 Asymmetric structure and non-linear transition behaviour of the wakes of toroidal bodies. *Eur. J. Mech. B-Fluid* **23** (1), 167–179.

Shercliff, J. 1953 Steady motion of conducting fluids in pipes under transverse magnetic fields. In *Proc. Camb. Phil. Soc*, , vol. 49, pp. 136–144. Cambridge Univ Press.

Shercliff, J. A. 1965 *Textbook of magnetohydrodynamics*. Pergamon Press, New York.

Sherwin, S. & Blackburn, H. M. 2005 Three-dimensional instabilities and transition of steady and pulsatile axisymmetric stenotic flows. *J. Fluid Mech.* **533**, 297–327.

Slavin, V. S., Gavrilov, V. M., Zelinsky, N. I. & Bozhkov, A. R. 2001 Magnetohydrodynamics generator with plasma layers as power source aboard a hypersonic airplane. *J. Propul. Power* **17** (1), 19–26.

Smolentsev, S. & Moreau, R. 2007 One-equation model for quasi-two-dimensional turbulent magnetohydrodynamic flows. *Phys. Fluids* **19** (7), 078101.

Smolentsev, S., Moreau, R., Bühler, L. & Mistrangelo, C. 2010 MHD thermofluid issues of liquid-metal blankets: phenomena and advances. *Fusion Eng. Des.* **85** (7), 1196–1205.

Sommeria, J. & Moreau, R. 1982 Why, how, and when, MHD turbulence becomes two-dimensional. *J. Fluid Mech.* **118** (1), 507–518.

Spedding, P., Benard, E. & McNally, G. 2004 Fluid flow through 90 degree bends. *Asia-Pac. J. Chem. Eng.* **12** (1-2), 107–128.

Sturrock, P. A. 1958 Kinematics of growing waves. *Phys. Rev.* **112** (5), 1488.

Sudo, K., Sumida, M. & Hibara, H. 1998 Experimental investigation on turbulent flow in a circular-sectioned 90-degree bend. *Exp. Fluids* **25** (1), 42–49.

Sudo, K., Sumida, M. & Hibara, H. 2001 Experimental investigation on turbulent flow in a square-sectioned 90-degree bend. *Exp. Fluids* **30** (3), 246–252.

Sukoriansky, S., Klaiman, D., Branover, H. & Greenspan, E. 1989 Mhd enhancement of heat transfer and its relevance to fusion reactor blanket design. *Fusion Eng. Des.* **8**, 277–282.

Taneda, S. 1979 Visualization of separating stokes flows. *J. Phys. Soc. Jpn* **46**, 1935–1942.

Taylor, A., Whitelaw, J. & Yianneskis, M. 1982 Curved ducts with strong secondary motion: velocity measurements of developing laminar and turbulent flow. *J. Fluids Eng.* **104** (3), 350–359.

Terzi, V. & Alexander, D. 2004 Numerical investigation of transitional and turbulent backward-facing step flows .

Thompson, M., Leweke, T. & Williamson, C. 2001 The physical mechanism of transition in bluff body wakes. *J. Fluids Struct.* **15** (3), 607–616.

Thompson, M. C., Hourigan, K. & Sheridan, J. 1996 Three-dimensional instabilities in the wake of a circular cylinder. *Exp. Therm Fluid Sci.* **12** (2), 190–196.

Thompson, M. C. & Le Gal, P. 2004 The stuart–landau model applied to wake transition revisited. *Eur. J. Mech. B-Fluid* **23** (1), 219–228.

Thomson, G. 1958 Thermonuclear fusion: The task and the triumph. *New Sci.* **3**.

Thomson, J. 1876 On the origin of windings of rivers in alluvial plains, with remarks on the flow of water round bends in pipes. *Proc. Roy. Soc. London* **25** (171-178), 5–8.

Tomboulides, A. G. & Orszag, S. A. 2000 Numerical investigation of transitional and weak turbulent flow past a sphere. *J. Fluid Mech.* **416** (1), 45–73.

Vo, T., Montabone, L. & Sheard, G. J. 2014 Linear stability analysis of a shear layer induced by differential coaxial rotation within a cylindrical enclosure. *J. Fluid Mech.* **738**, 299–334.

Vo, T., Montabone, L. & Sheard, G. J. 2015 Effect of enclosure height on the structure and stability of shear layers induced by differential rotation. *J. Fluid Mech.* **765**, 45–81.

Walter, H. U. 2012 *Fluid sciences and materials science in space: a European perspective*. Springer Science & Business Media.

Wang, T.-S. & Chyu, M. K. 1994 Heat convection in a 180-deg turning duct with different turn configurations. *J. Thermophys. Heat Tr.* **8** (3), 595–601.

Wee, D., Yi, T., Annaswamy, A. & Ghoniem, A. F. 2004 Self-sustained oscillations and vortex shedding in backward-facing step flows: Simulation and linear instability analysis. *Phys. Fluids* **16** (9), 3361–3373.

White, F. 1991 *Viscous Fluid Flow*. McGraw-Hill, New York.

Williamson, C. H. 1988 Defining a universal and continuous strouhal–reynolds number relationship for the laminar vortex shedding of a circular cylinder. *Phys. Fluids* **31** (10), 2742–2744.

Yamashita, H., Izumi, R. & Kushida, G. 1987 Fluid flow and heat transfer in a two-dimensional miter-bend: Study of unsteady motion by numerical calculations: Heat transfer, combustion, power, thermophysical properties. *JSME Int. J.* **30** (259), 93–99.

Yamashita, H., Izumi, R., Kushida, G. & Mizuno, T. 1986 Fluid flow and heat transfer in a two-dimensional miter-bend: 1st report, experiments and analyses. *B. JSME* **29** (258), 4164–4169.

Yang, J.-C., Qi, T.-Y., Ni, M.-J. & Wang, Z.-H. 2016 Flow patterns of gainsn liquid on inclined stainless steel plate under a range of magnetic field. *Fusion Eng. Des.* **109**, 861–865.

Yeo, R., Wood, P. & Hrymak, A. 1991 A numerical study of laminar 90-degree bend duct flow with different discretization schemes. *J. Fluids Eng.* **113** (4), 563–568.

Zhang, L. & Pothérat, A. 2013 Influence of the geometry on the two-and three-dimensional dynamics of the flow in a 180 degree sharp bend. *Phys. Fluids* **25**, 053605.

Zikanov, O. & Thess, A. 1998 Direct numerical simulation of forced mhd turbulence at low magnetic reynolds number. *J. Fluid Mech.* **358**, 299–333.

Zikanov, O. Y. 1996 On the instability of pipe poiseuille flow. *Phys. Fluids* **8** (11), 2923–2932.